University of Strathclyde

Department of Civil and Environmental Engineering

Exploiting induced carbonate precipitation to improve reservoir storage integrity and geothermal system efficiency

Philip James Salter

A Thesis presented in fulfilment of

the requirements for the degree of

Doctor of Philosophy

2026

Declaration of Authorship

This thesis is the result of the author's original research. It has been composed by the author and had not been previously submitted for the examinations which has led to the award of a degree.

Signed: 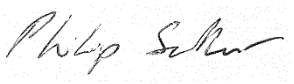 Date: 26/01/2026

Enzyme induced bio-block, Glasgow – August 2024

"*Nature does not hurry, yet everything is accomplished. The leaves do not struggle to fall, nor the rivers to flow; they simply follow the logic of the earth. The most resilient systems are those that adapt, regenerate, and integrate rather than dominate. If we are to build a future in harmony with our planet, we must learn from these principles – not by imposing control, but by working with natural processes. Sustainable innovation does not mean resisting nature's forces; it means aligning with them.*" – Inspired by Lao Tzu

Abstract

Induced carbonate precipitation (ICP), through microbial (MICP) and enzyme-induced (EICP) pathways, offers a sustainable means of reinforcing porous media, tuning permeability, and enhancing thermal performance across soils, engineered backfills, and subsurface formations for applications in carbon storage, geothermal energy, and construction. Yet its wider deployment is prevented by limited understanding of how pore-scale precipitation processes shape bulk material behaviour, particularly when relying on crude, low-cost enzyme extracts essential for scalable treatments.

This thesis aims to show how pore-scale precipitation processes govern material performance and how they can be directed to achieve specific outcomes. Time-lapse X-ray computed tomography and flow modelling revealed that density driven mixing controls where and when $CaCO_3$ forms, with precipitation concentrated in regions of high enzyme availability. This highlights that density driven flow, such as injecting cementing solution above enzyme solution in deep formations, can be exploited to deliberately control where precipitation occurs.

By varying enzyme source, organic additives, flow regimes, and pH, new levers were identified for modulating reaction kinetics and lag periods. Crude soybean urease generates extended protein-mediated lag phases that allow cementing and enzyme solutions to be mixed ex situ prior to injection. This strategy produced more uniform precipitation, even across fine layers (<100 μm) that were otherwise inaccessible to bacterial cells in MICP and enabled extended treatments of up to 25 cycles due to sustained uniform precipitation. As an alternative, pulsed-flow injection was shown through flow modelling to enhance pore-scale mixing between cementing and enzyme solutions, offering another pathway for improved treatment uniformity.

Linking these optimised treatments to bulk properties showed that repeated EICP injections could achieve unconfined compressive strengths up to 17.9 MPa while increasing thermal conductivity by ~600% and preserving hydraulic conductivity, a tuneable balance between reinforcement and flow. XCT demonstrated that strength gains were associated with crystal bridging at grain contacts, which also facilitated efficient heat transfer.

Functional optimisation using conductive and phase-change additives established ICP-treated porous media as multifunctional composites. Expanded graphite formed

conductive networks that delivered anisotropic heat conduction, while paraffin-infused graphite enabled latent heat storage. Additives thus delivered equal or greater thermal enhancements with far fewer treatment cycles than enzyme-only treatments.

Overall, this work demonstrates that precipitation uniformity and mixing dynamics are central to ICP performance. By connecting pore-scale mechanisms to engineering outcomes and extending ICP to multifunctional applications, this thesis advances both the mechanistic understanding and the practical potential of biomineralisation, moving it significantly closer to deployment in CO_2 sequestration, geothermal energy, and sustainable construction.

Acknowledgments

Firstly, I would like to thank my wife, Tania, without whose love and support this work would not have been possible. I am also grateful to my daughter, Maria, and son, Alexander, who give me inspiration every day to keep striving to make the world a better place.

I would like to thank my supervisors, Professor Katherine Dobson and Dr James Minto. I began this PhD with no background in X-ray imaging or image analysis, and Kate's patience, guidance, and encouragement were invaluable in helping me develop in this area. James has been a constant source of support, always willing to help others, and a brilliant scientist. His practical approach made a real difference to my early experiments and troubleshooting.

I am also grateful to the technical staff who supported my experiments, particularly Derek McNee and Jim Francis, whose expertise and assistance were crucial across different stages of this project.

Finally, I would like to thank the GeoNetZero Centre for Doctoral Training. The programme provided not only a strong academic foundation in the role of the subsurface in the net-zero energy transition, but also a community of lifelong friends through its many field trips and activities.

Table of Contents

List of Figures

List of Tables

List of Abbreviations

ACC – Amorphous Calcium Carbonate

BS – Bacterial Solution

BTES – Borehole Thermal Energy Storage

CCS – Carbon Capture and Sequestration

CF – Milled Carbon Fibre

CFD – Computational Fluid Dynamics

CS – Cementing Solution

CT – Computed Tomography

EICP – Enzyme-Induced Carbonate Precipitation

EG – Expanded Graphite

ES – Enzyme Solution

GF – Graphite Flake

ICP – Induced Carbonate Precipitation

IRT – Infrared Thermography

K – Hydraulic Conductivity

JBB – Ground Jack Beans

JBM – Commercial Jack Bean Meal

MICP – Microbial-Induced Carbonate Precipitation

NFM – Non-fat Milk Powder

OD600 – Optical Density at 600nm

PI-EG – Paraffin-Infused Expanded Graphite

SB-EICP – Soybean-Based Enzyme-Induced Carbonate Precipitation

UCS – Unconfined Compressive Strength

XCT – X-ray Computed Tomography

λ – Thermal Conductivity

Chapter 1: Introduction

1.1 Motivation for Research

Microbial and enzyme induced carbonate precipitation (MICP and EICP), have emerged as versatile biocementation techniques with applications spanning environmental engineering, energy systems, and geotechnical materials. Originally developed to reduce permeability and strengthen soils, induced carbonate precipitation (ICP) is now recognised for its potential across a wide range of subsurface technologies, offering a controllable means of forming $CaCO_3$ in situ to alter flow, mechanical behaviour, and thermal transport. Its flexibility makes it especially attractive in sectors where conventional grouts or cements are either too viscous, or too disruptive.

One of the most significant application areas is geological carbon capture and sequestration (CCS). Global warming has already raised average temperatures by 1.45 °C above pre-industrial levels (WMO, 2023), while atmospheric CO_2 concentrations now exceed 420 ppm. Large-scale CCS is therefore needed to complement decarbonisation efforts and mitigate ongoing emissions. The long-term integrity of storage sites depends on effective sealing of leakage pathways, permeability control, and mechanical stability of reservoir and caprock formations; areas where ICP has shown strong potential. Both MICP and EICP can reduce permeability (Peng et al., 2020; Tobler et al., 2018; Yasuhara et al., 2012), stabilise granular media (Meng et al., 2021; Van Paassen, 2009), and seal preferential flow channels or fractures (Zhu et al., 2021), improving overall storage performance.

Beyond CCS, ICP offers advantages in geothermal energy systems (Venuleo et al., 2016), where enhancing soil thermal conductivity can increase the efficiency of ground-source heat pumps and shallow thermal energy storage (Ahmed et al., 2022; Sarbu & Sebarchievici, 2014). In geotechnical engineering, ICP offers advantages over cement and chemical grouts because its low-viscosity solutions can infiltrate fine or sensitive soils with minimal pressure (Fig. 1.1), reducing ground disturbance and enabling treatment in zones that conventional grouts cannot reach. These emerging applications highlight ICP as a multifunctional technology for modifying subsurface flow and mechanical behaviour.

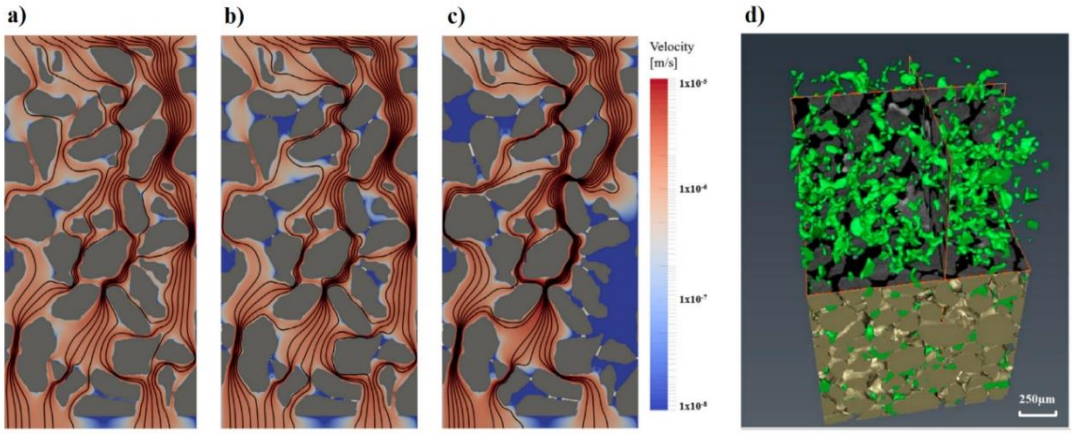

Figure 1.1 Flow path migration during MICP (**a**), (**b**) and (**c**) 2D illustrated representation of gradual calcite precipitation altering flow velocity and direction. Adapted from Minto et al. (2018) (**d**) 3D volume reconstruction of MICP treated silica sand (brown) with calcite bonds (green) reducing permeability and increasing grain connectivity. Adapted from (Terzis & Laloui, 2018)

Despite these advances, controlling ICP reliably remains difficult. The macroscopic behaviour of treated materials ultimately depends on pore-scale biochemical and transport processes that govern ureolysis, ion availability, mixing, and nucleation. Achieving reliable performance requires controlling where carbonate forms, how much is deposited, and how it evolves over repeated treatment cycles. Non-uniform precipitation, sensitivity to enzyme source and reaction conditions, and difficulty predicting permeability or strength outcomes remain key limitations. X-ray computed tomography (XCT) offers a powerful means to resolve these behaviours *in situ*, enabling non-destructive 3D imaging of evolving pore structures and $CaCO_3$ distributions (Dadda et al., 2018; Godinho & Withers, 2018).

These pore-scale precipitation dynamics directly govern the mechanical, hydraulic, and thermal response of treated soils. Enhancements such as increased strength (Almajed et al., 2019), reduced or tuneable permeability (Kirkland et al., 2020; Mo et al., 2021; Peng et al., 2020), and improved thermal conductivity (Martinez et al., 2019; Venuleo et al., 2016; Z. Wang et al., 2019) have been reported, though challenges persist regarding uniformity and long-term durability.

Key uncertainties remain regarding the influence of pore-scale mixing on $CaCO_3$ localisation, the behaviour of different enzyme sources, and the extent to which treatment uniformity can be achieved in heterogeneous media. Addressing these gaps requires a clearer understanding of ureolytic mechanisms, environmental controls, and precipitation processes, which are examined in the sections that follow.

1.2 Fundamentals of Biomineralisation

Biomineralisation induces calcium carbonate ($CaCO_3$) precipitation within soil and rock matrices, strengthening porous media by forming new intergranular contacts and reducing pore space. This can be achieved either microbially (MICP), using urease-producing bacteria, or enzymatically (EICP), by directly introducing urease extracted from biological sources. Both approaches have shown promise for improving unconsolidated soils and sands (Wang et al., 2017). $CaCO_3$ precipitated through ICP strengthens existing contacts between soil grains and creates new ones, increasing unconfined compressive strength and altering the hydromechanical and thermal properties of the treated material.

Because soils and porous rocks both consist of grains, pore bodies, and pore throats, induced carbonate precipitation is relevant for controlling permeability and stability across a range of substrates. Loose sand is frequently used as an analogue for porous rock in CCS studies, since even small permeability changes can divert fluid flow and enhance CO_2 trapping efficiency (Bump et al., 2023; Tobler et al., 2014).

Although carbonate precipitation can be driven by several microbial pathways (denitrification, ferric iron reduction, sulphate reduction), these routes are limited by slow kinetics, costly growth requirements, or undesirable by-products such as hydrogen sulphide (Van Paassen, 2009), and therefore these pathways are not considered further in this thesis. In contrast, urea hydrolysis is more controllable, efficient, and cost-effective, making it the most widely explored pathway for both MICP and EICP.

1.2.1 Urea hydrolysis

The urea hydrolysis reaction is catalysed by the enzyme urease, produced naturally by certain bacterial strains or extracted from plant-based sources. In the presence of dissolved calcium, hydrolysis drives the precipitation of $CaCO_3$, which binds soil grains and alters pore structure.

During the process, urea ($CO(NH_2)_2$) is enzymatically hydrolysed to ammonium (NH_4^+) and bicarbonate (HCO_3^-) ions (Equation 1). To maintain charge balance, hydroxide ions (OH^-) are also generated, raising solution pH and promoting the conversion of bicarbonate to carbonate (CO_3^{2-}) (Equation 2). Meanwhile, calcium chloride ($CaCl_2$), commonly used as the calcium source, dissociates to yield calcium (Ca^{2+}) and

chloride (Cl^-) ions. When the ion activity product of Ca^{2+} and CO_3^{2-} exceeds the solubility product of $CaCO_3$, nucleation occurs and calcite crystals precipitate (Equation 4).

The biochemical sequence can be summarised as follows:

$$CO(NH_2)_2 + 3H_2O \xrightarrow[urease\ enzyme]{} 2NH_4^+ + HCO_3^- + OH^- \quad (1)$$

$$HCO_3^- \rightarrow CO_3^{2-} + H^+ \quad (2)$$

$$CaCl_2 \rightarrow Ca^{2+} + 2Cl^- \quad (3)$$

$$Ca^{2+} + CO_3^{2-} \rightarrow CaCO_3 \quad (4)$$

In MICP, negatively charged groups on bacterial cell walls can promote nucleation by binding Ca^{2+} prior to precipitation (Fig. 1.2). In contrast, EICP lacks this microbial surface interaction, with precipitation occurring directly within the pore fluid. Under standard atmospheric conditions, the dominant polymorph formed is calcite, although other forms such as aragonite may occur depending on the calcium source (Zambare et al., 2020) or under specific environmental conditions, for example in anoxic systems using non-ureolytic pure-culture bacteria (Zhang et al., 2019; Zhang et al., 2014).

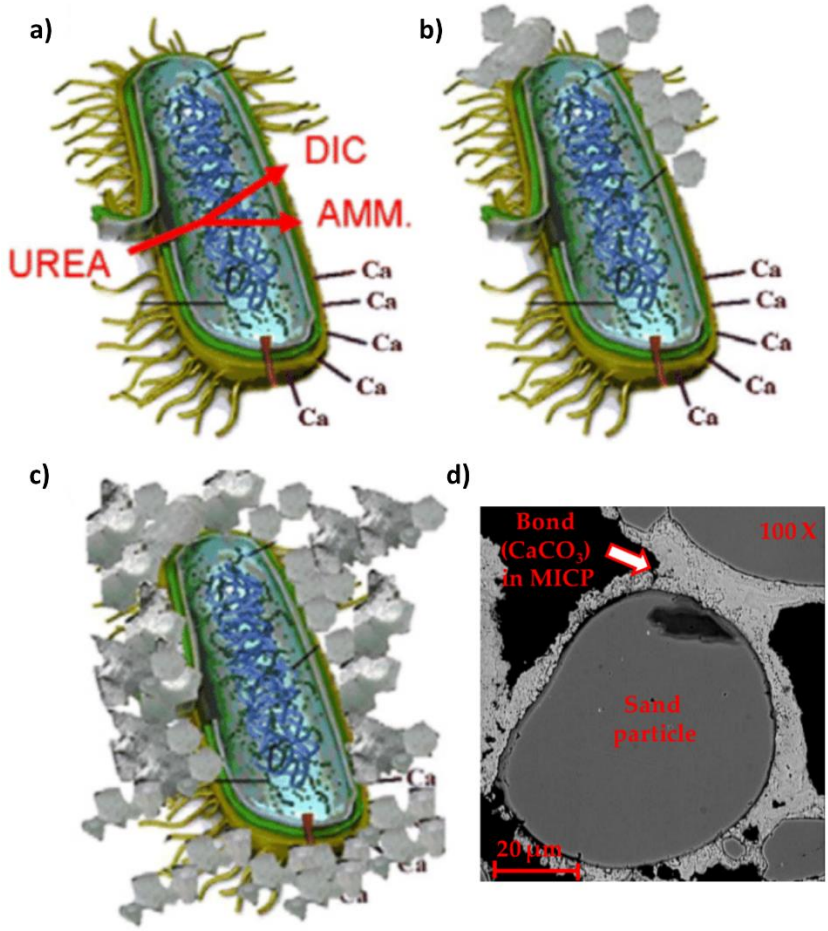

Figure 1.2 MICP schematic of calcium carbonate precipitation (**a**), (**b**) and (**c**) from DeJong et al. (2006) the mechanism of calcite nucleation on the cell walls of urease producing bacteria and (**d**) from Rahman et al. (2020) how calcite precipitation in bio-cemented sand is focussed preferentially within pore throats and on grain surfaces.

Together, these reactions provide a highly efficient and controllable pathway compared to alternative biomineralisation routes, making urea hydrolysis the basis of most MICP studies, all EICP formulations, and the central mechanism examined in this thesis.

1.2.2 Mechanistic controls on ICP

Although MICP and EICP share the same underlying hydrolysis reaction, the way it is catalysed: by whole bacterial cells in MICP or free enzymes in EICP, introduces important differences in efficiency, reaction onset, and spatial uniformity. The kinetics of hydrolysis follow Michaelis-Menten behaviour (Fig. 1.3), with reaction rates governed by urea concentration and the catalytic properties of the ureolytic agent. In

microbial systems, urease activity depends on cell viability, metabolic state, and local microenvironments, whereas in EICP it is determined directly by enzyme concentration, stability, and solution chemistry.

As hydrolysis progresses, hydroxide, bicarbonate, and ammonium ions elevate solution pH, shifting carbonate equilibria and controlling the saturation state of $CaCO_3$. The rate and extent of this pH evolution determine when and where crystals nucleate, influencing precipitation efficiency and the distribution of mineral phases (Zehner et al., 2020).

1.2.2.1 Mechanisms governing precipitation in MICP

In MICP, the evolution of pH is a dynamic, multi-phase process influenced by bacterial metabolic activity, local saturation conditions, and mineral phase transitions (Zehner et al., 2020). *Sporosarcina pasteurii* is the preferred bacterial strain, exhibiting high enzymatic efficiency at elevated urea concentrations (Whiffin et al., 2007) and therefore supporting efficient hydrolysis in engineered environments (Fig. 1.3).

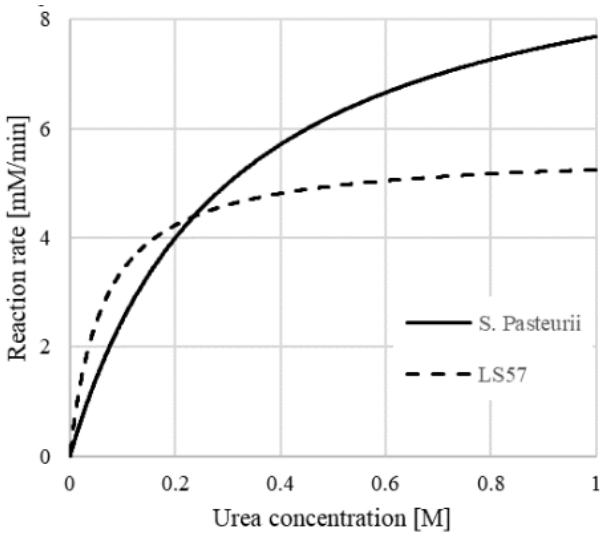

Figure 1.3 Michaelis-Menten kinetics of two strains of ureolytic bacteria (S. Pasteurii and LS57) used in the MICP process(Tarantino et al., 2019).

Calcium carbonate does not immediately precipitate as calcite but typically forms through a sequence of metastable phases. Amorphous calcium carbonate (ACC) or vaterite often appear first, later recrystalising into calcite in accordance with Ostwald's Rule of Stages (Mullin, 2001). Supersaturation, ionic strength, and local pH

fluctuations govern how long ACC persists or whether vaterite is stabilised before transformation (Rodriguez-Blanco et al., 2011; Sheng Han et al., 2006). Dissolution-reprecipitation cycles, coupled with ion exchange and organic interactions, may further extend the persistence of metastable phases (Khanjani et al., 2021; Zehner et al., 2020).

Beyond chemical kinetics, bacterial surface properties and extracellular polymeric substances (EPS) strongly influence precipitation dynamics. The negatively charged surface of *S. pasteurii* attracts Ca^{2+} ions, increasing local supersaturation and promoting nucleation directly on cell walls (DeJong et al., 2006). EPS further modifies the microenvironment by binding ions, altering diffusion pathways, and providing organic templates that influence crystal morphology and aggregation. These effects can stabilise metastable phases such as ACC or vaterite (Tourney & Ngwenya, 2009), delay transformation to calcite, or promote clustered rather than grain-contact precipitation. Such shifts in nucleation location and crystal habit directly impact permeability reduction, mechanical reinforcement, and the uniformity of MICP treatments.

Bacterial concentration also shapes precipitation behaviour. When cell density is uniformly high, total $CaCO_3$ yield increases (Okwadha & Li, 2010). However, when bacteria accumulate in localised clusters, the resulting high local cell volume fractions promote EPS-rich flocs and strong pH gradients. These microenvironments favour spherical or aggregated $CaCO_3$ morphologies rather than grain-contact bridging (Fig. 1.4) (Al-Thawadi & Cord-Ruwisch, 2012; Cheng et al., 2007). The tendency of bacteria to flocculate under certain ionic and flow conditions further amplifies this effect by creating concentrated nucleation zones. These changes in nucleation environment and crystal habit directly influence permeability reduction and the mechanical performance of treated soils (Chen et al., 2024).

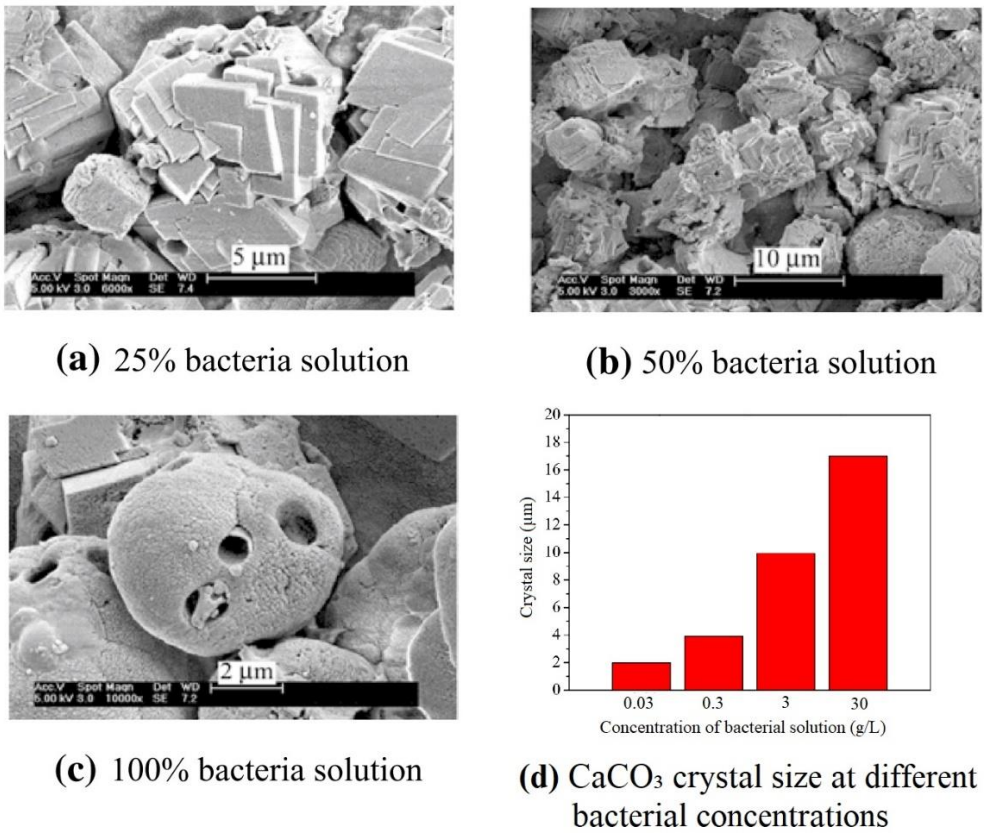

(a) 25% bacteria solution

(b) 50% bacteria solution

(c) 100% bacteria solution

(d) $CaCO_3$ crystal size at different bacterial concentrations

Figure 1.4 Crystal size and shape as a function of bacterial concentration during MICP (**a**), (**b**) and (**c**) adapted from Cheng et al. (2007) (**d**) adapted from Al-Thawadi and Cord-Ruwisch (2012)

1.2.2.2 Mechanisms governing precipitation in EICP

In contrast to MICP, where bacterial activity and biofilm growth affect precipitation, EICP is controlled purely by enzyme kinetics and solution chemistry. Singh et al. (2021) demonstrated that with optimal reactant concentrations (1 M urea, 0.67 M $CaCl_2$, and 5 g/L jack bean urease), complete conversion of $CaCl_2$ to $CaCO_3$ could be achieved in sand columns over 21 days. While bulk $CaCO_3$ production was confirmed, the absence of pore-scale imaging left uncertainties about precipitation distribution, clogging, and local supersaturation dynamics.

Recent work has focused on crude urease extracts from plant materials as a cost-effective alternative to purified urease. Such extracts inevitably contain proteins, fats, and carbohydrates that may modify precipitation behaviour. Potential effects include:

- **pH buffering**: amino acids and proteins may alter hydrolysis rates and local supersaturation (Yang et al., 2022), which is important because temporary pH

suppression can delay the onset of $CaCO_3$ precipitation, allowing deeper penetration and better mixing of reagents before nucleation begins.

- **Polymorph stabilisation**: organic matter can promote ACC or vaterite persistence (Khanjani et al., 2021). Stabilising metastable phases affects the timing of calcite formation and can influence crystal morphology and the development of grain-bridging bonds, with direct consequences for strength and permeability.
- **Enzyme protection**: certain organic compounds can stabilise urease and reduce denaturation in high-ionic-strength environments. Excessive chloride ions are known to inhibit enzymatic activity (Bao et al., 2025), and organic cofactors in crude extracts may extend enzyme lifetime, enabling more sustained hydrolysis.

Organic additives have also been trialled to enhance EICP performance. Additions such as non-fat milk powder (Almajed et al., 2019), casein (Miyake et al., 2022), xanthan gum (Hamdan et al., 2016), and sodium alginate (Arab et al., 2024) have produced higher unconfined compressive strengths at lower $CaCO_3$ contents. Mechanistic explanations include:

- **Protein interactions**: milk proteins may act as nucleation templates, enhancing interparticle bonding (Miyake et al., 2022).
- **Polysaccharides and ion transport**: xanthan and alginate may modulate ion mobility, controlling precipitation location and morphology (Arab et al., 2024).

Despite promising results, few studies have systematically linked these additives to precipitation kinetics or pore-scale distribution.

These biochemical effects also influence the mineralogical outcome of precipitation. For example, EICP commonly produces smaller and more densely packed $CaCO_3$ crystals than MICP (Gowthaman et al., 2022) a feature that may enhance permeability reduction in narrow pore throats. However, excessive organic content can drive pore clogging near injection points, leading to non-uniform treatment (Venda Oliveira & Neves, 2019). Together, these findings show that enzyme source, organic composition, and solution chemistry play central roles in governing precipitation uniformity and phase evolution in EICP systems.

1.2.2.3 Crude urease extraction: A new approach

Crude urease extraction from plant sources offers a cost-effective alternative to purified urease, which can account for 70–80% of total chemical costs in EICP (Ahenkorah et al., 2021). Among candidate plants, jack beans (*Canavalia ensiformis*) exhibit the highest ureolytic activity (2700–3500 μmol urea/min·mg) (Liu et al., 2023), but limited commercial cultivation constrains large-scale use. Soybeans (*Glycine max*) provide moderate activity (650–800 μmol urea/min·mg) (Shu, Yan, Ge, et al., 2022), yet benefit from global availability and well-established supply chains. Watermelon seeds (*Citrullus lanatus*), a by-product of food processing, offer comparable activity (600–950 μmol urea/min·mg) (Imran et al., 2021; N. Javadi et al., 2018) but are limited by seasonal variability and supply volumes. In practice, this creates a trade-off between enzymatic activity and scalability: jack bean extracts are highly active but scarce, watermelon seeds sustainable but constrained, while soybeans strike the most practical balance of cost, availability, and performance. For these reasons, soybeans have emerged as one of the most promising crude enzyme sources for large-scale EICP (Dilrukshi et al., 2015).

However, crude extracts also introduce substantial variability in enzyme purity, stability, and co-extracted organic components, all of which directly influence precipitation dynamics. Unlike purified urease, plant-derived extracts contain residual proteins, fats, carbohydrates, and small organic molecules whose concentrations depend on the extraction and coagulation steps used. These constituents can alter solution pH, buffer capacity, and nucleation behaviour, affecting reaction kinetics, and $CaCO_3$ polymorphism. Because such variability is rarely quantified or discussed in the EICP literature, despite clear implications for lag phases, spatial distribution, and treatment uniformity, understanding how crude formulations behave under different regimes is essential for scalable application.

The practical implications of these mechanisms are reflected in how MICP and EICP are delivered in porous media, motivating a closer examination of their respective injection strategies and limitations.

1.2.3 MICP injection strategies and limitations

MICP treatment is typically performed using cyclic injection, in which bacterial solution and cementing solution (CS) are introduced sequentially, often with rest periods between steps. A standard cycle involves (i) injecting a bacterial suspension to allow

cell attachment, (ii) flushing or resting to promote redistribution and minimise clogging of the injection point, and (iii) injecting a CS containing urea and $CaCl_2$ to induce $CaCO_3$ precipitation. Several cycles are typically required to build sufficient carbonate content, because precipitation during each step progressively reduces pore connectivity and limits cell access for subsequent reactions.

- **Bacterial placement and flow rate:** Flow rate strongly influences bacterial attachment and distribution: excessively high velocities detach cells, while low velocities cause localised accumulation. Tobler et al. (2014) demonstrated that an intermediate flow velocity (~0.23 m h^{-1} in 37 mm sandstone cores) promotes a more uniform distribution without causing premature clogging.
- **Delayed precipitation strategies:** Adjusting solution pH can delay crystal nucleation during injection. For example, acidifying the CS with HCl (Cheng et al., 2018) or acetic acid (Yang et al., 2022) temporarily buffers pH, enabling co-injection of bacteria and cementation fluids without immediate precipitation. Such strategies help reactants penetrate more deeply before crystallisation begins.

Together, these measures improve injectability and uniformity in laboratory settings but scaling them to field conditions remains difficult (DeJong et al., 2009; DeJong et al., 2010; Gomez et al., 2015), and several intrinsic limitations continue to constrain the efficiency and reliability of MICP. These include:

- **Biological limitations:** As crystallization progresses, bacteria become progressively entombed within precipitates, cutting off access to urea, calcium, and oxygenated porewater. This is the primary reason why treatment is cyclic: after each cementation step, additional bacterial injections are required to replenish active cells in regions where entombment has already occurred. Experimental studies typically use 4–5 optimised cycles (Cheng & Cord-Ruwisch, 2014; Minto et al., 2018), with individual injections ranging from tens to hundreds of millilitres for laboratory columns and several litres for pilot-scale tests. Continuous injection approaches (Hommel et al., 2015) can reduce cycling frequency by maintaining a low but steady supply of bacteria and reagents, but entombment still occurs and can lead to preferential clogging near injection points. Nutrient injections may stimulate in situ regrowth and biofilm formation (Landa-Marbán et al., 2021), reducing the

number of bacterial reinjections required, but they introduce additional nutrient loading and operational steps that increase overall treatment complexity.

- **Physical limitations:** Microbial transport is restricted by pore throats in consolidated or fine-grained media. When pore diameters approach bacterial cell dimensions (0.5–3 μm), cells are strained at constrictions and $CaCO_3$ nucleates preferentially at these bottlenecks (Mitchell & Santamarina, 2005). This leads to localised clogging, impedes uniform reactant transport, and restricts mineralisation to flow-accessible pathways. Achieving consistent treatment therefore requires attention to cell size, ureolytic activity, motility, and stress tolerance (Ma et al., 2020; Madigan et al., 2018).

Taken together, these biological and physical factors explain why MICP often exhibits strong localisation and why achieving uniform, reliable treatment across heterogeneous media remains a central challenge. Such non-uniformity limits the usefulness of MICP in applications where sealing or strength must extend throughout a formation rather than concentrate near injection points. For example, in consolidated rocks and fine-grained or layered sediments, pore throats may be too small for bacterial transport, restricting precipitation to accessible flow paths and leaving large untreated zones. In CO_2 storage settings, this can compromise the sealing of leakage pathways away from the injection well; in fracture remediation, it may lead to premature clogging at injection faces rather than distributed sealing; and in geotechnical ground improvement, it may produce spatially variable strength gains. These constraints motivate interest in enzyme-based alternatives, where the much smaller enzyme molecules (~13 nm) can penetrate finer pores and bypass many of the transport limitations inherent to whole-cell MICP.

1.2.4 EICP injection strategies and limitations

EICP has been explored for engineering applications such as soil stabilization (Carmona et al., 2016; Putra et al., 2018; Putra et al., 2016), permeability reduction (Yasuhara et al., 2012), and treating hydrocarbon-contaminated sands (Singh et al., 2021). Instead of relying on living bacteria, EICP directly employs urease enzymes extracted from plants or microbes (Cui et al., 2020; Feder et al., 2020) to catalyse $CaCO_3$ precipitation.

This approach offers several advantages over MICP:

- **No bacterial handling:** EICP avoids flocculation, bio-clogging, and the costs of maintaining bioreactors under sterile conditions.
- **Greater injectability:** At ~13 nm in diameter (Turbett et al., 1992) urease molecules are orders of magnitude smaller than bacterial cells, making pore throat size far less restrictive to transport and avoiding the mechanical filtering effects observed in MICP (Section 1.2.3).
- **Immediate activity:** Because active urease is present at injection, precipitation begins immediately, avoiding delays associated with bacterial growth or urease expression.
- **No bacterial encapsulation:** EICP avoids the entombment of cells within $CaCO_3$ precipitates, eliminating the progressive loss of reactivity that limits multi-cycle MICP treatments.
- **Fewer injection cycles:** Without the need to replenish living cells, EICP treatments typically require fewer injections and simpler cycling protocols.
- **No biofilm degradation:** Whereas biofilm decay in MICP can increase permeability over time, the crystalline $CaCO_3$ formed via EICP provides a more durable and predictable modification of porous media (Nemati et al., 2005).

In practice, EICP treatments typically involve injecting a urea-calcium solution containing free urease or a crude enzyme extract, with carbonate precipitation initiating as soon as pH and ionic conditions allow; as a result, controlling the timing and location of nucleation during injection remains a central operational challenge (Kohlhaas et al., 2025; Weinhardt et al., 2021; Xiao et al., 2025). Two main strategies have been explored:

(i) Dual-line injection

Traditionally, enzyme and CS are injected simultaneously through separate lines, mixing only after entering the porous medium (Weinhardt et al., 2021). This reduces the chance of premature precipitation in tubing or injection wells.

(ii) Single-phase injection

More recently, single-phase strategies have been tested, where enzyme and CS are premixed into one solution (Cui et al., 2020; H. Wang, L. Miao, et al., 2022). To delay precipitation during injection, the solution is typically acidified to a lower initial pH. This approach eliminates the need for in situ mixing, potentially yielding a more uniform

$CaCO_3$ distribution. However, it also increases the risk of scaling and blockage within injection lines, requiring careful control in field applications.

While both strategies show promise, translating laboratory protocols into reliable field-scale methods remains a key challenge for EICP. Historically, the high cost of purified urease and the limited development of stable crude enzyme formulations constrained large-volume treatments, and early studies often reported highly localised precipitation, with most $CaCO_3$ forming close to the injection point (Handley-Sidhu et al., 2013). At larger scales, single-phase injections risk premature precipitation and line clogging, whereas dual-line approaches require precise synchronisation of mixing fronts over long distances, both of which complicate implementation. In contrast, most field demonstrations to date have relied on MICP (Gomez et al., 2015; Gowthaman et al., 2023; Zeng et al., 2021), meaning operational experience, equipment, and established protocols are far more developed for microbial systems than for enzyme-based approaches. These factors together help explain why EICP has seen little field deployment so far. Dual-line injection is further explored in Chapter 3, while the potential of single-phase strategies is investigated in Chapters 4–6.

1.2.5 Environmental factors affecting ICP performance

Beyond intrinsic reaction kinetics, several environmental variables strongly influence the performance of MICP and EICP. These include pH, salinity, reactant concentrations, temperature, and the pore structure of the treated medium. Understanding their role is essential for translating laboratory protocols into field applications.

1.2.5.1 Substrate chemistry and localized pH effects

Urease activity is optimal near neutral to mildly alkaline conditions (pH 7–8) (Ciurli et al., 1996; Ng et al., 2012). Although precipitation can be initiated from lower starting pH values (~4–6) to delay crystallisation (Cheng et al., 2018; Yang et al., 2022), acidic environments may suppress long-term calcite formation. This distinction is particularly relevant to Chapter 4, where low-pH single-phase MICP treatments are compared against standard EICP systems.

1.2.5.2 Salinity and cementing solution effects

High ionic strength influences MICP and EICP differently: in MICP, salinity can enhance bacterial adhesion (“fixer effect”) but may reduce ureolytic activity at very

high levels (Hammes & Verstraete, 2002; Zhao et al., 2022), In EICP, salinity affects enzyme stability, with some studies showing that seawater can support precipitation (Lin et al., 2023; Q. Zhang et al., 2023). The concentration of the CS also strongly influences efficiency: yields increase with higher concentrations, but calcium conversion declines above ~1.0 M, and urease activity may be inhibited at >2.5 M (Lai et al., 2021; Kai Xu, Ming Huang, Jiajie Zhen, et al., 2023) and at comparable concentrations in EICP (Kai Xu, Ming Huang, Jiajie Zhen, et al., 2023). The choice of 1.0 M equimolar urea:$CaCl_2$ in this thesis reflects a balance between efficiency and stability, and provides a basis for comparability across Chapters 4–6.

1.2.5.3 Temperature effects on urease activity and $CaCO_3$ precipitation

Temperature influences urease activity, carbonate precipitation rates, and mineral phase stability in both MICP and EICP. The optimal range for maximizing MICP-treated soil strength is generally agreed to be between 20–28°C (De Muynck et al., 2013; Nayanthara et al., 2019). At higher temperatures (~50°C), urease activity accelerates significantly (Cheng & Cord-Ruwisch, 2014) however, at temperatures below 10°C, urease activity is nearly completely inhibited, restricting carbonate precipitation (Y. Wang, H. Liu, et al., 2019).

Above ~80 °C, enzyme-based ureolysis ceases entirely, and carbonate precipitation instead occurs through thermal decomposition of urea (Kumar et al., 2023). While temperature is a critical factor for field application, all experiments in this thesis were conducted under controlled laboratory conditions (~20 °C), and temperature effects are not examined further.

1.2.5.4 Pore structure and geometry

The grain size distribution and pore geometry of soils and rocks strongly influence where and how $CaCO_3$ precipitates, with direct implications for permeability, mechanical strength, and thermal conductivity (Sang et al., 2023; Xiao et al., 2021). Medium-grained sands (e.g. 200–400 μm diameter) often yield more homogeneous precipitation than very fine or coarse soils, which either restrict flow or provide limited intergranular bonding (Terzis & Laloui, 2018).

For biocemented materials, precipitation patterns are best understood at the pore scale. XCT imaging has been used to quantify how grain size, shape, and packing affect the extent of $CaCO_3$ bonding during MICP and the efficiency of mechanical

reinforcement. For example, Terzis and Laloui (2018) developed segmentation workflows to evaluate $CaCO_3$-grain contacts in MICP-treated sands (Fig. 1.5), providing a template for analysing how microstructural bonding translates to bulk behaviour of the treated soil. Well-graded grain size distributions, where smaller grains fill voids between larger particles, can enhance mechanical strength (Sang et al., 2023) but may also reduce initial porosity and permeability. This in turn influences how reactants flow through the medium and where calcium carbonate is deposited. Optimizing grain structure is therefore crucial for achieving targeted mechanical and hydraulic performance in bio-cemented materials.

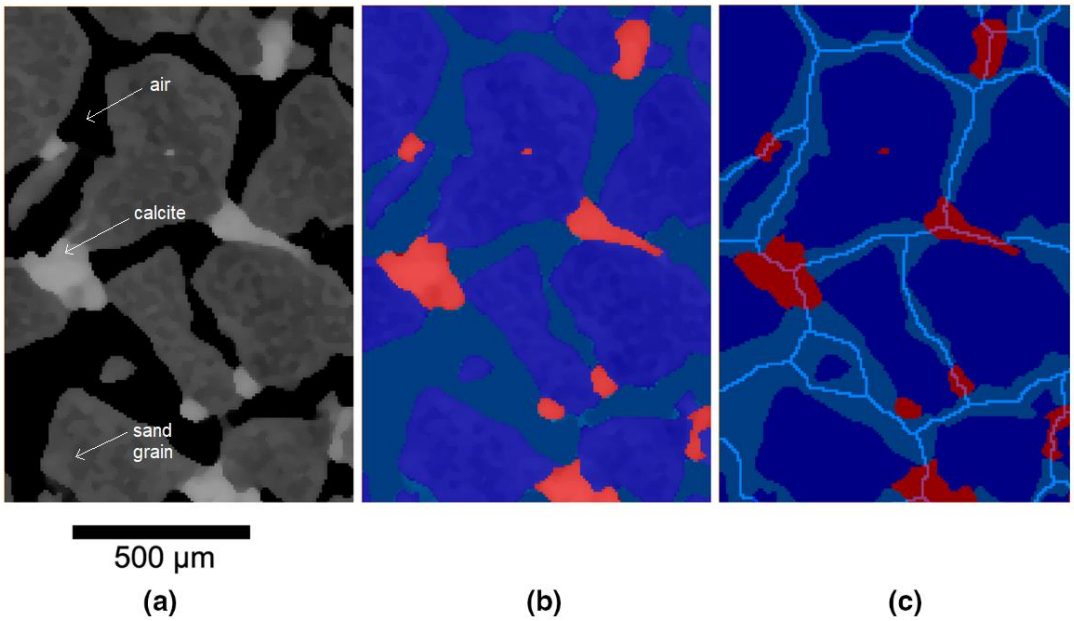

Figure 1.5 Image processing of MICP in a silica sand column (**a**) The original image filtered in Avizo (ThermoFisher Scientific, n.d) to reduce noise at grain boundaries. (**b**) The image is segmented using a 'watershed' module, allowing further quantification steps of silica sand, $CaCO_3$ and pore properties (**c**) Particles separated using a 'split lines' module – This is necessary since contact surfaces between soil grains were undetectable via XCT, due to inadequate spatial resolution. (Adapted from Figure 3. Terzis and Laloui (2018))

1.2.6 Strengths and weaknesses of MICP and EICP

The differing mechanistic behaviours of MICP and EICP give rise to distinct advantages and limitations in engineering applications. Table 1.1 summarises the key contrasts relevant to permeability control, strength development, and treatment uniformity.

Table 1.1 Strengths and weaknesses of MICP and EICP

Feature	MICP Strengths	MICP Weaknesses	EICP Strengths	EICP Weaknesses
Environmental Robustness	Biofilms may make bacteria resilient in harsh conditions (Yin et al., 2019).	May require sterile growth, increasing cost and complexity at scale (Achal & Mukherjee, 2015)	No sterility needed; simpler scale-up. Functions in anoxic environments (Shu, Yan, Meng, et al., 2022)	Purified enzymes may be less robust under extreme salinity, acidity, or heat (Almajed, 2017).
Injection Suitability in Fine Sand (<100 µm)	Inability to precipitate across fine-grained layers could be advantageous for selective treatment.	Limited in fine-grained substrates (< 100 µm) due to bacterial size and pore clogging (Mitchell & Santamarina, 2005)	Effective in fine-grained substrates due to smaller enzyme size and better penetration (Gao et al., 2019).	Difficult to confine precipitation spatially; enzymes penetrate fine layers that bacterial systems may naturally bypass, reducing selectivity.
Crystal Distribution	Precipitation at grain contacts increases strength (Mujah et al., 2019) and thermal conductivity (Venuleo et al., 2016).	Bacterial flocculation may reduce uniformity in fine-grained soil/rock (Wu et al., 2019).	Homogeneous distribution possible via low-pH (Cui et al., 2020) or single-phase strategies (H. Wang, L. Miao, et al., 2022).	Poorly targeted mixing of enzyme and CS during dual-phase injection may result in less control over precipitate location (Kohlhaas et al., 2025)
Injection Strategies	Self-sustaining nature can extend reaction periods and increase overall precipitation efficiency (Landa-Marbán et al., 2021).	Risk of bacterial detachment (Tobler et al., 2018), cell encapsulation due to crystal growth. Nutrient solution required to maintain cell activity.	No nutrient solution required; Less injection phases than MICP due to co-injection of enzyme, urea, and $CaCl_2$ (Shu, Yan, Meng, et al., 2022).	Requires optimized mixing of enzyme and urea/calcium solution for uniform crystal distribution (Handley-Sidhu et al., 2013).
Temperature Range	Functions best at 20–30°C; tolerates up to ~40°C (De Muynck et al., 2013)	Limited effectiveness below 10°C or above 40°C (Peng & Liu, 2019).	Effective up to 80°C before enzyme inactivation (Feder et al., 2020).	Enzyme denatures above ~80°C (Feder et al., 2020).
Cost and Scalability	Cost-effective bacterial growth benefits from economies of scale (Sang et al., 2024).	Bioreactor/nutrient requirements raise costs and environmental footprint (DeJong et al., 2010)	Crude enzymes cut costs; plant-based options reduce dependency on purified urease (Shu, Yan, Ge, et al., 2022).	Purified urease is expensive, dominating chemical costs (Ahenkorah et al., 2021).
Salinity Tolerance	Works in saline conditions up to 100 g/L NaCl (Zhao et al., 2022).	Reaction efficiency drops at >1.0 M CS; halts entirely at ~2.5 M (Lai et al., 2021).	Retains activity in seawater, used successfully as a mixing medium (Lin et al., 2023).	Very high salinity suppresses activity in some crude extracts (Omarov et al., 2023).
Application Versatility	Suitable for shallow applications with targeted grain-boundary bonds.	Limited for deep/extreme environments due to bacterial inactivation (Peng & Liu, 2019).	Versatile for both shallow (Kai Xu, Ming Huang, Jiajie Zhen, et al., 2023) and high-temperature applications (H. Wang, L. Miao, et al., 2022).	Smaller crystals may limit mechanical enhancement (Ma et al., 2025).

1.3 Material-Scale impacts of ICP

The biochemical and physical processes governing urea hydrolysis, ion transport, and carbonate precipitation at the pore scale determine how ICP modifies the structure of a granular medium. As $CaCO_3$ forms at grain contacts and within pore throats, it alters contact geometry, pore connectivity, and the distribution of load bearing and flow-carrying pathways. These microstructural changes underpin the macroscale behaviour of ICP-treated materials, influencing their mechanical response, hydraulic behaviour, and thermal performance.

1.3.1 Mechanical behaviour

The precipitation of $CaCO_3$ at grain contacts increases interparticle bonding, improving soil stiffness and unconfined compressive strength (UCS). Numerous studies report UCS enhancements up to 52.5 MPa in MICP (Smirnova et al., 2023) and around 10 MPa in EICP-treated sands (Meng et al., 2021), with crystal bridging identified as the dominant strengthening mechanism. However, mechanical improvements are often spatially non-uniform: localized flocculation, straining, or preferential precipitation in high-flow zones can concentrate bonding in limited regions while leaving other zones weak (Cheng et al., 2007). This heterogeneity remains a critical challenge for scaling up ICP treatments. Furthermore, the exceptionally high strengths reported (e.g. 52.5 MPa in a laboratory MICP study) are heavily influenced by sample preparation (such as high packing density) (Smirnova et al., 2023), conditions which may not be representative of typical field soils (e.g. more loosely packed near-surface soils). Later chapters evaluate UCS and microstructural changes in both MICP and EICP systems, examining how enzyme source and injection strategy influence strength development and treatment uniformity.

1.3.2 Hydraulic behaviour

ICP can significantly reduce permeability by occluding pore throats and restricting flow pathways. This effect is desirable for applications such as CO_2 leakage remediation (Minto et al., 2017; Park & Choi, 2021), but can be detrimental in systems that rely on sustained flow, such as geothermal heat exchangers (Go et al., 2015). In MICP, permeability loss is often more severe due to bacterial straining and localised precipitation near injection points (Mitchell & Santamarina, 2005). EICP tends to produce smaller, more homogeneously distributed crystals (Gowthaman et al., 2022),

which can help retain some degree of hydraulic conductivity while still achieving strength gains.

1.3.3 Thermal behaviour

By creating solid bridges between grains, $CaCO_3$ precipitation improves thermal contact and increases effective conductivity of soils. Reported improvements range up to 300% relative to untreated sands (McCartney et al., 2020), with the greatest benefits in drier conditions where air-filled pores dominate heat transfer resistance. Microscopic observations confirm that calcite crystals act as “thermal bridges” (Venuleo et al., 2016; Z. Wang et al., 2019), reducing contact resistance between particles. Beyond $CaCO_3$ alone, additives such as expanded graphite (EG) and phase change materials (PCMs) have been proposed to further enhance soil conductivity and energy storage potential (Theo Renaud et al., 2021; Xie et al., 2021).

1.4 Applications of ICP

Having reviewed the underlying reaction mechanisms and factors controlling precipitation (Section 1.2), the resulting changes to material properties (Section 1.3), it is now possible to consider how ICP can be applied in practice. ICP has been proposed for a wide range of geotechnical and energy-related applications, but three domains are particularly relevant to this thesis: (i) permeability reduction and storage security in CCS, (ii) geotechnical strengthening of soils, and (iii) thermal and energy system optimisation. These applications each exploit the same fundamental processes (e.g. grain bonding, pore throat occlusion, and thermal bridging) but place different demands on treatment design and performance. The following sections review the state of knowledge in each area and establish the practical context for the experimental work presented in Chapters 3–6.

1.4.1 Permeability Reduction and CO_2 Storage

CCS is of fundamental importance to global decarbonisation strategies (Krevor et al., 2023), yet its success depends on ensuring the integrity and efficiency of geological reservoirs. Two persistent challenges are (i) sealing potential leakage pathways such as poorly sealed legacy wells, fractures, or caprock defects, and (ii) enhancing CO_2 sweep efficiency to maximise storage capacity and minimise localised overpressure.

ICP has emerged as a promising strategy for both, offering low-viscosity fluids that can penetrate pore networks and fractures inaccessible to cementitious grouts.

(i) Leakage remediation.

Laboratory studies have consistently demonstrated that both MICP and EICP can achieve significant permeability reduction in porous media (Minto et al., 2017; Park & Choi, 2021). Unlike conventional sealing methods such as cements, resins, or nanomaterials (Genedy et al., 2019; Todorovic et al., 2016), ICP solutions exhibit near-water viscosity, allowing them to infiltrate narrow pore throats and microfractures where leakage is most likely to initiate. Once urea hydrolysis proceeds, $CaCO_3$ precipitation can create durable seals at depth without extensive mechanical intervention. Field-scale demonstrations have reinforced this potential: Kirkland et al. (2021) reported that MICP injections successfully reduced permeability in CO_2-affected brine aquifers, achieving solidification tens of metres away from the wellbore. However, carbonate seals in CO_2-rich brines remain vulnerable to partial dissolution, requiring careful assessment of long-term stability (Minto et al., 2017). While dissolution may be partly offset by re-precipitation, balancing precipitation kinetics against acidic brine conditions is a key technical challenge.

(ii) Sweep efficiency

In addition to sealing leakage pathways, ICP may be used more strategically to manipulate reservoir flow paths. CO_2 is buoyant and tends to accumulate beneath caprock, reducing the radial spread of the plume and limiting storage efficiency. Even minor permeability contrasts can redirect flow paths significantly (Bump et al., 2023), suggesting that targeted carbonate ‘baffles’ within heterogeneous sediments could redirect flow into previously underutilised regions, reducing localised overpressure and improving storage distribution. This engineering of subtle permeability contrasts represents a more nuanced application of biomineralisation than simple sealing, but one with substantial implications for large-scale CCS deployment.

(iii) Geomechanical stability

A further application of ICP is to reinforce mechanically weak sediments in storage formations. Exposure to CO_2-saturated brines can weaken carbonate rocks (Lebedev et al., 2017), reducing their stiffness and increasing susceptibility to wormhole formation. In unconsolidated sediments, however, carbonate precipitation has been shown to significantly increase unconfined compressive strength (Almajed et al.,

2019; Meng et al., 2021), mitigating risks of collapse or compaction during injection. Tailoring treatments for strength versus permeability reduction requires careful optimisation, but the dual potential highlights ICP's versatility.

These applications all depend on controlling where and when precipitation occurs, a problem that remains poorly understood at the pore scale. While field-scale reactive transport models have suggested that density driven mixing between dense cementing solutions and enzyme-rich fluids governs spatial precipitation patterns (X. Li et al., 2024), it is not yet clear whether the same mechanisms apply within individual pore networks. Chapter 3 addresses this gap directly by using XCT and CFD simulations to investigate how mixing behaviour influences pore-scale precipitation dynamics and permeability evolution in EICP systems.

1.4.2 Soil Stabilisation and Geotechnical Applications

Induced carbonate precipitation has been proposed as an alternative to cement and chemical grouting for ground improvement. The motivation stems from the unique injection properties of ICP fluids: their water-like viscosity allows them to penetrate soils and interfaces that conventional grouts cannot reach.

(i) Ground reinforcement for slope stability and coastal protection

In loose or erodible soils, precipitation at grain contacts can provide cohesion, reduce liquefaction potential, and increase slope stability under cyclic loading (DeJong et al., 2010; Terzis & Laloui, 2019). This approach has been considered for coastal dune reinforcement (Y. Li et al., 2024) , where stabilisation is needed to resist wave and wind erosion without fully sealing the porous matrix, thereby maintaining groundwater recharge (Mujah et al., 2019).

(ii) Soil improvement in urban and infrastructure settings.

Unlike cement-based grouts, ICP can be introduced through low-pressure injection, allowing reinforcement in sensitive sites where excessive pore pressure could damage nearby structures (Dong et al., 2022). Potential applications include stabilising foundations, reducing settlement, or increasing bearing capacity beneath embankments and pavements (Cheng et al., 2013).

(iii) Balancing strength with permeability.

A critical distinction from CCS sealing applications is that in many geotechnical settings, some degree of hydraulic conductivity must be retained. For example, in

slope or embankment stabilisation, drainage pathways are essential to prevent pore pressure build-up (Sari et al., 2023). Similarly, in coastal or riverbank protection, maintaining hydraulic exchange is ecologically important (Mullaney et al., 2016). Here, EICP may offer advantages over MICP, as enzyme-only systems tend to form smaller, more uniformly distributed crystals that may strengthen the soil without fully occluding flow paths (Gowthaman et al., 2022).

Soil stabilisation through ICP provides a low-pressure alternative to cementitious grouts, with advantages in sensitive settings and cases where retaining permeability is beneficial. The main challenge is achieving consistent strength improvements at scale. Chapters 4–5 address this by testing how enzyme systems and injection strategies influence both reinforcement and hydraulic performance in biocemented sands.

1.4.3 Geothermal and Energy Systems

ICP has potential for improving the efficiency of shallow geothermal technologies such as energy piles, ground source heat pumps (GSHPs), and borehole thermal energy storage (BTES). Conventional cementitious grouts are often used for this purpose but can be costly, disruptive, and prone to long-term degradation (Delaleux et al., 2012). ICP provides an alternative means of enhancing heat transfer while maintaining greater flexibility in permeability control, making it particularly attractive for subsurface energy applications.

(i) Energy piles and GSHPs

By enhancing conductive pathways around heat exchangers, ICP could improve the efficiency of energy piles and borehole GSHPs (Fig. 1.6). More uniform heat dissipation may also help mitigate thermal imbalances that reduce GSHP efficiency in cooling-dominated climates (Belatrache et al., 2017).

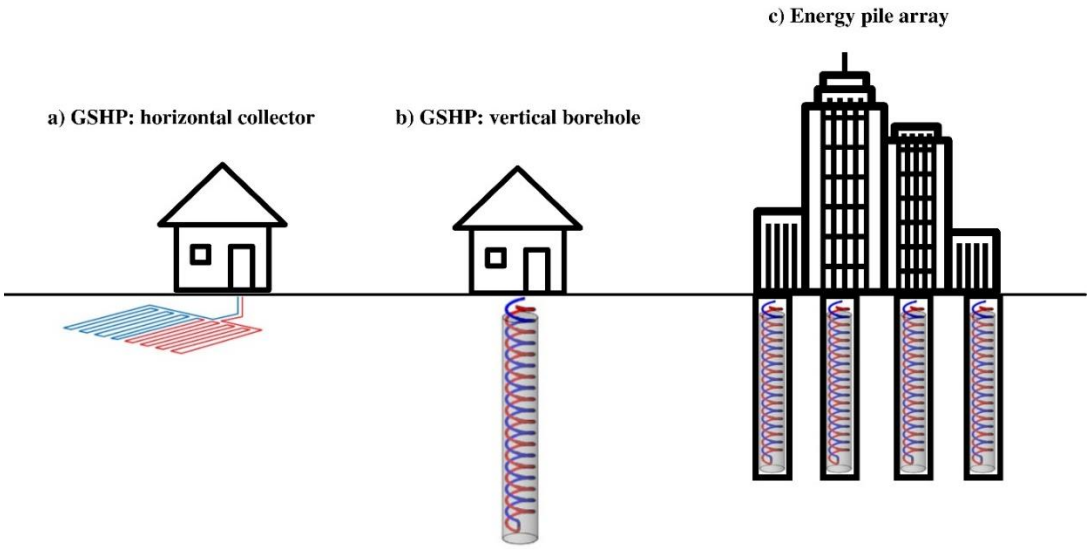

Figure 1.6 Shallow Geothermal Systems with potential for ground improvement with ureolytic biomineralisation (**a**) horizontal heat exchanger at a minimum of 1.3m depth (**b**) vertical borehole GSHPs at depths of typically 90–160m (**c**) depth is determined by the length of the foundation piles (up to ~150m).

(ii) Thermally conductive additives

Further gains may be achieved by integrating additives with high intrinsic conductivity. EG, for example, combines high thermal conductivity (>160 W/m·K) with a lightweight, porous structure that disperses well in granular media (Cermak et al., 2020). When incorporated into ICP-treated soils, EG has potential to form composite “thermal bridges,” which may improve both conductivity and stability while avoiding the corrosion and dispersion challenges of metallic fillers (Cheng et al., 2021) (Fig. 1.7). Phase change materials (PCMs), often supported by EG, provide an additional strategy by storing heat during periods of excess and releasing it during demand peaks, offering temperature regulation alongside conductivity gains (Xie et al., 2021).

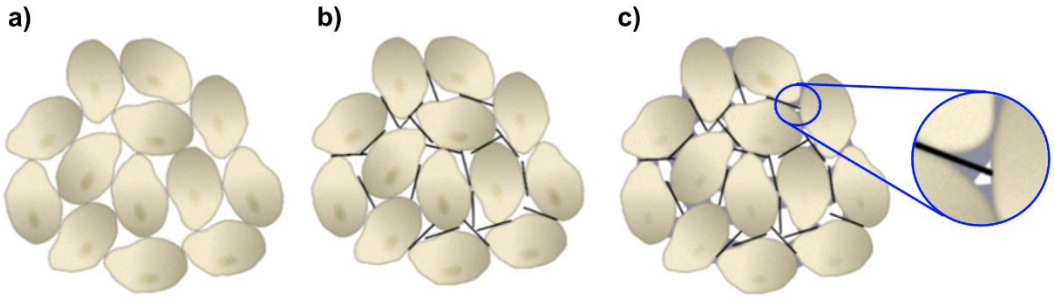

Figure 1.7 The formation of $CaCO_3$ thermal bridges in quartz sand (**a**) following addition of thermally conductive additives (**b**) and microbial or enzyme induced carbonate precipitation (**c**).

(iii) Balancing thermal and mechanical roles

A recurring challenge is that additives or high levels of $CaCO_3$ deposition may change permeability or compromise mechanical performance. For applications such as energy piles, improvements in thermal transfer must be weighed against long-term soil stability and drainage requirements.

Geothermal applications highlight ICP's potential beyond strength or sealing, extending its role to thermal management. The challenge lies in balancing conductivity gains with hydraulic and structural requirements. Chapters 5–6 address this directly, evaluating whether additive-enhanced MICP and EICP can deliver both heat transfer benefits and reliable mechanical performance.

1.5 Imaging of precipitation in porous media

While the ureolysis pathway itself is well defined, predicting the spatial and temporal evolution of $CaCO_3$ precipitation within porous media remains challenging. XCT has emerged as a critical tool for resolving these dynamics at the pore scale, offering non-destructive, time-resolved imaging of microstructural changes during biomineralisation.

1.5.1 XCT in biomineralisation research

XCT enables three-dimensional visualisation of precipitation within opaque materials, making it particularly suited to study pore-scale $CaCO_3$ formation in soils and rocks (Cnudde & Boone, 2013; Rawson et al., 2020). Laboratory systems now achieve scan

times below 1 minute (Pak et al., 2023), allowing dynamic imaging of evolving pore structures. This capability could potentially reveal how $CaCO_3$ bridges grains, occludes throats, and alters porosity-permeability relationships in real time.

XCT produces greyscale volumetric images in which different phases; pore fluid, sand grains and $CaCO_3$, often overlap in intensity. To quantify precipitation, these images must be segmented into pore and solid phases, but accurate identification and quantification of $CaCO_3$ in 3D datasets remains challenging. Threshold-based segmentation requires selecting greyscale cut-offs that are influenced by noise, contrast variation, and partial-volume effects. Because these decisions are typically validated visually, the resulting pore-solid boundary can vary between observers, leading to non-reproducible segmentation (Baveye et al., 2010). While recent advances in machine learning and direct grayscale rendering (Godinho & Withers, 2018) (Fig. 1.8) have improved reproducibility, biological samples add further complexity, as X-ray exposure can inhibit microbial viability (Armstrong & Ajo-Franklin, 2011). Despite these limitations, XCT remains the most widely used method for quantifying 3D spatial precipitation dynamics in ICP research.

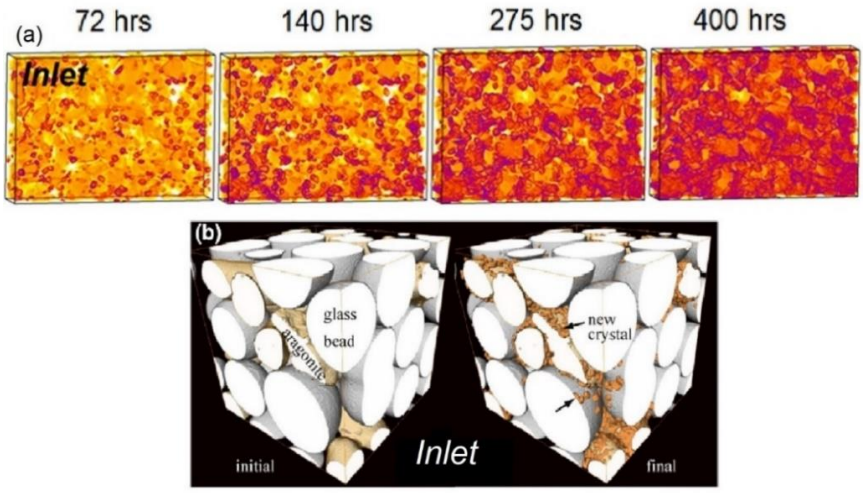

Figure 1.8 X-ray computed tomograms of pore-scale sub-volumes during calcite precipitation (**a**) Adapted from Figure 1 (Godinho & Withers, 2018) 3D sub-volumes (2500 × 1800 × 500μm) without segmentation at different time points during precipitation. The pore space is transparent, and the darker fragments represent calcite crystals. The voxel size is 2.24μm (**b**) Adapted from Figure 4, (Noiriel et al., 2016) segmented 3D sub-volume (1560 × 1560 × 1560μm) showing how calcite (orange) preferentially nucleates on aragonite grains over time. The voxel size is 4.46μm.

1.5.2 Microstructural imaging of MICP

XCT studies consistently show that in MICP, $CaCO_3$ preferentially precipitates on grain surfaces, often forming intergranular bridges (Dadda et al., 2018) (Fig. 1.9). This localisation improves mechanical stability but may leave much of the pore space unaffected unless throats are directly obstructed. Permeability therefore often declines non-linearly with $CaCO_3$ content, challenging the use of simple porosity-permeability models (Dadda et al., 2017). XCT-derived pore network models incorporating coordination number and pore throat dimensions may improve predictive accuracy (Qin et al., 2016; Rabbani et al., 2016).

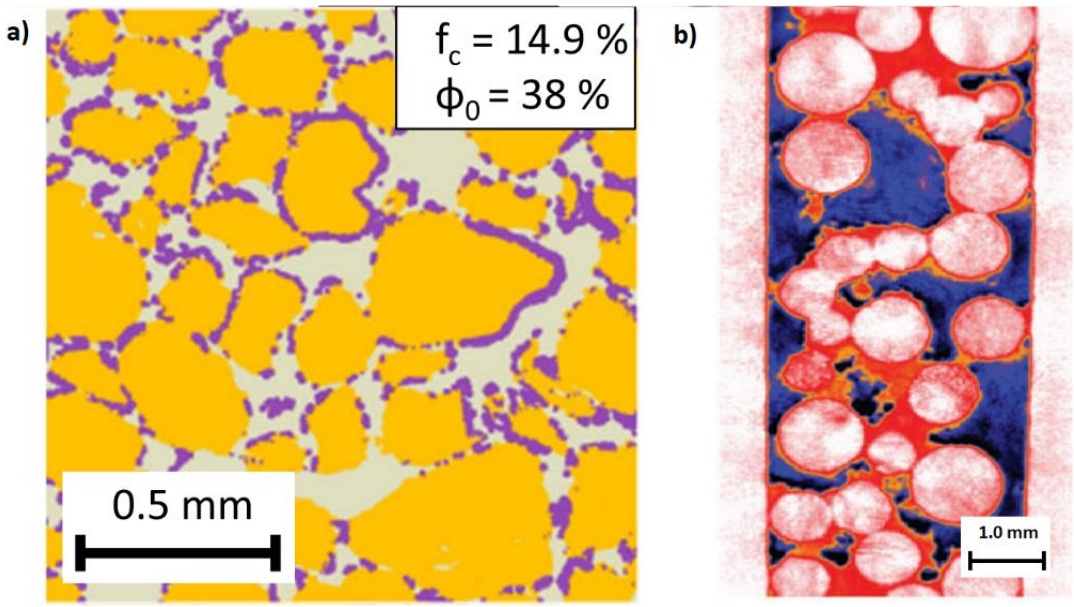

Figure 1.9 Spatial distribution of calcite and biofilm in porous media (**a**) XCT tomogram of calcite (blue) precipitation in sandstone (dark yellow) Adapted from Dadda et al. (2018) (**b**) XCT tomogram of biofilm growth (red) around expanded polystyrene beads (white) Adapted from Davit et al. (2011)

1.5.3 Microstructural imaging of EICP

Direct XCT studies of EICP are limited, with most work to date relying on 2D microfluidic flow cells (Kim et al., 2020; Weinhardt et al., 2021). These systems show that nucleation during EICP occurs largely within the pore fluid, producing more uniformly distributed crystals than in MICP, which preferentially nucleates on bacterial surfaces (Y. Wang, K. Soga, et al., 2019) (Fig. 1.10).

This distinction may allow EICP to reduce porosity while retaining some permeability, a property advantageous for geothermal systems or aquifers. Early evidence also indicates that EICP can achieve strength improvements without fully sealing pore networks (Meng et al., 2021). However, the lack of 3D *in situ* imaging limits current understanding of how precipitation pathways evolve under realistic flow conditions.

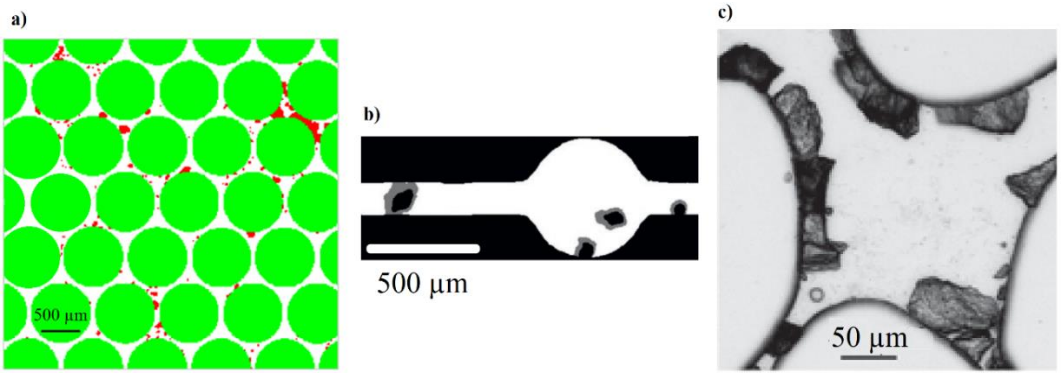

Figure 1.10 Crystal locality in microfluidic flow cells: An MICP/EICP comparison (**a**) spatial distribution of enzyme induced calcium carbonate crystals (red) in a uniform microfluidic chip Adapted from Kim et al. (2020) (**b**) a single 2D pore following EICP. G Grey denotes crystal growth after 100 minutes of fluid flow, and black an earlier stage of crystallisation. From Weinhardt et al. (2021) (**c**) a single 2D pore following MICP microfluidic flow experiments. From Y. Wang, K. Soga, et al. (2019)

1.5.4 Modelling and XCT integration

XCT-derived datasets underpin digital rock physics approaches that calculate local permeability and porosity at high resolution (Guibert et al., 2015). Reactive transport models, such as lattice-Boltzmann solvers and GeoChemFoam (Menke, 2021) integrate these data to simulate precipitation, dissolution, and flow feedbacks. Field-scale reactive transport models have demonstrated how mixing between dense cementing solutions and enzyme-rich fluids can govern spatial precipitation patterns (X. Li et al., 2024), motivating further research at the pore-scale.

Although powerful, these models rely heavily on XCT-informed calibration. Real-time XCT offers the potential to directly validate predicted precipitation dynamics, improving confidence in model forecasts of ICP performance in both engineered and natural settings.

In summary, XCT has revealed how pore-scale precipitation pathways shape the mechanical and hydraulic behaviour of ICP-treated materials. However, real-time 3D

imaging of EICP remains limited, particularly under realistic flow conditions, and we still lack a clear understanding of why spatial variations in precipitation occur. Later chapters (3–6) build on these advances by applying laboratory XCT to study precipitation dynamics and integrating the results with permeability simulations and treatment optimisation.

1.6 Critical Challenges

This thesis employs time-lapse XCT, image analysis, fluid-flow modelling, and thermal, hydraulic and mechanical testing to address five critical challenges in developing ICP as a reliable subsurface engineering technology. These challenges centre on mixing mechanisms, precipitation control, treatment efficiency, and application-specific performance requirements. The challenges identified from the literature are outlined below.

Critical Challenge 1: Understanding pore-scale precipitation dynamics

Objective: Use time-lapse XCT to resolve the dynamics and spatial distribution of $CaCO_3$ precipitation during EICP and relate these pore-scale processes to macroscopic properties such as permeability, strength, and thermal conductivity.

Despite advances in imaging, few studies link real-time biomineralisation to bulk engineering behaviour. The spatial distribution of $CaCO_3$ strongly influences treatment performance, yet the mechanisms governing its localisation, particularly in EICP, remain poorly constrained. This thesis addresses this gap through time-lapse XCT coupled with post-treatment characterisation.

Critical Challenge 2: Optimising biomineralisation strategies

Objective: Evaluate how crude enzyme sources and organic additives influence $CaCO_3$ distribution, strength, permeability, and thermal performance, and identify formulations that are both scalable and functional.

Crude urease extracts (e.g., soybean) and organic additives offer a cost-effective alternative to purified enzymes, but their effects on reaction kinetics, precipitation behaviour, and final material properties remain only partly understood. This work examines how biochemical formulation choices affect treatment uniformity, scalability, and mechanical/thermal outcomes.

Critical Challenge 3: Enhancing sweep efficiency in CCS

Objective: Investigate whether biomineralisation can create spatially targeted permeability contrasts that improve CO_2 distribution, trapping efficiency, and long-term storage security.

CO_2 injected into geological formations often follows high-permeability pathways, bypassing large reservoir regions and reducing storage efficiency. This challenge concerns whether controlled precipitation can redirect flow radially, increase sweep efficiency, and mitigate leakage risks.

Critical Challenge 4: Controlling permeability for engineering applications

Objective: Optimise MICP/EICP treatment protocols by assessing how organic content, injection strategy, and substrate characteristics influence permeability modification.

Different applications require different permeability outcomes; from near-complete sealing (CCS leakage prevention) to sustained flow (geothermal heat exchange) or intermediate values. Balancing mechanical reinforcement with controlled permeability modification remains a major challenge. This objective focuses on refining treatment protocols to deliver application-specific outcomes.

Critical Challenge 5: Enhancing the thermal performance of biocemented materials

Objective: Improve thermal conductivity and energy-storage capacity by incorporating conductive additives and phase-change materials, and evaluate formulations suitable for geothermal systems such as energy piles and ground-source heat pumps.

Although biomineralisation can enhance soil thermal conductivity, the integration of conductive additives and PCMs remains underexplored. This challenge involves developing additive-enhanced formulations that improve thermal functionality without compromising structural performance.

Together, these challenges and associated objectives underpin the experimental, analytical, and modelling approaches developed in Chapters 3–6. They frame the thesis's contributions to understanding precipitation dynamics, developing scalable treatment strategies, and demonstrating how biomineralisation can support CCS, geothermal, and geotechnical applications.

1.7 Thesis Structure

Building on these five critical challenges, the thesis is organised to show how each objective is addressed through a combination of literature review, methodological development, experimental investigation, and synthesis.

Chapter 1: Introduction – Establishes the scientific context for MICP and EICP, reviewing reaction mechanisms, imaging techniques, and engineering applications. This chapter situates the five objectives within existing research and identifies the gaps they target.

Chapter 2: Methodology – Outlines the methodological framework, including XCT, computational fluid dynamics (CFD) modelling, and laboratory testing, and explains how these approaches were adapted to link pore-scale precipitation behaviour to bulk material performance.

Chapter 3: The influence of density driven mixing mechanisms on ureolysis-induced carbonate precipitation – Addresses Objective 1 and 3 by investigating pore-scale precipitation dynamics using time-lapse XCT and CFD modelling, with a focus on how density driven flows govern the spatial distribution of $CaCO_3$ and influence permeability. This chapter has been published in full in the *InterPore Journal*.

Chapter 4: Developing physical and biochemical levers for targeted biocementation – Addresses Objectives 2 and 4 by evaluating how enzyme formulations and injection strategies influence the timing and location of $CaCO_3$ precipitation, enabling control over permeability and treatment uniformity.

Chapter 5: Bio-Cementation for structural and thermal soil enhancement with retained hydraulic conductivity – Addresses Objectives 2 and 4 by assessing how repeated EICP and MICP treatments affect strength, thermal conductivity, and

permeability. This chapter, published in part in *Biogeotechnics*, demonstrates the balance between reinforcement and hydraulic function in geotechnical and geothermal applications.

Chapter 6: From conductivity to storage: Multifunctional biocemented composites with graphite and paraffin additives – Addresses Objective 5 by testing the integration of conductive and phase-change additives, showing how expanded graphite and paraffin enhance both thermal conductivity and energy storage capacity.

Chapter 7: Applying induced carbonate precipitation: Insights, trade-offs, and future directions – Revisits all five objectives, integrating findings across Chapters 3–6. It highlights overarching scientific contributions, engineering implications, and priority areas for future research, with emphasis on scaling biocementation from laboratory validation toward field deployment.

Chapter 2: Methodology

This chapter outlines the methodological framework used in this thesis, summarising the key experimental, imaging, and modelling approaches and how they were adapted to meet the study objectives. Full procedural details are provided in Chapters 3–6; here the focus is on the rationale for each method and how they were integrated across scales.

In traditional ICP research, post-treatment measurements such as permeability reduction or $CaCO_3$ mass gain cannot reveal when and where precipitation begins, nor how it propagates through the pore space. The methods outlined here were therefore chosen to directly observe precipitation dynamics in real time, and to connect these observations to bulk-scale performance.

2.1 Optimising Laboratory Biocementation Treatments

Biocementation experiments in this thesis used two main specimen formats: small cylindrical samples for XCT imaging (5–10 mm diameter) and larger specimens (27–60 mm diameter) for mechanical, hydraulic, and thermal testing. Although detailed procedures appear in Chapters 3–6, a brief description of the core preparation steps is provided here to contextualise the optimisation strategies that follow.

2.1.1 Overview of Sample Preparation

Small XCT specimens were packed into custom 3D-printed flow cells designed to permit controlled injection and in situ scanning. A fine porous mesh was placed at both inlet and outlet openings to prevent sand migration (212–300 μm quartz sand was used throughout unless stated otherwise). Sand was added dry and lightly compacted using a 3D-printed rod; once the top cap was screwed into place, it applied light confinement to stabilise the grain structure during flow. Prior to biocementation, specimens were vacuum-saturated with deionised water to eliminate air pockets and preserve realistic flow pathways for reactive transport.

Larger specimens used for bulk testing were prepared in rigid moulds following standard geotechnical compaction practice. Sand (or sand-additive mixtures in Chapter 6) was placed in multiple thin layers (typically eight or more) with each layer

lightly scarified to minimise artificial density boundaries. To ensure consistent compaction across samples, a custom setup was used in which a metal plate was placed on top of each scarified layer and a spring-loaded punch applied a controlled downward force. This allowed each layer to be compacted with the same applied load, improving reproducibility of dry density and overall specimen uniformity. An initial moisture content of ~10% was adopted based on prior optimisation studies for similar sand (Waqas et al., 2017), providing consistent dry density and compaction behaviour. These samples were subsequently used for permeability, strength, thermal conductivity, and infrared thermography experiments (Chapters 4–6).

2.1.2 Treatment Protocol Development

Biocementation treatments in this thesis relied on two core reagent streams: a cementing solution (CS) containing urea and $CaCl_2$, and either a bacterial suspension for MICP, or a plant-derived enzyme solution (ES) for EICP. CS was prepared by first dissolving $CaCl_2$ in approximately half of the total required water volume and allowing the solution to cool before adding urea, preventing thermal degradation of the urea during mixing. The final volume was then adjusted to reach the desired molarity.

For MICP treatments, bacterial cultures were grown in nutrient media for ~24 hours before use. Because the growth medium contained urea, the resulting culture accumulated carbonate ions capable of triggering premature precipitation. To avoid instantaneous $CaCO_3$ formation during injection, cultures used in Chapters 4–6 were centrifuged and resuspended in tap water rather than deionised water, the latter avoided due to osmotic shock leading to potential cell lysis.

EICP treatments used urease-rich extracts prepared by stirring soybean or jack bean meal in water for ≥30 minutes, followed by optional protein coagulation, centrifugation, and filtration to remove solids. This produced a clarified enzymatic solution with reproducible ureolytic activity.

Two distinct pumping strategies were used in this thesis depending on sample scale. For small-volume XCT flow cells (Chapter 3), precise low-flow delivery was essential to avoid disturbing the grain structure and to ensure controlled mixing of ES and CS. Dual-syringe pumps were therefore used, providing highly stable flow rates and accurate co-injection required for time-resolved imaging.

In contrast, larger specimens used in Chapters 4–6 required higher flow rates to deliver full pore volumes within practical timeframes. For these upscaled treatments,

peristaltic pumps were used because they offered the necessary throughput, accommodated larger tubing diameters, and were more robust for long-duration, multi-cycle injections.

Cycle duration and frequency were tuned to the experimental objective. Each treatment cycle delivered at least one pore volume of reagent solution to ensure full replenishment of reactants, with flow rates adjusted according to sample geometry. For high-temporal-resolution XCT studies, short injection cycles and low flow rates were used to minimise precipitation within a single scan while still producing measurable changes between scans. For bulk performance testing, longer cycles and higher flow rates were used to promote near-complete reaction within each injection phase, reducing the number of cycles required to reach target strength or thermal properties. Enzyme solution chemistries were selected based on the optimisation studies described in Chapters 4–5, with compositions tailored to the intended performance outcome, whether maximising strength, controlling permeability, or enhancing thermal conductivity.

2.1.3 Integration of thermal additives

The integration of thermally conductive additives required careful selection of materials and modification of the standard sample preparation workflow to ensure chemical compatibility and reproducibility. Before compaction, the quartz sand was first “wetted out” to the target moisture content (~10%) and then mixed with the additives; this pre-wetting step helped prevent segregation of low-density materials such as expanded graphite (EG) and promoted a more uniform distribution prior to layered placement in the moulds.

Preliminary trials demonstrated that not all conductive materials were suitable for use in ureolytic systems. Tinned copper wire, for example, produced visible inhibition of MICP due to copper leaching from freshly cut ends, likely through antimicrobial effects, and was therefore excluded from further experiments.

For EG, intercalation chemistry proved critical. Early trials using sulphuric-acid-intercalated EG expanded by microwave heating resulted in strongly acidified injection fluids (pH < 1), attributed to residual intercalants released during wetting. This made the material incompatible with carbonate precipitation. To avoid this, a nitric-acid-intercalated EG was sourced and expanded; when suspended in tap water

during initial screening, it produced no measurable pH change, indicating the absence of residual acids and making it suitable for Chapter 6 experiments.

Compaction effects were also important, as the effective thermal conductivity of EG-sand mixtures is sensitive to applied pressure (Cermak et al., 2020). To maintain consistency across samples, a spring-loaded punch and metal plate were used to apply a controlled, repeatable compaction force to each layer. This ensured comparable densities between specimens while preserving the low-compaction regime required for subsequent infiltration of biocementation fluids.

2.2 Urease Activity Measurement

Urease activity was measured using changes in electrical conductivity (EC) as a proxy for urea hydrolysis, following the approach first established for MICP by Whiffin et al. (2007). In MICP, mixing bacterial suspensions with a urea solution produces a near-linear increase in EC over time, enabling straightforward calculation of activity rates from the slope of the EC-time relationship.

In contrast, EICP systems exhibited a markedly different profile: upon mixing enzyme solution (3 mL) with 1.1 M urea solution (27 mL), EC spiked immediately, dropped sharply, and then stabilised at a lower value. This behaviour, observed consistently across experiments, likely reflects rapid initial ammonium ion release, which has been shown to inhibit urease activity (Ahenkorah et al., 2021). All EC measurements were conducted at 20 °C to maintain comparability between tests.

Because of this non-linear EC profile in EICP, the method was used here solely for relative comparison between enzyme sources under identical conditions, rather than for absolute benchmarking against MICP literature values. Activity was calculated as the average change in EC over a fixed 7-minute period following mixing, consistent with Whiffin's original recommendations. These measurements were primarily used to assess whether differences in lag period observed in Chapter 4 could be explained by variation in urease activity.

2.3 X-Ray Computed Tomography (XCT)

XCT was selected as the primary imaging tool because it enables non-destructive, high-resolution, 3D visualisation of $CaCO_3$ precipitation within opaque porous media. XCT reconstructs the sample as a greyscale volumetric dataset, where voxel intensity reflects X-ray attenuation and therefore material density. This provides direct access to pore geometry, grain contacts, and evolving $CaCO_3$ distributions, offering information that cannot be obtained from end-point measurements. Figure 2.1 shows a representative XCT slice with the main phases annotated.

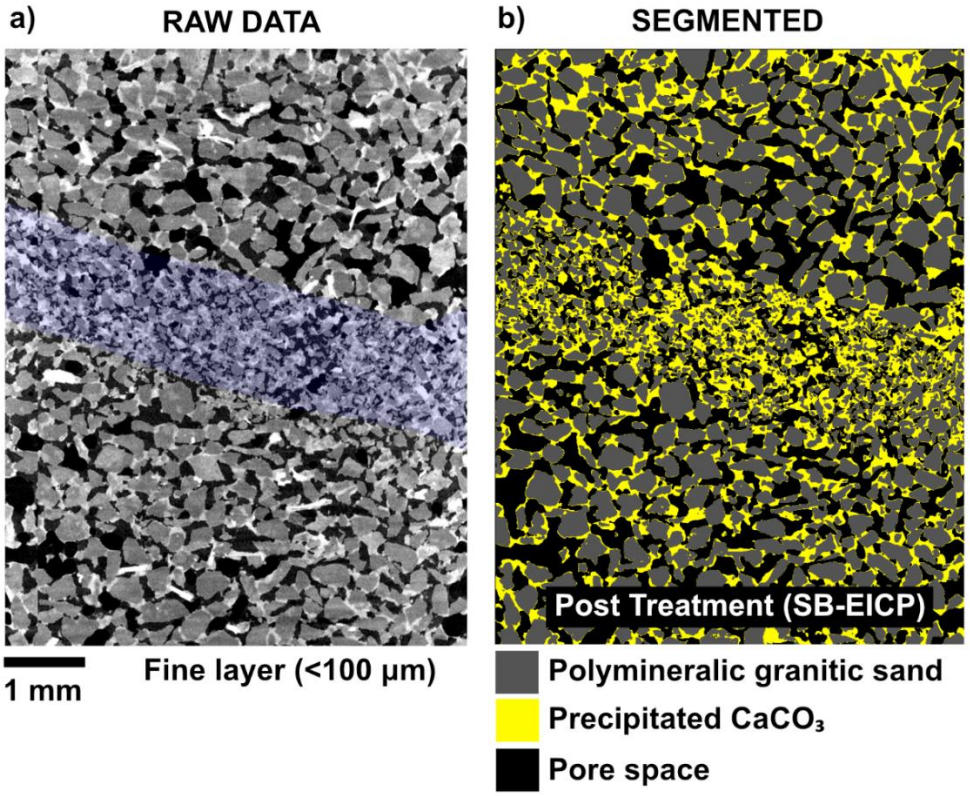

Figure 2.1 Representative XCT slice illustrating phase contrast and segmentation used throughout this thesis. (**a**) Raw greyscale XCT slice of a layered polymineralic granitic sand, highlighting the fine-grained layer (<100 µm) embedded within coarser material. (**b**) Corresponding segmented image after 7 cycles of soybean EICP treatment, identifying granitic sand (grey), precipitated calcium carbonate (yellow), and pore space (black). This phase separation underpins all subsequent analyses of carbonate distribution, pore-scale flow simulation, and permeability evolution presented in Chapters 3–5.

The general workflow used throughout this thesis involved: (i) image acquisition under scan parameter selected to minimise accelerating voltage, while maintaining at least ~30% X-ray transmission through the sample centre, (ii) reconstruction into 3D volumes, (iii) pre-processing steps such as noise filtering and greyscale normalisation, and (iv) segmentation or greyscale-based quantification depending on the analysis required. This approach made it possible to track crystal growth and mixing-driven precipitation patterns in Chapter 3 and to link pore-scale evolution with macro-scale mechanical, hydraulic, and thermal behaviour in Chapters 4–6.

Custom 3D-printed flow cells were designed in Fusion 360 to fit within the scanner's field of view while allowing continuous fluid injection (Chapters 3–5). The geometry was optimised to minimise movement artefacts during repeated scans, keep the entire sample within the field of view at high voxel resolution (<10 μm), and arrange inlet/outlet ports to promote uniform reagent distribution.

The design principles for the 3D-printed cells were to:

- **Minimise sample size to match the scanner's optimal resolution range.** For the Tescan UniTOM XL used in Chapter 3, specimens of 6–7 mm diameter yielded voxel sizes of ~5–8 μm, which is sufficient to resolve pore geometry and early-stage $CaCO_3$ nucleation. For the Nikon XT H 225 used in Chapters 4–6, larger samples (27–60 mm diameter) were required, giving voxel sizes in the range of 15–50 μm, appropriate for quantifying precipitation patterns and solid-pore distributions at the macro scale.
- **Use X-ray transparent resins to reduce attenuation from the sample holder.** This minimises the amount of X-ray energy absorbed by the holder, allowing the scan to be performed at lower voltages and with a narrower energy spectrum. Lower attenuation improves phase contrast between quartz, pore space, and $CaCO_3$, reduces beam-hardening artefacts, and increases overall signal-to-noise, which is especially important when distinguishing small or early-stage precipitation features.
- **Maintain flow symmetry at inlet/outlet boundaries to avoid preferential paths unrelated to density driven mixing.** Asymmetric inlet geometries can result in channelization driven by boundary effects rather than by the density contrasts or reaction-induced redirection of flow. Ensuring symmetric inflow and outflow conditions helps isolate the true mixing mechanisms and prevents

artefacts that would otherwise bias both experimental observations and CFD simulations.

Scan parameters (voxel size, tube voltage/current, exposure time, number of projections) were determined through preliminary test scans to balance spatial resolution, noise level, and scan time. The primary constraint was achieving at least ~30% X-ray transmission through the densest part of the sample without excessive exposure, ensuring measurable $CaCO_3$ growth while limiting blurring from precipitation occurring during a single scan. Where possible, lower accelerating voltages were preferred to reduce beam-hardening artefacts and improve phase contrast between quartz and calcite; higher voltages were only used where attenuation became prohibitive (e.g., larger specimens in Chapters 5 and 6). Excessive X-ray exposure can impair biological and enzymatic activity during biomineralisation experiments. Armstrong and Ajo-Franklin (2011) reported that a 40-minute, 30 kV synchrotron scan killed ~99% of bacteria, and pilot tests conducted during this project similarly confirmed that repeated X-ray exposure inhibited bacterially induced $CaCO_3$ precipitation. During method development, synchrotron XCT was also tested at Diamond Light Source synchrotron facility to assess whether higher-flux imaging could improve temporal resolution during active EICP. However, replicate EICP samples prepared at the same time showed substantially different precipitation behaviour depending on scan exposure: samples scanned repeatedly over approximately one hour produced much less $CaCO_3$ than paired samples scanned only once at the end of the same reaction period. This indicated that X-ray exposure in this energy range reduced ureolytic activity and/or inhibited the precipitation pathway, including in jack bean and soybean enzyme systems. Visible colour changes in the 3D-printed resin flow cells after scanning further indicated that the radiation dose was sufficient to alter the experimental environment. For these reasons, dynamic time-lapse imaging in this thesis was limited to laboratory XCT under scan settings chosen to balance temporal resolution, phase contrast, X-ray transmission, and preservation of ureolytic activity, while MICP samples were only imaged after treatments had completed.

Procedural details, including specific flow cell dimensions, injection rates, and scan settings for each experiment, are provided in the relevant results chapters.

2.4 Image Analysis & Uncertainty

The primary objective of image analysis in this work was to quantify $CaCO_3$ precipitation with sufficient accuracy to compare treatment strategies (Chapters 3–5) and additive mixtures (Chapter 6), while recognising the inherent limits of XCT resolution. Processing workflows were therefore designed to minimise bias from operator input, maximise reproducibility within a given experimental series, and maintain consistency in absolute quantitative analysis. Direct comparison of $CaCO_3$ volumes between chapters was avoided due to differences in sample size, bulk density, and scan resolution, which are considered a limitation of cross-study interpretation.

While threshold-based binarisation offers rapid quantification, it is susceptible to the partial volume effect, where a single voxel contains both solid and fluid. This leads to systematic over- or under-estimation of particle size and volume, particularly for irregularly shaped crystals or clusters. To mitigate this, features of interest were imaged at a resolution providing ≥3 voxels across the smallest relevant feature, and segmentation parameters were fixed within each experimental series to ensure comparability.

For quartz-calcite systems, the narrow density contrast between phases (2.71 g cm^{-3} for calcite, 2.65 g cm^{-3} for quartz) introduced further segmentation uncertainty, even when scans were acquired at low voltage (e.g. 40 kV, Chapter 3). As noted in X-ray attenuation models (e.g. MuCalc (Geosciences, n.d.)), a mineral's attenuation is primarily governed by its density and composition; effective mineral discrimination in XCT relies on selecting an X-ray energy where attenuation coefficients differ sufficiently between phases, which is not always achievable in quartz-calcite mixtures. Although recent advances such as machine learning-based segmentation and direct grayscale rendering (e.g. Godinho and Withers (2018)) have been shown to reduce bias, these approaches were not adopted here. Instead, a temporal subtraction approach, comparing post-precipitation scans to an earlier "baseline" scan, proved more reliable than multi-phase segmentation for identifying newly formed $CaCO_3$. This was especially important in time-lapse XCT studies (Sections 3.4.1 and 5.4.5).

Uncertainty also arose from the interplay between spatial and temporal resolution. In Chapter 3, scan intervals were selected to ensure measurable changes between time points while minimising artefacts from precipitation occurring during acquisition. Tests confirmed that blurring from intra-scan growth was minimal, and any residual effect

was considered to be encompassed within the partial volume error. Overall, absolute $CaCO_3$ volumes should be regarded as semi-quantitative, while relative changes within a given dataset can be interpreted with high confidence.

2.5 CFD Modelling Using XCT-Derived Pore Geometries

CFD modelling was used to provide insight into pore-scale flow and mixing processes that cannot be directly observed or easily controlled in laboratory experiments. While XCT offers high-resolution structural information, it cannot resolve the instantaneous velocity fields or solute mixing fronts that govern early-stage $CaCO_3$ localisation. CFD therefore served as a complementary tool that allowed flow regimes, density contrasts, and reagent interactions to be explored rapidly across a range of controlled scenarios without requiring extensive experimental replication.

Within this study, the primary purpose of CFD was not to simulate precipitation directly, but to quantify how the mixing of ES and CS shaped local flow paths, transport dynamics, and ultimately the spatial patterns of $CaCO_3$ observed in the XCT experiments.

The solver *twoLiquidMixingFoam* (OpenFOAM) was selected over multiphase or species-transport alternatives because it is specifically designed for transient simulations of two incompressible, isothermal, miscible fluids with differing densities and viscosities. Flow in the pore geometries considered here is firmly within the laminar regime ($Re \ll 1$), meaning that inertial effects are negligible and mixing is dominated by diffusion and density driven convection rather than turbulence. Under these conditions, *twoLiquidMixingFoam* provides an appropriate physical representation of the ES-CS system, where density contrasts are the primary driver of mixing behaviour.

Its implementation of the PIMPLE algorithm (a merged PISO–SIMPLE scheme) ensured numerical stability at the relatively large time steps required for long-duration simulations, while still capturing the transient development of the mixing interface. The solver also allowed passive scalar transport and buoyancy terms to be included without the additional computational overhead associated with multiphase or turbulence-resolving solvers, which are unnecessary for slow, laminar, density driven flows.

Geometries were generated from XCT-derived datasets of experimental flow cells, ensuring direct correspondence between simulated and imaged pore structures. Full-resolution meshes were computationally prohibitive for transient simulations; down-sampling by a factor of two provided a practical compromise, preserving sufficient detail to capture primary flow paths while reducing computational cost to feasible levels. Mesh independence tests showed this resolution altered absolute permeability predictions by ~18% (Appendix Fig. B1) but did not significantly affect the structure of the main flow channels, validating its use for mixing analysis.

Simulation inputs prioritised accurate representation of experimentally measured ES and CS densities and viscosities, as these parameters most strongly influence density driven mixing. Other flow parameters were retained from the validated tutorial case to avoid introducing uncertainty from untested solver settings. In addition to modelling the injection phase, post-injection simulations were run to capture buoyancy-driven mixing during the static reaction phase (Chapter 3), which was critical for interpreting precipitation patterns observed in later XCT time points.

While CFD provided valuable insight into the hydrodynamic drivers of precipitation heterogeneity, predictive accuracy was constrained by the absence of reaction kinetics and crystal growth feedback on pore geometry. Including these effects would have been computationally prohibitive and beyond the scope of this work; moreover, the imaged precipitation distribution in Chapter 3 aligned closely with the ES concentration field predicted by the simulations. The results should therefore be interpreted as a qualitative mapping of likely mixing zones and stagnation regions, rather than as direct predictors of precipitation rate or extent.

2.6 Absolute Permeability Simulations

Absolute permeability simulations were performed on XCT-derived pore structures in Chapters 3–5 to quantify how treatment strategies influenced hydraulic behaviour without requiring destructive experimental measurement. In the low-Reynolds-number regime characteristic of pore-scale flow ($Re \ll 1$), fluid motion is well described by the steady Stokes equations, allowing permeability to be computed directly from the XCT geometry. Darcy's law relates the resulting flow rate to the applied pressure gradient, enabling absolute permeability to be derived as an intrinsic property of the pore structure rather than inferred indirectly. This approach provided

a consistent and high-resolution means of tracking permeability evolution over time, even for small volumes where experimental measurements would be impractical.

Two key sensitivity analyses were carried out to ensure reliability:

- **Subvolume size effects** – Multiple cubic subvolumes (e.g., 100^3, 150^3, 200^3 voxels) were extracted from the same dataset and simulated to assess how the chosen volume influenced predicted permeability. Larger subvolumes incorporate more flow pathways and reduce sampling effects, but at increased computational cost. Results showed diminishing change beyond 150^3 voxels (Fig. 2.2), which was then adopted as the standard subvolume size. Although the sensitivity analysis was conducted on data with a voxel size of 8.156 µm (Chapter 3), the resulting minimum subvolume dimension corresponds to a physical length (~1.2 mm) that remains appropriate across the voxel sizes used in subsequent chapters (5–10 µm). This size was therefore adopted consistently as a conservative minimum representative volume for comparative permeability analysis.
- **Solver convergence criteria** – The residual tolerance controlling the Stokes solver was progressively tightened (from 1×10^{-3} to 1×10^{-6}) to determine when the numerical solution became independent of solver settings. Insufficient convergence can distort the pressure gradient and therefore the calculated Darcy flux, leading to inaccurate permeability values. The tolerance of 1×10^{-6} was selected as the point where further reductions produced no measurable change in predicted permeability and was applied consistently across all datasets.

In some samples, the original voxel resolution produced pore geometries that were too large to simulate within reasonable computational timeframes. In these cases, the datasets were down-sampled by a factor of 2 in each spatial dimension (eight original voxels combined into one). This down-sampling protocol was applied consistently whenever required, and no alternative levels of down-sampling were used.

The rationale for down-sampling was that the Stokes solver either failed to converge for the full-resolution geometry, or the memory/time requirements exceeded available resources. Down-sampling reduces the number of cells by a factor of eight, which stabilises solver behaviour and significantly reduces run time while preserving the general pore topology.

To assess the impact of down-sampling, permeability simulations were run on both the original and down-sampled volumes for representative samples. Down-sampling altered the absolute permeability by ~18%, which reflects the loss of fine-scale pore detail; however, the dominant flow pathways remained unchanged, and relative differences in permeability between treatment stages were preserved. Because the primary purpose of these simulations was to track relative permeability evolution rather than obtain an exact absolute value, this level of error was considered acceptable.

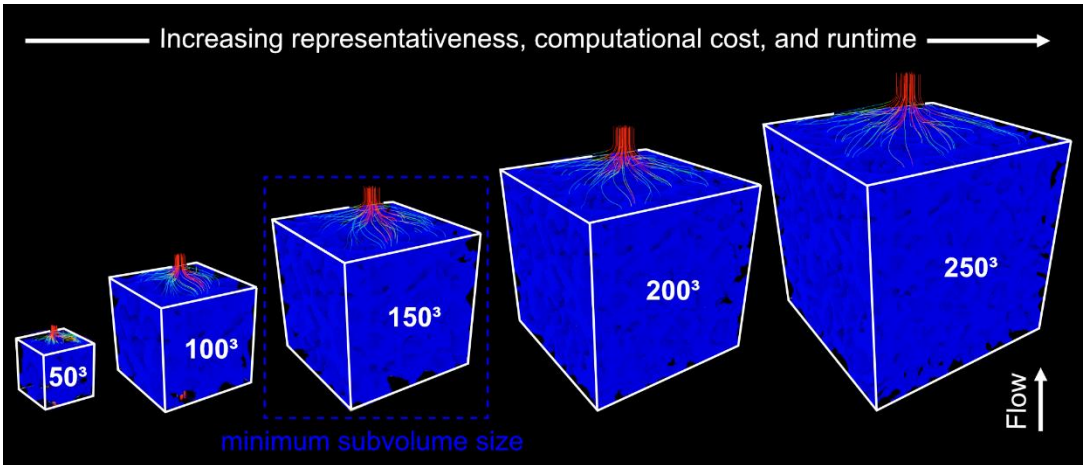

Side length (voxels)	Simulated k [d]	Porosity (vol %)
250	43.8	0.389
200	42.7	0.392
150	41.5	0.393
100	38.9	0.397
50	17.4	0.406

Figure 2.2 Sensitivity of absolute permeability simulations to subvolume size. Cubic subvolumes of increasing side length (50³–250³ voxels) were extracted from the same XCT-derived pore structure (voxel size = 8.156 µm, as used in Chapter 3) and used for absolute permeability simulations. The blue volume in each case represents the segmented pore space, with streamlines from the Stokes-flow simulation shown at the inlet to illustrate dominant flow pathways. Flow is imposed from bottom to top under fixed pressure boundary conditions. Larger subvolumes incorporate a greater number of connected flow pathways, improving representativeness at increased computational cost. Simulated permeability shows progressively smaller changes beyond a side length of ~150³ voxels, which was therefore adopted as the minimum subvolume size for subsequent analyses. The table reports the corresponding simulated permeability and porosity for each subvolume.

2.7 Optical Microscopy

While XCT provided three-dimensional, non-destructive visualisation of $CaCO_3$ precipitation within porous media, optical microscopy complemented this by offering higher-resolution, surface-level observations of crystal morphology. The increased spatial resolution allowed individual crystals to be resolved more clearly than in XCT datasets, which was particularly important for identifying crystal size and shape (e.g. rhombohedral versus spherical calcite) (Fig. 2.3).

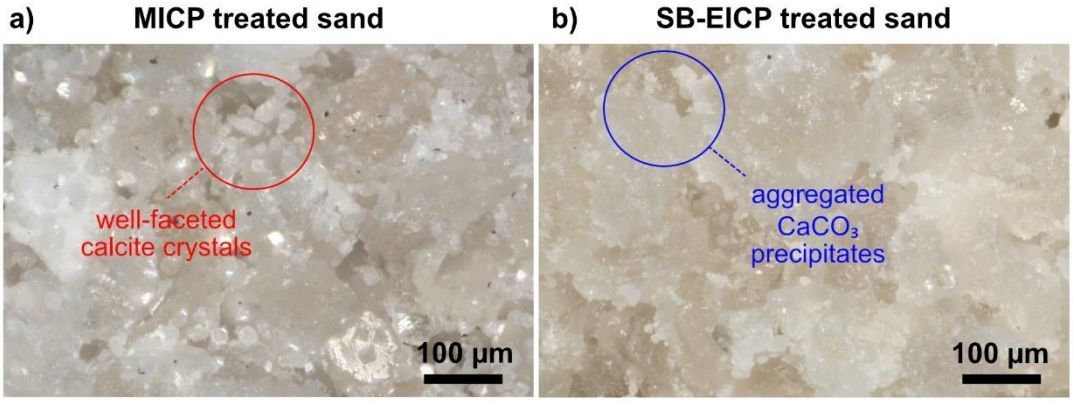

Figure 2.3 Optical microscopy images of calcium carbonate precipitation on sand grains following (**a**) MICP treatment and (**b**) soybean-derived EICP (SB-EICP) treatment. Optical microscopy allows surface-level crystal morphology to be resolved. MICP-treated samples show more well-faceted calcite crystals, whereas SB-EICP samples exhibit finer, more irregular and aggregated $CaCO_3$ precipitates. Images are representative examples used to qualitatively illustrate differences in crystal morphology. Scale bar = 100 µm.

In Chapter 6, this was particularly important for linking microstructural evidence of precipitation on additive surfaces to the thermal performance trends measured in conductivity and infrared thermography tests.

Time-lapse optical imaging was additionally employed in Chapter 4 to capture crystal growth in real time under no-flow conditions. Although these tests were conducted outside porous media and therefore did not replicate the *in situ* conditions monitored by XCT, they provided valuable insight into precipitation kinetics and morphological evolution at the grain scale.

2.8 Thermal Analysis Methods

The thermal experiments in this thesis were introduced to quantify how biocementation and functional additives alter heat transfer in treated granular materials, particularly in cases where precipitation or additive distribution introduces directional effects. Conventional isotropic thermal conductivity measurements cannot capture these behaviours, yet materials such as EG are known to exhibit strong anisotropy due to particle alignment and layered sample preparation (Cermak et al., 2020). To resolve these direction-dependent properties, an anisotropic transient-plane-source method was required, enabling separate measurement of conductivity parallel and perpendicular to the compaction layers.

Furthermore, thermal performance in Chapter 6 was not limited to steady-state conductivity. Phase-change additives such as paraffin required a method capable of capturing dynamic heat storage and release, behaviour that cannot be inferred from XCT or steady-state conductivity alone. Infrared thermography (IRT) was therefore incorporated to track real-time heating and cooling responses under controlled conditions, providing spatially and temporally resolved insight into thermal regulation mechanisms within the samples.

Early in the project, preliminary measurements were conducted using a Xiatech TC3000E thermal conductivity analyser on untreated sand-additive mixtures. While not retained for inclusion in the thesis, these data provided a rapid screening tool for identifying promising additives. At this stage, only isotropic thermal conductivity could be measured, prompting a later switch to the Hot Disk Thermal Analyzer TPS2500S, which offered anisotropic measurements as well as specific heat capacity testing.

The TPS method was selected because it allowed:

- Measurement of both isotropic and anisotropic conductivity within the same apparatus.
- Specific heat capacity determination, enabling accurate volumetric heat capacity calculations for anisotropy measurements.
- Testing of small slices cut from samples, facilitating controlled comparisons between additive types and loadings.
- Profiling of thermal conductivity along the inlet–outlet axis of samples, which was particularly important for interpreting bacterial transport behaviour during biocementation (Fig. 2.4).

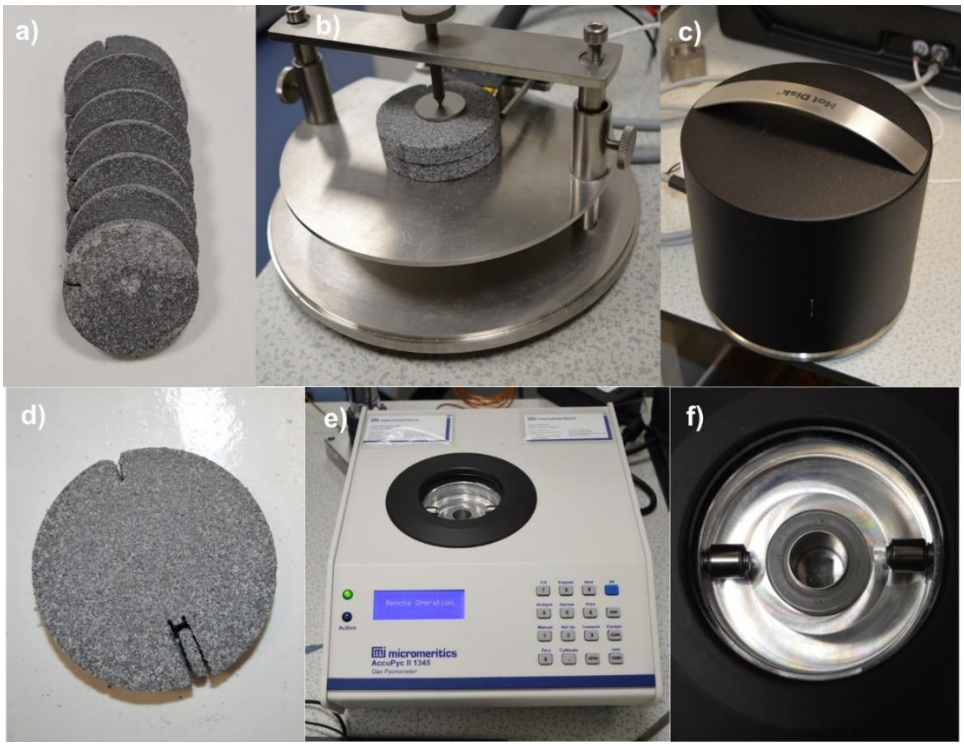

Figure 2.4 Thermal property characterisation using the transient plane source (TPS) method with complementary density measurements. (**a**) Slices cut from cylindrical biocemented specimens for thermal testing. (**b**) TPS sensor positioned between sample slices during measurement. (**c**) Enclosed sample holder used to minimise thermal influence from the laboratory environment. (**d**) Representative slice after cutting, showing the planar faces required for TPS analysis and the removal of a small subsample for density measurement. (**e**) Subsample extracted for density and volumetric heat capacity determination using a gas pycnometer. (**f**) Pycnometer measurement chamber used for density determination. Together, the TPS and density measurements enabled isotropic and anisotropic thermal conductivity, specific heat capacity, and volumetric heat capacity to be quantified, including profiling along the inlet–outlet axis of samples.

IRT was integrated into the workflow (Chapter 6) to capture real-time heating and cooling behaviour, particularly in paraffin-infused samples where latent heat storage was expected to influence cooling rates. The setup, comprising an insulated polystyrene enclosure and controlled heat input, was designed to minimise environmental variability and isolate the thermal response of the sample.

The testing approach progressed from rapid preliminary screening to targeted, high-resolution assessments, with thermal measurements paired to microstructural analyses to link additive distribution and precipitation patterns to thermal performance.

2.9 Integrated Experimental Framework

In summary, this thesis employed a linked sequence of methods to connect pore-scale precipitation processes with bulk material performance. Laboratory biocementation treatments formed the experimental basis of this work and were developed across multiple scales, from finely controlled co-injection in imaging cells to larger samples designed for mechanical, hydraulic, and thermal testing. XCT provided the core three-dimensional characterisation of precipitation behaviour, supported by optical microscopy for detailed crystal morphology. CFD modelling and absolute permeability simulations enabled interpretation of flow and transport processes within XCT-derived pore geometries. Thermal behaviour was assessed through isotropic and anisotropic conductivity measurements and infrared thermography, while urease activity testing enabled controlled comparison of enzyme sources.

With this methodological framework established, the thesis now turns to the first major research challenge: understanding how density driven mixing during co-injection governs the spatial distribution of carbonate precipitation. This question forms the focus of Chapter 3, which uses XCT imaging and CFD modelling to quantify how contrasting reagent densities influence flow paths, reaction localisation, and early-stage precipitation dynamics. These findings establish the mechanistic foundation for the optimisation and scale-up studies presented in Chapters 4–6.

Chapter 3: The influence of density driven mixing mechanisms on ureolysis induced carbonate precipitation.

This chapter addresses Critical Challenge 1 of the thesis by using time-lapse XCT to directly observe how calcium carbonate precipitation develops and localises within porous media during EICP treatment. Although bulk measurements such as hydraulic conductivity or compressive strength can reveal the outcomes of biocementation, they do not explain *when*, *where*, or *why* precipitation forms specific spatial patterns. The experiment presented here resolves the pore-scale dynamics of mixing and reaction under controlled co-injection, quantifying how density contrasts between reagents shape the geometry and progression of precipitation fronts. By coupling XCT observations with CFD-derived flow fields, this chapter establishes the mechanistic foundation required to link microscale processes to macroscale behaviour, informing later chapters that focus on permeability control (Critical Challenge 4) and, more broadly, on strategies to direct flow and improve sweep efficiency in subsurface applications (Critical Challenge 3). The central question addressed here is: How do density driven mixing mechanisms control the spatial distribution of $CaCO_3$ during EICP, and what are the implications for subsequent transport and treatment uniformity?

Citation:

This chapter has been published in part: Salter, P.J., Minto J.M., Warnett, J and Dobson, K, J. (2025). 'The influence of density driven mixing mechanisms on ureolysis induced carbonate precipitation'. *Interpore Journal, Published 25 February 2025.* https://doi.org/10.69631/ipj.v2i1nr59

Author Affiliations:

Philip J. Salter[1*], James Minto[1], Jay Warnett[2,3], Katherine J. Dobson[1]

[1] Department of Civil & Environmental Engineering, University of Strathclyde, James Weir Building, 75 Montrose Street, Glasgow, G1 1XJ, UK

[2.] International Manufacturing Centre, WMG, University of Warwick, Coventry, CV4 7AL, UK

[3.] NXCT

Author Contributions

PS: Conceptualization, Methodology, Analysis, lead on all stages of MS preparation.

JM: Funding, Data Acquisition, Supervision, Modelling, MS preparation.

JW: Data acquisition, MS review.

KD: Project design & funding, Analysis, Supervision, MS preparation.

3.1 Abstract

Engineered subsurface barriers with reduced porosity and permeability are critical for safe storage of CO_2 and H_2, prevention of pollutant transport and for several other subsurface flow challenges. This study investigates enzyme-induced carbonate precipitation (EICP), a promising technique with the potential to achieve uniform precipitation in otherwise inaccessible regions, provided the mechanisms of pore-scale mixing are well understood. High-speed lab x-ray computed tomography and flow modelling were used to study the mechanisms of reagent mixing and precipitation. Our experiments show that initially crystallization occurs homogeneously across grain surfaces, then localizes in pores with high enzyme concentrations. In these regions we see crystal growth throughout the 65 minute experiment. Simulation of reagent injection produces a mixing front that matches the distribution of crystals seen in the experiments if we model mixing as density driven flow. Overall, we see substantial reductions in simulated permeability (11–37%) depending on efficiency of mixing. Our validated model then allows us to predict and propose tailored injection strategies for optimizing mixing, bringing us closer to real-world deployment of EICP for subsurface barriers.

Key words: MICP, EICP, permeability, high-speed XCT, tomography

3.2 Introduction

Enzyme induced carbonate precipitation (EICP) is a bio-cementation technique that can be used to seal microfractures and pore throats that are inaccessible to cement and chemical based grouts (H. Wang, X. Sun, et al., 2022), with many similarities to the better-studied microbially induced carbonate precipitation (MICP). Although explored in 2D microfluidic flow cells (Kim et al., 2020; Weinhardt et al., 2021) and for engineering applications including the stabilization and strengthening of soils (Carmona et al., 2016; Putra et al., 2018; Putra et al., 2016), reducing soil permeability (Yasuhara et al., 2012) and the treatment of hydrocarbon contaminated sands (Singh et al., 2021), EICP is still not routinely deployed, partly this is because we do not have the necessary understanding of 3D pore-scale precipitation. We therefore cannot predict, control or exploit the distribution of $CaCO_3$ through time and space using different injection strategies.

Large scale geological sequestration of carbon dioxide (CO_2) is an essential component in tackling climate change (Krevor et al., 2023) and we need at least another 10,000 CO_2 injection wells globally by 2050 (Ringrose & Meckel, 2019). At present there are only 26 projects worldwide, most of which only have CO_2 injection/storage to enhance oil recovery. Key challenges preventing more widespread development include the need to prevent CO_2 leakage to atmosphere or into groundwater (Chedburn et al., 2022), managing injection into heterogeneous natural rocks, and converting existing hydrocarbon extraction systems for CO_2 injection and storage. Enzyme induced carbonate precipitation (EICP) is a technique that could be used to create spatially targeted impermeable barriers in the subsurface and seal leakage pathways around wellbores (Nemati, 2003), and therefore a key tool in controlling injection of and preventing leakage of geo-sequestered CO_2 (and H_2).

EICP involves injection of two reagents – a solution of ureolytic enzyme (usually called the enzyme solution – ES) and a solution of urea and calcium (usually called the cementing solution – CS), both of which have low viscosity. On mixing, calcium carbonate precipitates following Equations 1 to 4.

$$CO(NH_2)_2 + 3H_2O \xrightarrow[urease\ enzyme]{} 2NH_4^+ + HCO_3^- + OH^- \quad (1)$$

$$CaCl_2 \rightarrow Ca^{2+} + 2Cl^- \quad (2)$$

$$HCO_3^- \rightarrow CO_3^{2-} + H^+ \quad (3)$$

$$Ca^{2+} + CO_3^{2-} \rightarrow CaCO_3 \quad (4)$$

For optimal permeability reduction an ideal EICP treatment would achieve well mixed fluids and homogenous precipitation of large volumes of $CaCO_3$. By controlling the injection points and the spatial and temporal evolution of the mixing profile in the sample, it should be possible to control where in the sample precipitation occurs, and therefore how the permeability of the sample changes.

To fully develop deployable EICP strategies we need experimental data for how mixing occurs in the pore structure, how this mixing controls when and where $CaCO_3$ precipitates, and a numerical model that can predict this behaviour in subsurface systems. Previous studies have observed bulk permeability reductions in soil (Nemati et al., 2005) and fractured rocks (Peng et al., 2020) but have not quantified the spatial and temporal evolution of the precipitation, or the pore-scale distribution of $CaCO_3$, therefore numerical modelling of this system remains challenging and largely unvalidated.

Here we exploit high speed laboratory X-ray computed tomography (XCT) to visualise and quantify the spatial and temporal distribution of $CaCO_3$, capturing precipitation dynamics, flow path migration and the evolving porosity (Dobson et al., 2016; Godinho et al., 2019; Menke et al., 2018). We measure crystal volume and position relative to pore throats and grain contacts and validate numerical models for permeability, flow velocity and fluid mixing behaviour in the pore structure of the experiments. This is carried out with the aim of gaining a fundamental understanding the EICP process sufficient to design up-scaled injection strategies.

3.3 Materials And Methods

3.3.1 In situ observation of enzyme induced carbonate precipitation

The enzyme solution (ES) was prepared from 12 g/L urease active jack bean meal (Fisher Scientific), and syringe filtered (<0.45µm) after 30 mins homogenisation. Jack bean meal was used as it is 70–90% less expensive and has lower urease activity (1500 U/g) than purified urease sources, allowing a slower reaction rate that has been shown to lead to more compact and harder $CaCO_3$ (Chunxiang et al., 2009). The cementing solution (CS) was made by dissolving 4M urea and 2.67M calcium chloride in deionised water. The CS pH was adjusted to 6.89 using 4M HCl prior to injection to delay the immediate onset of precipitation (after Minto et al. (2017), Cheng et al. (2018)).

Custom made 3D-printed (5 mm diameter, 0.39 cm^3 volume) flow cells (Figure 3.1) were filled with quartz sand (Sigma Aldrich, silica content <= 100 %, particle size range of 210–297 µm), with a porosity of 39%. The columns were saturated with a 3 g/L NaCl solution to simulate a subsurface brine, and mounted into a Tescan UniTOM XL lab scanner (University of Warwick, WMG). 1.5mL of the CS and ES were injected simultaneously at 0.5 mL/min through the two inlet ports (Figure 3.1) equating to ~6 pore volumes/min. The ES enters the sample at a single central feed point surrounded by the 4 CS feed points (Figure 3.1b). After 3 minutes of injection (18 pore volumes), the flow is stopped and XCT data collected.

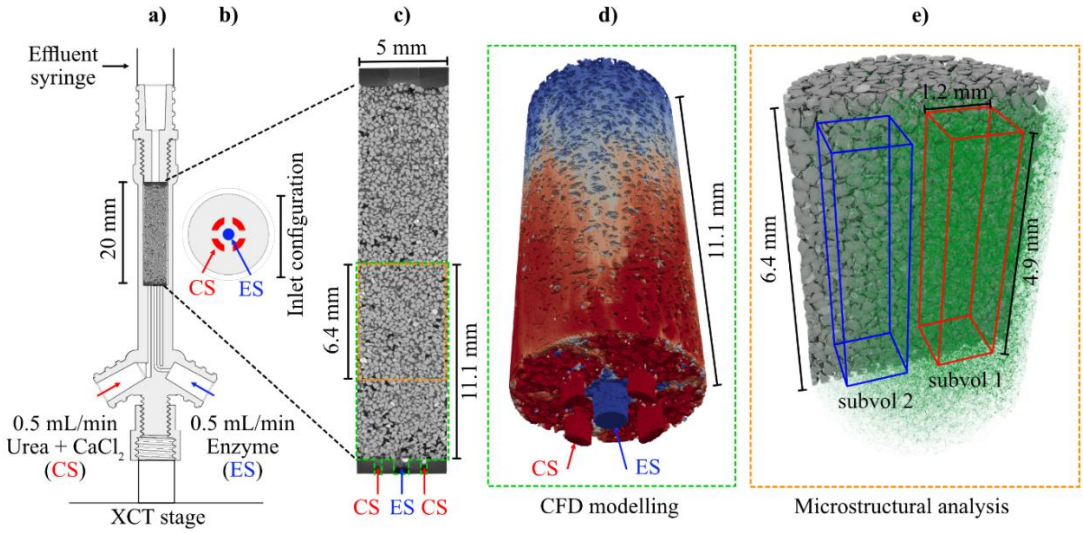

Figure 3.1 Experimental setup, analysis and modelling (**a**) 3D printed flow cell (**b**) inlet configuration showing urea/calcium chloride (red) and enzyme (blue) entry points (**c**) vertical slice through entire sand pack volume **d** 3D rendering of CFD modelling volume **e** imaging window captured during sequential scans showing sub-volume 1 (red), sub-volume 2 (blue)

All XCT data were collected at 40kV and 15W/375µA, with 1440 projections/scan (205 ms exposure time). 12 scans were acquired over a 1-hour period with each scan lasting 5 minutes. Each scan was started immediately after the previous scan completed. Crystal growth was continuous over the scanning period so there will be a difference in the sample structure at projection 1 and at projection 1440. This difference will mean some blurring of the data. 5 minutes per scan ensured this difference was minimised and scans could be reconstructed with minimal blurring artefacts, while still seeing $CaCO_3$ growth that was measurable. The proprietary Tescan reconstruction code generated 3D datasets with 8.156µm resolution (voxel edge length). Image processing and analysis was completed in Avizo® (v2022.2, ThermoFisher) and the full workflow shown in Appendix Fig. A1.

3.3.2 Image analysis

The sample was not moved between scans but to ensure perfect spatial alignment through time the data were registered (Studholme et al., 1999), and an edge preserving denoising anisotropic diffusion filter (Bernard et al., 2011) applied. A post reconstruction beam-hardening correction was also applied to each dataset. Segmentation was completed using the histogram based Auto Thresholding Avizo module (Otsu, 1979) to remove human bias in processing datasets where the bulk

greyscale values are changing through time as precipitation occurs (Appendix Fig. A1). This segmentation generated binary map of the pore phase was inverted to generate a binary map of the solid phases. The similarity of the attenuation (greyscale) prevented the segmentation of the $CaCO_3$ from the quartz. The quartz does not change through time and there is no $CaCO_3$ at t=0. $CaCO_3$ volume was calculated by subtracting the t=0 scan (quartz only) from the segmented quartz + $CaCO_3$ in later scans (Figure 3.2). The porosity was determined by calculating the volume fraction of the non-solid phase relative to the entire cylinder volume.

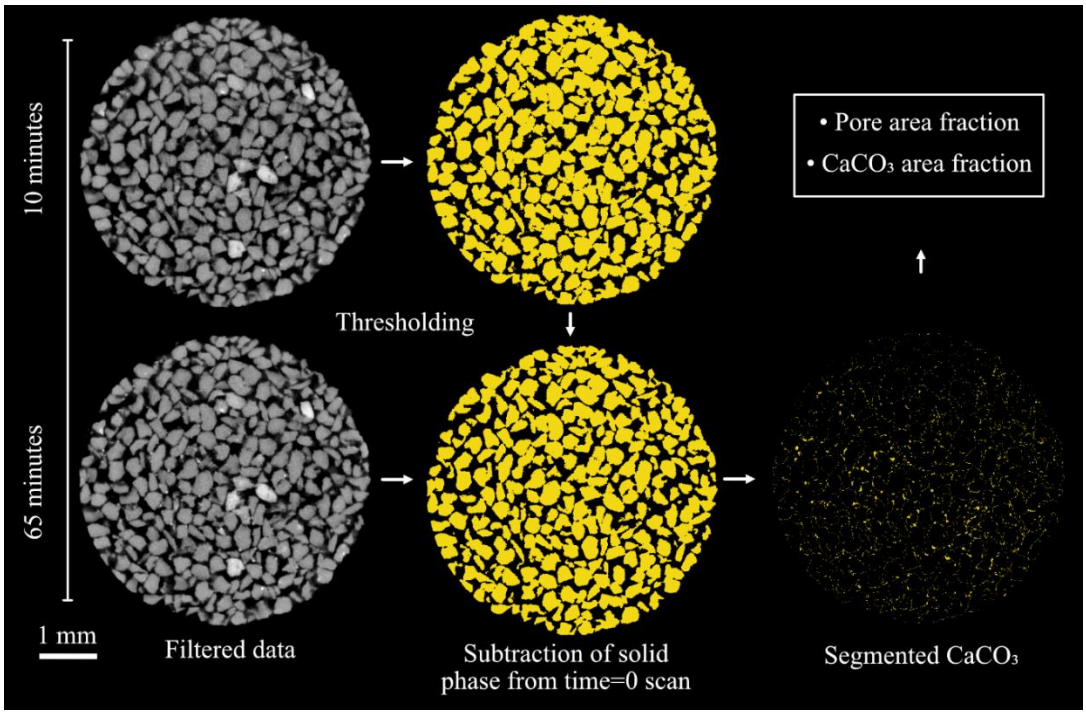

Figure 3.2 Segmentation of solid phases and calculation of $CaCO_3$ by subtraction of t=0 (quartz only) from t=n (quartz + $CaCO_3$)

The volumes and positions of the crystals were measured from the binary maps of $CaCO_3$. We use the term crystal to mean each individual object in the binary map, although some may be crystal clusters if we could image at higher resolution.

The pore network morphology was determined at t=0 using a separation based on a Random Walk Distance Map (Baum et al., 2019) and the pore volume, geometry and coordination numbers measured for every pore and the pore throat locations identified. The sand grains do not move but the volume and geometry of the pores will change due to precipitation and hence the number and location of pore throats

could change. We therefore use the pore throats defined at t=0 for all t≠0 datasets, applying the segmented t≠0 pore network as a mask to the t=0 separated 3D pore map (see Figure B1). This mapping of properties over time onto a consistent geometry allows quantification in the change in volume and geometry at the pore scale. The location of the pore throats, their area and geometry at t=0 was extracted from the Local H-Maxima output (see Figure B1) and the distance of every point within the pore network to the nearest throat calculated using a Distance Map. The distance of each crystal of $CaCO_3$ to the nearest pore throat was then extracted from a Label Analysis applied to the distance map output masked by the $CaCO_3$ 3D location map (See Figure B1 for details). At each time point the permeability of the pore network was calculated using the Absolute Permeability Simulation available within the XLab Simulation package of Avizo.

A second Random Walk Distance Map was applied to the inverted pore network at t=0, and the volume, surface area, sphericity, and coordination number (i.e. number of solid-solid contact points) of the quartz grains measured using a Label Analysis.

By integrating the pore geometry and $CaCO_3$ 3D location maps with the outputs of the permeability simulation, we can also determine the mean velocity of the flow in each pore, through each pore throat, and at each crystal location during the initial injection phase. Pore and $CaCO_3$ analysis and Absolute Permeability Simulations were also performed on 2 smaller sub volumes selected from different regions of the sample (Figure 3.1).

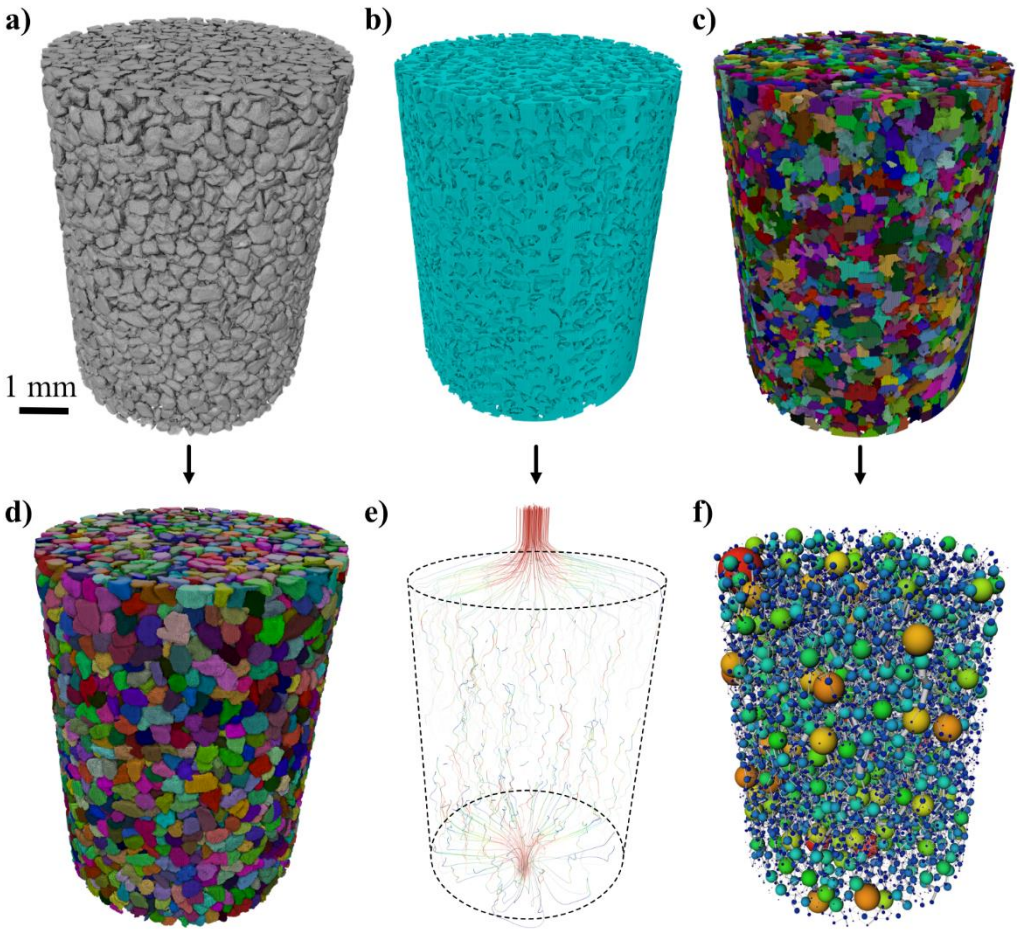

Figure 3.3 4D Image processing workflow: (**a**) binarized solid regions, (**b**) connected pore space, (**c**) separated pores by random walk distance map, (**d**) separated grains, (**e**) output streamlines from absolute permeability simulation, (**f**) pore network model

3.3.2.1 Uncertainty in the image analysis

The small volume of the $CaCO_3$ crystals (542 μm^3 (a single voxel) to $4.5x10^8$ μm^3, mean = 6766 μm^3) and the common formation of crystal clusters is the main source of uncertainty in quantitative data. The partial volume effect comes from defining any irregular particle as a group of voxels. The greyscale values of voxels that intersect the surface of the particle will be proportional to the relative volume of particle and surrounding media within the voxel. As the segmentation process will include or exclude a voxel based on that greyscale value, the binarised (segmented) data will locally (at the voxel scale) over or under estimate the location of the particle surface. For $CaCO_3$ crystal clusters this may be further complicated as the internal voxels can also have both particle and pore fluid within them. The value of the uncertainty on any

individual particle and any particle population can be calculated (Lin et al., 2015). The pores and sand grains are all large relative to the voxel size (mean volume of 4180 and 18200 voxels respectively) so the uncertainty cannot be seen when plotted on the size distributions.

The other potential source of uncertainty is the combination of spatial and temporal resolution. We see no evidence of crystal motion during the experiment, nor for nucleation and growth away from the sand grain surfaces; but the resolution of the images means very small crystals may not be captured. However, crystals are observed to form on all sides of sand grains with no clear preference for the upper surface, suggesting that nucleation primarily occurs directly on the grain surfaces rather than in the solution, followed by settling on the tops of grains. Each 3D acquisition takes 4 minutes, 55 seconds with a scan started every 5 minutes so the data reconstruction could be affected by the change in $CaCO_3$ volume during a scan. However, we can see measurable differences in crystal volume between time points and find minimal blurring artefacts in the data that would suggest an individual data set is significantly impacted by crystal growth. We therefore assume any effect is captured in the partial volume effect in the reconstructed data.

3.3.3 Modelling of fluid mixing

Fluid mixing was simulated with the computational fluid dynamics software OpenFOAM with a domain extending from inlet to the top of the dynamic imaging window (Figure 3.1) and injection parameters that replicate experimental conditions in which the four outer inlets injected CS (density=1234 kg m^{-3}, viscosity=2.1157×10^{-6} Pa.s), while one central inlet injected ES (density=998 kg m^{-3}, viscosity=1×10^{-6} Pa.s). The mesh was generated from a full sample scan with a voxel edge length of 13.768 µm; however, this resolution was computationally prohibitive for dynamic flow simulations. Down-sampling by a factor of 2 resulted in a voxel edge length of 27.536 µm, which balanced computational efficiency with sufficient resolution to capture flow behaviour while enabling feasible simulation times. A mesh independence verification was conducted by comparing Absolute Permeability Simulations for the original (13.768 µm) and down-sampled (27.536 µm) meshes. This sensitivity analysis on permeability showed that while down-sampling did alter the simulated permeability value (18%), it did not significantly alter flow path dynamics (Appendix Fig. B1). The code used to convert voxel data into a mesh readable by OpenFOAM, with appropriate boundary patches, was written as an ImageJ script implemented in Fiji

(Schindelin et al., 2012), following the methodology outlined in Section 3.5 of Willems et al. (2021).

Within OpenFOAM, the twoLiquidMixingFoam solver was used to model injection and subsequent density driven flow of the miscible ES and CS. The solver employed second-order spatial discretization schemes for key terms, ensuring accurate representation of flow dynamics. Temporal discretization was handled using the first-order implicit Euler method for stability in transient simulations. A detailed list of parameter settings and schemes is provided in Table B1 (Appendix B).

The focus was placed on adjusting density and viscosity parameters, as these were critical for capturing mixing behaviour, while all other parameters were retained from the validated twoLiquidMixingFoam tutorial. The post-injection flow phase was also modelled to account for the density driven mixing during crystal formation.

3.4 Results

3.4.1 Quantification of EICP in 4D

Data were collected across 12 time points during crystallisation (no injection). Over the period we see the $CaCO_3$ content increase steadily. Small crystals form initially, before larger ones grow preferentially in a distinctive cone-shaped region in the centre of the column/imaging region (Figure 3.4).

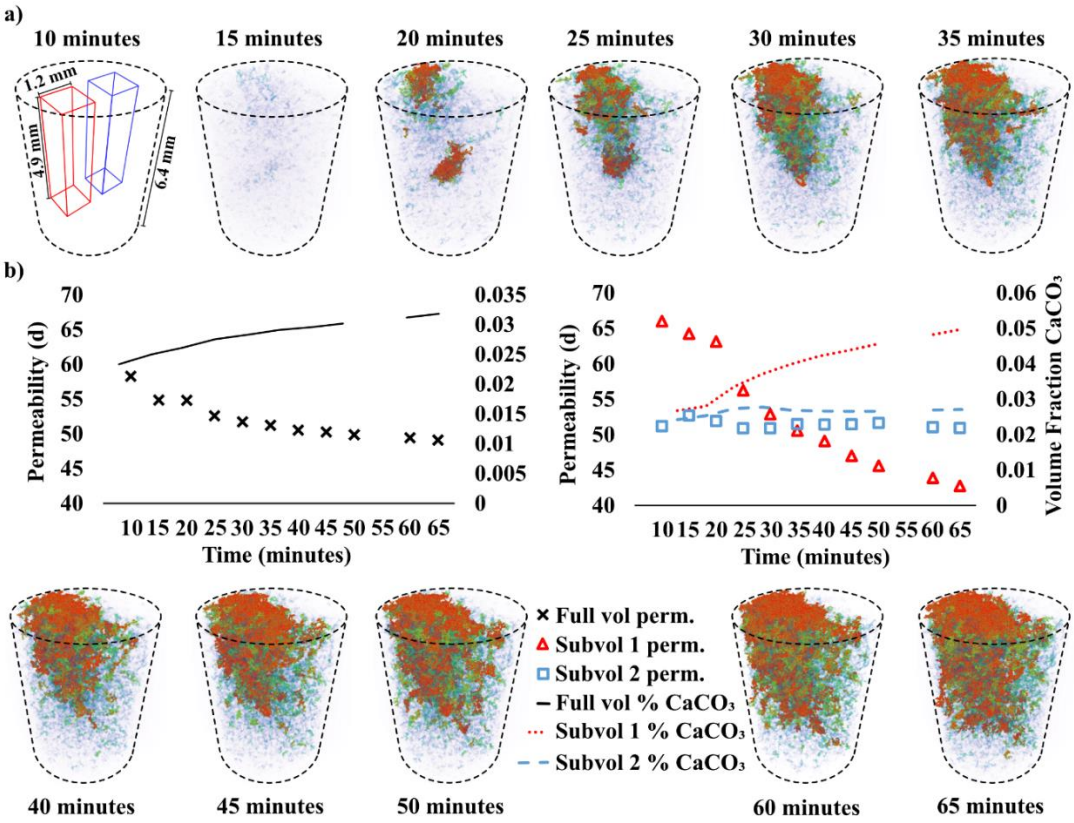

c)

Volume	Time (mins)	Vol. Fraction $CaCO_3$	Simulated Permeability (Darcy)
Full Volume	20	0.0250	54.85
	35	0.0283	51.25
	50	0.0302	49.86
	65	0.0318	49.12
Sub-volume 1	20	0.0280	63.14
	35	0.0400	50.58
	50	0.0455	45.61
	65	0.0498	42.77
Sub-volume 2	20	0.0254	51.92
	35	0.0269	51.48
	50	0.0266	51.66
	65	0.0271	50.93

Figure 3.4 $CaCO_3$ precipitation over time: (**a**) Spatial distribution of $CaCO_3$ over time with crystals coloured with red representing the largest and blue the smallest volumes (**b**) Graph of permeability/time/volumetric % $CaCO_3$ for the full volume (black), highly precipitated sub-volume 1 (red), and low precipitation sub-volume 2 (blue) (**c**) Simulated Permeability and Vol. Fraction $CaCO_3$ for the Full Volume and Sub-volumes at Selected Time Points During EICP.

The injection points are lower than the imaging window (Figure 3.1) and it was therefore anticipated, due to the miscibility of the two fluids, that sufficient mixing would have occurred beneath this to promote uniform crystallization across the imaging region. The simulated permeability across the red sub-volume 1, where ~5% $CaCO_3$ eventually formed, is reduced much more rapidly than the blue sub-volume 2 or the whole domain.

Figure 3.4c summarizes simulated permeability and vol. fraction of $CaCO_3$ for the full imaging volume and sub-volumes 1 and 2 at 20, 35, 50 and 65 minutes, highlighting localized effects of $CaCO_3$ precipitation on hydraulic properties.

3.4.2 Porosity evolution during EICP

During the first 20 minutes of the reaction the vertical distribution of $CaCO_3$ is relatively homogenous. However, as the reaction progresses the volume fraction of $CaCO_3$ increases gradually from inlet to outlet (Figure 3.5). Once nucleated the crystals formed in the lower portion of the column (< 5 mm) do not exhibit a large increase in volume over time, while the crystals formed towards the outlet continue to grow larger. To quantify porosity evolution in the flow direction, we plot the 2D percentage of $CaCO_3$ from the base of the imaging region (near-inlet) to the top of it (Figure 3.5).

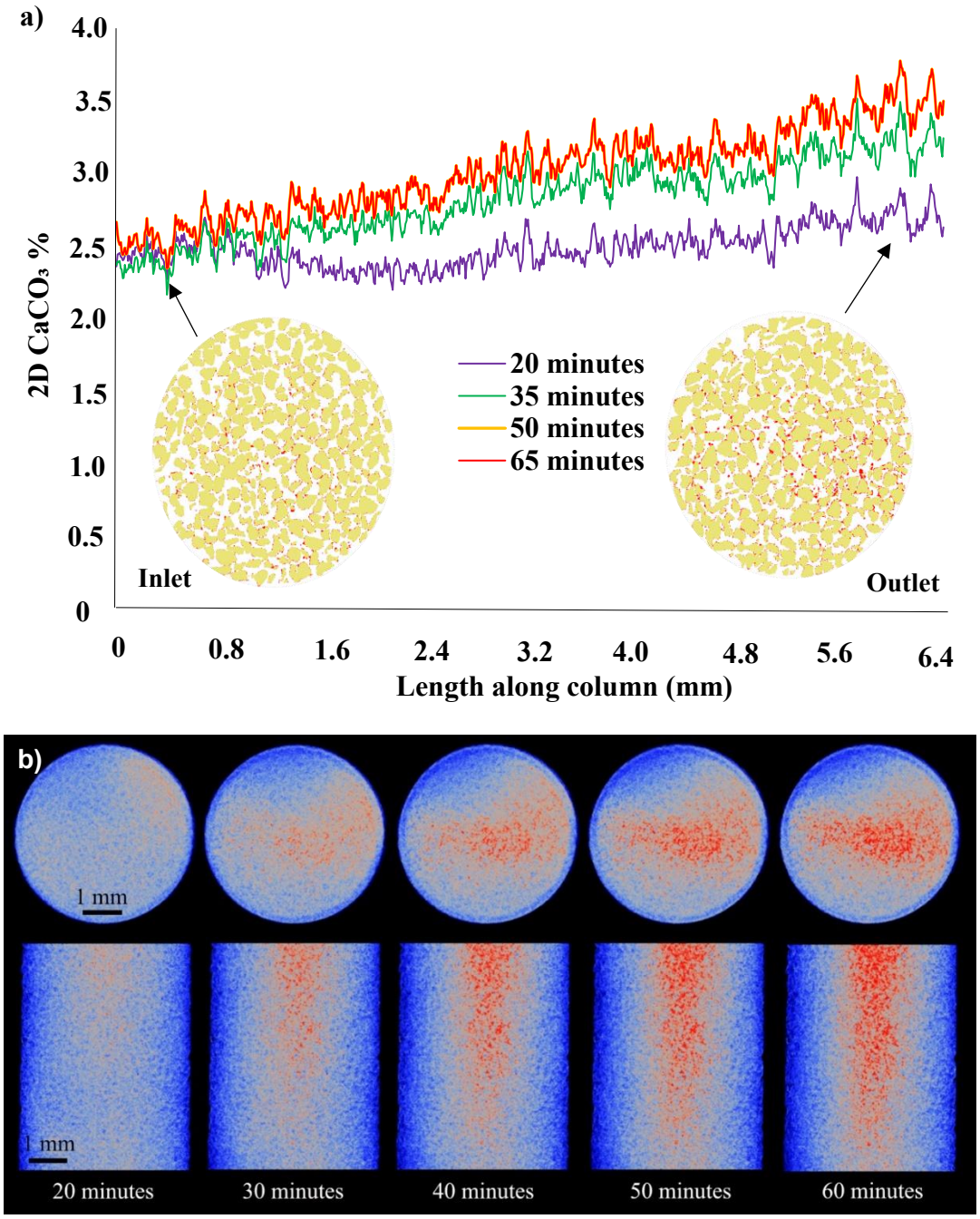

Figure 3.5 Distribution of $CaCO_3$ over time with: (**a**) Column depth – The inset images are at 65 minutes and approximately 0.4mm (left) and 6.1mm (right) from the bottom of the dynamic imaging window with $CaCO_3$ coloured red, (**b**) radial and axial $CaCO_3$ distribution (red) over time

While the evolution of $CaCO_3$ distribution is explored relative to column height in Figure 3.5a, the 3D distribution of $CaCO_3$ can be more effectively visualized by plotting the average radial and axial concentration for each individual pixel (Figure 3.5b). The

main precipitation zone forms a cone-like shape, with the highest concentrations of $CaCO_3$ occurring centrally and towards the outlet. The position of precipitated $CaCO_3$ relative to quartz grain surfaces, as determined by random walk distance map, is explored in Figure 3.6.

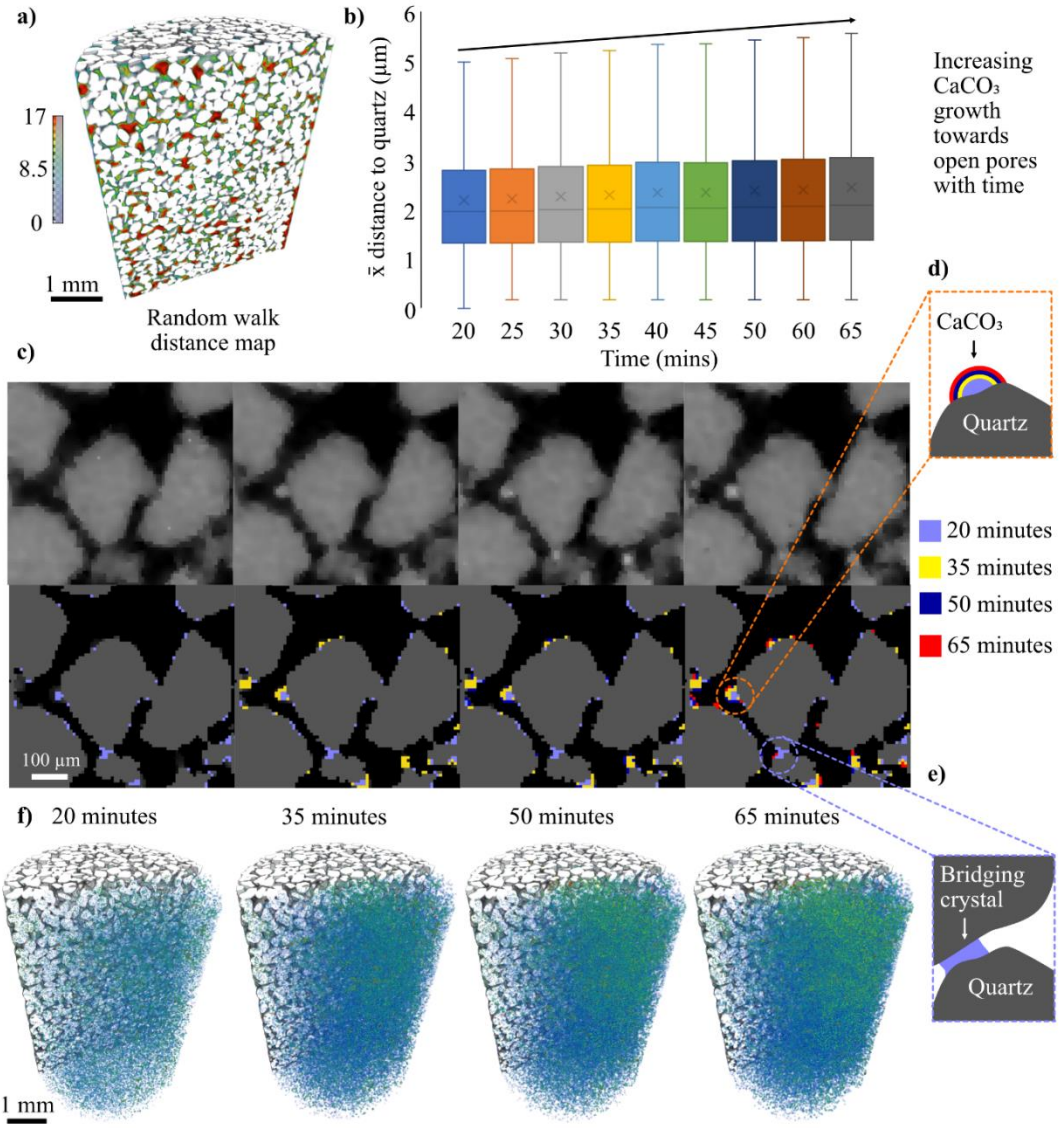

Figure 3.6 Crystal locations relative to quartz grain surfaces as determined by random walk distance map: (**a**) random walk distance map with near grain surfaces coloured blue and open pores (red), (**b**) box plots of the mean distance of new $CaCO_3$ (grown between scans) to quartz grain surfaces for each time point, (**c**) zoomed in view of XCT data showing how crystals form over time, (**d**) schematic of $CaCO_3$ growth into open pores, (**e**) schematic of $CaCO_3$ growth at grain contact points and (**f**) crystals coloured by distance map value over time with colouring as per (a).

Unlike MICP, where cells tend to attach at grain contact points before acting as nucleation sites for crystal growth (I.e. the solution immediately around them becomes supersaturated with respect $CaCO_3$) (Minto et al., 2017), we observe many small crystals nucleating throughout the column, before growing out into open pores on existing $CaCO_3$ (Figure 3.6f). This precipitation mechanism (schematically represented in Figure 3.6d) appears to be more dominant than $CaCO_3$ growth at grain contact points (Figure 3.6e). The mean distance map values for $CaCO_3$ that then forms between scans (Figure 3.6b) shows a subtle upward trend in crystals growing towards open pores over time rather than continued grain surface growth. By colouring $CaCO_3$ crystals by their mean distance map value (Figure 3.6f) we see that the crystals that grow towards open pores (I.e. warmer colours) are primarily found within the main precipitation band. The continued growth in this region is therefore on pre-existing $CaCO_3$.

3.4.3 Absolute permeability evolution and mixing during EICP

Absolute permeability refers to the ability of a porous material to transmit a single-phase fluid and is characterized by a constant coefficient that relates fluid flow and material parameters in Darcy's law (Eq. (6)):

$$\frac{Q}{A} = -\frac{k}{\mu}\frac{\Delta P}{L} \tag{6}$$

Where the global flow rate that goes through the porous medium is represented by Q, which is measured in units of m^3/s. The cross-sectional area of the sample through which the fluid flows is represented by A and is measured in m^2. The dynamic viscosity of the fluid flowing through the sample is represented by μ and is measured in Pa.s. The pressure difference applied across the sample is represented by ΔP and is measured in units of Pa. L represents the length of the sample in the direction of flow and is measured in m. Permeability, k with units in m^2, is therefore a function of the pore geometry and connectivity within the sample and a bulk value of permeability can be obtained for the entire sample by experimentally measuring pressure drop for a given flow rate, as is typically done for cylindrical cores in a core holder.

Permeability can also be estimated numerically based on XCT derived pore geometry and connectivity together with simulated fluid flow and pressure drop across samples of any shape or size without limitations imposed by core holder design or pressure sensor resolution. In this study, Avizo XLab Simulation module was used for the determination of the absolute permeability with the added benefits that flow paths are

also calculated and, rather than a single bulk measure of permeability, multiple permeabilities can be calculated for different regions of the sample.

In addition to simulation of the initial (pre-EICP) pore geometry, permeabilities were also calculated at different time points during the static EICP reaction period to understand how the precipitating $CaCO_3$ and evolving pore geometry was shaping the hydraulic properties. The results of permeability/porosity and permeability/time calculations are shown in Figure 3.4.

By running absolute permeability simulations at each time point, the output velocity field can be used to visualize and quantify the effect that each individual crystal would be having on flow at that particular instance in time (Figure 3.7):

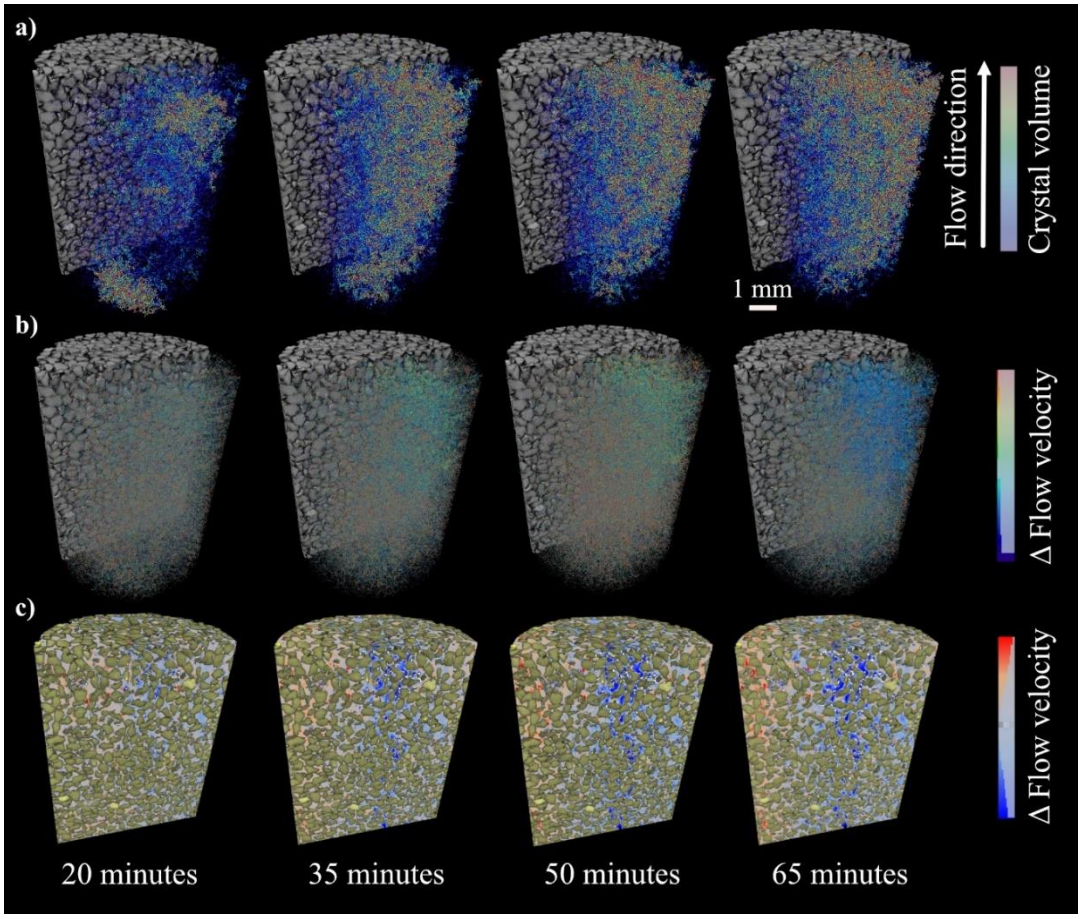

Figure 3.7 The effect of enzyme induced $CaCO_3$ on flow: (a) crystals are coloured by volume, (**b**) their effect on simulated flow velocity relative to t=0 and, (**c**) with crystals coloured white, and pore space coloured by the flow velocity at t≠0 minus the flow velocity at t=0 from flow simulations.

The location of the extracted sub-volumes is shown in the Fig. 3.1e. While the initial permeability of sub-volume 1 (61.4 Darcy) is higher than that of sub-volume 2 (46.4 Darcy), it experiences a 37.1% reduction in simulated permeability over the course of the experiment. There is negligible (0.8%) reduction in permeability within the blue sub-volume 2. The full imaging volume experiences an intermediate reduction (11.4%) as a result of both regions. Flow is diverted to the column's peripheries as crystals form in the central region, shown by the red areas of the pore space in Fig. 3.7c – 65 minutes. We hypothesize that ES and CS were mixed sufficiently within sub-volume 1 to induce rapid $CaCO_3$ precipitation and the altering of flow paths (Figure 3.8), but that fluid mixing was limited within sub-volume 2, resulting in less precipitation. This is explored further in section 3.4.3.1.

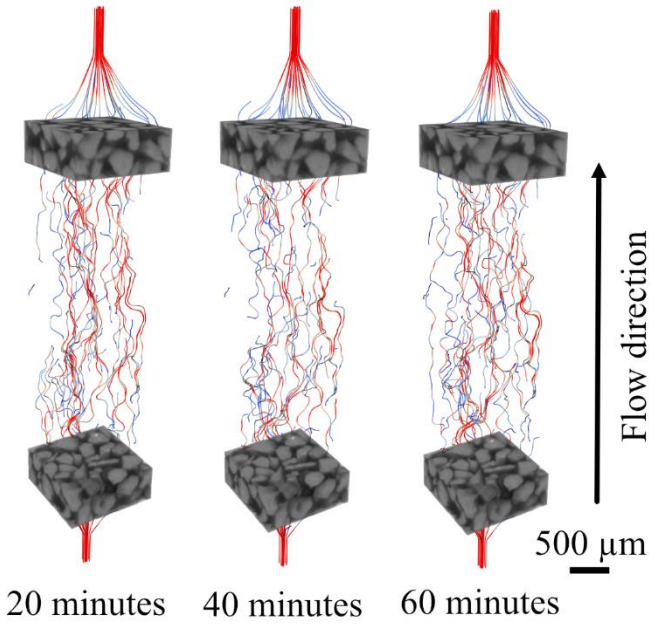

Figure 3.8 Streamlines of flow paths across high precipitation sub-volume 1 over time

Overall, these observations suggest that the impact of EICP on porosity and permeability in sand is highly dependent on the spatial distribution of $CaCO_3$. As expected, regions with high crystal growth experience a greater reduction in permeability compared to regions with minimal crystal growth.

3.4.3.1 Simulation of fluid mixing

The distinctive cone-shaped crystal region can be better understood by simulating the mixing of CS and ES within the sample. We also simulate the fluid behaviour after flow cessation during imaging. Three mechanisms hinder uniform mixing in the pore space. Firstly, the smaller cross-sectional area of the central inlet (0.486 mm^2), used for injecting ES, when compared to the four outer inlets used for injection of CS (0.760 mm^2) results in a higher flow velocity, which leads to an initial cone-like geometry to the enzyme fluid field (Figure 3.9a). Secondly, the higher kinematic viscosity of CS

physically inhibits further mixing. Thirdly, when flow stops, density driven currents cause CS to settle at the sample's lower part, reducing the available surface area for diffusion of urea and calcium ions, but improving advective mixing (Figure 3.11b). The observed fluid flow behaviour is shown in Figure 3.9. Note that the simulation was carried out in 3D and mesh generated as described in section 3.2.

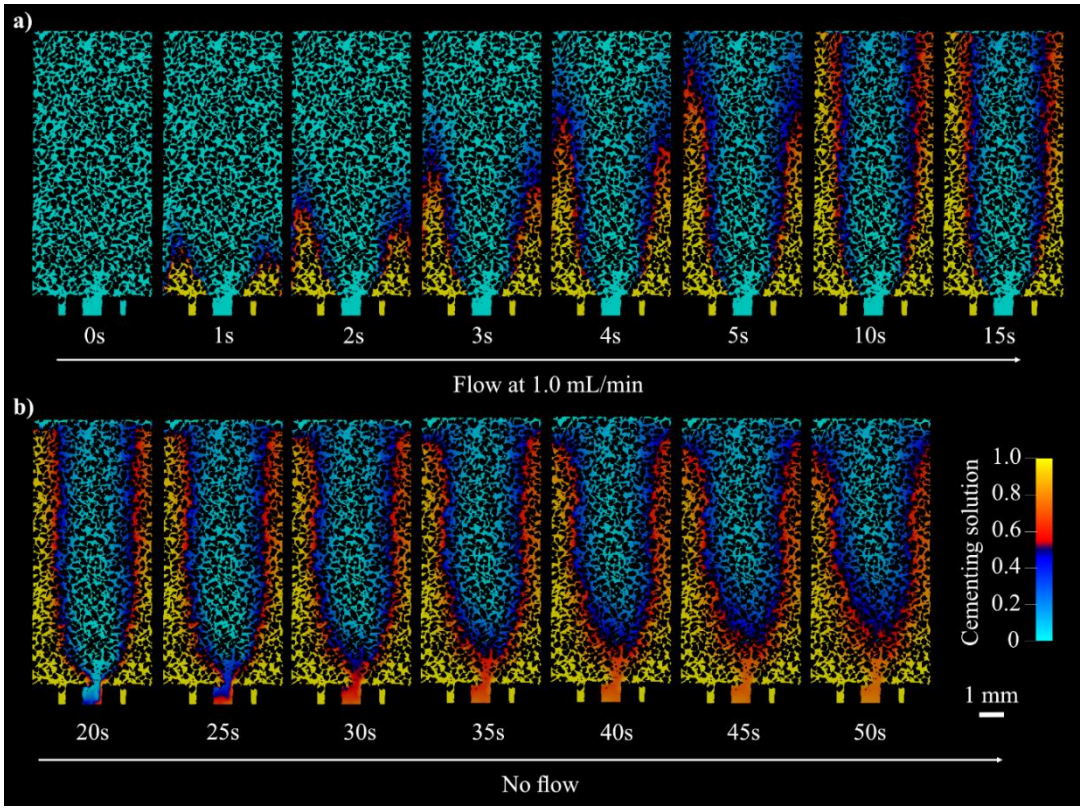

Figure 3.9 Cross sectional view of enzyme and cementing solution mixing during (**a**) flow of 15s, at which point the injection reaches a steady state, and (**b**) the static period when crystallization occurred.

The simulations were repeated, to assess if a lower concentration of cementing solution would improve fluid mixing due to a reduced difference in density and viscosity between CS and ES. This entailed adjusting the fluid properties (kinematic viscosity and density) of the CS in the model to correspond with those of a) a 2M urea, 1.33M $CaCl_2$ solution, and b) water. The outcomes of these simulations are shown alongside the initial simulation of the experimental setup in Figure 3.10.

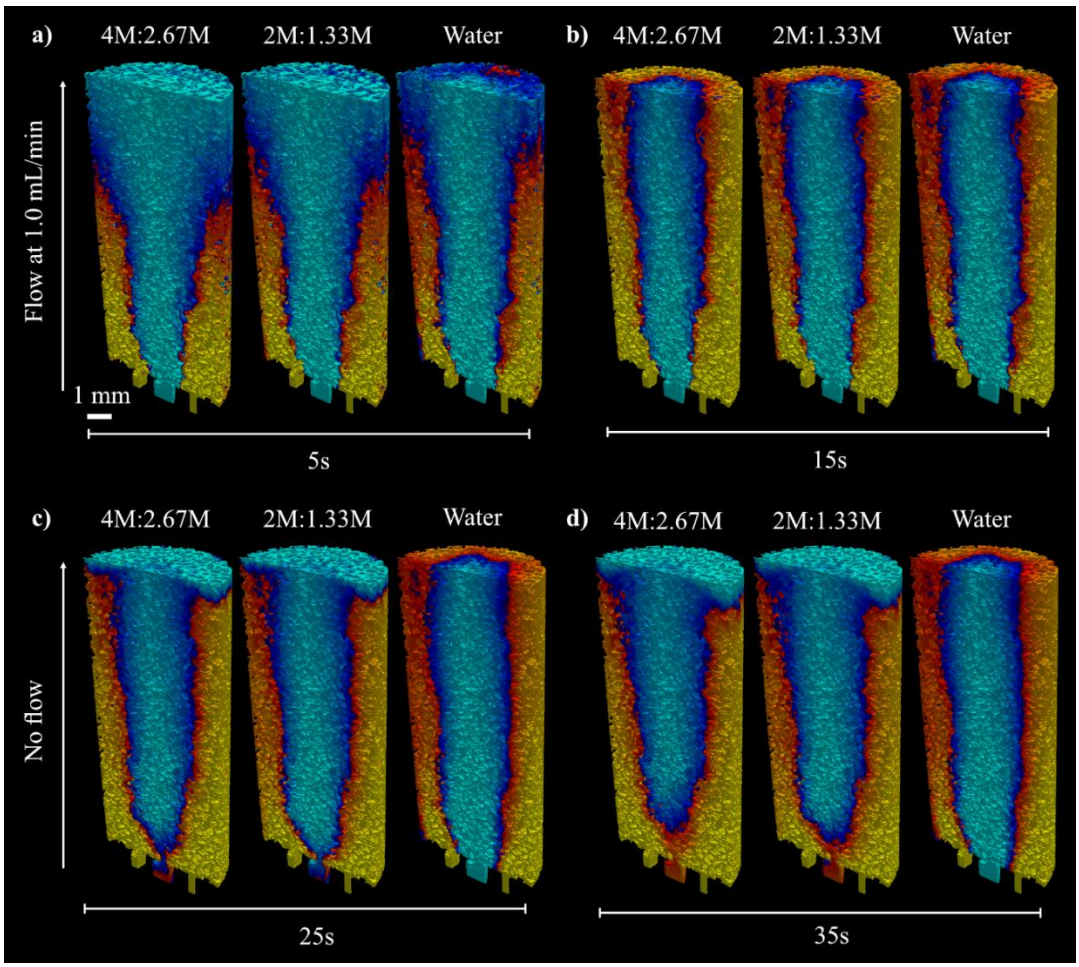

Figure 3.10 Mixing of fluids under different urea:$CaCl_2$ cementing solution concentrations. (**a**) 5s of flow, (**b**) 15s of flow, (**c**) 10s after flow cessation, (**d**) 20s after flow cessation

In the early stages of flow (5s) the breakthrough of CS to the top (outlet) boundary is earlier for water than the more concentrated CS. The injection flow rate is the same in all examples therefore as CS concentration increases, the proportion of the porosity occupied by the CS also does. This is due to the gravitational effect of the denser solution “pooling” towards the inlet boundary during flow and potentially viscous displacement. After 15s the flow is turned off to simulate the no flow period in which crystals formed. From this point we observe density driven flow forcing CS downwards into an inverse cone shape. The resultant enzyme field (light blue) closely resembles the geometry of the observed crystallization (Figures 3.4 – 3.7).

To better quantify these different flow mechanisms, we monitor the standard deviation and mean of the CS field over time to track the evolution of mixing (Figure 3.11).

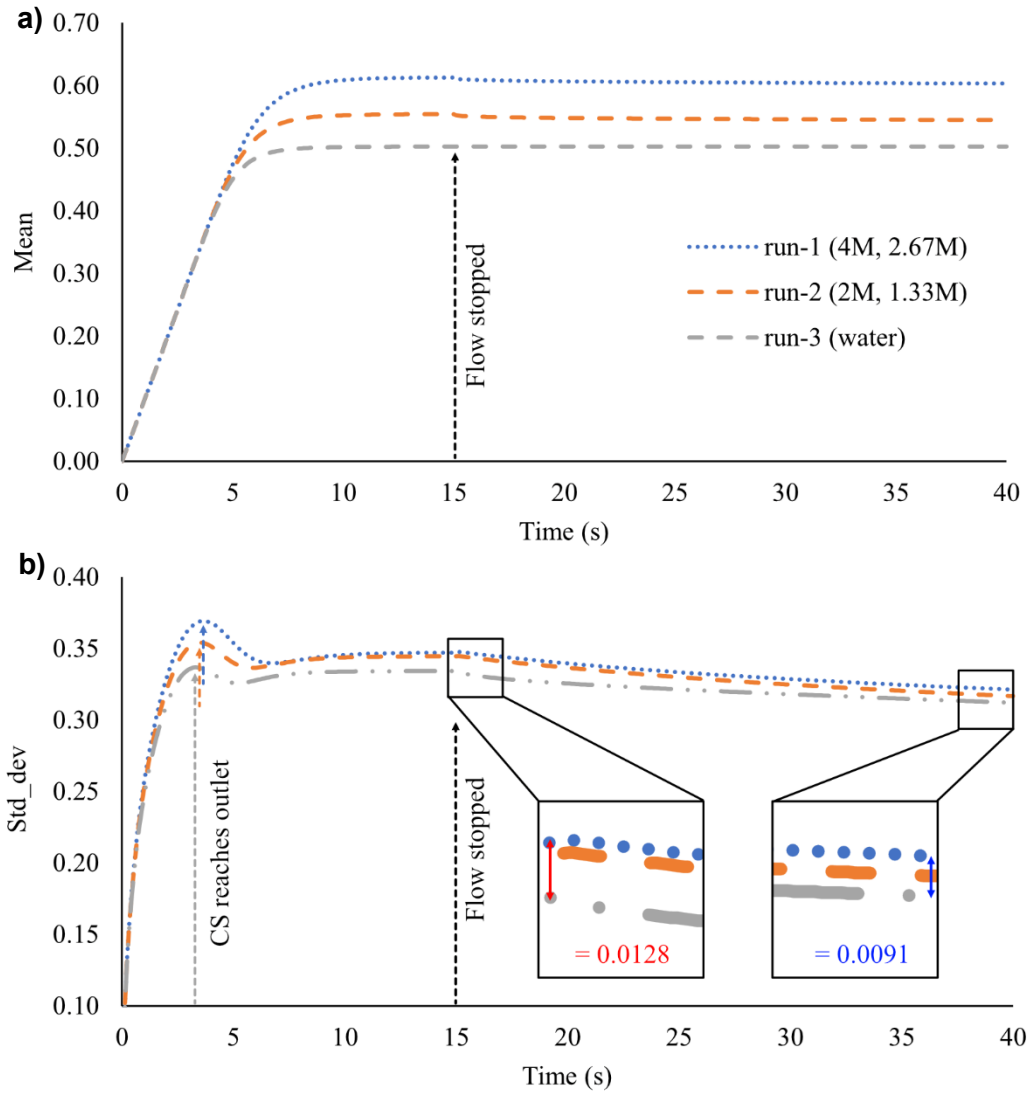

Figure 3.11 Mixing of fluids under different cementing solution concentrations. (**a**) mean CS over time (**b**) standard deviation over time

The standard deviation (std_dev) is a measure of the spread from the average CS value. A lower std_dev represents more elements closer to the mean value, and therefore better mixing. The slight drop in std_dev once CS reaches the outlet boundary (3–5s), is due to CS branching radially inwards towards the centre of the cylinder (Figure 10a–b), which encourages better mixing. After this point (~7.5s), the std_dev and mean values stabilise under all CS conditions. When flow is turned off at 15s there is a relatively larger drop in std_dev for run-1 and run-2 than run-3, suggesting that density driven flow is promoting mixing, particularly towards the bottom of the flow cell (Figure 3.10d). The inset boxes (Figure 3.11b) show that the

difference in std_dev between the 4M:2.67M and water cases reduces from 0.0128 at 15s to 0.0091 at 40s.

In summary, reducing CS concentration is unlikely to change the observed crystallization geometry (Fig. 3.10d, 4M:2.67M to 2M:1.33M), but is more likely to reduce the volume of precipitated material through lack of available CO_3^{2-} and/or Ca^{2+} ions.

3.5 Discussion

3.5.1 Comparison with previous permeability measurements and simulation

Our finding that crystal growth primarily extends out into open pores rather than concentrating at grain contact points suggests that a larger volume of $CaCO_3$ is required with this EICP injection strategy to achieve a similar reduction in permeability as MICP in a similar porous media and at the same $CaCO_3$ vol% (Konstantinou et al., 2023). However, permeability reduction following MICP is often due to biomass formation, which is not a permanent plugging agent (Nemati et al., 2005). Further, the urease enzyme is more likely to penetrate smaller pore throats due to its nanoscale proportions (~9 nm) and is therefore more suited for applications in microfractures and where a greater treatment extent is required, for instance sealing leakage pathways around a CO_2 storage injection well.

We have demonstrated that $CaCO_3$ precipitated after a single EICP cycle is sufficient to divert flow during subsequent cycles, thereby shifting precipitation to less well-treated regions. Consequently, we anticipate that precipitation will become more homogeneously distributed in porous media over repeated cycles.

3.5.2 Implications on future treatment strategies

Through targeted mixing across a salt gradient (e.g. by perforating injection casing at different depths and injecting CS through the upper perforation and ES through the lower one), we may be able to create subsurface barriers to flow using the described methods. Mixing solutions directly within the rock rather than in the wellbore, surface, or injection tubing reduces the risk of wellbore scaling and encourages better penetration of injection solutions into the rock formation. Several single-phase injection strategies, that allow mixing of CS and enzyme/bacteria prior to injection have also been explored (Cheng et al., 2018; Cui et al., 2020; Yang et al., 2022).

However, these approaches may face challenges, such as wellbore scaling, unless water is injected between treatment cycles to mitigate this issue. Our findings indicate that density currents, which form once flow is turned off, significantly influence mixing behaviour and consequently the location of precipitated $CaCO_3$. While the small simulation volume used in this study is largely affected by the boundary walls of the flow cell, our results align with previous studies on MICP in shallow submerged conditions (X. Li et al., 2024), confirming that density driven flow controls the location of $CaCO_3$ precipitation. In a future paper, we will investigate larger-scale mixing behaviour of the proposed EICP treatment strategy for near-wellbore environments using numerical modelling. We will also compare this with single-phase injection methods to assess their potential for achieving more homogeneous and widespread precipitation. Additionally, future work will consider the impact of varying subsurface conditions such as heterogeneity in permeability, temperature gradients, and varying salinity levels, all of which could further influence the effectiveness of these treatment strategies.

3.6 Conclusions

The study investigated the kinetics of enzyme induced $CaCO_3$ formation. High speed XCT imaging allowed quantification of the distribution of $CaCO_3$ precipitates along the diameter and height of the column over time. CFD modelling from the XCT data enabled qualitative and quantitative analysis of fluid mixing and density driven flow at experimental and theoretical urea/$CaCl_2$ concentrations. The main conclusions of the study are:

1) **Porosity Evolution:** More precipitation occurs downstream from the injection point, with limited precipitation in the inlet region due to poor mixing. Precipitates form mainly within the enzyme fluid field rather than in the cementing solution field, showing no obvious relationship with grain contact points. After initial nucleation (within 20 minutes), crystals preferentially grow on existing $CaCO_3$.
2) **Permeability Evolution:** Flow simulations indicate that overall permeability reduction is low (-11%) within the full volume. However, in more highly precipitated regions, a 37% reduction is possible within 65 minutes following a single injection cycle. A mostly linear reduction in permeability is observed, closely following the increase in $CaCO_3$ precipitate volume percentage.

3) **Fluid mixing:** CFD modelling indicates that the observed crystallization geometry is influenced by density driven flow once injection ceases. Lower concentrations of urea/$CaCl_2$ are unlikely to alter this observed geometry but may reduce the volume of precipitated material, thereby affecting permeability reduction.
4) **Multiple treatments:** While only a single EICP treatment cycle was injected here, the spatial evolution in permeability during that cycle suggests that flow during subsequent cycles would take a different route through the porous media. This could act to localise $CaCO_3$ precipitation in different regions during each cycle with the result that treatment becomes more uniform over time.

In addition to this density driven mixing mechanism, other factors will also affect mixing such as heterogeneity in permeability, and environmental conditions are likely to influence treatment effectiveness and these were not explored. Nonetheless, this work highlights the potential of combining high-speed XCT imaging with CFD modelling to improve the understanding and optimization of EICP treatment strategies. These findings have broader implications for environmental and geotechnical applications, including carbon storage, hydraulic control, and ground stabilization. Future studies should scale these methods to larger volumes, directly compare alternative injection strategies, and evaluate the long-term stability of $CaCO_3$ precipitates under variable environmental conditions.

Data Availability Statement:

The data and analysis supporting the findings of this study are available from DOI: 10.5281/zenodo.14246214 https://doi.org/10.5281/zenodo.14246214

Acknowledgment

Simulations were performed on the ARCHIE-WeSt High Performance Computer (www.archie-west.ac.uk) based at the University of Strathclyde. The data analysis was supported by NERC NE/T00908X/1 and EPSRC EP/T023198/1, and data acquisition was supported by the NXCT (EP/T02593X) under their FaPOA scheme.

PS is supported by the Centre for Doctoral Training (CDT) in Geoscience and the Low Carbon Energy Transition, and KJD was supported by NE/M018687/2.

3.7 Implications for permeability control and treatment uniformity

Although these experiments were carried out under simplified, homogeneous conditions, the pore-scale behaviour revealed here has direct implications for the broader aims of the thesis. The time-lapse XCT and CFD analyses show that EICP precipitation does not naturally propagate uniformly through a treated volume; instead, its spatial pattern is governed by how the two injection fluids mix, and by the density contrasts that evolve during and after injection. This finding addresses Critical Challenge 1 by clarifying the mechanisms that initiate and localise $CaCO_3$ formation, but it also exposes the limitations of relying solely on co-injection if uniform treatment or predictable permeability modification is required. The observation that subsequent cycles may redirect flow as pore geometry evolves suggests new opportunities for controlled permeability reduction (Critical Challenge 4) and for steering flow in ways that could eventually enhance sweep efficiency in subsurface applications (Critical Challenge 3).

These insights naturally lead to the next stage of investigation: whether biochemical tuning and alternative injection strategies can reshape these mixing dynamics to achieve more uniform, predictable, or application-specific precipitation patterns.

Chapter 4: Developing physical and biochemical levers for targeted biocementation

Chapter 3 (Salter, Minto, Warnett, et al., 2025) showed that density driven mixing fundamentally shapes the spatial distribution of $CaCO_3$ during EICP, producing precipitation patterns that follow reagent mixing fronts rather than filling the accessible pore space uniformly. These results highlighted an important limitation for practical biocementation: uniform mixing cannot be assumed even in simple, homogeneous granular media, and without intervention, EICP may localise along density gradients or cause premature pore blockage.

Chapter 4 tests how those constraints can be altered by examining two complementary approaches:

- **Biochemical adjustment of the enzyme system** to change reaction onset and mixing behaviour; and
- **Modification of injection regimes** (including single-phase vs. co-injection and pulsating flow).

Together, these strategies address the key question arising from Chapter 3:

How can we transition from precipitation that passively follows mixing fronts to precipitation that is shaped to achieve uniform treatment or application-specific performance?

They also establish the framework required for Chapter 5, which applies these optimised treatment strategies to larger specimens suitable for comprehensive thermal, hydraulic, and mechanical testing.

4.1 Visual comparison of precipitation across enzyme sources

While jack bean urease is often used in laboratory EICP studies for its exceptionally high activity (Salter, Minto, Warnett, et al., 2025), large-scale implementation may depend on lower-cost, more readily available enzyme sources. Soybeans offer a globally abundant alternative (Section 1.2.2.3), albeit with lower urease activity, while also introducing other organic constituents through crude extraction.

Previous studies have shown that adding protein-rich materials, such as milk powder or casein, can enhance the compressive strength of EICP-treated sand (Almajed et al., 2019; Miyake et al., 2022). In MICP, bacterial cells provide natural nucleation points for $CaCO_3$ (Gat et al., 2014); in cell-free systems, proteins may fulfil a similar role. However, proteins may also affect the kinetics and pathways of precipitation, potentially delaying calcite nucleation under certain conditions (Khanjani et al., 2021).

From an engineering perspective, this delay is highly desirable: if enzyme and cementing solutions can be fully mixed before nucleation begins, the spatial distribution of precipitation is governed solely by where the mixed fluid flows, rather than by the mixing dynamics of two separate fluids. This has the potential to overcome the mixing dilemma described in Chapter 3, enabling more uniform treatment and improved performance.

To assess these effects, a series of visual “tube tests” were conducted, with precipitation onset and crystal growth monitored over time. Three urease sources were tested: commercial jack bean meal (JBM), ground jack bean (JBB), and ground soybean (SB). Raw beans were milled, sieved to <212 μm, and extracted with deionised water (10 g/L for JBM and JBB; 100 g/L for SB) for 30 minutes, then rested for 1 hour. Suspensions were centrifuged (6000 rpm, 8 min) and filtered (<1 μm). For SB extracts, 10 g/L calcium sulphate dihydrate was added after the initial mixing to enhance coagulation.

Additional formulations included:

- JBB + NFM: 10 g/L JBB with 8 g/L non-fat milk powder.
- JBB + SB: 10 g/L JBB with 10, 20, or 30 g/L SB (no calcium sulphate) to vary soy organic content.

The CS contained 2.0 M urea and 2.0 M $CaCl_2$ (Kai Xu, Ming Huang, Mingjuan Cui, et al., 2023) mixed 1:1 with the enzyme solution immediately prior to use. Ureolytic activity was measured via conductivity change during urea hydrolysis (Whiffin et al., 2007), and lag period was estimated visually from simple test-tube precipitation trials (Fig. 4.1). Additionally, optical density (OD600) was measured for each enzyme mixture using a UV-Vis spectrophotometer at 600 nm to quantify suspended solids (Table 4.1).

Table 4.1 Summary of EICP enzyme sources and organic additives with corresponding initial solution properties and precipitation lag periods.

Solution	Activity[a]	OD600	Lag period (mins)[b]	Initial pH
SB	3.4	0.313	180–240	6.10
JBM	4.8	0.092	30–60	7.08
JBB	2.8	0.068	15–40	7.12
JBB + NFM	2.6	0.191	30–70	7.06
JBM + NFM	5.0	0.311	30–70	7.14
JBB + SB 10 g/L	3.5	0.398	20–90	6.78
JBB + SB 20 g/L	3.8	1.017	60–105	6.74
JBB + SB 30 g/L	4.0	1.064	60–105	6.76

[a]Activity = mmol of urea hydrolysed per minute

Visual observations from the EICP tube tests show clear differences in the onset of dense $CaCO_3$ precipitation across enzyme sources (Fig. 4.1).

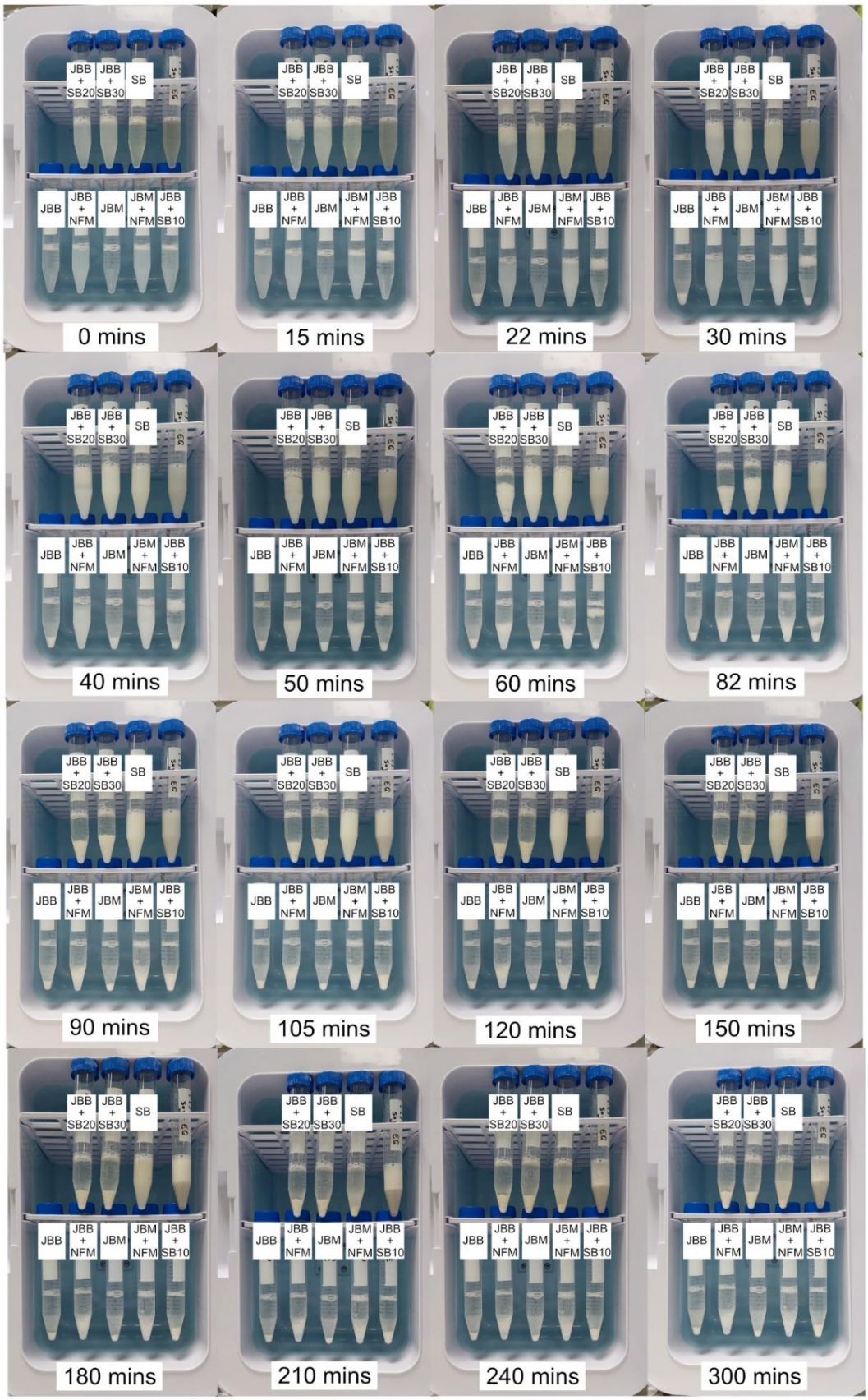

Figure 4.1 Onset of visible $CaCO_3$ precipitation in tube tests for different enzyme sources.

All mixed enzyme-cementing solutions follow a similar progression: they are initially clear, then gradually turn cloudy, and finally form dense $CaCO_3$ crystals that settle at the bottom of the tubes. Lag period (Table 4.1) is defined here as the time between mixing the CS and ES and the first obvious formation of dense $CaCO_3$ at the bottom of the tubes. There are clear differences in precipitation lag periods between enzyme sources (Fig. 4.1). Soybean (SB) solutions exhibited the longest delay in dense $CaCO_3$ formation (180–240 min) despite having one of the highest ureolytic activities (3.4 mmol min^{-1}), indicating that activity alone does not control precipitation onset. Jack bean meal (JBM), with the highest measured activity (4.8), precipitated later than ground jack bean (JBB), which had lower activity (2.8) but the shortest lag (15–40 min). The addition of non-fat milk powder and soybean curds (JBB + SB 10–30 g/L) consistently extended lag periods, in some cases by more than an hour. These observations indicate that the lag period between fluid mixing and visible $CaCO_3$ precipitation is governed primarily by initial pH and buffering capacity, rather than enzyme activity or turbidity (OD600).

4.2 Protein-mediated delays in EICP

While soybean urease-based EICP is increasingly explored as a low-cost bio-cementation strategy (Shu, Yan, Ge, et al., 2022; J. Zhang et al., 2023), the influence of co-extracted proteins and other organic constituents from the crude enzyme preparation remains poorly understood. Such interactions could potentially introduce protein-mediated effects that delay the onset of $CaCO_3$ precipitation (Khanjani et al., 2021).

Monitoring pH during EICP provides a useful proxy for tracking urea hydrolysis and the onset of carbonate precipitation and has been proposed as a control mechanism for managing when and where precipitation occurs (Cheng et al., 2018; Yang et al., 2022). In the present study, pH measurements were used to test whether the delayed precipitation observed in visual experiments (Section 4.1) could be explained solely by the pH evolution of the enzyme solution, or whether additional factors – such as protein-mediated effects in crude soybean urease – contribute to the lag period. Figure 4.2 presents the pH evolution of EICP using soybean urease under conditions relevant to the experiments in this chapter and in Chapter 5.

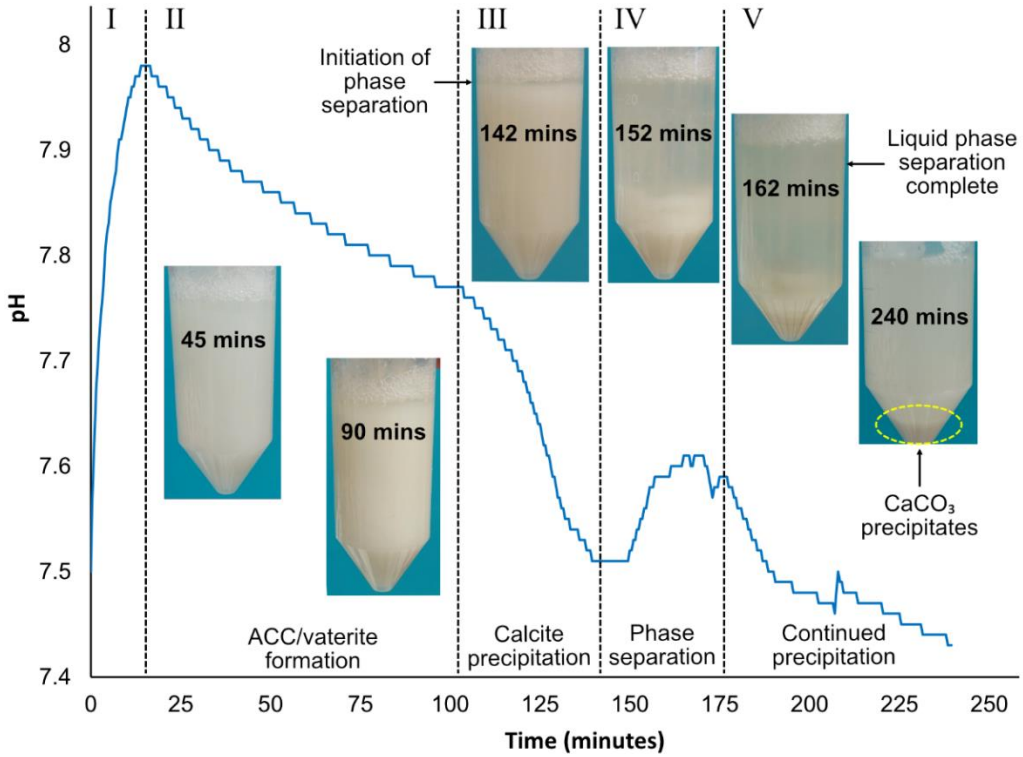

Figure 4.2 pH evolution of a soybean urease solution (100 g/L) mixed 1:1 with equimolar urea and $CaCl_2$ (2M) over a 4-hour periodwith corresponding images showing solution phase changes. Accompanying tube images show changes in suspension appearance. Dashed lines indicate the five main phases described in the text: (I) initial pH rise, (II) gradual pH decline, (III) onset of visible $CaCO_3$ precipitation, (IV) solid-liquid phase separation, and (V) continued precipitation. Time stamps on images correspond to when samples were removed for photography.

The pH trajectory during soybean EICP (Fig. 4.2) illustrates a multi-phase progression consistent with urea hydrolysis and subsequent carbonate precipitation (Van Paassen, 2009). During the initial phase (Phase I: ~0–10 minutes), pH rises rapidly from ~6.5 to above 8.5. This increase reflects the enzymatic breakdown of urea into ammonium (NH_4^+), hydroxide (OH^-), and bicarbonate (HCO_3^-), as expected in ureolytic systems (Equation 1, Section 1.2.1).

In Phase II (~10–140 minutes), a gradual decline in pH is observed. This trend suggests progressive consumption of carbonate species as $CaCO_3$ begins to precipitate from solution. During this phase, the solution becomes increasingly opaque, indicating the formation of suspended solids – likely amorphous calcium carbonate (ACC) or other poorly crystalline intermediates. However, no distinct crystals are visible to the naked eye, and the suspension remains relatively

homogeneous. This suggests that while supersaturation is being approached or indeed exceeded, nucleation of well-ordered $CaCO_3$ polymorphs is delayed. To explore whether metastable phases such as ACC or vaterite contribute to this lag, the evolving crystal morphology was examined using optical microscopy (Fig. 4.3).

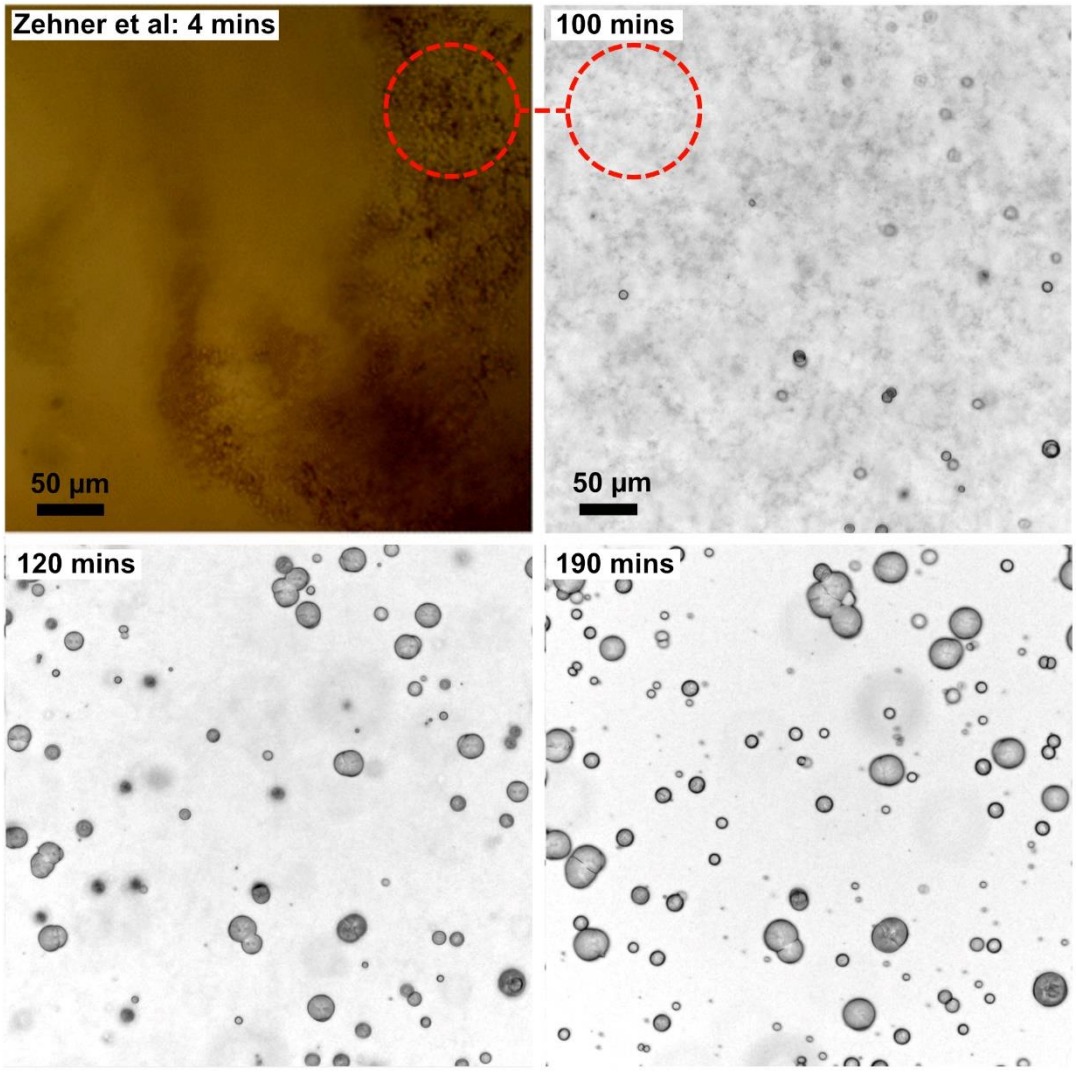

Figure 4.3 Optical microscopy images showing the progression of $CaCO_3$ precipitation in soybean EICP over time compared with a reference image from Zehner et al. (2020) (top left). Zehner et al. (2020) observed a fine-grained ACC/vaterite network within minutes of mixing (red annotation), confirmed via Raman spectroscopy. A similar microstructure is visible at 100 minutes in our system (top right: red annotation), after which spherical $CaCO_3$ particles appear and grow in size from 120 to 190 minutes. Scale bars = 50 µm. A sped-up 42-second video of the full 4-hour progression is available (See Appendix D1).

Zehner et al. (2020) observed a dense network of fine-grained ACC/vaterite during MICP just minutes after mixing, confirmed by Raman spectroscopy. In our soybean EICP system, the red circled particles at 100 minutes (Fig. 4.3) show a highly similar microstructure – a fine, opaque dispersion with no large crystals. This close visual match suggests that the early-stage precipitate in soybean EICP may include metastable ACC/vaterite-like material, although phase identity was not confirmed directly in this study.

From 100 to 120 minutes, small spherical $CaCO_3$ particles begin to appear within this suspension, coinciding with the steeper pH decline (Fig. 4.2). As time progresses to 190 minutes, these spheres grow to ~30 μm in diameter and become more numerous, while the dense fine-grained network progressively disappears. This transformation is consistent with a dissolution-reprecipitation process, in which metastable or poorly crystalline calcium carbonate phases transform toward more stable crystalline $CaCO_3$. This behaviour follows Ostwald's Rule of Stages: phases closer in free energy to the parent solution form first, then transition to the most stable polymorph. The gradual lightening of the bulk liquid between 100 and 190 minutes supports this interpretation, indicating a reduction in suspended metastable particles as larger $CaCO_3$ particles develop.

Phase separation in the bulk solution becomes visible at ~140–160 minutes (Fig. 4.2), overlapping with the main period of calcite growth. This separation is likely caused by the settling of larger, denser $CaCO_3$ particles, which begin to form during this stage. In contrast, the earlier ACC/vaterite-like fine-grained material may be sufficiently fine to remain suspended, giving the appearance of a uniform dispersion. Notably, the $CaCO_3$ particles produced remain predominantly spherical (Fig. 4.3) – a morphology often reported in soybean EICP systems (Liu et al., 2023; Kai. Xu et al., 2023) – which may influence contact area between grains, and therefore both mechanical strength and thermal conductivity in treated materials.

Soybeans are naturally rich in organic matter, containing ~40 wt% protein, ~20 wt% fats, and a range of carbohydrates, minerals, and other phytochemicals (Medic et al., 2014). Even after soaking and extraction, crude soybean urease solutions retain a significant fraction of soluble proteins and other organic molecules. This contrasts with other common urease sources such as purified jack bean urease, nutrient broth, or bacterial cell suspensions, which have markedly lower concentrations of extraneous organic material. Such compositional differences are likely to influence carbonate

precipitation pathways, as proteins and other macromolecules can adsorb to growing mineral surfaces, alter interfacial energies, and stabilise metastable phases.

These observations suggest that proteins and other organic components within the crude soybean urease extract may be stabilising metastable or poorly crystalline carbonate species and delaying the onset of crystalline $CaCO_3$ nucleation, consistent with previous observations that organic macromolecules can modulate polymorph selection and transformation kinetics (Khanjani et al., 2021). By extending the metastable phase, proteins may also modulate the transformation pathway from poorly crystalline carbonate phases toward more stable crystalline $CaCO_3$ and influence final particle morphology. From an engineering perspective, such a delay is advantageous: if precipitation can be postponed until after fluid placement, the resulting carbonate distribution will reflect the flow path of a single, well-mixed solution rather than the mixing dynamics of two separate fluids. This has the potential to improve treatment uniformity, reduce the risk of premature scaling in delivery systems, and enhance material performance – aspects that are explored further in Chapter 5.

It should be noted that while the timing of these transitions (Fig. 4.3) is consistent with the pH evolution (Fig. 4.2), factors such as gas exchange and local temperature variation could introduce minor shifts. In addition, precipitation occurring within porous media, where mineral surfaces provide nucleation sites and surface energy constraints differ, may alter both the timing and pathways of phase transformations compared to bulk-solution conditions. Future work incorporating in situ pH mapping and Raman spectroscopy would provide a more definitive understanding of phase identity and transformation dynamics in soybean EICP.

4.2.1 Effect of initial pH and extraction method on precipitation timing

The low initial pH of the soybean urease solution may also contribute to differences in precipitation timing. Prior to mixing with urea and $CaCl_2$, the urease solution had a pH of 6.1 at 20 °C (see Table 4.1). This contrasts with alternative extraction methods, such as those reported by Weng et al. (2024), where 30 % ethanol in water was used instead of a salt-based coagulant, resulting in a higher soybean urease pH (~6.8). The higher pH may reflect ethanol's more aggressive removal or denaturation of acidic proteins and other buffering species, potentially diminishing the protein-mediated delay mechanisms observed in the previous section.

While the lower initial pH likely contributes to the delayed onset of $CaCO_3$ precipitation, the persistence of the effect even after pH has risen above neutral (Fig. 4.2) suggests that protein interactions remain a dominant factor in crystalline $CaCO_3$ nucleation inhibition. From an application standpoint, altering the extraction method or coagulant chemistry could be used to tune the lag period before crystalline $CaCO_3$ nucleation – shortening it where rapid precipitation is desired, or extending it to maximise the distance and uniformity of fluid penetration within porous media.

4.3 Flow and precipitation behaviour in layered porous media

Alongside biochemical controls, the physical structure of the porous medium exerts a major influence on where and how biocementation develops. Most laboratory studies rely on homogeneous sand packs, yet natural and engineered environments rarely behave so simply. Subsurface formations, engineered backfills, and compacted granular materials typically contain thin fine-grained interbeds, laminations and grain-size contrasts that redirect flow, trap reagents, or block transport entirely. Even millimetre-scale layers can create strong anisotropy in permeability and alter the spatial progression of carbonate precipitation.

Fine layers therefore represent both a limitation (because they can inhibit transport, particularly for microbial systems) and a design opportunity, since engineered contrasts could potentially be used to steer flow or concentrate precipitation in targeted regions. Previous studies have shown that very fine sand layers can restrict the passage of bacterial cells and cause near-inlet clogging in MICP (Wang et al., 2025). Whether enzyme-based EICP, and SB-EICP in particular, can infiltrate such layers more effectively remains poorly understood.

Recognising that homogeneous systems cannot capture these behaviours; this experiment uses a simplified coarse-fine-coarse configuration to test how stratification alters flow and precipitation. The hypothesis is that:

- Single-phase MICP will exhibit transport failure across the fine layer, leading to upstream clogging and limited downstream precipitation; whereas
- SB-EICP, with its nanometre-scale enzymes, will permeate the fine layer and precipitate more uniformly across and beyond it.

This experiment therefore addresses a key practical question: *Can EICP overcome grain-size barriers that routinely impede MICP, and could such layered systems be exploited intentionally for targeted permeability control?*

4.3.1 Sample Assembly

Layered samples were prepared in a coarse-fine-coarse configuration using a polymineralic granitic sand packed into the same 6.6 mm-diameter 3D-printed flow cell used in previous experiments (see Section 5.3.2.3 for full design details). A schematic of the assembly method is shown in Fig. 4.4.

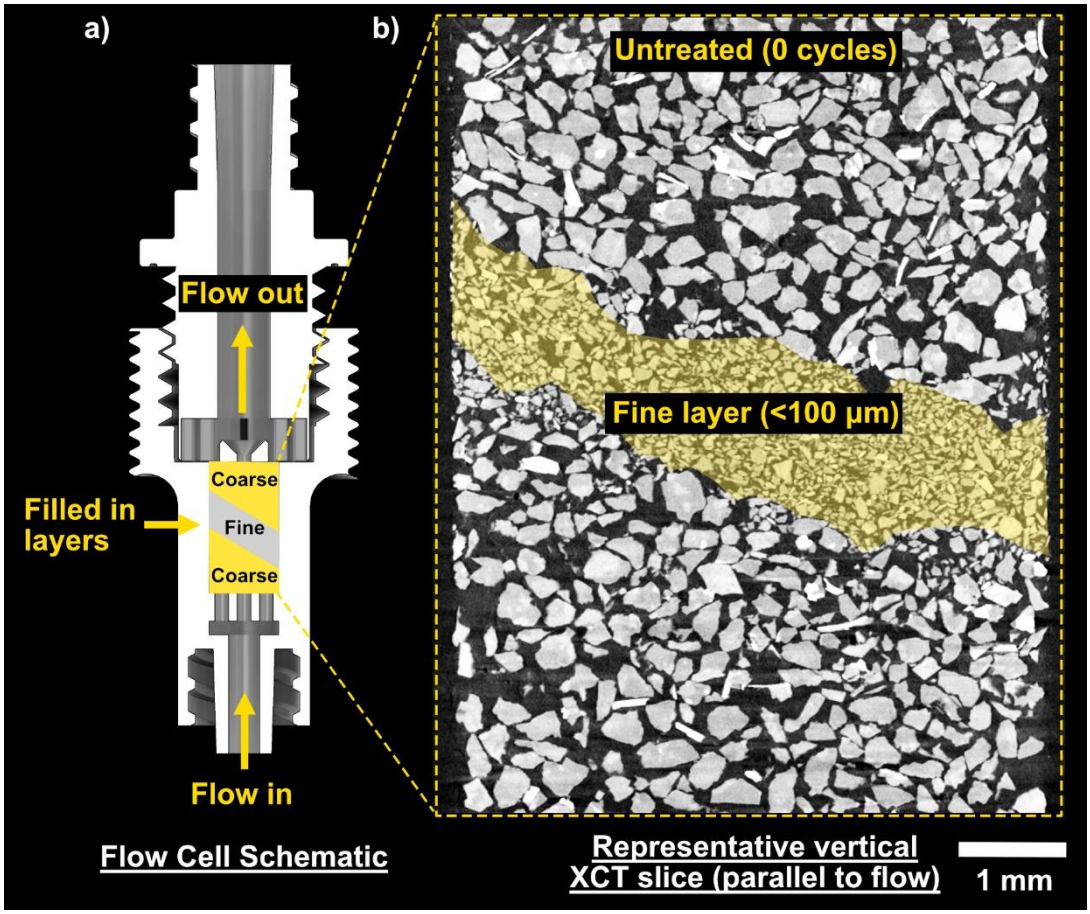

Figure 4.4 Layered sample geometry used for XCT imaging and flow simulations. (**a**) Schematic of the flow cell showing the imposed flow direction and the coarse-fine-coarse packing sequence used to create a layered porous medium. (**b**) Representative vertical XCT slice of the untreated sample (0 cycles), oriented parallel to the flow direction, showing the central fine-grained layer (<100 µm) embedded between coarser granitic sand fractions. Scale bar = 1 mm.

The fine layer (<100 µm particles) was compacted to approximately 2 mm thickness at the sample mid-height. A 3D-printed tamping rod with a 30° angled end was used not to mimic natural “stratification” per se, but to reflect the fact that fine layers in real soils and rocks are rarely perfectly horizontal relative to the imposed flow direction and often contain small irregularities or inclined boundaries.

Coarse layers were packed above and below the fine layer in two equal lifts with light tamping. This approach was identical to the preparation of homogeneous samples (Section 3.3), ensuring that the only intentional difference between the two sample types was the presence of the fine layer. Minor variations in packing density between layers are unavoidable and are representative of natural systems, but the use of the same compaction method minimised additional flow artefacts.

All samples were vacuum-saturated with water prior to treatment to remove trapped air and ensure consistent baseline permeability.

4.3.2 Reagent preparation & treatment protocol

MICP and EICP treatments were prepared to maintain the same overall reagent molarity so that precipitation behaviour reflected transport differences rather than chemical strength.

4.3.2.1 Soybean EICP (SB-EICP)

Soybean urease extract was prepared as described in Section 4.2 and used immediately after clarification. The cementing solution consisted of 2.0 M urea and 2.0 M $CaCl_2$ dissolved in <12 Ω deionised water.

4.3.2.2 Single-phase MICP

A single-phase MICP formulation was selected to minimise premature clogging and to improve the homogeneity of $CaCO_3$ distribution; limitations identified in Chapter 3. *Sporosarcina pasteurii* (DSMZ No. 33) was cultured for ~24 h (see Section 5.3.1 for full details), then centrifuged and resuspended in tap water to achieve OD_{600} = 1.0. The pH was adjusted to 4.8–4.9 using glacial acetic acid following Yang et al. (2022), providing a short lag period before carbonate nucleation. Immediately prior to injection, the cell suspension was combined with the cementing solution to produce the same urea and $CaCl_2$ molarities as the SB-EICP system.

This non-standard single-phase MICP protocol was used deliberately: the low-pH lag extends the transport window and helps the mixture penetrate past the inlet before reaction initiates, addressing one of the main limitations exposed in Chapter 3.

For both MICP and SB-EICP, the mixed reagent was injected into the flow cell immediately after preparation at 1 mL min^{-1}, delivering a total of 5 mL per cycle. Treatments were applied over seven cycles. The MICP sample became blocked at this point and could not be treated further, whereas the SB-EICP sample remained permeable and was subsequently treated for additional cycles. However, to ensure strict comparability, only the first seven cycles were used in side-by-side analyses.

4.3.3 XCT Imaging and Analysis

XCT imaging was conducted on a Nikon XT H 225 system (University of Strathclyde) to visualise carbonate precipitation in layered samples across multiple treatment cycles. Scans were acquired at 60 kV, 5.9 W, 98.3 µA, with 3141 projections at 4 s exposure, yielding a voxel size of 6.0 µm. These settings maximised mineral-pore contrast while maintaining ~30% X-ray transmission through the sample centre. Imaging was carried out after 0, 1, 2, 3, 6, and 7 treatment cycles, with samples left for ≥6 h prior to scanning to ensure that most precipitation had completed (see Fig. 4.1).

Pre- and post-treatment volumes were registered to the initial scan, enabling direct voxel-wise comparison of structural evolution. Datasets were denoised using a non-local means filter, and $CaCO_3$ was segmented using the Otsu-based auto-thresholding protocol (Chapter 3). This workflow produced fully 3D time-series volumes showing the progressive development of precipitation within, across, and beyond the fine-grained layer. No grain rearrangement was detected during treatment, indicating that changes in greyscale reflect true mineral growth rather than sample disturbance.

For flow analysis, a long subvolume (275 × 275 × 1100 voxels) was extracted from each timepoint. This geometry was chosen so that a single domain spanned the inlet region, the entire fine layer, and the outlet region, while remaining small enough for repeated permeability simulations. Absolute-permeability simulations were then run on the segmented pore space within this subvolume in Avizo, and the resulting velocity-magnitude field was calculated for both the untreated and treated states. The full processing workflow used for the layered samples is shown in Fig. 4.5.

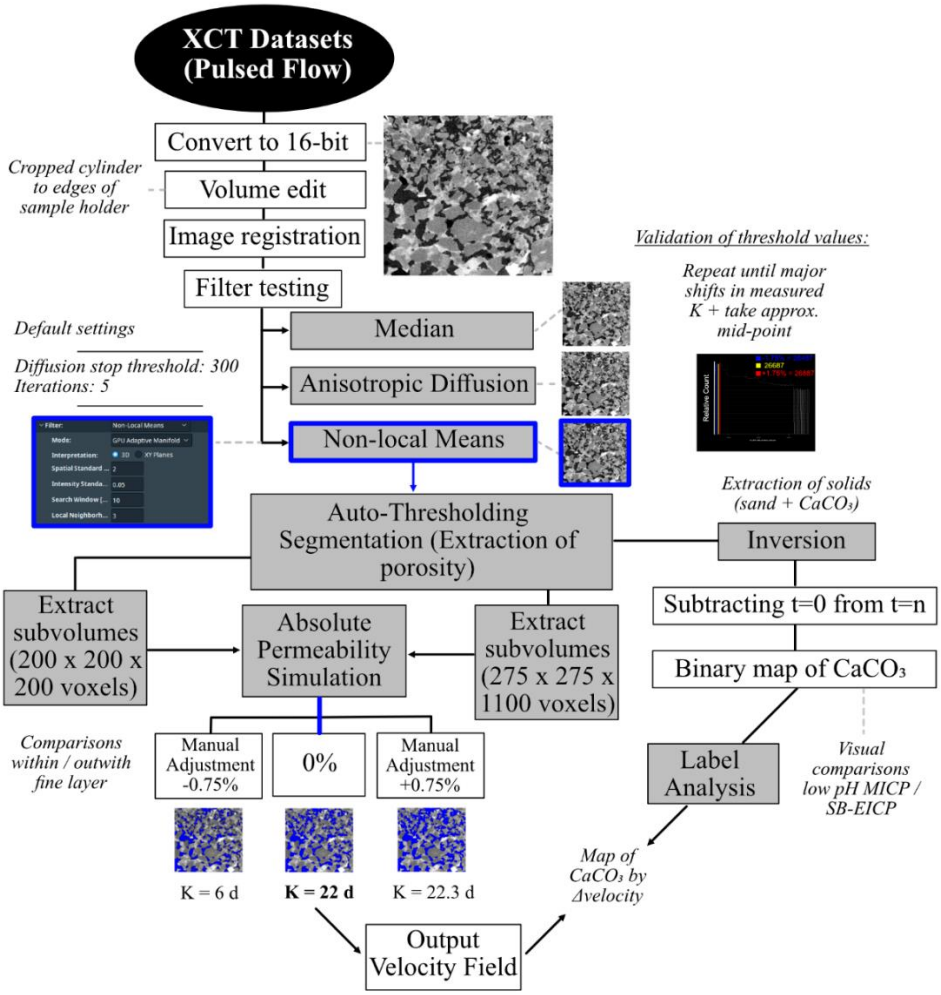

Figure 4.5 XCT processing, segmentation, and simulation workflow used to quantify precipitation patterns and flow alteration in layered biocementation experiments. Raw XCT datasets were converted to 16-bit, cropped, spatially registered, and subjected to comparative filter testing; non-local means filtering was selected to maximise noise suppression while preserving grain boundaries. Auto-threshold segmentation produced porosity volumes for absolute-permeability simulation and inversion of solids (sand + $CaCO_3$). $CaCO_3$ was isolated by subtracting the untreated scan (t = 0) from subsequent time points. Two classes of subvolumes were extracted: (i) cubic subvolumes (200 × 200 × 200 voxels) to compare permeability within and outside the fine layer, and (ii) long subvolumes (275 × 275 × 1100 voxels) spanning the full sample height for Δ-velocity analysis. Output velocity fields were combined with $CaCO_3$ label maps to identify where precipitation most strongly altered pore-scale flow pathways, forming the basis for the comparisons between SB-EICP and single-phase MICP.

The difference in velocity magnitude between the treated and untreated simulations was computed voxel-wise to generate the Δ-velocity field which were then used to

create velocity-change maps. Under the applied fixed-pressure boundary conditions, these maps reveal where flow was locally slowed or accelerated by precipitation across the layered structure.

To link these hydrodynamic changes directly to the precipitated phase, the Δ-velocity field was used as the greyscale input to the Label Analysis and Label-to-Attribute modules (see Chapter 3). By masking the Δ-velocity field with the segmented $CaCO_3$, a mean local change in velocity was calculated for each individual calcite label, yielding $CaCO_3$-label maps. This step quantifies which crystal clusters are most strongly associated with local flow reduction or rerouting, rather than simply visualising where calcite is present.

Average $CaCO_3$ distributions were obtained by projecting the segmented calcite volume along the flow direction using the Z-project function in ImageJ (Willems et al., 2021). By combining information from all slices, this representation emphasises where precipitation preferentially accumulates relative to the fine layer, rather than focusing on individual pore-scale features (Fig. 4.6).

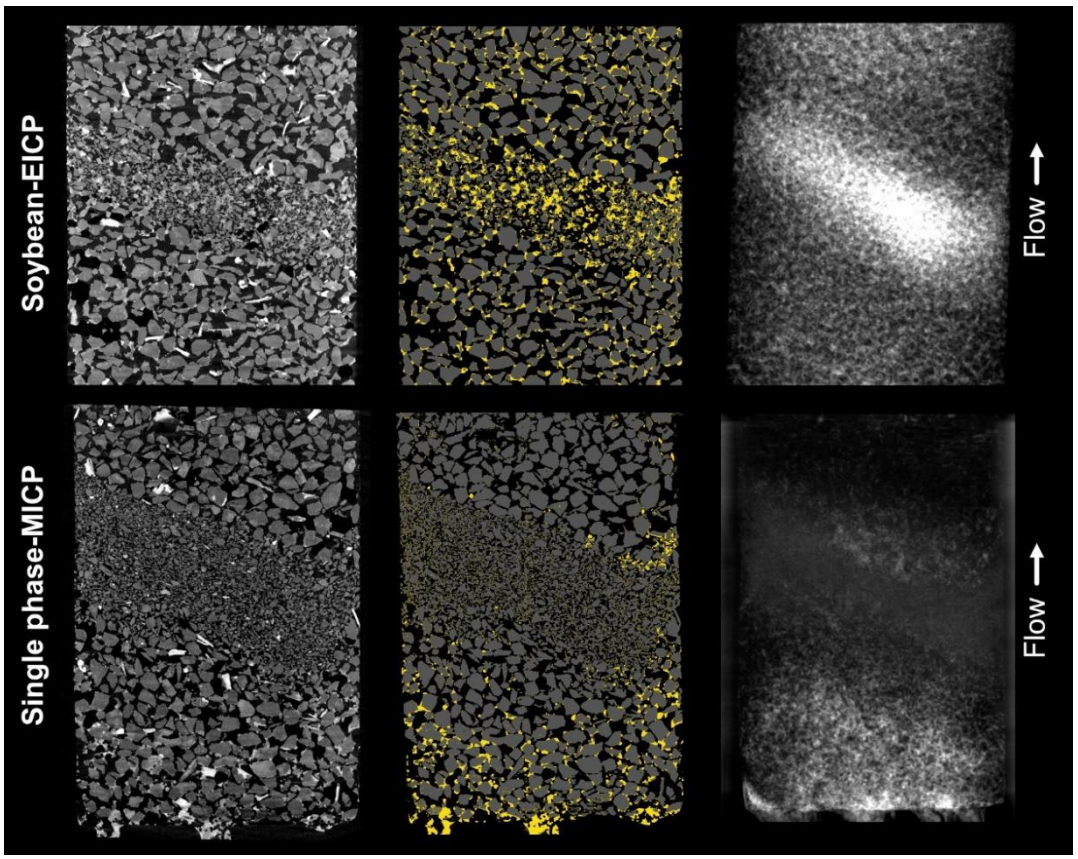

Figure 4.6 Comparison of SB-EICP and single-phase MICP in a layered coarse-fine-coarse sand column after seven treatment cycles. Top row (SB-EICP): XCT cross-section through the layered sample (left), segmented $CaCO_3$ shown in yellow (middle), and projection of $CaCO_3$ along the flow direction (right). Precipitation occurs within the fine layer and extends both upstream and downstream into the coarse regions, indicating effective transport across the permeability contrast. Bottom row (single-phase MICP): Corresponding XCT cross-section, segmented $CaCO_3$, and projected calcite distribution. Precipitation is strongly localised near the inlet, with limited penetration into or beyond the fine layer, consistent with early pore blockage and restricted downstream transport. Flow direction is indicated on the right.

In the SB-EICP sample, $CaCO_3$ precipitation is distributed across the fine layer and extends into both upstream and downstream coarse regions, indicating that the reactive fluid continues to access new pore space over repeated treatment cycles. This spatial pattern suggests that partial throat occlusion progressively redirects subsequent injections through adjacent pathways, enabling precipitation to develop across the full layered system over multiple cycles.

The higher concentration of $CaCO_3$ observed within the fine layer under SB-EICP is consistent with mechanisms identified in Section 4.1, including increased available

surface area and gravity-influenced redistribution of early amorphous or weakly crystalline phases. Importantly, the presence of continued precipitation beyond the fine layer argues against reagent starvation within smaller pores and indicates that enzyme transport and activity are maintained throughout the structure.

By contrast, the single-phase MICP treatment exhibits a significantly different distribution. While some precipitation occurs within the downstream coarse region, the majority of $CaCO_3$ accumulates within the inlet region, with substantially reduced mineralisation across the fine layer itself. This pattern indicates that bacterial transport is limited by a combination of filtration, attachment, and early constriction of the pore network as carbonate forms, rather than complete blockage at the fine-layer boundary. The minor precipitation observed downstream suggests that a small fraction of cells can traverse the layered interface, but not in sufficient numbers to sustain uniform cementation.

Once this inlet-dominated precipitation develops, subsequent injections are likely to be diverted around the treated region or prevented altogether, reducing the effectiveness of repeated treatments in stratified media. Beyond these physical transport limitations, the single-phase MICP formulation also introduced operational challenges. The buffering capacity of the single-phase MICP solution was found to vary strongly with cell density (OD600), the residual pH of the nutrient broth after bacterial growth, and the ureolytic activity of the cells. These factors meant that a different volume of acetic acid was required for each cycle, making the pH correction difficult to reproduce consistently and limiting the controllability of precipitation.

A multiphase MICP strategy, in which bacterial and cementing solutions are injected sequentially, could potentially improve penetration into finer pores by allowing cell migration prior to reaction. However, even in such systems, transport across sharp permeability contrasts remains sensitive to cell size (~3–4 μm), motility, attachment behaviour, and local pore geometry. In the present study, a single-phase formulation was deliberately chosen to maximise transport during injection and to provide a conservative, like-for-like comparison with SB-EICP under identical molar conditions.

Given the ability of SB-EICP to precipitate within fine layers, unlike single-phase MICP, the following analysis focuses on absolute permeability simulations for the SB-EICP-treated sample to examine how precipitation within and around the fine layer alters flow pathways and bulk hydraulic response (Fig. 4.7).

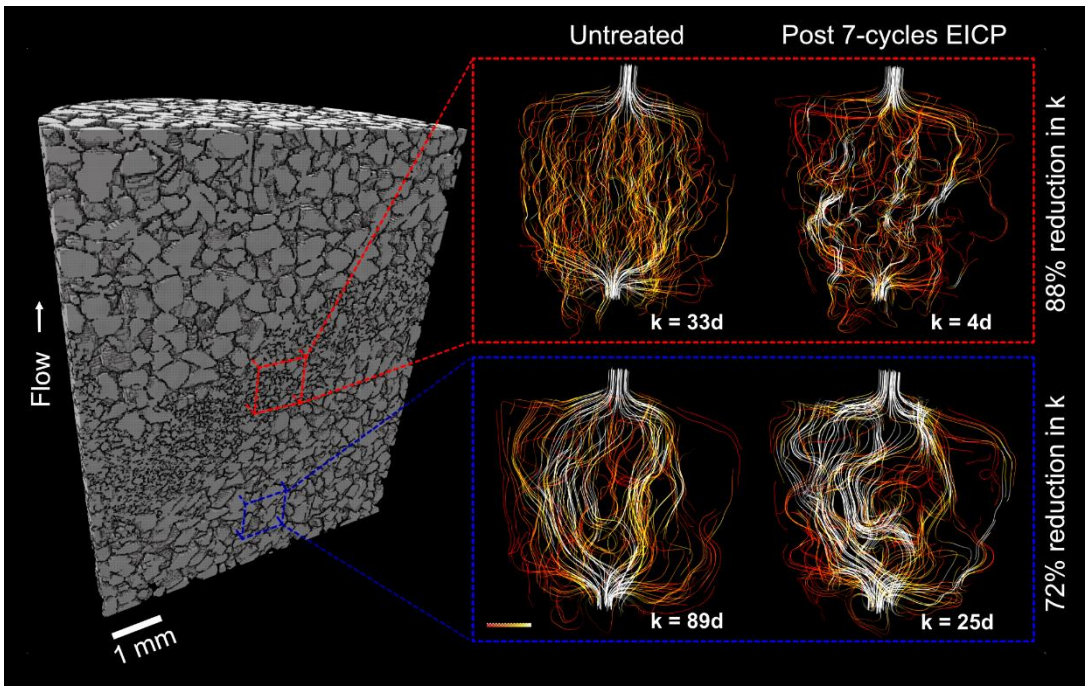

Figure 4.7 Localised flow alterations in layered sand columns treated with SB-EICP. Left: 3D rendering of the untreated sample showing the coarse-fine-coarse configuration. **Right**: cubic subvolumes (1.2 mm per side) extracted from (top row) the fine-grained layer and (bottom row) the coarse-grained layer beneath it, shown in the untreated state and after seven treatment cycles. Streamlines represent simulated pore-scale flow under fixed-pressure boundary conditions, coloured by velocity magnitude (white = high, red = low). Permeability (k) is given in darcys, with percentage reductions shown relative to the untreated state.

Cubic subvolumes (200 × 200 × 200 voxels), selected based on the sensitivity analysis (Section 2.6), were extracted from the fine layer and adjacent coarse-grained zones. The simulated permeability reduction in the fine-grained subvolume (88%) was substantially greater than in the adjacent coarse-grained subvolume (72%), despite the fine layer starting from a much lower baseline permeability (33 d compared with 89 d). All simulations were performed under identical boundary conditions, indicating that the contrast arises from differences in pore structure rather than modelling artefacts. This behaviour reflects the greater sensitivity of fine-grained media to carbonate precipitation, where modest volumes of $CaCO_3$ are sufficient to occlude smaller pore throats and disrupt connected flow pathways.

Streamline visualisations show that, within the coarse-grained subvolume, precipitation modifies local velocities, but dominant flow channels remain largely intact. In contrast, within the fine-grained subvolume, precipitation produces a more fragmented flow field, with pathways repeatedly diverted or rerouted around partially

occluded throats. This behaviour reflects the layered pore architecture, in which flow is governed by the least-permeable elements of the system.

This response depends on factors such as the thickness of the fine layer, the contrast in grain size between layers, and whether transitions are abrupt or gradational. Exploring these dependencies systematically would require a broader set of geometries and volumes than considered here. The present experiments instead demonstrate that even a single fine-grained horizon is sufficient to exert strong hydraulic control once precipitation initiates, highlighting the sensitivity of layered systems to biocementation.

This behaviour is explored further by simulating absolute permeability across extended subvolumes spanning the full coarse-fine-coarse sequence and mapping local changes in flow velocity induced by $CaCO_3$ precipitation (Fig. 4.8).

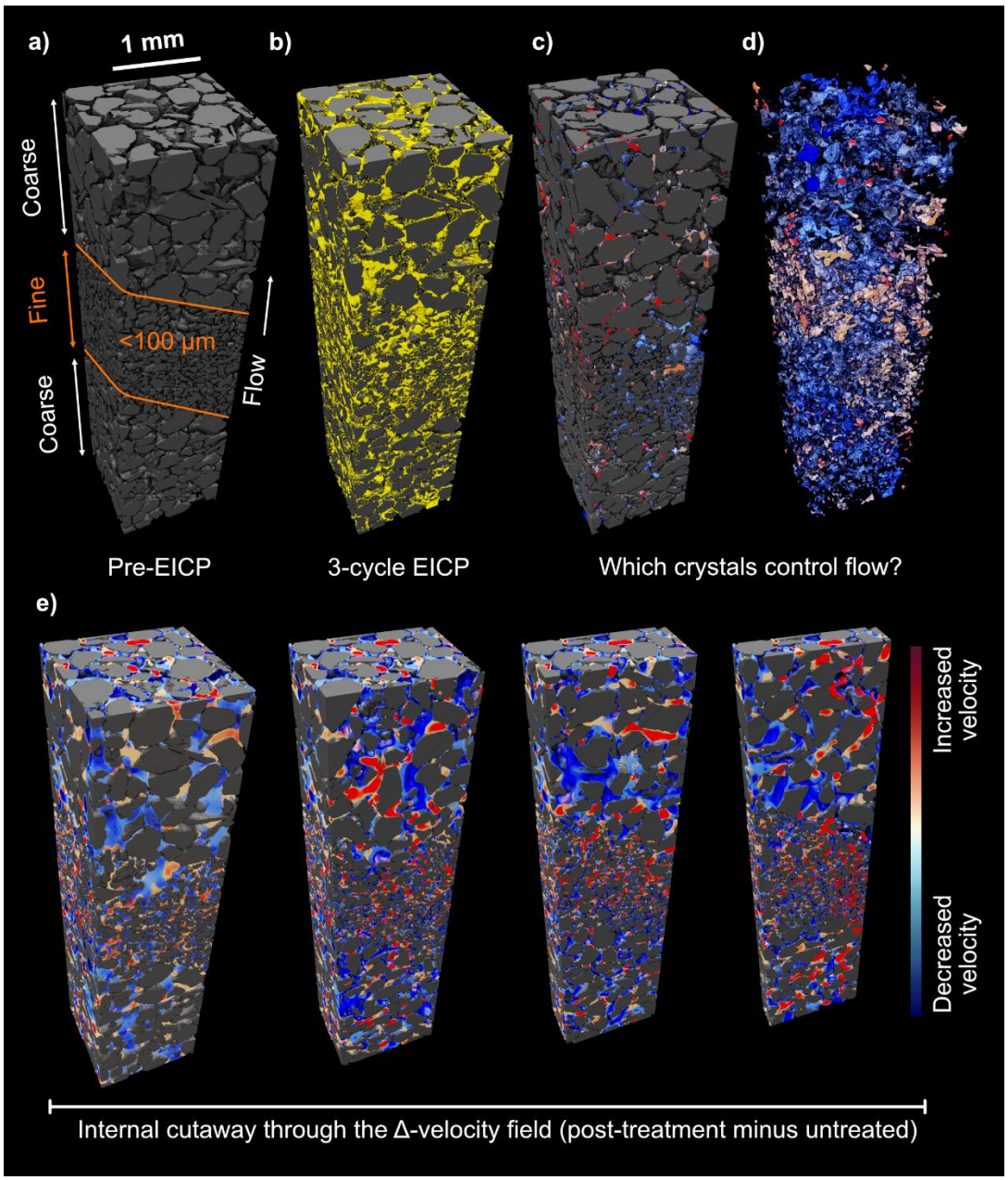

Figure 4.8 Biocementation in a coarse-fine-coarse layered sand using soybean EICP (SB-EICP). (**a**) Untreated polymineralic granitic sand showing a central fine-grained layer (<100 µm) between coarser fractions. (**b**) Same sample after three SB-EICP treatment cycles, with segmented $CaCO_3$ shown in yellow. (**c**) $CaCO_3$ labels coloured by the mean local change in flow velocity (Δ-velocity) in the surrounding pore space, highlighting crystals associated with local flow reduction (blue) or acceleration (red). (**d**) $CaCO_3$-only rendering of (c), with the granular matrix removed to isolate precipitated crystals and their associated Δ-velocity response. (**e**) Internal cutaways through the Δ-velocity field (post-treatment minus untreated) from absolute-permeability simulations. Four vertical cutting planes through the same dataset are shown to expose internal features; blue indicates decreased velocity and red increased velocity. Localised velocity increases within the fine layer reflect flow rerouting around partially occluded pore throats.

Simulated permeability across the layered SB-EICP subvolume decreased by ~50%, from 73 d in the untreated state to 36 d after just three treatment cycles. Localised regions of increased flow velocity (red) are most evident where flow is rerouted around partially occluded pore throats, particularly within and immediately adjacent to the fine layer (Fig. 4.8c–e). Under the fixed-pressure boundary conditions applied here, the permeability reduction lowers the total volumetric flow rate. At the same time, flow becomes redistributed into fewer connected pathways, producing localised velocity increases within those channels despite an overall reduction in flow. In contrast, large open pores within the coarse layer remain comparatively unaffected by precipitation and are associated with reduced velocities (blue).

$CaCO_3$ labels (Fig. 4.8c–d) are coloured by the mean Δ-velocity in adjacent local pore space, showing where precipitation coincides with local flow slowing or acceleration. However, these results should not be interpreted as the effect of individual crystals acting in isolation. Instead, they reflect the collective interaction between precipitation, local pore geometry, and the evolving connectivity of the surrounding pore network. Flow control in SB-EICP systems therefore emerges from distributed pore-scale restructuring rather than singular blocking events.

It is important to note that the simulations presented here impose impermeable side boundaries, forcing flow to traverse the layered structure. In natural stratified soils or rocks, lateral flow diversion would be expected wherever adjacent higher-permeability pathways exist. As a result, reactive fluids are unlikely to enter fine-grained layers until the permeability of surrounding coarse material has been sufficiently reduced. Under such conditions, fine layers initially act as hydraulic barriers irrespective of treatment strategy.

The distinction between SB-EICP and single-phase MICP becomes critical once flow is redirected toward these lower-permeability pathways. While fine layers may remain largely inaccessible to bacterial transport due to pore-throat size constraints, enzyme-based systems retain the ability to penetrate and precipitate within them once sufficient pressure gradients develop. In remedial scenarios, such as mitigating CO_2 leakage along preferential pathways, SB-EICP offers a means of sealing narrow conduits that may be inaccessible to bacteria but remain permeable to CO_2. Conversely, when biocementation is applied prior to CO_2 injection to enhance sweep efficiency in unconsolidated sediments, the preferential reduction of permeability

within fine layers may suppress early vertical plume migration, promoting lateral spreading and more effective utilisation of available pore space.

These results show why layered and heterogeneous media are likely to exhibit larger hydraulic responses than homogeneous sands under the same treatment strategy. In such systems, once reactive fluids access fine-grained horizons, SB-EICP can concentrate its hydraulic impact within these layers, where relatively small structural changes exert strong control over bulk flow. While extension to larger volumes, more complex stratigraphy, and fully coupled reaction-transport models would be required to translate these findings directly to field-scale systems, the pore-scale mechanisms identified here provide a clear basis for refining injection strategies.

Beyond demonstrating that SB-EICP can overcome grain-size barriers that routinely impede MICP, these results indicate that layered systems may be deliberately exploited to achieve targeted permeability control. In engineered settings, fine-grained interlayers could be intentionally introduced within granular backfill to localise cementation, enabling structural stabilisation while preserving drainage or directing flow toward designated channels, or collection zones. In natural stratified soils and rocks, existing fine layers may similarly be used as functional targets rather than obstacles, concentrating mineralisation where hydraulic control is most effective once access is achieved. In both cases, the ability of enzyme-based systems to precipitate within pore spaces inaccessible to bacteria provides a mechanism for selectively modifying flow without uniformly cementing the surrounding medium.

Despite the advantages of single-phase SB-EICP, practical deployment raises concerns around premature reaction and blockage within injection infrastructure if reagents are mixed upstream of the porous medium. This motivates exploration of alternative delivery strategies that promote mixing within the pore space itself, while avoiding both injection-line clogging and the density driven transport limitations identified in Chapter 3. Pulsed injection offers one such approach.

4.4 Enhancing mixing with pulsed flow

Flow pulsation has been proposed as a method to enhance fluid mixing in porous media across various subsurface engineering applications (Claria et al., 2012; Ni & Meckel, 2021). In groundwater remediation, pulsed flow could improve the distribution of treatment agents, increasing contaminant removal efficiency. Similarly, in subsurface fluid injection systems, controlled pulsation may aid in managing fines

mobilization (Kozhevnikov et al., 2023), mitigating salt precipitation (Khosravi et al., 2024), and optimizing pressure distribution during water injection for reservoir pressure management (Civan, 2023).

The distinct concentration fronts observed between enzyme and cementing solutions under steady, monotonic injection (Fig. 3.9) highlight a key transport limitation: under laminar flow, mixing is governed primarily by slow diffusion rather than convective exchange. As a result, reagent overlap can remain spatially restricted, limiting the volume over which carbonate precipitation can occur by preventing both reactive fluids from accessing the same pore space. In layered or otherwise heterogeneous media (Section 4.3), this effect is likely to be intensified, as permeability contrasts redirect flow and further inhibit mixing, although the degree of segregation depends on injection configuration and the contribution of density driven transport (Section 3.4.3.1).

Controlled flow pulsation offers a potential means of alleviating these constraints by periodically perturbing local velocity fields and concentration gradients. Transient variations in injection pressure and flow rate can induce inertial effects, promote vortex formation in stagnant regions, and temporarily alter dominant flow pathways, thereby increasing interfacial contact between reacting fluids. Enhanced mixing would be expected to increase the effective reaction volume and promote more spatially uniform carbonate precipitation. To assess whether such behaviour could arise under realistic pulsing conditions, a series of computational simulations was performed to examine mixing under controlled flow pulsation.

4.4.1 Simulation setup and modelling assumptions

CFD simulations (Section 3.4.3) employed tetrahedral meshes with a characteristic edge length of ~27 μm, a resolution constrained by computational limits. This mesh density was sufficient to reproduce inlet-scale flow behaviour and dominant flow paths within the experimental flow cell. Mesh adequacy is supported by the mesh-independence analysis reported in Section 3.3.3, where comparison between the original (13.8 μm) and down-sampled (27.5 μm) meshes showed that, although absolute permeability differed by ~18%, flow path geometry and velocity-field structure were not significantly affected (Appendix Fig. B2).

To examine finer pore-scale effects, a smaller subvolume (150 × 150 × 150 voxels; ~1.2 mm side length) was extracted from the inlet region of the same XCT dataset

used in Section 3.3.1 (https://doi.org/10.5281/zenodo.14246214) and simulated at higher effective resolution. This approach allowed closer inspection of low-velocity regions and dead-end pores, enabling assessment of whether flow pulsation could enhance mixing in zones that remain weakly connected or stagnant under steady injection.

The segmented pore space from the extracted inlet subvolume was converted into an OpenFOAM-compatible mesh using an ImageJ macro in Fiji (Schindelin et al., 2012; Willems et al., 2021), following the workflow described in Section 2.5 and Section 3.3.1. This approach preserves pore connectivity while enabling direct pore-scale flow simulations from XCT data.

Mixing was simulated using the *twoLiquidMixingFoam* solver in OpenFOAM, which models transient mixing of two incompressible, miscible fluids with different densities and viscosities under laminar flow conditions. Although flow pulsation introduces transient acceleration and weak inertial effects, Reynolds numbers in the pore geometries considered remain low ($Re \ll 1$), such that flow remains laminar and mixing is governed by diffusion and density driven convection rather than turbulence.

The model treats the system as two generic fluids, parameterised to represent the enzyme solution (ES) and cementing solution (CS). The CS was assigned a higher density and viscosity corresponding to 4.0 M urea and 2.67 M $CaCl_2$, while the ES was approximated as water (For full fluid properties see Appendix Table B1).

4.4.2 Pulsed injection configurations

Four pulsing strategies were tested to evaluate their effect on mixing efficiency and, by extension, their potential to influence the spatial distribution and effective volume of $CaCO_3$ precipitation (Fig. 4.9). The configurations were: (a) steady-state flow, where both ES and CS were injected continuously; (b) synchronous pulsation, where both fluids were pulsed in phase with identical timing; (c) alternating-phase pulsation, where ES and CS were pulsed out of phase such that one fluid was injected while the other was paused; and (d) hybrid pulsation, where CS was pulsed while ES was injected continuously. The pulse frequency, duration, peak velocity, and ramp characteristics defining each configuration are summarised in Table B2. These configurations were designed to isolate the influence of pulsing symmetry, timing, and flow regularity on mixing behaviour in dual-fluid EICP systems.

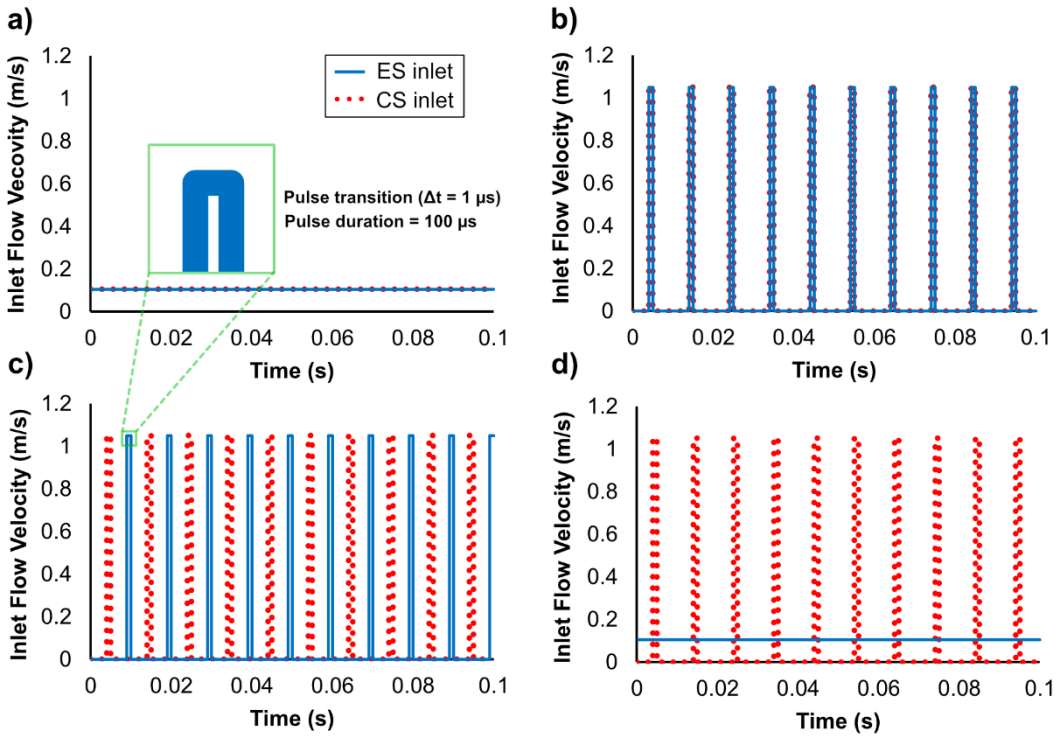

Figure 4.9 Inlet flow velocity profiles for different injection strategies used in the pulsed flow mixing simulations. The inlet velocity of the cementing solution (CS; red dotted line) and enzyme solution (ES; solid blue line) is shown as a function of time for four injection conditions: (**a**) steady-state injection, where both fluids are injected continuously; (**b**) synchronous pulsation (100 Hz), where CS and ES are pulsed with identical frequency, duration, and phase; (**c**) alternating-phase pulsation (100 Hz), where CS and ES are pulsed with identical frequency and pulse duration but out of phase, such that injection alternates between fluids; and (**d**) hybrid pulsation (100 Hz), where CS is pulsed while ES is injected at a constant flow rate. In all cases, the total injected fluid volume is matched to ensure direct comparability between injection strategies. Insets highlight representative pulse transitions, illustrating both the finite pulse duration and the non-instantaneous ramping of inlet velocity at pulse onset and termination. Velocity transitions are implemented using a short linear ramp ($\Delta t = 1 \times 10^{-6}$ s) to avoid numerical discontinuities, resulting in a gradual reduction in acceleration as the maximum and minimum velocities are approached.

Although the simulations focus on co-injection of two miscible fluids, the transport mechanisms explored are also relevant to MICP delivery strategies. Pulsed injection may reduce stagnation in weakly connected pore regions and improve reagent access to larger pore networks under sequential MICP injection schemes, where bacterial and cementing solutions are introduced separately. The present analysis is nevertheless restricted to dual fluid mixing to provide a controlled and tractable framework.

The pulsation frequency was fixed at 100 Hz for all cases to enable direct comparison between pulsing regimes rather than exploring frequency effects. While changing frequency would alter the strength and spatial extent of transient flow perturbations, similar qualitative trends are expected across regimes. A frequency of 100 Hz was selected as a representative upper-bound case that maximises transient effects while remaining conceptually feasible for downhole or shutter-based injection systems.

For field or larger-scale applications, the appropriate pulsing frequency would need to be scaled to the characteristic pore length, advective residence time, and hydraulic response time of the treated system, rather than adopted directly from the pore-scale simulation.

All model parameters, solver settings, and flow boundary conditions are provided in Appendix Table B2, with supplementary material detailing the implementation of the different pulsed inlet conditions.

4.4.3 Mixing behaviour under pulsed flow

The resulting concentration fields reveal clear differences in reactant distribution and local mixing behaviour between steady and pulsed injection regimes (Fig. 4.10). Under steady flow (Fig. 4.10b), the interface between the CS and ES remains sharp over the duration simulated, with CS concentrations predominantly close to either 0 or 1. This reflects laminar, diffusion-dominated transport, where fluids follow stable streamlines and interfacial mixing is limited.

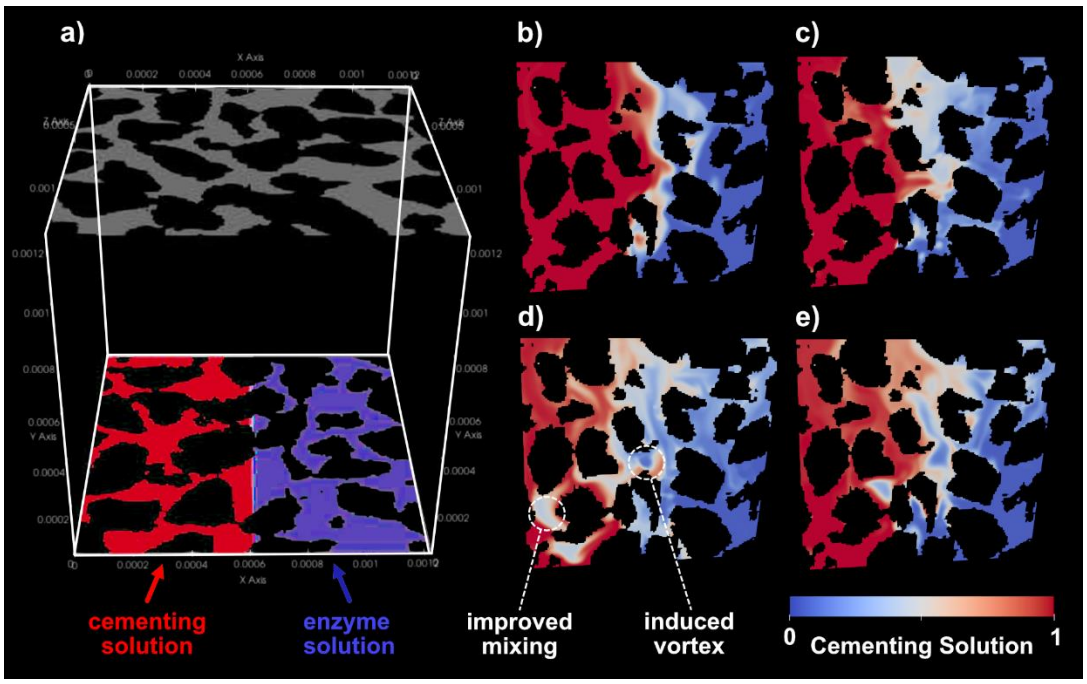

Figure 4.10 Effect of pulsed injection on mixing behaviour in porous media. (**a**) XCT-derived subvolume (150 × 150 × 150 voxels; voxel edge length = 8.156 µm) showing the pore geometry used for simulations, with enzyme solution (ES; blue) and cementing solution (CS; red) injected from separate inlets at the lower boundary. (**b–e**) Representative cutting planes through the same subvolume after 0.1 s of simulated flow (corresponding to 10 pulses at 100 Hz), showing CS concentration fields under different injection strategies: (**b**) steady flow, (**c**) synchronous pulsation, (**d**) alternating-phase pulsation, and (**e**) CS pulsed with ES injected steadily. Dashed circles in (d) highlight local regions of enhanced mixing and transient vortex formation, where pulsed flow disrupts sharp phase boundaries and promotes interfacial contact between fluids. Colour scale indicates normalised CS concentration (0–1).

Controlled pulsation during EICP injection promotes localised transient, inertia-influenced perturbations to otherwise laminar flow and enhances fluid mixing within the pore space, with potential implications for the spatial uniformity of $CaCO_3$ precipitation (Fig. 4.10). In the simulations, the concentration field represents the normalised volume fraction of CS, such that CS = 1 corresponds to pure cementing solution, CS = 0 corresponds to pure ES, and intermediate values indicate local mixing between the two fluids. A value of CS ≈ 0.5 therefore represents near-equal volumetric contributions of ES and CS within a given pore region.

Under steady flow conditions (Fig. 4.10b), the boundary between CS- and ES-dominated regions remains sharp, with limited deformation of the interface and minimal occurrence of intermediate concentration values. This reflects laminar,

diffusion-dominated transport, where fluids follow stable streamlines and remain segregated across much of the pore space. In contrast, pulsed injection strategies (Fig. 4.10c–e) generate a broader distribution of intermediate CS concentrations, indicating enhanced local mixing in pore regions that remain weakly connected or stagnant under steady injection.

The strongest mixing is observed under alternating-phase pulsation (Fig. 4.10d), where CS and ES are injected in non-overlapping phases. Although the two fluids are fully miscible, differences in density and viscosity (Section 3.4.3.1), combined with gravitational effects, promote stratification and stable interfaces under steady flow. Alternating-phase pulsation repeatedly disrupts these interfaces, promoting transient vortex formation and enhanced dispersion into otherwise poorly accessed pore volumes. This mechanism appears particularly effective in dual-fluid systems with contrasting physical properties and may reduce the likelihood of premature mixing and $CaCO_3$ scaling within injection infrastructure by delaying reagent overlap until fluids enter the porous medium, in contrast to single-phase injection strategies (Sections 4.1–4.2).

To quantify differences in mixing behaviour across injection strategies, the standard deviation (σ) of CS concentration over time within the simulated domain was calculated (Fig. 4.11). Here, σ serves as a measure of spatial heterogeneity in reactant distribution rather than a direct proxy for precipitation. High σ values indicate strong segregation between CS- and ES-rich regions, whereas lower σ values reflect an increased prevalence of intermediate concentrations.

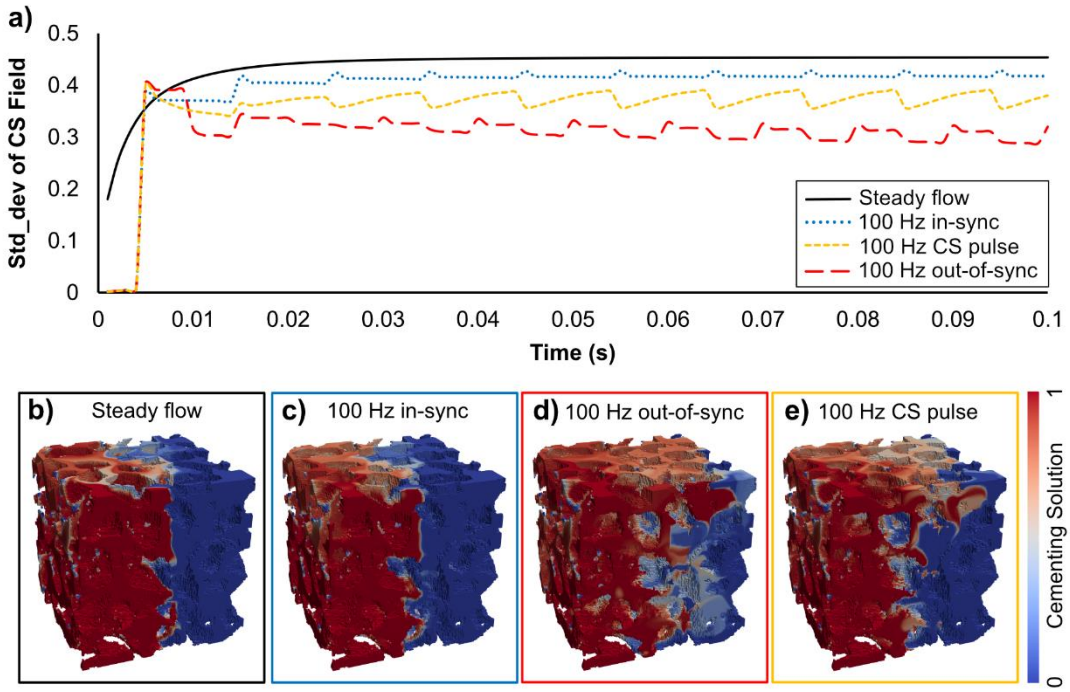

Figure 4.11 Effect of injection strategy on pore-scale mixing, quantified using the standard deviation (σ) of the CS concentration field. (**a**) Temporal evolution of σ, calculated over the full simulated pore volume using ParaView Quantitative Statistics, for four injection strategies: steady flow (solid black), 100 Hz in-sync pulsation (dotted blue), 100 Hz out-of-sync pulsation (long-dashed red), and 100 Hz CS-only pulsation with ES injected steadily (dashed yellow). Here, σ reflects the spatial heterogeneity of CS concentration within the domain; lower values indicate a narrower concentration distribution and increased prevalence of intermediate CS concentrations, rather than complete homogenisation. (**b–e**) Three-dimensional renderings of the CS concentration field at 0.1 s for the corresponding injection strategies, illustrating qualitative differences in spatial mixing and phase boundary deformation. Out-of-sync pulsation (d) produces the most disrupted interface and the greatest spatial dispersion of CS relative to steady injection.

The standard deviation σ is used here as a relative metric to compare mixing behaviour between injection strategies, rather than as a direct indicator of precipitation efficiency or an “optimal” reactant ratio. A perfectly uniform CS field (σ ≈ 0) would correspond to complete homogenisation, while higher σ values indicate stronger segregation between CS- and ES-rich regions. In the present simulations, reductions in σ reflect increased interfacial deformation and local mixing, consistent with the qualitative 2D patterns observed in Fig. 4.10c–e and the three-dimensional fields shown in Fig. 4.11b–e. Interpretation of these trends in terms of carbonate precipitation is therefore limited to assessing the potential for increased reagent overlap, rather than predicting precipitation rates or spatial patterns directly.

Under steady injection, σ increases gradually as the cementing solution progressively occupies the pore space and stabilises at ~0.45 after approximately 0.03 s, coinciding with CS reaching the outlet boundary and the total CS volume within the domain becoming approximately constant. This stabilisation indicates that, despite continued injection, mixing remains limited once preferential flow paths are established and interfacial deformation ceases. Although the simulated domain represents only a small section of the flow cell, the persistence of high σ suggests that under steady flow, mixing within low-connectivity or stagnant pore regions may remain incomplete even over longer durations.

In contrast, pulsed injection produces an immediate reduction in σ at the onset of the first pulse at 0.004 s (Fig. 4.11a), reflecting disruption of the stable CS-ES interface. Following this initial response, the pulsed cases exhibit sustained oscillations in σ around lower mean values than steady flow, indicating continued interfacial deformation and enhanced local mixing. Under in-sync pulsation, where CS and ES are pulsed simultaneously with identical timing, σ decreases to 0.412 by 0.03 s and remains nearly constant at 0.417 by 0.1 s, suggesting that mixing plateaus early and that additional pulses provide limited further benefit in this configuration.

Alternating-phase pulsation exhibits a continued decline in σ over time, from 0.338 at 0.03 s to 0.288 by 0.1 s, indicating progressively enhanced mixing. This behaviour suggests that alternating injection phases enable CS to access pore regions that remain poorly connected under steady or in-sync pulsed injection, promoting more effective dispersion across the pore network. This trend is consistent with the three-dimensional CS concentration field shown in Fig. 4.11d, where CS appears more uniformly distributed relative to the other injection strategies.

Several limitations of the present simulations should be noted. First, the analysis is restricted to a small sub-volume (~1.2 mm^3) and therefore does not capture larger-scale flow reorganisation or upstream stratification effects, limiting direct comparison with the density driven phase separation observed earlier (Section 3.4.3.1). Second, while realistic density and viscosity contrasts between fluids are represented, $CaCO_3$ precipitation is not explicitly modelled, and the relationship between enhanced mixing and mineralisation efficiency is therefore inferred rather than resolved directly. Finally, the use of high-frequency pulsation (100 Hz) represents an upper-bound scenario intended to maximise transient flow perturbations; lower-frequency regimes and alternative delivery strategies would be required to assess practical field applicability.

These aspects are being explored further in ongoing work supported by IDRIC, which focuses on translating pulsed-flow concepts to applied subsurface engineering and carbon storage contexts.

4.5 Discussion & Concluding Remarks

Under laminar flow conditions, $CaCO_3$ precipitation during EICP tends to follow reagent mixing fronts rather than uniformly accessing available pore space, restricting treatment efficiency and limiting control over precipitation patterns (Section 3.4.3.1). The results in this chapter show that this behaviour is not an inherent constraint of EICP, but emerges from the interaction between reaction timing, pore structure, and fluid delivery. By adjusting these levers, precipitation can be decoupled from passive mixing and instead shaped to achieve more uniform or more spatially targeted outcomes.

4.5.1 Implications for Controlling Precipitation and Permeability

Reaction timing relative to transport strongly governs where $CaCO_3$ forms. Delaying nucleation – whether through protein-mediated stabilisation of metastable phases or through buffering effects – allows precipitation to occur after fluids have penetrated deeper into the pore network. This shifts control from the dynamics of two-fluid mixing to the flow path of a single, well-mixed solution, providing a route to more uniform treatment.

The layered experiments demonstrate that heterogeneity increases sensitivity to biocementation rather than diminishing its effectiveness. Once reactive fluids access fine-grained layers, precipitation within these regions produces strong hydraulic responses, redirecting flow and concentrating permeability reduction where it is most effective. This contrasts with single-phase MICP, where bacterial filtration and early pore blockage limited penetration across permeability contrasts. Enzyme-based systems therefore offer a distinct advantage in stratified media, where control of narrow pore throats is often critical.

Injection strategy further modulates reagent overlap and injectability. Pulsed-flow simulations show that transient perturbations to otherwise laminar flow can disrupt stable interfaces between enzyme and cementing solutions, increasing mixing in stagnant pore regions. Although precipitation is not modelled directly, these results

demonstrate a mechanism for increasing the volume of pore space in which reagents can coexist without requiring upstream mixing that may risk premature scaling.

4.5.2 Limitations, Uncertainty, and Scope Boundaries

Several limitations constrain the interpretation and generalisation of these results. Pulsed-flow simulations were performed on small sub-volumes and do not incorporate fully coupled reactive transport or evolving pore geometry due to precipitation. Fluid–surface interactions were treated implicitly, and enzyme and cementing solutions were assumed to have identical wetting behaviour. Consequently, mixing metrics such as concentration standard deviation can only be interpreted as indicators of potential reagent overlap rather than predictors of precipitation rate, morphology, or mechanical outcome.

Experimentally, precipitation under pulsed flow was inferred from mixing behaviour rather than observed directly using time-resolved imaging. While earlier XCT results demonstrate that precipitation localises where reagent overlap is sustained, the precise relationship between transient mixing, nucleation kinetics, and final crystal distribution remains unresolved. These uncertainties become increasingly important when extrapolating to larger or more complex systems, where pressure gradients, lateral diversion, geochemical buffering and other environmental factors (Section 1.2.5) will further influence behaviour.

The scope of this chapter is therefore intentionally bounded. Fully coupled reaction–transport modelling, systematic exploration of pulsing frequency and waveform, and in situ imaging of precipitation under transient flow conditions would provide valuable insight but would be premature without first constraining the biochemical controls on precipitation timing. Rather than extending modelling complexity, the work proceeds to evaluate the consequences of these mechanisms through macro-scale hydraulic, mechanical, and thermal measurements, where performance can be assessed directly.

4.5.3 Closing Perspective

By demonstrating how biochemical formulation, pore structure, and injection regime influence when and where carbonate forms, this chapter establishes the conditions under which biocementation can be treated as an engineered process rather than a passive outcome of fluid mixing. In terms of the thesis objectives, it directly addresses Critical Challenge 1 by resolving pore-scale precipitation dynamics using XCT and flow modelling, Critical Challenge 2 by demonstrating how crude enzyme formulations and organic constituents influence precipitation pathways and timing, and Critical Challenge 4 by showing how permeability modification can be spatially targeted through structural and operational control levers. These mechanistic insights also provide grounding relevant to Critical Challenge 3, by clarifying how engineered permeability contrasts could be created to influence subsurface flow. This provides a foundation for evaluating how such control translates to material-scale hydraulic, mechanical, and thermal performance in the chapters that follow.

Chapter 5: Bio-Cementation for structural and thermal soil enhancement with retained hydraulic conductivity

This chapter addresses the translation of pore-scale biocementation mechanisms into measurable material performance. While Chapters 3 and 4 establish how mixing behaviour, enzyme formulation, and injection strategy control when and where $CaCO_3$ forms during EICP, engineering application ultimately depends on how these precipitation patterns influence bulk properties such as strength, permeability, and thermal conductivity. Resolving this link is essential if biocementation is to move beyond laboratory demonstrations toward predictable, application-specific design.

Focusing on soybean-derived enzyme systems and mixed-enzyme formulations, this chapter evaluates how protein-mediated delays, and carbonate distribution affect the mechanical, hydraulic, and thermal response of biocemented sand. Unconfined compressive strength testing, permeability measurements, thermal conductivity analysis, and complementary XCT imaging are used to quantify performance outcomes and relate them directly to the precipitation behaviours identified in earlier chapters.

In doing so, this chapter advances beyond mechanistic control toward functional assessment, directly addressing Critical Challenge 2 by evaluating scalable enzyme formulations, and Critical Challenge 4 by examining permeability modification under controlled precipitation regimes. The central question addressed is: *How do controlled precipitation pathways identified at the pore scale manifest in the macroscopic hydraulic, mechanical, and thermal behaviour of EICP-treated materials?*

Citation:

This chapter has been published in part: Salter, P.J., Minto J.M., and Dobson, K, J. (2025). ‘Bio-Cementation for structural and thermal soil enhancement with retained hydraulic conductivity’. *Biogeotechnics, Published 5 December 2025.* https://doi.org/10.1016/j.bgtech.2025.100216

Author Affiliations:

Philip J. Salter[1*], James Minto[1], Katherine J. Dobson[1]

[1] Department of Civil & Environmental Engineering, University of Strathclyde, James Weir Building, 75 Montrose Street, Glasgow, G1 1XJ, UK

Author Contributions

PS: Conceptualization, Methodology, Data Acquisition, Analysis, lead on all stages of MS preparation.

JM: Funding, Supervision, MS preparation.

KD: Project design & funding, Analysis, Supervision, MS preparation.

5.1 Abstract

In hot, dry climates, geothermal systems often underperform due to low soil thermal conductivity and heat capacity. Periodic water ingress helps restore both, enabling more effective ground heat transfer. Remediation must therefore improve thermal and mechanical properties without blocking flow. This study tests whether bio-cementation can achieve that balance. We combined unconfined compressive strength, thermal and hydraulic conductivity testing with X-ray computed tomography and flow modelling to track microstructural evolution during microbial and enzyme induced carbonate precipitation (MICP and EICP). While final $CaCO_3$ distributions were visualized across all strategies, we captured time-lapse 3D X-ray imaging of soybean EICP for the first time, showing that precipitation at grain contacts enhanced strength and thermal conductivity while preserving flow pathways. In contrast, MICP provided comparatively uniform thermal conductivity enhancement before clogging at nine cycles. Jack bean meal achieved the highest thermal conductivity increase (up to 781%), but this enhancement was highly localized. In contrast, soybean EICP produced more uniform $CaCO_3$ precipitation, yielding consistent thermal conductivity gains (~600%) and an unconfined compressive strength of 17.9 MPa at 26.6 wt% $CaCO_3$. Soybean curds reduced hydraulic conductivity but conferred no significant improvement in thermal or mechanical performance. These findings support targeted bio-cementation strategies that enhance subsurface thermal functionality without compromising flow, with direct applications in energy piles and geothermal systems in arid climates.

KEYWORDS: EICP, MICP, time-lapse XCT, hydraulic conductivity, thermal conductivity

HIGHLIGHTS:

- Soybean EICP reached 17.9 MPa UCS while retaining permeability over 25 cycles.
- Time-lapse XCT tracked $CaCO_3$ growth and flow changes across EICP cycles.
- Thermal conductivity increased up to 781% via EICP.
- Soybean EICP formed thermal bridges by $CaCO_3$ layering at grain contacts, seen in XCT.
- Organic additives lowered permeability without improving thermal conductivity in EICP.

5.2 Introduction

In hot, arid regions, the performance of geothermal systems and energy piles is often limited by the poor thermal conductivity and heat capacity of dry soil (Adebayo et al., 2024; Eze et al., 2025; Sani & Singh, 2020). Dry soils act as a thermal bottleneck, requiring larger ground loop collector areas or deeper boreholes to compensate for reduced heat exchange. This can increase installation complexity and significantly raise initial capital costs (Eze et al., 2025). Moreover, the low thermal conductivity of dry soil causes the surrounding material to heat up or cool down more quickly, diminishing long-term system efficiency. These systems typically rely on periodic water infiltration, through rainfall, irrigation, or shallow groundwater to restore thermal performance and enable sustained subsurface heat rejection (Go et al., 2015). However, many soil thermal enhancement strategies either overlook this need or unintentionally block long-term fluid flow (Nemati, 2003), leading to localised heat buildup and performance degradation over time (Sani & Singh, 2020). In addition to geothermal applications, conventional construction materials significantly contribute to global energy use, pollution, and greenhouse gas emissions, particularly through the manufacture of fired-clay bricks and cement-based blocks (B.V Venkatarama Reddy, 2003). Environmentally friendly alternatives capable of providing comparable

structural strength and performance, while reducing the reliance on fossil fuels and lowering emissions, are therefore urgently needed.

Microbially and enzyme-induced carbonate precipitation (MICP and EICP) have emerged as promising ground improvement techniques, capable of modifying soil properties for a range of engineering applications. These processes can significantly increase unconfined compressive strength (UCS) (Almajed et al., 2019; Whiffin et al., 2007), reduce liquefaction potential (Montoya et al., 2012; Wang et al., 2023), enhance thermal conductivity (Li et al., 2023; McCartney et al., 2020; Venuleo et al., 2016; Z. Wang et al., 2020), and alter soil hydraulic conductivity (Chu et al., 2013). However, despite this progress, a key challenge remains: how to enhance thermal and mechanical properties without excessively reducing hydraulic conductivity, especially in applications where fluid flow is critical to performance.

While previous studies have demonstrated that bio-cementation can improve strength (Putra et al., 2018; Whiffin et al., 2007), enhance thermal conductivity through thermal bridging (McCartney et al., 2020; Z. Wang et al., 2020) or reduce hydraulic conductivity through pore blocking (Chu et al., 2013), these effects have typically been investigated in isolation. The influence of crystal distribution, particularly differences between MICP and various plant-based urease sources for EICP, on combined hydromechanical and thermal performance remains poorly quantified. In addition, although soluble milk proteins have been shown to improve uniaxial strength at low $CaCO_3$ contents (Almajed et al., 2019; Whiffin et al., 2007), their effect on hydraulic and thermal conductivity is not well understood. A three-dimensional microstructural perspective is needed to explain these relationships and guide the design of treatment protocols that balance strength, thermal performance, and flow.

To address these challenges, we apply X-ray computed tomography (XCT) to investigate how carbonate precipitation evolves during treatment. XCT enables direct comparison of $CaCO_3$ distribution across injection strategies and allows pore-scale analysis of how flow paths, thermal conductivity, and strength evolve over time (Dadda et al., 2018). By capturing internal structure non-destructively, this method provides a unique window into how microstructural changes control macro-scale performance during bio-cementation.

Our study systematically evaluates how different MICP and plant-based EICP treatments affect the interplay between UCS, thermal conductivity (λ), and hydraulic conductivity (K) across multiple treatment cycles. By combining macro-scale

measurements with pore-scale imaging, we benchmark the relative benefits and trade-offs of different enzyme sources, organic additives, and injection regimes. This integrated approach enables the identification of treatment strategies that deliver durable thermal and mechanical improvements without compromising long-term water ingress, supporting the design of bio-cementation protocols for both subsurface thermal applications in arid environments and as sustainable alternatives to conventional construction materials.

5.3 Materials & Methods

5.3.1 MICP and EICP solutions

For MICP treatments, the ureolytically active bacterial strain *Sporosarcina pasteurii* (DSMZ, DSM No. 33) was cultured in a solution of 5.5 g/L yeast, 5 g/L NaCl, 0.4 g/L K_2HPO_4, 0.4 g/L D-Glucose, 20 g/L urea, and 5 μM NiCl for ~24 hours. The growth media was then centrifuged (6000 rpm, 8 minutes) and the bacteria resuspended in tap water. The optical density of the bacterial suspension and enzyme solutions was measured at a wavelength of 600 nm using a UV-Vis spectrophotometer. This measurement, referred to as OD600, estimates the bacterial concentration in the suspension and quantifies suspended solids in the enzyme solutions. The MICP treatment cementing solution (MICP-CS) was a mixture of 1.0 M urea and 1.0 M $CaCl_2$ dissolved in <12MΩ deionised water.

For EICP treatments, several enzyme sources were tested. A Jack Bean (*Canavalia ensiformis*) enzyme solution (JBM) was prepared from pre-prepared commercial sources (jack bean meal, Fisher Scientific™). Jack Bean (JBB) and Soya Bean (SB) (*Glycine Max*) enzyme solutions were also prepared from raw dried beans that were ground to <212 μm using a blade mill (Shu, Yan, Meng, et al., 2022). All three enzyme sources were extracted by mixing with deionised water (10 g/L for JBM and JBB, 100 g/L for SB) for 30 minutes, followed by a 1-hour resting period to allow coagulation. The suspensions were then centrifuged (6000 rpm, 8 minutes) and filtered through a <1 μm sieve. To enhance removal of excess proteins in SB extracts, 10 g/L of calcium sulphate dihydrate was added after the initial 30-minute mixing step, followed by 5 minutes of stirring before the 1-hour rest (Meng et al., 2021).

A mixture of JBB (10 g/L) + non-fat milk (NFM) powder (8 g/L) was prepared to test the impact of soluble milk proteins. This allowed casein-rich JBB+NFM to be compared directly to JBM, which contains urease but no milk proteins. Additional

mixtures of JBB (10 g/L) with SB at 10, 20, and 30 g/L were prepared to investigate the effect of increasing soy protein content on ureolytic activity and precipitation behaviour. Calcium sulphate dihydrate was omitted from these blends to assess the role of insoluble soy proteins in bio-clogging and permeability reduction.

For long-term experiments (medium and small flow cells), a single batch of each enzyme solution was prepared in advance and frozen at −18 °C. Unlike previous studies, we did not observe an increase in ureolytic activity after thawing (Ng & Chu, 2024). The EICP treatment cementing solution (EICP-CS) was prepared by dissolving 2.0 M urea and 2.0 M $CaCl_2$ in deionised water. This solution was mixed in a 1:1 ratio with the enzyme solution immediately before injection, yielding a final concentration of 1.0 M urea and 1.0 M $CaCl_2$ – matching the composition of the MICP cementing solution formed by in situ mixing.

Ureolytic activity was measured using the conductivity method, which tracks changes in electroconductivity as non-ionic urea is hydrolysed to ionic ammonium (Whiffin et al., 2007) for both the enzyme and bacterial solutions. Test tube experiments were also conducted to estimate the lag period between mixing and visible $CaCO_3$ precipitation, by combining 2 mL of enzyme solution with 2 mL of cementing solution (see Table 5.1).

Table 5.1 Overview of the 3 experiment sets, including source of urease additives, resultant solution properties, number of treatment cycles applied, and sample diameter.

Solution	Activity[a]	OD600	Lag period (mins)[b]	Initial pH	Cycle	⌀ (mm)
Experiment set 1: Comparing MICP to SB EICP						
MICP	4.1	1.00	N.A	-	9	60
SB	3.4	0.313	180–240	6.10	9	60
Experiment set 2: Evaluating SB EICP treatment cycles and XCT imaging for pore scale observations						
SB	3.4	0.313	180–240	6.10	10	27
					25	27
					3	60
					6	60
					9	60
					9	6.6
Experiment set 3: Comparing enzyme sources and organic additives						
SB	3.4	0.313	180–240	6.10	10	27
SB	3.4	0.313	180–240	6.10	25	27
JBM	4.8	0.092	30–60	7.08	10	27
JBB	2.8	0.068	15–40	7.12	10	27
JBB + NFM	2.6	0.191	30–70	7.06	10	27
JBM + NFM	5.0	0.311	30–70	7.14	10	27
JBB + SB 10 g/L	3.5	0.398	20–90	6.78	10	27
JBB + SB 20 g/L	3.8	1.017	60–105	6.74	10	27
JBB + SB 30 g/L	4.0	1.064	60–105	6.76	10	27
[a]Activity = mmol of urea hydrolysed per minute						
[b]Lag period = time between mixing and visual onset of precipitation						
All samples were XCT imaged, providing detailed pore-scale characterization of $CaCO_3$ distribution. Given this high-resolution data, additional replicates were not required.						

5.3.2 Treatment strategies

To simulate $CaCO_3$ precipitation and treatment behaviour under arid climate conditions, three sizes of XCT-compatible flow cells were used: large (60 mm × 100 mm), medium (27 mm × 55 mm), and small (6.6 mm × 10 mm) (Fig. 5.1a–c). Each was filled with quartz sand (210–297 µm, Sigma Aldrich) pre-mixed with 10 wt% deionised water.

To ensure consistent packing, samples were constructed in 10 layers, with each layer compressed 10 times using a spring-loaded punch applying 100 N. Layers were scarified prior to adding the subsequent layer to avoid layering effects (Fig. 5.1b). This procedure produced a dry density of 1.50 g/cm^3 for the untreated sand, corresponding to a void ratio $e \approx 0.77$.

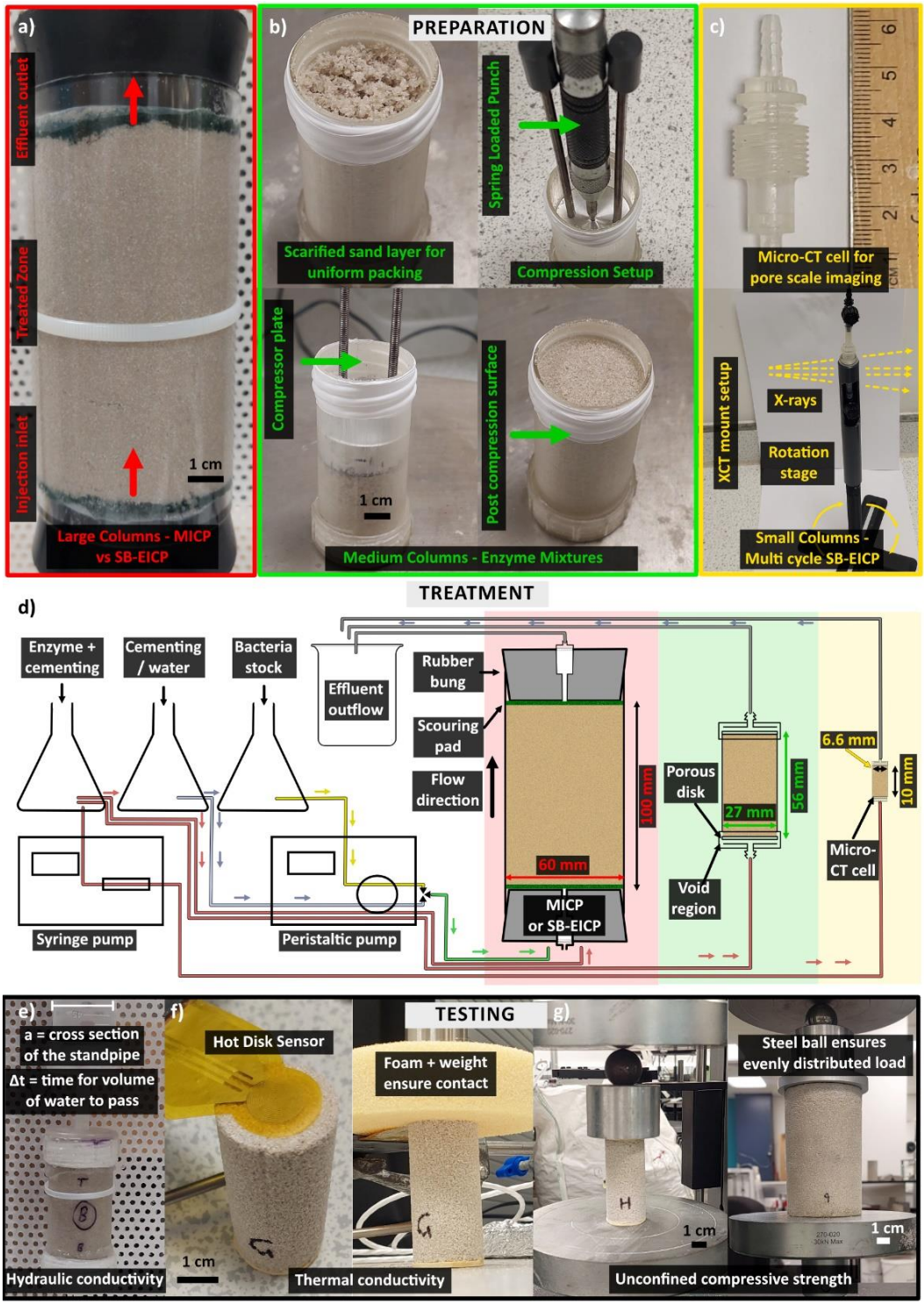

Figure 5.1 Experimental setup and testing workflow across three length scales. (**a–c**) Column preparation and configurations used for MICP and SB-EICP treatments at large (60 mm), medium (27 mm), and small (6.6 mm) scales. The small columns were designed for in-situ X-ray CT imaging of precipitation during multi-cycle SB-EICP treatment. (**d**) Schematic of the injection and flow system showing enzyme and cementing solution delivery, effluent collection, and XCT integration. (**e–g**) Post-treatment testing methods used to determine hydraulic conductivity, thermal conductivity, and unconfined compressive strength.

5.3.2.1 Large diameter flow cells (60 mm)

The large-diameter flow cells were used to compare two-phase MICP with single-phase soybean EICP (SB), providing an initial assessment of the relative performance of each treatment approach.

For MICP, 140 mL of bacterial solution (approximately 1.1 pore volumes) was injected at 35 mL/min, followed by a 1-hour resting period to allow bacterial attachment. To prevent inlet blockage, 5 mL of tap water was then injected to flush the port, as recommended by previous studies (Minto et al., 2017). This was followed by 140 mL of MICP cementing solution (MICP-CS), also injected at 35 mL/min. The sample was then left undisturbed for 24 hours to allow $CaCO_3$ precipitation. This sequence was repeated for nine treatment cycles. On the final MICP cycle, only 120 mL of bacterial solution could be injected before blockage occurred, although 140 mL of MICP-CS was still delivered. This is likely due to physical straining from the higher suspended load in the bacterial solution.

For the SB treatment, equal volumes of SB enzyme solution and EICP-CS (70 mL each) were pre-mixed and immediately injected at 35 mL/min, followed by 24 hours of reaction time. This procedure was repeated for 3, 6, or 9 cycles to quantify the evolution of $CaCO_3$ volume, distribution, and effect on material properties (Fig. 5.1d). No clogging was observed in any of the SB-treated samples. Effluents were collected during each cycle but not systematically analysed, as the study focus was on material properties rather than effluent chemistry.

As nine MICP cycles were expected to be necessary for sufficient cementation, no partial-cycle (3 or 6) MICP samples were prepared. The number of MICP cycles and calcite content have been investigated in previous work (McCartney et al., 2020).

5.3.2.2 Medium diameter flow cells (27 mm)

The 27 mm diameter flow cells were used to compare the performance of different EICP treatments and their mixtures. For each cycle, 7.5 mL of enzyme solution was mixed with 7.5 mL of EICP-CS (1:1 ratio), then immediately injected at 17.5 mL/min. This rate was selected to maintain practical injection times and to minimize the risk of premature reaction in the flow lines for more reactive enzyme solutions (e.g., JBM). Although this resulted in a different pore-scale velocity compared to the large-diameter cells, precipitation lag periods were substantially longer than the injection durations (typically >10 minutes and up to 4 hours for SB-EICP, see Fig. 4.1). These

differences were therefore not expected to affect $CaCO_3$ precipitation. Samples were left undisturbed for 24 hours to allow $CaCO_3$ precipitation. All enzyme variants were subjected to 10 injection cycles, with an additional SB-treated sample extended to 25 cycles to evaluate longer-term treatment performance.

5.3.2.3 Small diameter flow cells (6.6 mm)

The small-diameter flow cell was used exclusively for in situ XCT imaging to capture pore-scale precipitation processes. The column was pre-saturated under vacuum with deionised water, then 5 mL of a 1:1 mixture of SB enzyme solution and EICP-CS was injected at 1 mL/min.

Based on prior test tube trials and the larger-scale experiments, the majority of $CaCO_3$ precipitation was observed to occur within 4 hours (Section 4.1). As a result, at least 6 hours of reaction time was allowed before each CT scan, with 24 hours between successive injection cycles.

5.3.3 Property testing methods

5.3.3.1 Hydraulic conductivity tests

Hydraulic conductivity (K) was measured using falling head tests conducted in triplicate on all large and medium flow cell samples prior to removal (Fig. 5.1e). Values were calculated using:

$$K = [2.3\ a.L\ /\ (A.\Delta t)].log(h0/\ h1)$$

[Eq. 5.1]

Where K is the hydraulic conductivity, a is the cross-sectional area of the standpipe, L is the length of the column, A is the cross-sectional area of the sample, Δt is the recorded time for 10 mL of water to flow through the column, and h0 and h1 are the initial and final water levels in the standpipe.

Tests were performed in situ with samples left inside their rigid 3D-printed flow cells to avoid disturbance and minimize preferential flow around the sample edges. As shown in Fig. 5.1e, the standpipe comprised a short section of tubing connected to a graduated syringe used as a reservoir. Measurements were taken only after ≥ 9

treatment cycles, ensuring that samples were fully saturated and free of entrapped air at the top surface. For each replicate, the time required for 10 mL of water to pass through the sample was recorded, and the average was used to calculate K.

5.3.3.2 Thermal conductivity tests

Thermal conductivity of the samples was measured using a Hot Disk Thermal Analyzer TPS2500S (University of Strathclyde) using the single-sided transient plane source (TPS) method and a 6.4 mm diameter double spiral sensor (Gustafsson, 1991; Gustavsson et al., 1994) acting as both heating source and resistance thermometer, and recording the temperature increase over time. The thermal conductivity of the untreated packed sand was measured using a powder holder in which the sensor is fully covered. For treated samples, the sensor was placed between the sample and a piece of low-density foam of known thermal conductivity (Fig 5.1f). All measurements were performed on completely dry samples, as thermal enhancements are most pronounced in dry conditions and the baseline conductivity of untreated dry sand (~0.247 W/m·K) aligns with values reported for loose quartz sand. Triplicate measurements were collected at both the inlet and outlet for all samples from the large and medium flow cells.

5.3.3.3 Unconfined compressive strength tests

Prior to UCS testing, gypsum plaster (Crystacast, compressive strength: 55.2 MPa) was applied to the top and bottom surfaces of each core. This ensured flat, even loading surfaces and minimized stress concentrations. UCS tests were then performed at a loading rate of 0.1 MPa/s (Fig. 5.1g), continuing until sample failure. All UCS measurements were performed on completely dry samples, consistent with the thermal conductivity testing protocol. Only the 60 mm diameter columns deviated from the standard height-to-diameter ratio (2:1) required by BS EN ISO 17892-7:2018 for UCS testing. To account for this, measured peak stress values were adjusted by dividing by a factor of 1.024, as recommended by prior work (Turk & Dearman, 1986), to yield the corrected UCS values.

Following UCS testing, the plaster caps were carefully removed using a diamond blade saw. Samples were dried and weighed to obtain their dry mass before acid dissolution (Mortensen et al., 2011). $CaCO_3$ content was determined by submerging samples in 4 M HCl for 12 hours, then refreshing the acid and confirming the reaction had ceased (i.e. no remaining bubbles). The residual sand was rinsed, dried, and

reweighed. The $CaCO_3$ content was calculated as the difference in mass pre- and post-dissolution and expressed as a ratio relative to the final sand mass.

5.3.4 XCT imaging and analysis

To better understand how different treatment strategies influence internal $CaCO_3$ formation, XCT imaging was used to visualize density gradients and pore structure across all samples (Fig. 5.1c). This enabled direct comparison of density and porosity with thermal conductivity, across enzyme sources and treatment durations. Scans were conducted on a Nikon XT H 225 system (University of Strathclyde) using the acquisition settings listed in Table 5.2.

Table 5.2 XCT acquisition conditions for different sample diameters

⌀ (mm)	Accelerating Voltage (kV)	Current (µA)	Projections	Exposure time (ms)	Voxel Resolution (µm)	Filter	Saturation conditions
60	170	71	3141	4000	37	1mm Cu	Dry
27	170	94	2021–2313	354	40	No	Dry
6.6	60	123	3142	4000	7.5	No	Saturated

Key parameters used for XCT scans across three sample diameters, including accelerating voltage, current, projections, exposure time, voxel resolution, and saturation conditions. Although scans were captured on different dates, potentially introducing variability in filament brightness, the segmentation process relies on statistical thresholding based on contrast between phases (e.g., air, quartz, water), ensuring consistent results irrespective of absolute brightness differences.

Scanning conditions were selected to minimize accelerating voltage while maintaining at least ~30% X-ray transmission through the sample centre. Exposure times were capped at 4000 ms to limit overall scan duration. All datasets were reconstructed using Nikon's proprietary reconstruction algorithms.

XCT datasets were processed in Avizo® v2023.1 (ThermoFisher™) to extract porosity (all samples) and, for 6.6 mm samples, to quantify $CaCO_3$ distribution after treatment. Pre- and post-treatment scans were spatially registered and segmented using histogram-based thresholding (Otsu, 1979) to distinguish pore space from solid material. We assume negligible grain motion or dissolution, with changes attributed solely to MICP/EICP activity. For 6.6 mm samples, $CaCO_3$ volume was computed by

subtracting the untreated volume from the post-treatment scan (Salter, Minto, Warnett, et al., 2025). Pore geometry was further analysed using random-walk distance separation (Baum et al., 2019) to distinguish intergranular porosity from trapped gas bubbles, defined as voids > 0.6 mm³ with sphericity > 0.8. $CaCO_3$ density profiles (6.6 mm) and bulk density estimates (27 mm and 60 mm) were obtained using the Z-project function in ImageJ (Willems et al., 2021). Due to limited resolution, individual $CaCO_3$ crystals could not be identified in larger samples. Absolute permeability simulations were performed on 6.6 mm scans at t = 0, 3, 6, and 9 cycles, using downsampled volumes (15 µm) to ensure convergence. Full processing details are provided in Appendix Fig. A2.

5.4 Results & Discussion

5.4.1 Hydraulic conductivity retention depends on enzyme source and treatment strategy

Groundwater flow and occasional rainfall can occur even in arid climates (G. Wang et al., 2020), and fluctuations in groundwater level may also result from atmospheric pressure changes. To be effective in such environments, MICP or EICP treatment strategies must retain hydraulic conductivity to allow periodic water ingress. Restricting flow into the treated zone would impair heat transfer, as partially saturated soils exhibit significantly higher thermal conductivity than dry soils (Venuleo et al., 2016). Initial large-diameter flow cell tests showed comparable K values for MICP and soybean EICP treatments. However, complete blockage in the MICP sample after nine cycles was likely caused by localized inlet clogging (Fig. 5.2a, inset, red), which redirected flow into a less-cemented perimeter zone (blue).

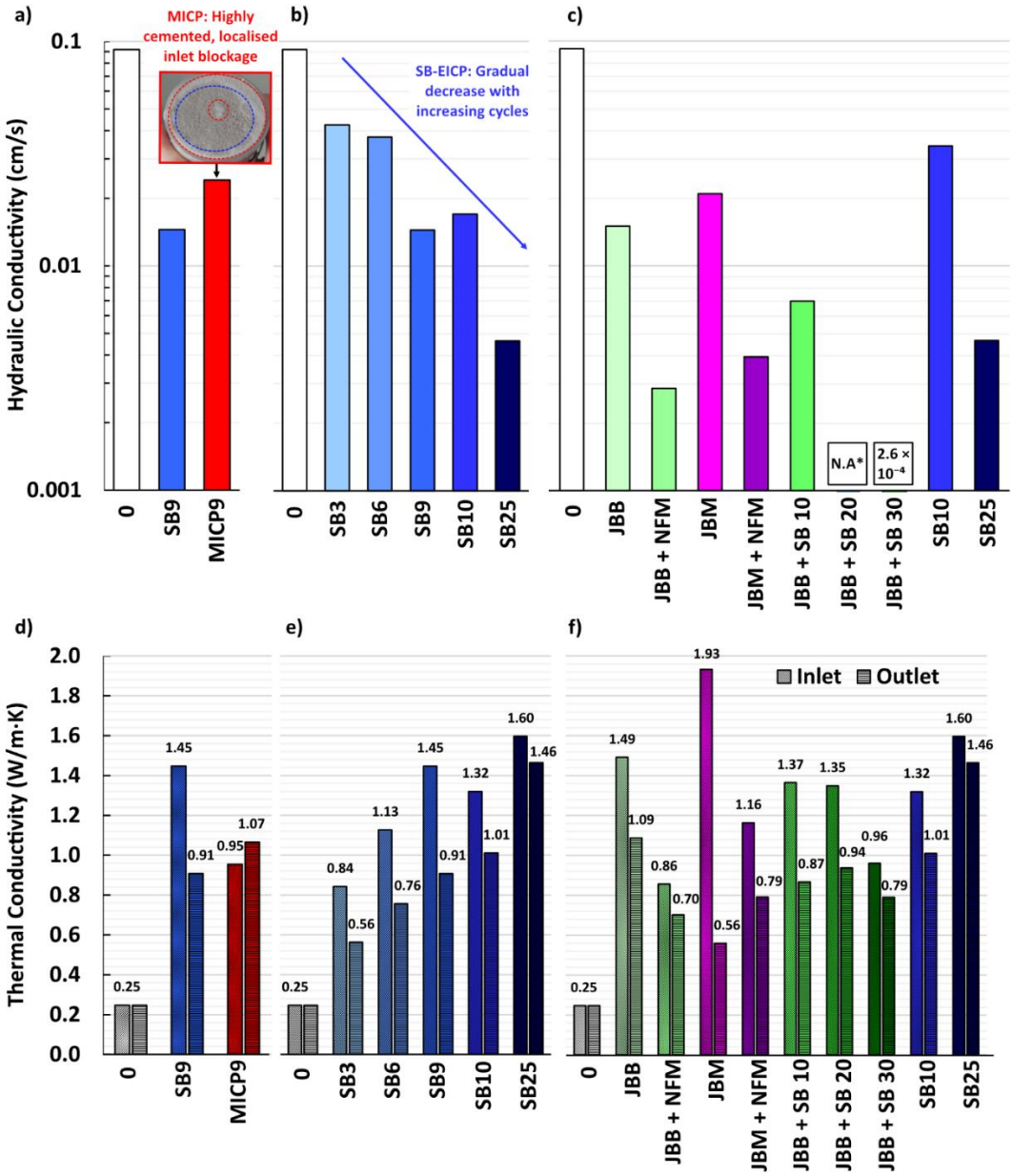

Figure 5.2 Hydraulic and thermal conductivity evolution across MICP and EICP treatments. (**a–c**) Hydraulic conductivity for untreated sand, MICP, and EICP samples, showing the effects of treatment type, cycle number, and enzyme mixtures. SB-EICP maintains permeability while MICP exhibits localised clogging. (**d–f**) Corresponding thermal conductivity at the inlet and outlet for the same treatments. SB-EICP produces a progressive and uniform increase in thermal conductivity with successive cycles and enzyme mixtures, exceeding 600% enhancement after 25 cycles. Hydraulic conductivity for JBB + SB 20 was below the measurable range. SB10 and SB25 denote soybean EICP samples treated for 10 and 25 cycles, respectively. Corresponding $CaCO_3$ contents for the different treatment groups are shown in Fig. 5.5.

Comparing SB-EICP across time (3, 6, and 9 cycles) and scale (large and medium flow cells) (Fig. 5.2b) highlights its potential to retain hydraulic conductivity even at high levels of bio-cementation. K dropped by 51% after 3 cycles, followed by a further 6% reduction from cycles 4 to 6, and 27% from cycles 7 to 9. This suggests early-stage pore constriction followed by more localized crystal growth.

The medium-diameter SB10 sample retained slightly higher K (0.034 cm s^{-1}) than the SB9 large-diameter sample (0.029 cm s^{-1}), likely due to slight packing variability. After 25 cycles, K was reduced by ~97% (to 0.003 cm s^{-1}), though significant absorbance capacity remained (see Appendix D2). Figure 5.2c compares K across various SB, JBB, JBM, and NFM mixtures. Broadly, hydraulic conductivity declined with increasing organic content. The addition of non-fat milk powder (JBB + NFM, JBM + NFM) or soybean curds (JBB + SB 10–30 g/L) lowered K relative to JBM, JBB, or SB alone. At higher soy dosages, the JBB + SB 30 g/L sample exhibited slightly greater permeability than the 20 g/L sample, which was below the measurable range (no water flow observed). Notably, JBB + SB 10 g/L retained more permeability than either milk powder blend, suggesting that low concentrations of soybean solids may act as organic stabilizers, enabling bio-cementation without full pore occlusion.

5.4.2 Thermal conductivity varies along flow path by enzyme type

Enhancing thermal conductivity is a key objective in bio-cementation for geothermal applications. The spatial distribution of $CaCO_3$ along flow paths can lead to non-uniform thermal performance, particularly if precipitation is localised near the injection point. To evaluate this, thermal conductivity was measured at both the inlet and outlet of each treated sample, enabling assessment of uniformity across different enzyme sources and additive compositions. All treated samples showed a substantial increase in λ relative to untreated sand (0.247 W/m·K), with gains ranging from 226% to 781% (Fig. 5.2d–f). However, all EICP-treated samples exhibited a decrease in λ from inlet to outlet, ranging from 8% to 71%, due to uneven $CaCO_3$ precipitation.

SB-EICP treated to 25 cycles showed the highest outlet λ (1.464 W/m·K, 592% increase) and second-highest inlet λ (1.597 W/m·K, 646% increase), indicating relatively uniform thermal improvement. In contrast, JBM treatment produced the highest λ at the inlet (1.932 W/m·K), but much lower λ at the outlet (0.559 W/m·K), suggesting strongly localised $CaCO_3$ precipitation.

The MICP sample displayed a more uniform thermal conductivity profile, with a modest difference between inlet and outlet. Its outlet λ (431% increase) was slightly higher than the large-diameter SB sample treated for 9 cycles (367% increase), despite the SB-EICP sample having a much higher inlet λ. This uniformity is likely due to bacteria acting as nucleation points during MICP, enabling more evenly distributed $CaCO_3$ precipitation throughout the sample. Unlike EICP, MICP is less affected by gravity-driven settling, as the reaction occurs primarily on the surface of cells rather than within pore fluids (Tarantino et al., 2019).

Over repeated SB-EICP treatments in large samples, both inlet and outlet λ increased linearly between cycles 3 and 9. A similar trend was observed in the SB10 sample (27 mm, 10 cycles), which exhibited slightly lower inlet and outlet λ than its larger counterpart after 9 cycles. This difference may reflect boundary effects, as the larger samples were fitted with scouring pads at both ends. These may have allowed trapped air to escape more easily during treatment, reducing the presence of occluded air bubbles and improving thermal contact between grains. In contrast, smaller samples may have retained residual air, locally reducing λ despite similar $CaCO_3$ contents.

Between 10 and 25 cycles of SB-EICP, precipitation shifted toward the outlet, reducing inlet–outlet differences and improving uniformity. However, the additional gains were smaller: λ increased by only 21% at the inlet and 45% at the outlet, compared to 534% and 409% between 0 and 10 cycles. This diminishing return likely reflects: (1) reduced pore volume available for treatment, (2) a plateau in thermal bridging efficiency after initial crystal formation, and (3) thinner or more diffuse $CaCO_3$ layers forming over larger surface areas (Tobler et al., 2012).

While the MICP sample retained high permeability, inlet clogging limited further treatment and thereby its maximum achievable thermal conductivity. In contrast, the main advantage of SB-EICP was its continued injectability, allowing higher cumulative $CaCO_3$ precipitation and more uniform thermal enhancement – an important feature for geothermal applications that require both efficient heat transfer and long-term water ingress.

5.4.3 3D $CaCO_3$ distribution across treatment strategies

If $CaCO_3$ precipitation alone were responsible for the observed reduction in hydraulic conductivity, a clearer relationship would be expected between XCT-derived density, pore connectivity, and measured K. However, the samples retain good pore

connectivity, with >98% of pore volume connected. As shown in Figure 5.3, there is no consistent correlation between XCT-derived density and measured hydraulic conductivity, suggesting that permeability is also influenced by pore-throat connectivity and unresolved organic clogging.

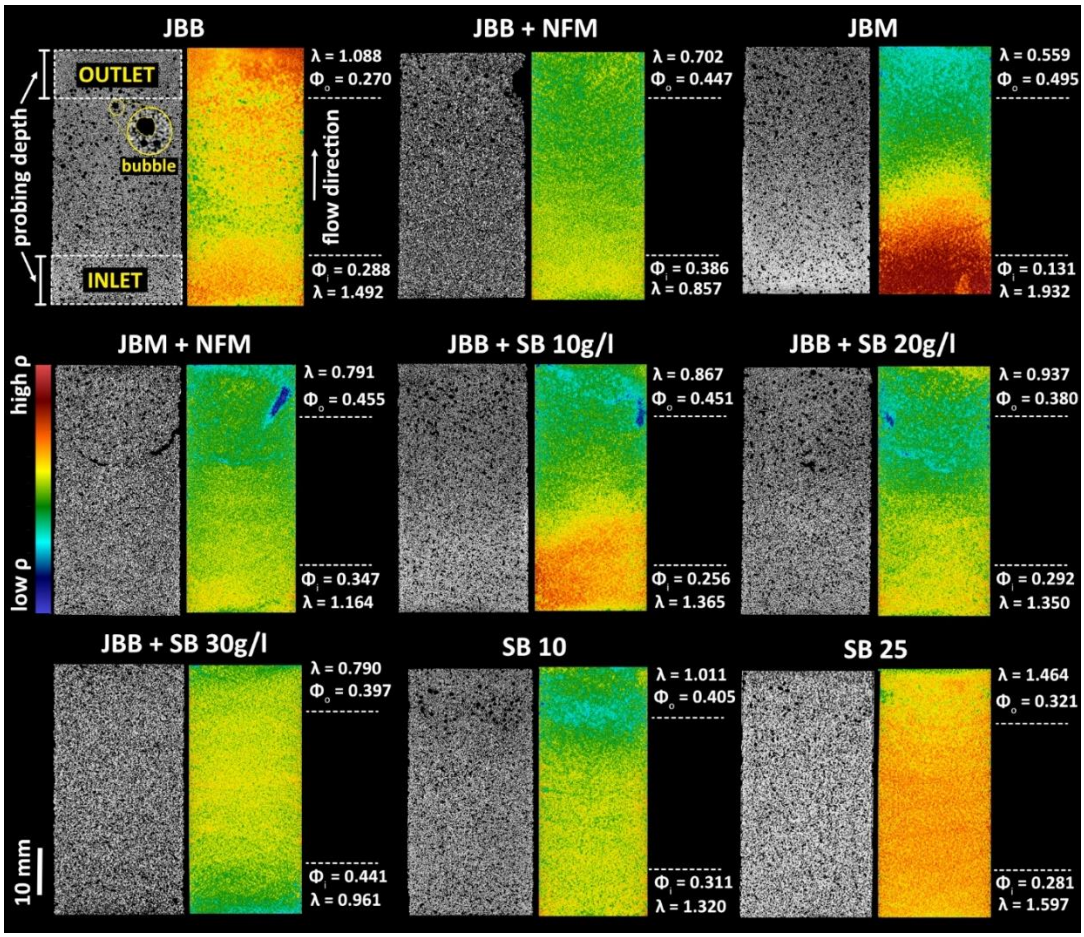

Figure 5.3 XCT-Derived Density Distributions and Their Effect on Thermal Conductivity (λ). The mean slice-by-slice density plots (coloured heatmaps) illustrate the spatial distribution of calcium carbonate precipitation across different enzyme treatments, highlighting regions of high (red) and low (blue) density. Measured λ for the inlet (bottom) and outlet (top) regions and the porosity (Φ) of the thermal probing depth (~10 mm) at both regions (Φi and Φo) are labelled for each sample. Direct comparisons of treatment uniformity and the relationship between crystal distribution and thermal conductivity are explored across enzyme mixtures. The influence of localized versus distributed precipitation on thermal conductivity enhancement is evident, with variations attributed to enzyme source and mixture. The colour scale represents relative voxel intensities from XCT segmentation (low-high) and is used to illustrate spatial variations rather than absolute density values. Bubble-rich regions, corresponding to low-density voids, are visible in some samples and have been annotated on JBB.

JBM, which shows substantial near-inlet precipitation and reduced porosity, was expected to have the lowest hydraulic conductivity. Yet it performed better than most high-organic-content samples and retained higher K than all but the MICP and SB-EICP treatments. In contrast, SB25, with the longest treatment duration and highest cumulative $CaCO_3$ content, exhibited relatively high K despite significant biocementation. This is qualitatively supported by the water-droplet infiltration behaviour shown in Supplementary Media D2. This finding is particularly notable given its high UCS (see Section 5.4.4). We therefore propose that permeability reduction in the organic-rich treatments is primarily caused by the accumulation of organic matter, such as soybean curds or milk proteins, rather than $CaCO_3$. This organic clogging is not detectable under XCT imaging conditions.

Despite higher urease activity in the hybrid SB/JB solutions (Table 5.1), these treatments did not significantly increase λ at either the inlet or outlet compared to the baseline JBB sample. To clarify these trends, Figure 5.3 presents XCT-derived density distributions alongside λ and porosity values over the ~10 mm thermal probing depth.

The steepest density gradient is observed in the JBM sample, which corresponds with its large drop in λ from inlet to outlet. Given the early crystallization and high urease activity of commercial JBM (Table 5.1), we suggest that nascent $CaCO_3$ crystals formed prematurely in suspension during injection, then filtered out at the column inlet. This is consistent with previous observations of straining effects for high activity urease solutions (Mujah et al., 2019).

Although JBB achieves one of the highest overall density profiles after 9 to 10 cycles, its thermal conductivity does not exceed that of SB10. This disparity likely reflects differences in where $CaCO_3$ precipitates within the pore structure, particularly in relation to grain contacts, which is examined further in Section 5.4.5. SB25 exhibits both higher overall density and more spatially uniform precipitation than any other EICP treatment. These improvements occur between 10 and 25 cycles and correlate with enhanced λ and a more even density distribution.

Among the hybrid mixtures, JBB + SB 30 g/L shows relatively even $CaCO_3$ distribution, but its central region, where the XCT detects higher density, likely lies outside the TPS sensor's probing depth. This could explain why λ appears lower than expected from the internal structure. Notably, high organic content in the JBB + SB

20 to 30 g/L treatments led to early clogging, limiting further injections beyond 10 cycles.

In the JBM sample, premature $CaCO_3$ formation reduces porosity at the inlet. However, this cannot explain the density profiles observed in SB-EICP, where crystallization begins only after a 3 to 4-hour lag (see Table 5.1). In these samples, air bubbles trapped during repeated treatment cycles may migrate upward, reducing local λ. These bubbles are visible in XCT scans (Fig. 5.3) and are further quantified by treatment type in Figure 5.4.

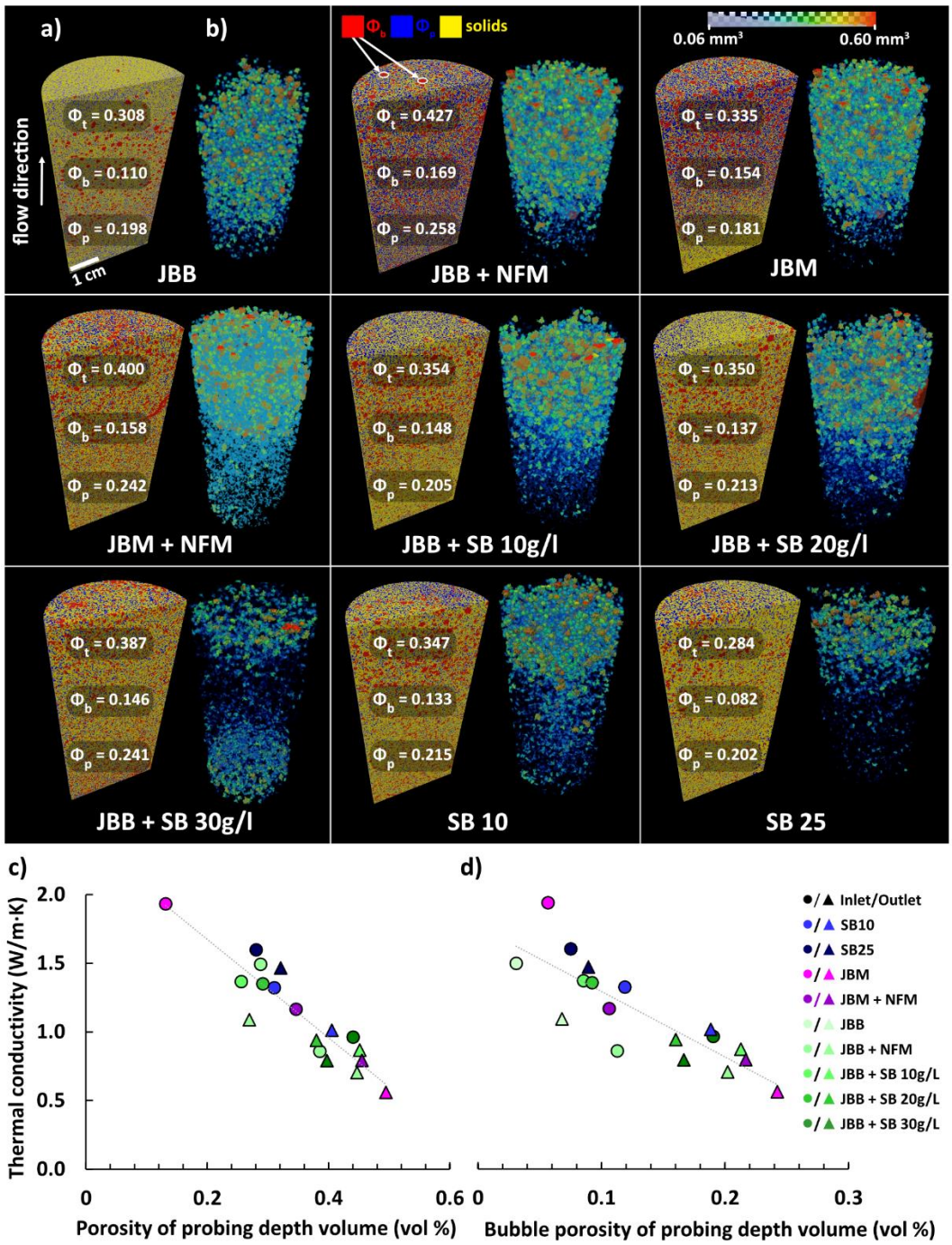

Figure 5.4 Porosity, Bubble Distribution, and Thermal Conductivity (**a**) XCT-derived renderings showing solids (yellow), bubbles (red), and remaining pores (blue) (**b**) bubble volume distribution (colored by volume, 0.06–0.60 mm³) for each enzyme mixture, illustrating spatial variations across the flow direction (**c, d**) Thermal conductivity (λ) as a function of total porosity (Φ_t) and bubble porosity (Φ_b) within the thermal probing depth (~10 mm). Inlet (●) and outlet (▲) measurements colour-coded by enzyme mixture. Points above the average trendline in (c, d) achieve greater thermal enhancement per unit of $CaCO_3$, indicating more effective crystal distribution or enhanced thermal bridging.

The origin of the gas bubbles is unclear, but three mechanisms are considered: (i) residual air trapped during initial packing of the partially saturated sand (10 wt% water), (ii) air introduced during fluid injection, and (iii) ammonia gas evolved during urea hydrolysis and the associated pH increase. Mechanisms (ii) and (iii) are less likely, as the high number of bubbles observed is inconsistent with these sources alone. Furthermore, under the neutral-to-low initial pH conditions observed in these experiments (Table 5.1), ammonia primarily exists in its ionized form (NH_4^+), rather than as gaseous ammonia (NH_3). This is due to the pH-dependent speciation of ammonia/ammonium, with ammonium (NH_4^+) dominating at pH below ~9.25 (Cui et al., 2020). The initial high permeability of the quartz sand implies that multiple flow paths were available, allowing injected fluid to bypass air-filled regions rather than displacing trapped gas (Hou & Lowengrub, 1994). This supports mechanism (i) as the most probable cause of the observed bubbles.

Bubble distribution varies between treatments. In most cases, more bubbles accumulate toward the top of the sample, likely due to buoyant migration over repeated treatment cycles. Notable exceptions include JBB + SB 30 g/L, which shows bubbles primarily at the inlet and outlet, and JBB, where bubbles appear more uniformly distributed. The likely explanation is that high organic content in JBB + SB 30 g/L caused partial clogging, restricting vertical bubble migration. In all samples, bubble-rich regions correspond closely with areas of reduced average density in XCT scans (Fig. 5.3).

As expected, thermal conductivity increases with decreasing porosity (Φp, Fig. 5.4c) and bubble porosity (Φb, Fig. 5.4d) within the sensor probing depth. Interestingly, SB-EICP samples achieve higher λ for smaller reductions in porosity, with both inlet and outlet measurements lying above the trendline in Figure 5.4c. This suggests that the crystals formed via SB-EICP are more efficient in bridging grains and enhancing thermal contact compared to those formed using jack bean-derived enzymes. These findings motivate further high-resolution imaging across additional treatment cycles to better resolve the grain-scale mechanisms responsible for this effect.

5.4.4 Strength gain depends on carbonate content and cementation uniformity

Strengthening of soil around energy piles via bio-cementation may also reduce risk of uneven settlement and failure due to soil thermomechanical behaviour (Zhang et al., 2022). Therefore, enhancing soil strength is a key consideration when evaluating MICP and EICP strategies for thermal infrastructure applications.

While thermal conductivity plateaued after ~10 cycles (Fig. 5.2e), UCS continued to increase in proportion to $CaCO_3$ content (Fig. 5.5). This distinction reflects differences in the dominant mechanisms governing thermal vs. mechanical performance. Whereas thermal conductivity depends heavily on early-stage thermal bridging and crystal connectivity, UCS benefits from cumulative $CaCO_3$ bridging and interparticle bonding throughout the treatment period.

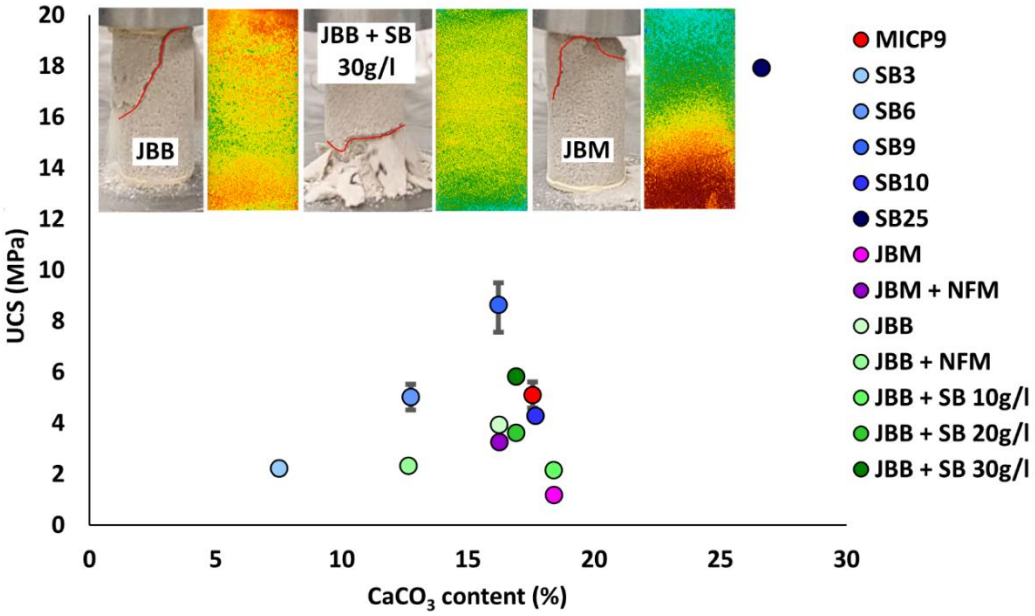

Figure 5.5 Unconfined compressive strength (UCS) as a function of $CaCO_3$ content for different enzyme mixtures. UCS values are plotted against $CaCO_3$ content for all enzyme treatments, colour-coded by enzyme mixture. Error bars account for variability due to conversion factors for non-standard height-to-diameter ratios and repeated testing for SB9 (See Appendix C). Inset images show XCT-derived density maps (right) and failure planes (left) for selected samples, illustrating variations in crack propagation influenced by crystal distribution. Notably, SB-EICP samples achieve high UCS values with relatively low $CaCO_3$ content, indicating effective pore-scale bridging and enhanced mechanical performance.

There was a clear correlation between increasing $CaCO_3$ content and UCS, as expected. However, not all samples followed the same trajectory. UCS varied significantly among medium-diameter samples with similar $CaCO_3$ contents, underscoring the importance of cementation uniformity rather than just total precipitate volume (Fig. 5.3). The strongest samples, such as JBB + SB 30 g/L (5.8 MPa after 10 cycles), exhibited a more uniform axial distribution of $CaCO_3$, while weaker samples like JBM (1.2 MPa after 10 cycles) showed large density gradients from bottom to top. A similar discrepancy was observed between large-diameter SB9 and medium-diameter SB10, where the lower UCS of the smaller sample may be explained by trapped air retained during injection (See Section 5.4.3). This effect could locally reduce effective bonding and explains the distinct failure planes seen across samples (Fig. 5.5, inset): samples tended to fail near regions where XCT analysis revealed higher bubble porosity.

These findings support earlier studies reporting that organic stabilisers, such as non-fat milk powder (NFM) (Almajed et al., 2019) and casein (Miyake et al., 2022), enhance UCS by promoting more uniform crystal growth. In our experiments, SB curds likely achieved this uniform growth through a lower initial pH (Table 5.1), which suppresses early-stage crystal formation, leading to more homogeneous precipitation. Similarly, NFM appeared to delay crystallisation (see Figure 4.1), possibly by buffering pH rise during early treatment stages, even though its buffering capacity is not directly linked to its starting pH (Table 5.1).

However, NFM addition also appeared to reduce overall precipitation efficiency. JBB + NFM yielded the lowest $CaCO_3$ content after 10 cycles, and JBM + NFM showed lower-than-expected UCS, although this may have resulted from a fracture introduced during demoulding (Fig. 5.4). In contrast, SB-EICP maintained permeability over 25 treatment cycles, enabling a $CaCO_3$ content of 26.6 wt% and achieving a UCS of 17.9 MPa – the highest value reported for EICP-treated sand to date.

5.4.5 Mechanisms of flow retention revealed by time-lapse XCT and simulation of SB-EICP

To investigate how SB-EICP retains hydraulic conductivity while achieving high strength and thermal conductivity at relatively low $CaCO_3$ content, we conducted high-resolution XCT imaging on a single sample before treatment and after 1, 2, 3, 6, and 9 injection cycles (Fig. 5.6).

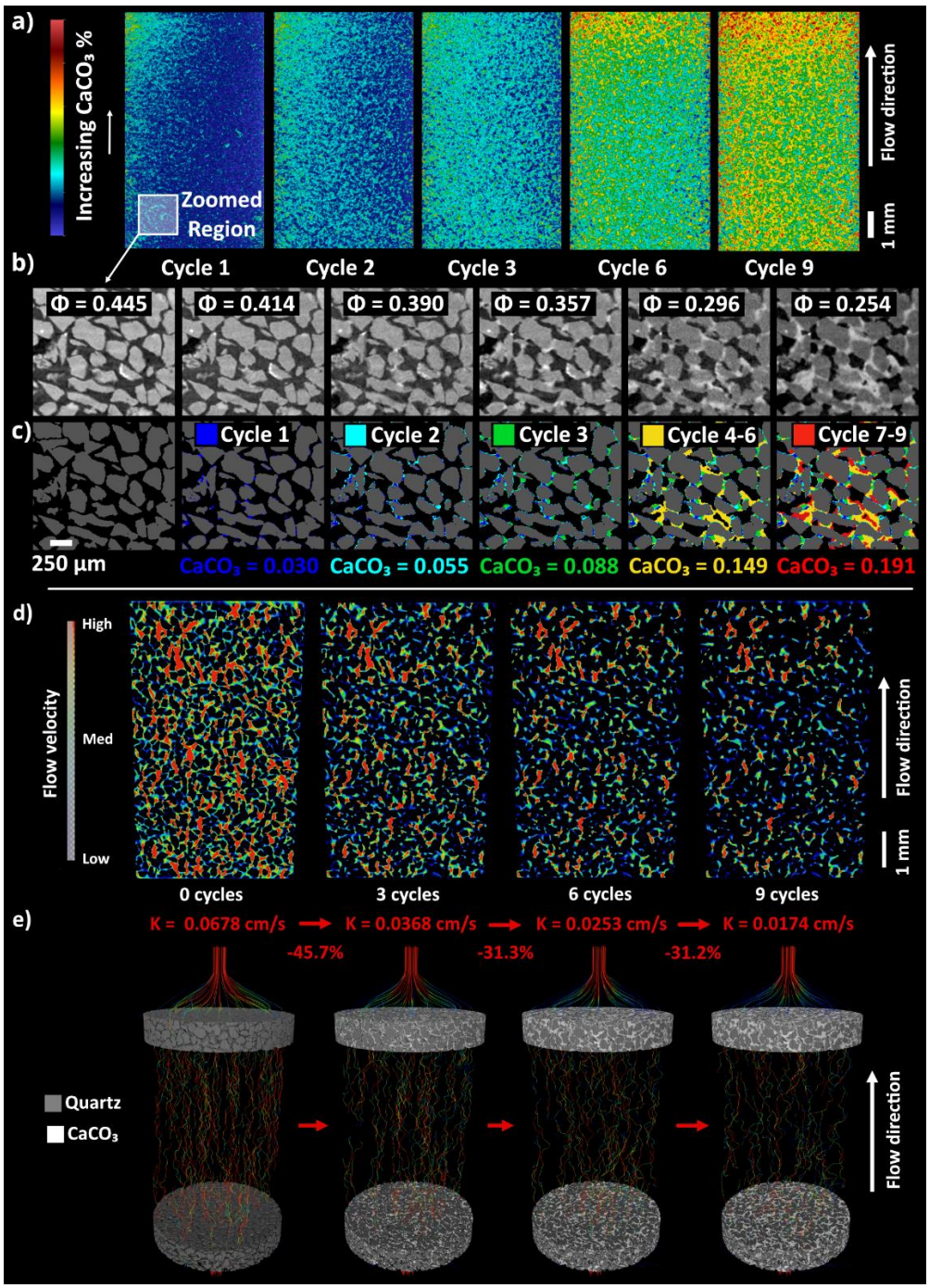

Figure 5.6 Pore-scale precipitation and flow evolution during multi-cycle SB-EICP treatment. (**a**) XCT-derived $CaCO_3$ distribution maps showing progressive carbonate accumulation with increasing treatment cycles. (**b–c**) Corresponding greyscale and segmented sub-regions illustrating pore reduction (porosity Φ) and spatial growth of $CaCO_3$ at grain contacts. (**d**) Simulated flow-velocity fields through the treated volumes under fixed-pressure boundary conditions, highlighting decreasing velocity magnitude with successive cycles. (**e**) 3D streamline visualisations linking precipitation to hydraulic conductivity (K) reduction, where $CaCO_3$ accumulation progressively confines flow to fewer connected pathways.

Unlike the larger samples, which were only partially saturated with 10 wt% water, the 6.6 mm diameter samples were fully saturated under vacuum conditions. Consequently, the upward migration of trapped gas bubbles is negligible, resulting in more uniform $CaCO_3$ precipitation throughout the sample (Fig. 5.6a). After a single treatment cycle, $CaCO_3$ primarily precipitates at grain contact points between quartz particles (Fig. 5.6b). During the first three cycles, $CaCO_3$ appears to precipitate preferentially on pre-existing crystals (Zehner et al., 2021), progressively enlarging contact areas between grains. From cycles 4–6, precipitation zones shift, likely due to evolving flow paths caused by pore blockage or redirection between treatments. These grain-bridging crystals, or 'thermal bridges', help explain the combination of high strength and enhanced thermal conductivity observed in SB-EICP-treated samples. In later cycles, precipitation may continue to concentrate on existing $CaCO_3$ along new flow paths, reinforcing this trend.

To explore the mechanism behind retained permeability in these treatments, Fig. 5.6d–e present the results of absolute permeability simulations based on the XCT datasets.

The modelled and measured hydraulic conductivity values for the untreated sand differ significantly (0.0678 cm s^{-1} vs. 0.179 cm s^{-1}, respectively), likely due to differences in segmentation thresholds and the idealized assumptions applied in the computational domain. However, the relative reductions in hydraulic conductivity across treatment cycles follow broadly similar trends, despite these differences in absolute values.

The largest decrease in simulated conductivity occurred between cycles 0 and 3 (−45.7%), closely matching the experimental reduction (−51%). Between cycles 4 and 6, the modelled reduction (−31%) was much larger than the measured value (−6%), whereas the final interval between cycles 7 and 9 showed better agreement (−31% modelled vs. −27% measured).

Although a progressive decline in flow velocity is observed with increasing $CaCO_3$ precipitation (Fig. 5.6d), this reduction is not localised. Instead, flow becomes increasingly concentrated into fewer, more tortuous paths, with continuous streamlines maintained until porosity falls significantly. This behaviour may explain the relatively high K retained in the SB25 sample (see Appendix D2). The persistence of connected pathways is further supported by the streamline visualizations derived from the simulated velocity field (Fig. 5.6e).

Discrepancies between simulated and experimental results likely arise from simplified modelling assumptions (e.g., uniform fluid properties, idealized boundary conditions) and limitations in XCT-based segmentation. In particular, small-scale pore connectivity may be underestimated in early cycles, exaggerating reductions in modelled K. Additionally, the spatial heterogeneity in $CaCO_3$ distribution observed in partially saturated samples (Fig. 5.3) differs markedly from the more homogeneous precipitation in the fully saturated micro-CT cell (Fig. 5.6), contributing to divergence between the datasets.

5.4.6 Practical implications and performance trade-offs of bio-cementation strategies

The increase in thermal conductivity observed across multiple cycles of EICP treatment (up to 781%) suggests its potential as a thermal enhancement method. However, the cost of reagents and extended treatment durations may limit practical use in energy pile foundations. While the marginal thermal gain between 10 and 25 SB-EICP cycles (~21%) may not justify extended treatment for thermal purposes alone, the associated strength gain does. Achieving a UCS of 17.9 MPa after 25 cycles – a value comparable to structural concrete and unprecedented for biocemented sand – SB-EICP demonstrates promise as a low-carbon alternative to conventional construction materials, provided that scalable and sustainable feedstocks can be secured (Alotaibi et al., 2022).

The retention of hydraulic conductivity in SB-EICP-treated samples, even after 25 treatment cycles, distinguishes it from MICP, where inlet clogging hindered further treatment. SB-EICP's continued injectability supports ongoing water ingress, enabling both convective heat transfer and further strengthening, which is particularly advantageous for geothermal or subsurface energy systems. This retained hydraulic conductivity may also benefit infrastructure applications where simultaneous soil stabilization and fluid flow are required, such as stabilizing soils around underground infrastructure while still allowing fluid injection for maintenance or carbon sequestration.

In the context of CO_2 geosequestration, SB-EICP offers a degree of permeability control that can help improve sweep efficiency. While more aggressive permeability reduction could be achieved using uncoagulated curds or MICP, these strategies may rely on biofilm formation (Nemati et al., 2005) which is less durable over long timescales. A more permanent solution may be achieved by reducing the organic load

of SB-EICP solutions, as indicated by OD600 values below 0.4, enabling the maintenance of stable hydraulic conductivity after treatment.

XCT analysis provides critical insight into the internal structure of SB-EICP-treated sand. Rather than widespread pore blocking, SB-EICP induces highly localized $CaCO_3$ formation at grain contacts – forming thermal bridges that enhance both strength and λ. This spatial selectivity explains how high mechanical and thermal performance can be achieved without compromising fluid flow.

However, it is important to acknowledge that the present study was conducted on laboratory-scale quartz sand under controlled injection and saturation conditions. To fully assess SB-EICP's broader feasibility, further work should evaluate its performance in field soils with greater textural and mineralogical variability, as well as under partial saturation conditions. Future injection strategies should be tailored for heterogeneous, real-world conditions, informed by field-scale modelling to ensure uniformity and scalability. Ultimately, long-term field trials and life-cycle assessments will be essential to validate performance and quantify environmental benefits under operational conditions.

5.5 Conclusions

In this study, EICP and MICP treatment strategies were experimentally optimized to enhance unconfined compressive strength and thermal conductivity while retaining hydraulic conductivity. The main conclusions are summarized below:

1. SB-EICP treatments achieved unconfined compressive strengths up to 17.9 MPa – surpassing previous EICP studies and approaching structural-grade performance. This highlights its potential as a low-carbon alternative to cement in masonry or prefabricated construction materials.
2. Thermal conductivity increased by over 600% after 25 SB-EICP cycles, with uniform improvement across the sample. This makes SB-EICP well-suited for geothermal systems, energy piles, and subsurface thermal management applications.
3. Unlike conventional EICP approaches prone to pore blockage, SB-EICP maintained hydraulic conductivity even at high treatment levels. In contrast, MICP samples experienced inlet clogging after nine cycles, limiting further strengthening and thermal enhancement. This highlights SB-EICP's

advantage in enabling repeated fluid injection and sustained convective heat transfer over time.

4. XCT imaging revealed that $CaCO_3$ precipitation was localized at grain contacts, enhancing mechanical and thermal performance without compromising pore connectivity. This spatial pattern supports the development of more accurate predictive models for bio-cemented media.

Overall, SB-EICP emerges as a promising biocementation technology, capable of delivering consistent strength and thermal improvements without compromising fluid flow – an essential combination for subsurface energy and infrastructure applications. Compared to MICP, SB-EICP also benefits from simpler injection protocols and greater resistance to inlet blockage, reinforcing its potential for scalable deployment. The potential for low-cost enzyme sourcing, repeated treatment feasibility, and compatibility with non-sterile workflows further strengthen SB-EICP's attractiveness for field deployment, particularly in sustainability-focused or resource-constrained scenarios.

Supporting Information

Appendix D2: Water droplets on SB25 sample to demonstrate absorbance/ permeability.

Data Availability Statement:

The data and analysis supporting the findings of this study are available from DOI: 10.5281/zenodo.15720206

Corresponding Author

Philip J. Salter Philip.salter@strath.ac.uk Department of Civil & Environmental Engineering, University of Strathclyde, James Weir Building, 75 Montrose Street, Glasgow, G1 1XJ

Acknowledgment

The data acquisition and analysis were supported by NERC NE/T00908X/1 and EPSRC EP/T023198/1. PS is supported by the Centre for Doctoral Training (CDT) in Geoscience and the Low Carbon Energy Transition, and KJD was supported by NE/M018687/2.6.6

5.6 Optimizing thermal performance and cost efficiency in EICP-treated materials

Beyond improving thermal conductivity, the volumetric heat capacity of ICP-treated materials also plays a crucial role in determining their suitability for energy storage applications. As $CaCO_3$ precipitation replaces pore space, its impact on heat retention capacity must be considered, particularly for applications where both conductivity and volumetric heat capacity are important factors.

5.6.1 Volumetric heat capacity & thermal conductivity relationship

While the specific heat capacity of all ICP-treated materials was not directly measured in this study, it can be estimated from $CaCO_3$ content using XCT data (Section 5.4.5). Unlike traditional cementation, where bulk material replacement occurs, $CaCO_3$ precipitation primarily fills pore space, replacing air rather than quartz grains. In untreated samples, the composition is 55.5 vol% quartz and 44.5 vol% air, whereas in a 9-cycle treated sample, $CaCO_3$ occupies 19.1% of the total volume, reducing air content to 25.4%. Since $CaCO_3$ has a higher volumetric heat capacity (~2.34e+06 $J/m^3 \cdot K$) than air (~0.001 $J/m^3 \cdot K$), this improves overall heat storage capacity. Furthermore, retaining permeability allows air-filled pores to become saturated with water, which has an even higher volumetric heat capacity (~4.17e+06 $J/m^3 \cdot K$). However, as $CaCO_3$ replaces pore water, there is a trade-off between increased thermal conductivity and reduced saturated heat capacity (Fig. 5.7), which should be considered when designing ICP treatment strategies.

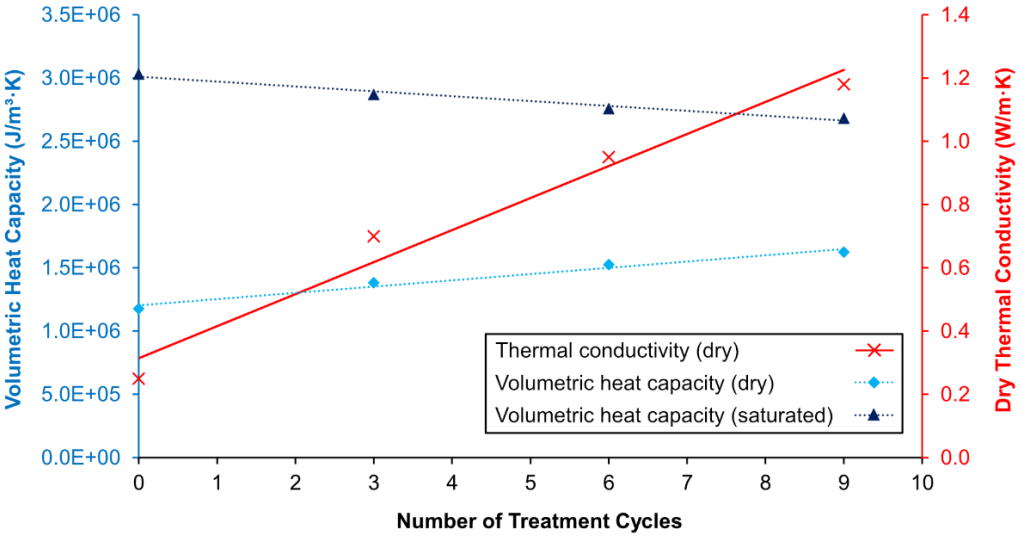

Component	Specific Heat (Jkg·K)	Density (kg m^{-3})	Volumetric heat capacity (J m^{-3}·K)
Quartz	799	2650	2.12e+06
$CaCO_3$	834	2810	2.34e+06
Air	1000	1.293	1293
Water	4184	998	4.17e+06

Figure 5.7 Relationship between volumetric heat capacity and thermal conductivity with increasing soybean EICP treatment cycles Volumetric heat capacity is estimated based on the volume fractions of $CaCO_3$ and air derived from XCT imaging (Section 5.4.5). The thermal conductivity values represent the average of inlet and outlet measurements from larger cylindrical samples (Section 5.4.2). As treatment cycles progress, increased $CaCO_3$ precipitation enhances thermal conductivity, while volumetric heat capacity trends differ depending on saturation state. The unsaturated volumetric heat capacity (diamonds) increases with additional $CaCO_3$ precipitation, as air is replaced with a solid phase. However, the saturated volumetric heat capacity (triangles) remains relatively stable, as replacing water with $CaCO_3$ reduces the overall heat capacity of the system. Thermal conductivity (red markers) shows a near-linear increase with additional treatment cycles, reflecting enhanced grain contact and reduced thermal resistance.

5.6.2 Cost-benefit analysis of EICP for thermal enhancement

As porosity decreases with additional treatment cycles, the optimal injection volume per cycle decreases, reducing reagent requirements. However, thermal conductivity improvements exhibit diminishing returns beyond 9–10 cycles, with only a ~21% increase between cycles 10 and 25 (Fig. 5.2e). While additional cycles may be necessary for applications requiring higher mechanical strength, the cost-benefit trade-off suggests that fewer cycles may be preferable when thermal improvement is the primary goal. In cases such as borehole heat exchangers and engineered backfills, an optimized number of EICP treatments can provide sufficient thermal enhancement without unnecessary material use or processing time.

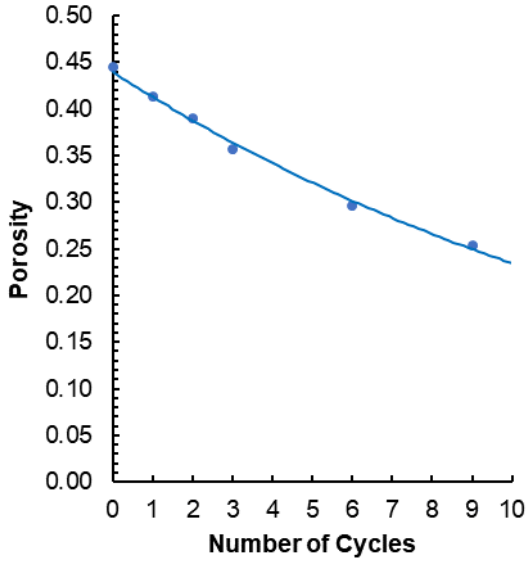

Figure 5.8 Reduction in porosity as a function of EICP treatment cycles, based on XCT data. This decreasing pore space influences the optimal injection volume per cycle, reducing reagent requirements as treatment progresses.

While the porosity of the quartz sand used in this study starts off high (~44.5%), repeated soybean EICP cycles progressively reduce pore space (Fig. 5.8). This directly influences the volume of treatment solution required per cycle, affecting both material efficiency and practical implementation at scale.

For applications such as engineered thermal backfill, where cost-effectiveness is a key factor alongside performance, it is important to assess whether soybean EICP can compete with conventional materials. One widely used alternative, fluidized thermal backfill (FTB), offers a thermal conductivity of 1.54 W/m·K at a cost of ~$131/m³ (Ocłoń, 2021). To determine how soybean EICP compares, we calculate the injection volume per cycle based on the XCT-derived porosity shown in Figure 5.6 and estimate the corresponding material costs (Table. 5.3) per cubic metre in Table 5.4.

Table 5.3 Cost of raw materials used in soybean EICP treatment.

Raw material	Unit Price ($/kg)	Content (g/L)	Cost ($/L)
Urea	0.320	60	0.01920
Calcium Chloride	0.230	111	0.02553
Soya beans	0.455	50	0.02275
Gypsum	0.130	5	0.00065

Raw material costs are based on reported market prices: Urea (Business Analytiq, 2024), $CaCl_2$ (IMARC Group, 2024), Soybeans (Statista, 2024b), and Gypsum (Statista, 2024a). Prices reflect global averages and may vary by region and supplier.

Table 5.4 Estimated cost per cubic metre of biocemented soil for different numbers of EICP cycles, alongside thermal conductivity and UCS performance.

Number of cycles	Total cost per m^3 ($)	Thermal conductivity (W/m·K)	UCS (MPa)
3	109	0.70	2.22
6	174	0.95	5.02
9	228	1.18	7.56

Injection volumes are optimised to 1 pore volume per cycle based on observed porosity reductions (Fig. 5.6). Thermal conductivity values represent the average between inlet and outlet measurements. Thermal conductivity measurements were carried out dry and therefore represent the minimum value across all environmental conditions.

Soybean EICP is more expensive per cubic metre than cement-based thermal backfill materials such as FTB (Table 5.4), which provides a higher thermal conductivity (1.54 W/m·K) at a lower cost (~$131/m³). However, unlike cement-based materials, EICP can retain permeability, making it a viable option for applications requiring controlled fluid flow rather than complete hydraulic isolation. These cost estimates assume that excavated soil from high-voltage cable trenches is reused as backfill, with the quartz sand used in this study serving as an analogue. However, variations in initial porosity, compression and moisture content may influence final cost projections.

A major advantage of EICP over conventional thermal backfills is its ability to modify *in situ* soils without requiring complete excavation and replacement. This eliminates

the need for large-scale material transport and site disruption while enabling simultaneous permeability control and thermal enhancement. Such an approach could be particularly beneficial in high-voltage transmission corridors, where excavation restrictions and logistical constraints often limit the feasibility of bulk material replacement.

Although thermal conductivity measurements (Section 5.4.2) were conducted under dry conditions, EICP-treated soils are expected to demonstrate even greater thermal conductivities in partially saturated states. Based on previous studies of MICP-treated sands (Z. Wang et al., 2022), the thermal conductivity of EICP-treated materials under >50% saturation could be estimated in the range of 2.0–2.5 W/m·K, substantially higher than FTB. This suggests that EICP could offer competitive performance while preserving permeability for controlled drainage and convective heat dissipation where required. However, it should be noted that high-voltage power cables often reach temperatures of ~80°C, which would promote evaporation within the backfill.

While the cost of key reagents (urea and $CaCl_2$) is unlikely to decrease significantly, alternative low-cost enzyme sources could improve economic feasibility. Recent studies have explored soybean hulls as a crude urease source, offering a cheaper alternative to dried soybeans with comparable precipitation efficiency (Kai. Xu et al., 2023). Additionally, recycling bio-cementation effluent for ammonia recovery offers a potential strategy for improving economic feasibility. Other approaches, such as using animal urine as a urea source (Comadran-Casas et al., 2022), have been suggested, though these raise scalability and health and safety challenges.

5.6.3 Integrating pore-scale control with material performance

Although the experiments presented in this chapter focus on material-scale performance rather than injection dynamics or field-scale deployment, they provide a critical bridge between pore-scale control and functional engineering outcomes. Combining time-lapse XCT with hydraulic, thermal, and mechanical testing, demonstrates that the precipitation pathways identified in earlier chapters translate directly into measurable differences in strength gain, permeability retention, and thermal enhancement. In doing so, it resolves Critical Challenge 1 by linking pore-scale $CaCO_3$ localisation to macroscopic behaviour, and Critical Challenge 2 by showing that crude, soybean-derived enzyme systems can deliver scalable, high-

performance outcomes when precipitation timing and organic content are appropriately controlled.

The results further address Critical Challenge 4 by demonstrating that permeability modification in EICP-treated media is governed less by total $CaCO_3$ content than by how and where carbonate accumulates within the pore network. In particular, the ability of soybean EICP to form grain-bridging crystals while preserving connected flow pathways explains how high strength and thermal conductivity can be achieved without full loss of permeability – a limitation observed in microbial systems under comparable conditions.

Finally, by quantifying the trade-offs between thermal conductivity, volumetric heat capacity, permeability, and treatment cost, this chapter defines the practical performance envelope within which biocementation strategies must operate. These findings set clear constraints on what biochemical and microstructural control can achieve alone, motivating the next stage of the thesis: the introduction of functional additives and tighter pore structures to further tailor thermal behaviour.

Chapter 6: From conductivity to storage: multifunctional bio-cemented composites with graphite and paraffin additives

While Chapter 5 (Salter, Minto, & Dobson, 2025) showed that repeated EICP treatments can improve both strength and thermal conductivity, the achievable gains are ultimately constrained by the intrinsic thermal properties of $CaCO_3$ and by the practical cost of multiple treatment cycles (Section 5.6.2). Chapter 6 therefore tests a complementary route: introducing conductive and phase-change additives and using bio-cementation to stabilise them within the granular matrix.

Expanded graphite (EG) is investigated as a means of forming conductive networks, and paraffin-infused EG is assessed for latent heat storage. Together, anisotropic conduction and latent heat storage allow thermal behaviour to be engineered rather than merely increased, by shaping both the direction and timing of heat transfer. These composites extend MICP and soybean EICP from soil stabilisation toward thermally engineered media with enhanced heat transfer and controllable heat storage.

Author Affiliations:

Philip J. Salter[1*], James Minto[1], Katherine J. Dobson[1]

[1] Department of Civil & Environmental Engineering, University of Strathclyde, James Weir Building, 75 Montrose Street, Glasgow, G1 1XJ, UK

*Corresponding author: Philip J. Salter: Philip.salter@strath.ac.uk

Author Contributions

PS: Conceptualization, Data Acquisition, Methodology, Analysis, lead on all stages of MS preparation.

JM: Funding, Supervision, MS preparation.

KD: Project design & funding, Analysis, Supervision, MS preparation.

6.1 Abstract

Improving ground thermal performance often requires replacing native soil with engineered backfill, a process that is costly, disruptive, and carbon intensive. This study explores an alternative strategy: modifying in situ soils with expanded graphite (EG) and paraffin-infused EG, combined with bio-cementation to lock additives in place and create thermally engineered composites. Isotropic thermal conductivity (λ) increased by up to 753% with 5 wt% EG, while lower contents produced strong anisotropy, with radial thermal conductivity rising by 956% compared to untreated dry quartz sand. Higher EG contents yielded more isotropic behaviour. These trends are consistent with shifts in $CaCO_3$ precipitation pathways: at low EG, quartz-$CaCO_3$-quartz bonding dominates, whereas at higher EG, thermal transport relies on direct EG connectivity. Incorporating paraffin introduced latent heat storage, with infrared thermography revealing a phase change plateau and extended cooling, demonstrating effective energy buffering without leakage. These results establish the potential for bio-cemented materials to function as thermally engineered composites rather than solely structural or hydraulic modifiers. By integrating conductive and phase-change additives, such systems achieve multifunctionality, combining enhanced conduction with thermal energy storage, and open new directions for bio-cementation in energy, infrastructure, and climate-resilient applications.

6.2 Background

Improving the thermal performance of the ground is often achieved by excavating and replacing native soil with engineered backfill materials designed for high thermal conductivity (Czapp & Ratkowski, 2021; H. Javadi et al., 2018). Such approaches are widely used in geothermal boreholes, cable backfills and shallow horizontal trench systems, where engineered mixtures of sand (Salhein et al., 2024), bentonite (Ahmed et al., 2022), or cementitious materials (Wu et al., 2024), often supplemented with conductive additives, enhance heat transfer around buried exchangers (e.g., energy piles or slinky-type coils). However, this replacement process is costly, logistically disruptive, and associated with significant carbon emissions from material production and transport (Chongxi & Zhang, 2024). These challenges limit the scalability of engineered backfills and motivate the search for alternative strategies that can reuse excavated soil in situ, reducing the need for material import and replacement.

Bio-cementation via microbial (MICP) and enzyme-induced carbonate precipitation (EICP) has been shown to improve both thermal and mechanical properties of soils while minimising environmental impact (Martinez et al., 2019; Rajasekar et al., 2017; Wang et al., 2024). Unlike conventional ground-improvement methods that rely on chemical grouts or energy-intensive processing, these techniques utilise urease enzymes to catalyse urea hydrolysis and drive calcium carbonate ($CaCO_3$) precipitation at grain contacts. Reaction pathways are detailed in Chapter 2; here, the focus is on combining precipitation with conductive additives to extend functional performance.

While repeated cycles of bio-cementation increase soil thermal conductivity (Chapter 5), the gains diminish at higher cycle numbers and precipitation alone cannot provide directional heat transfer or latent heat storage. Directional heat transfer (anisotropic thermal conductivity) matters because heat commonly moves between a source and a sink along a preferred path; increasing conductivity in that direction can raise the useful heat flux while reducing sideways spreading. This limits the potential of untreated MICP/EICP for advanced applications such as energy storage, transient heat buffering, or engineered heat sinks.

Recent studies have explored the incorporation of thermally conductive additives, such as steel fibres and carbon-based materials, to enhance bio-cemented soils (Cheng et al., 2021; Li et al., 2023). Steel fibres have proven unsuitable under the saline conditions of MICP treatment, where corrosion produced iron oxides less conductive than quartz. In contrast, carbon-based additives such as EG may offer superior conductivity and chemical stability, making them attractive for long-term soil modification.

EG is a lightweight carbon material produced through the intercalation and rapid thermal expansion of natural graphite flakes. Its vermicular structure exhibits high thermal and electrical conductivity (Murugan et al., 2021), and anisotropic heat transfer behaviour when compressed (Cermak et al., 2020). Its exceptionally low density (~6 g/L) enables incorporation at low weight percentages, enhancing conductivity while maintaining a lightweight mixture and minimising costs. Additionally, its extreme oil absorbency (Caniani et al., 2018) allows for integration with “shape-stabilized” PCMs, enabling thermal energy storage applications (Xie et al., 2021).

PCMs store and release heat through latent enthalpy during melting and solidification. Compared with sensible heat storage (e.g., heating water), this allows substantially larger energy exchange over a narrow temperature range, smoothing temperature swings and increasing heat-storage capacity without needing a large volume of material. Because the phase-transition temperature can be selected by chemistry, PCMs enable thermal behaviour to be tuned to a target operating window. However, most PCMs have low thermal conductivity and can suffer from leakage during melting, motivating “shape-stabilised” composites where the PCM is retained within a porous conductive scaffold such as expanded graphite.

Paraffin wax, a cost-effective PCM with a melting range of 40–60 °C, was selected for infusion into EG. This combination offers dual functionality: improved conductivity and latent heat storage. Such composites can buffer temperature swings while also improving heat transfer. Despite these promising attributes, the interaction of carbon-based additives with carbonate precipitation, and their influence on microstructural development, remains underexplored.

Our study evaluates the thermal and functional performance of bio-cemented quartz sand modified with EG and paraffin-infused EG (PI-EG). By combining XCT with thermal conductivity measurements and infrared thermography, additive distribution and microstructural change are related to bulk performance to identify formulations that improve both heat transfer and heat storage.

6.3 Materials & Methods

6.3.1 Aggregate Mixtures

Quartz sand, graphite flake (GF), milled carbon fibre (CF), EG and PI-EG were used (Table 6.1). EG was produced by microwave expansion of nitric-acid-intercalated graphite (400 W, 50 s), yielding a bulk density of ~6.3 g L^{-1} (≈1:96 expansion). PI-EG was prepared by infusing molten paraffin (~90 °C) into EG on a hot plate at a 9:1 paraffin:EG mass ratio until fully absorbed (Fig. 6.1).

Table 6.1 Properties and preparation of aggregate materials

Material	Source	Properties	Preparation Method
Quartz sand	Sigma Aldrich	Particle size: 210–297 µm	Used as received.
Graphite flake	ProGraphiteShop	70% over 500 µm grain size	Used as received.
Milled carbon fibre	Easy Composites	Diameter: 7 µm, Length: 100 µm	Used as received.
Expandable graphite	ProGraphiteShop	Pre-treated with nitric acid to weaken interlayer bonds	Expanded via microwave irradiation (400W, 50 s) to achieve a 1:96 expansion ratio and ~6.3 g/L density (Fig. 6.1a).
Paraffin-infused expanded graphite	Impact Test Equipment and ProGraphiteShop	Paraffin wax: weight ratio of 9:1	Molten paraffin wax (~90°C) fully absorbed into expanded graphite; stored after cooling (Fig. 6.1b).

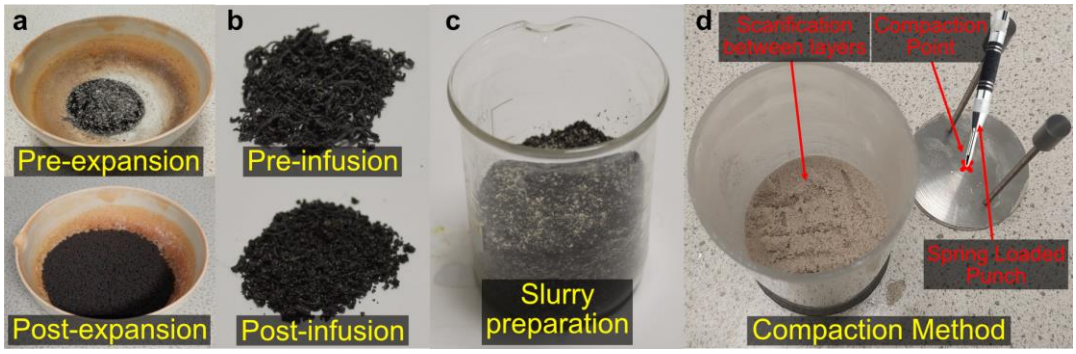

Figure 6.1 Aggregate preparation and sample assembly (**a**) Pre-expansion and post-expansion stages of expandable graphite (**b**) Pre-infusion and post-infusion stages of PI-EG. (**c**) preparation of bio-slurries by mixing sand with thermal additives and liquid components (bacterial solution for MICP or enzyme solution for EICP). (**d**) compaction method, showing a cross-section of the compacted sand with scarified layers and the spring-loaded punch used to compact each layer.

6.3.2 MICP and EICP solutions

The ureolytic bacterium *Sporosarcina pasteurii* (DSMZ, DSM No. 33) was cultured for 24 h in a nutrient medium containing 5.5 g L^{-1} yeast extract, 5 g L^{-1} NaCl, 0.4 g L^{-1} K_2HPO_4, 0.4 g L^{-1} D-glucose, 20 g L^{-1} urea, and 5 µM $NiCl_2$ under aerobic conditions. Cultures were centrifuged (6000 rpm, 8 min), the pellets resuspended in tap water, and bacterial suspension (BS) concentration quantified via optical density at 600 nm (OD600). The suspension was diluted to an OD600 of approximately 1 prior to

injection. The MICP cementing solution (MICP-CS) comprised 1.0 M urea and 1.0 M $CaCl_2$ in deionised water (≈ 18 MΩ·cm).

Soybean enzyme solution (ES) was prepared by grinding dried soybeans (<212 µm) and stirring the powder in deionised water (100 g L^{-1}, 30 min). The mixture was rested for 1 h to allow curd coagulation, after which 10 g L^{-1} calcium sulphate dihydrate was added and stirred for 5 min. Following a further 1 h settling period, the suspension was centrifuged (6000 rpm, 8 min) and the supernatant filtered (<1 µm) to yield the final ES. The EICP cementing solution (EICP-CS) was prepared at double strength (2.0 M urea + 2.0 M $CaCl_2$ in deionised water). Immediately prior to injection, it was combined volumetrically 1:1 with the enzyme solution, giving an injected mixture of 1.0 M urea and 1.0 M $CaCl_2$. This ensured the same in-column reagent concentrations as the MICP cementing solution delivered after bacterial injection. The ureolytic activity was measured each day using the conductivity method (Whiffin et al., 2007) yielding mean activities of 4.0 mmol min^{-1} for the BS and 3.4 mmol min^{-1} for the ES.

6.3.3 Sample Assembly

For all experiments, the liquid component, BS for MICP or ES for EICP, was first mixed with quartz sand to minimise clumping of thermal additives such as milled carbon fibre or expanded graphite. The slurry water content was fixed at ~13 wt%, based on quartz sand properties, and applied consistently across all samples. Thermal additives were incorporated in the proportions listed in Table 6.2. Percentages refer to the mass fraction relative to sand (e.g. 5 wt% additive = 95 wt% sand + 5 wt% additive) and exclude liquid content. Each mixture was manually blended for 10 minutes to ensure homogeneous distribution.

Table 6.2 Composition of slurries

Sample ID	Graphite Flake (%)	Milled Carbon Fibre (%)	Expanded graphite (%)	Paraffin Infused Graphite (%)	Treatment Type	Slurry solution
Experiment Set 1: Preliminary tests						
MICP Sand	0	0	0	0	MICP	BS
MICP GF5	5	-	-	-	MICP	BS
MICP CF5	-	5	-	-	MICP	BS
MICP EG5	-	-	5	-	MICP	BS
Experiment set 2: Expanded graphite						
MICP EG2	-	-	2	-	MICP	BS
MICP EG3	-	-	3	-	MICP	BS
MICP EG4	-	-	4	-	MICP	BS
Experiment set 3: EICP and phase change materials						
EICP Sand	0	0	0	0	EICP	ES
EICP EG4	-	-	4	-	EICP	ES
EICP PI-EG29	-	-	-	29.4[1]	EICP	ES

[1]*volumetric content of expanded graphite matched to EICP EG4*

For EICP PI-EG29, paraffin-infused expanded graphite was prepared by blending 8 g of expanded graphite with 72 g of paraffin wax (9:1 ratio). The infused material was then mixed with 192 g of sand to match the volumetric EG content of EICP EG4. Control samples containing only sand (no additives) were also prepared as MICP and EICP baselines.

The mixtures were packed into acrylic tubes (⌀ 60 mm, length 125 mm) for bio-cementation. To minimise compression effects on thermal conductivity, particularly with EG (Cermak et al., 2020), a rubber stopper was fixed at the tube base and each column was compacted in 10 layers, with 20 spring-loaded punches per layer (~100 N per punch; Fig. 6.1d). Layer surfaces were scarified to promote bonding between layers and reduce stratification, with packing uniformity later confirmed by XCT. The full sample preparation and packing workflow, including slurry preparation routes and staged compaction, is summarised in Fig. 6.2. After compaction, a second rubber stopper was fitted at the tube top to prevent movement during injection.

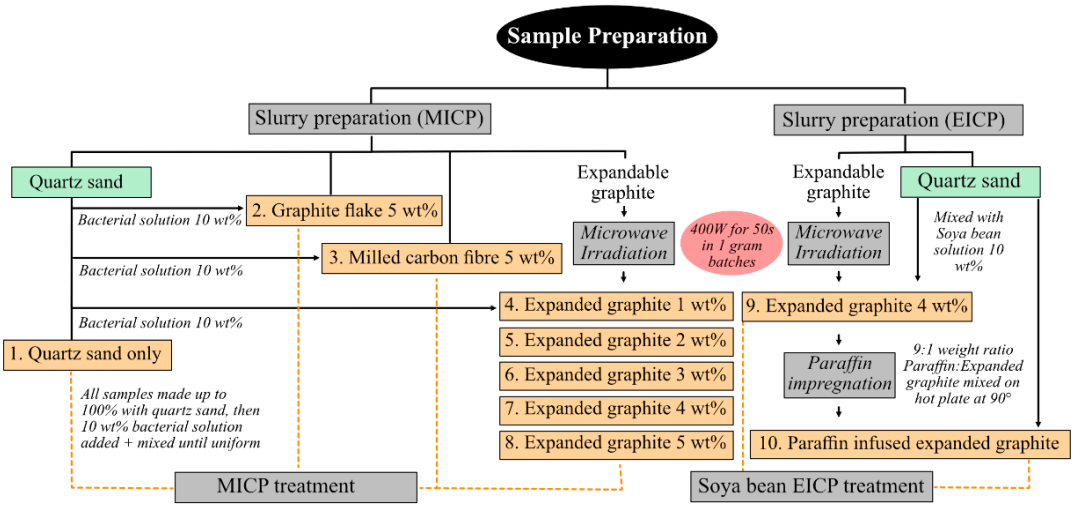

Figure 6.2 Sample preparation workflow for additive-containing biocemented sand specimens. The schematic summarises slurry preparation routes for MICP and soya bean EICP systems, including incorporation of conductive and phase-change additives, followed by staged placement and compaction. Layer scarification and controlled compaction were used to promote inter-layer bonding and reduce preferential flow or additive segregation during subsequent treatment cycles.

6.3.4 Treatment Protocol

For all but the first cycle, where bacteria were already present in the slurry, each MICP sample received 140 mL of bacterial suspension at 35 mL/min (~1.1 pore volumes, PV). This was followed by a 1-hour pause to allow bacterial adhesion. To prevent inlet clogging between cycles (Minto et al., 2017), 5 mL of tap water was flushed through at the same rate. Next, 140 mL of MICP-CS was injected at 35 mL/min, after which the sample was left undisturbed for 24 hours for $CaCO_3$ precipitation. This cycle was repeated nine times (Fig. 6.3).

For EICP treatments, 70 mL of ES was mixed with 70 mL of EICP-CS, immediately injected at 35 mL/min, and then left to react for 24 hours. This was also repeated for nine cycles.

After the final treatment cycle, each sample was flushed with ~10 pore volumes of deionised water (specific resistance <18 Ω) and oven-dried at 50 °C for 72 h, or until stable weight was achieved, representing full desaturation.

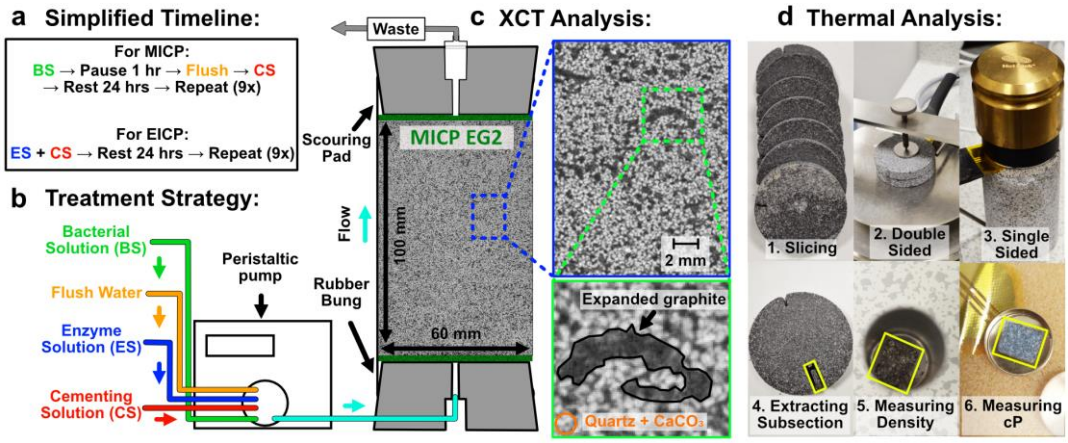

Figure 6.3 Treatment setup, timeline, XCT analysis, and thermal workflow. (**a**) 9-cycle protocol for MICP (BS → Pause → Flush → CS → Rest) and EICP (ES + CS → Rest). (**b**) Schematic of the treatment setup with reservoirs for BS, CS, ES, and flush water connected via peristaltic pump to the packed sand column; flow direction, volumes (140 mL BS/CS (1 M), 140 mL ES+CS (2 M), ~5 mL flush), and injection rate (35 mL/min) are shown; effluent exits to waste. (**c**) Vertical XCT slice of a treated column (S4: 2% EG), highlighting internal structure and additive distribution; zoom shows expanded graphite (black) and quartz grains with $CaCO_3$ (orange). (**d**) Thermal workflow: (1) Slice column into six segments; (2) measure double-sided thermal conductivity; (3) single-sided measurements on intact samples; (4) extract subsection for (5) density via helium pycnometer; and (6) volumetric heat capacity via Hot Disk gold-cup sensor.

6.3.5 Microstructural analysis using XCT

XCT was used to inspect the 3D internal structure of all samples. Data were collected on a Nikon XT H 225 scanner (University of Strathclyde) under the conditions in Table 6.3. Due to the height-diameter ratio, two scans were acquired per sample and reconstructed using the Nikon standard algorithm. Scan settings were chosen to achieve at least ~30% transmission through the sample centre, with a maximum exposure time of 4000 ms. Accelerating voltage was adjusted to maximize transmission, but filament demand meant higher voltages did not always yield more counts. Consequently, transmission optimisation was prioritised over minimising voltage.

Table 6.3 X-ray acquisition settings

Sample ID	Accelerating Voltage (kV)	Current (µA)	Projections	Exposure time (ms)	Voxel Resolution (µm)	Copper Filter (mm)
MICP Sand	105	123	3141	2s	37	0.1
MICP GF5	105	121	3141	2s	42	0.25
MICP CF5	130	98	3141	1s	42	0.25
MICP EG5	-	-	-	-	-	-
MICP EG2	110	115	3141	1.42s	42	0.1
MICP EG3	95	134	3141	2s	42	0.1
MICP EG4	95	134	3141	2s	42	0.1
EICP Sand	170	71	3141	4s	37	0.1
EICP EG4	130	98	3141	1s	42	0.25
EICP PI-EG29	130	98	3141	1s	42	0.25

The two scans were registered, resampled, and merged to produce a single composite volume. Datasets were cropped to remove the holder and artifacts. Using the Auto Thresholding module in Avizo (Otsu, 1979) dense solids – quartz sand and precipitated $CaCO_3$ – were segmented from porosity and low-density additives.

To visualise dense solid distribution, segmented volumes were exported as 2D TIFF stacks and processed in ImageJ. Pixels outside the cylindrical boundaries were masked as “not-a-number.” Data were re-sliced, rotated 90°, and averaged along the depth axis using the Z-project function. Final heat maps were rendered in ParaView to highlight density variations along the inlet–outlet axis.

For consistency, greyscale histograms were normalised between sample types using the Match Contrast module, with MICP EG4 as the reference. Dense solids segmented for Figure 6.4 were inverted to yield pore space, which was then applied as a mask to the contrast-matched images.

At the voxel resolutions required to image the full diameter of specimens suitable for bulk thermal conductivity and infrared measurements, individual $CaCO_3$ precipitates could not be reliably resolved or distinguished from quartz due to partial volume effects and limited phase contrast at the higher X-ray energies used. Rather than

attempting uncertain mineral segmentation, greyscale-derived effective pore density was therefore adopted as a proxy metric to capture spatial variations in carbonate precipitation associated with EG.

To quantify effective mean pore density, greyscale values were normalised to a 0–100 scale, where 100 corresponded to quartz (2.65 g/cm^3, from Fig. 6.5) and 0 to air (0 g/cm³). An Image Statistics module was applied to masked porosity values to calculate mean greyscale for each XY slice along the inlet–outlet axis. Effective pore density was then calculated as:

$$\text{Effective Density} = \left(\frac{\text{Mean Normalized Value}}{100}\right) \times 2.65\ \text{g/cm}^3$$

This enabled direct comparison of pore density distributions across samples, providing insight into variations in $CaCO_3$ precipitation and porosity modification due to EG content and treatment. This approach is subject to uncertainty arising from thresholding and partial volume effects, particularly where pore voxels contain mixed contributions from carbonate precipitates, air, and low-density additives. Effective pore density should therefore be interpreted as a relative, spatially averaged indicator of precipitation trends rather than an absolute measure of local $CaCO_3$ content.

6.3.6 Thermal analysis techniques

Thermal conductivity was measured using a Hot Disk TPS 2500S Thermal Analyzer (University of Strathclyde), which employs the transient plane source (TPS) method with a double spiral sensor (Gustafsson, 1991; Gustavsson et al., 1994). The conductivity of untreated sand was first established using a powder holder with the sensor fully embedded.

For isotropic conductivity, several samples were cut into six equal slices (Fig. 6.3d, Box 1; see Table 6.2). Double-sided TPS measurements were conducted along the length of sliced samples (MICP Sand and all MICP EG specimens) to compare EG-modified columns with MICP-treated sand without EG (Fig. 6.3d, Box 2).

To assess anisotropy, a subsection (~10 × 10 × 3 mm) was extracted from the outlet slice using a diamond-bladed saw (Fig. 6.3d, Box 4). Densities of these subsamples were determined with a helium pycnometer (Micromeritics AccuPyc II 1345; Fig. 6.3d, Box 5). Volumetric heat capacity was then measured using the Hot Disk gold cup

sensor, enabling calculation of radial and axial conductivity from the anisotropic outlet-slice test.

For intact specimens reserved for infrared thermography (IRT), slicing was avoided. Instead, single-sided TPS measurements were performed by placing the sensor between the inlet or outlet face and a reference foam block (λ = 0.03 W/m·K; Fig. 6.3d, Box 3).

IRT was used to characterise heat transfer behaviour under dynamic heating and cooling. Surface temperatures were recorded with a Topdon TC001 thermal camera (±2 °C accuracy, 40 mK sensitivity). The setup consisted of an insulated polystyrene box (45 mm thick, λ = 0.03 W/m·K) containing a pre-heated hot plate (HYCC SH2) at 90 °C. EICP EG4 and EICP PI-EG29 specimens (Table 6.2) were placed individually on the plate, and surface responses recorded for 30 min. The plate was then switched off, samples removed to ambient laboratory conditions (~20 °C), and cooling behaviour monitored for a further 30 min.

6.4 Results and Discussion

6.4.1 Thermal conductivity of bio-cemented sand with additives

Thermal conductivity is a key performance indicator for bio-cemented materials, as it reflects the efficiency of heat transfer through the treated matrix. Figure 6.4 presents the λ measurements for MICP and soybean EICP treated specimens incorporating various conductive additives at different weight percentages. Due to practical constraints, untreated λ measurements were not obtained for additive-containing mixtures (Section 2.1.3); percentage increases are therefore reported relative to untreated dry quartz sand.

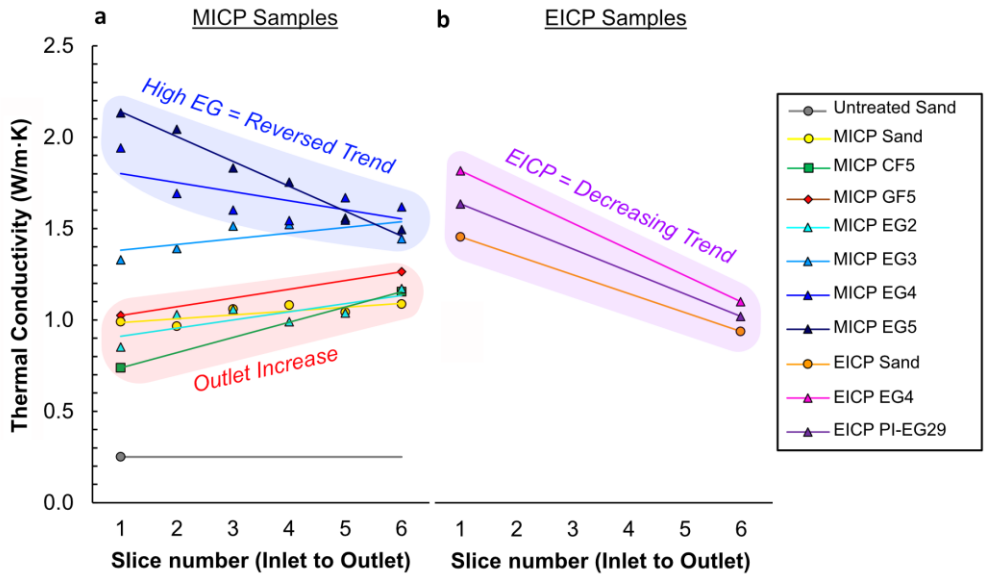

Figure 6.4 Isotropic thermal conductivity for MICP and EICP treated samples. (**a**) MICP-treated samples exhibit distinct trends based on additive type and content. At low EG content (2% and 3%), thermal conductivity gradually increases from inlet to outlet, consistent with trends observed for MICP-treated sand without additives. At high EG content (4% and 5%), the trend reverses, showing higher conductivity at the inlet. Milled carbon fibre (CF) and graphite flake (GF) samples display increasing thermal conductivity towards the outlet (**b**) EICP-treated samples show a consistent decrease in thermal conductivity from inlet to outlet. The paraffin-infused expanded graphite (PI-EG) sample demonstrates slightly lower thermal conductivity enhancement compared to its EG-only equivalent (EICP EG4).

A comparison of EICP and MICP-treated sand-only samples reveals a reversal in inlet–outlet λ trends. In EICP-treated samples, λ is notably higher at the inlet (1.472 W/m·K, a 488% increase over untreated sand) but lower at the outlet (0.949 W/m·K, a 283% increase), consistent with preferential $CaCO_3$ crystallization at quartz contacts (Section 5.4.5), with the inlet enrichment also consistent with gravity-driven redistribution effects observed previously (Section 5.4.2). MICP samples with GF and CF mimic the trend of the MICP-treated sand-only sample, exhibiting a gradual increase in λ from inlet to outlet. This trend may stem from bacterial detachment during injection (Tobler et al., 2014), where high inlet flow velocities push bacterial cells further into the column, enhancing nucleation downstream. CF slightly reduces λ (−25% inlet, +6% outlet), whereas GF modestly enhances it (+3% inlet, +16% outlet), though neither offers sufficient benefit to justify their cost.

EG samples treated with MICP exhibit unique behaviour. At low EG contents (2–3%), λ increases from inlet to outlet, following the trend observed in sand-only samples.

However, at higher contents (4–5%), this trend reverses, with λ highest at the inlet. This reversal may result from limited bacterial transport in high EG content samples. Unlike rigid quartz sand, EG is compressible, and increased EG content likely reduces pore sizes and increases tortuosity, which may restrict bacterial motility and precipitation further downstream. Despite this, EG consistently improves thermal conductivity over MICP-treated sand, except for the 2% EG sample, which has comparable isotropic values.

The maximum thermal conductivity enhancement is observed at the inlet of the 5% EG sample, reaching 2.133 W/m·K, a 753% increase over untreated sand. The 4% EG sample, however, achieves the highest outlet thermal conductivity (1.618 W/m·K, a 547% increase). These results highlight two likely contributing mechanisms of λ enhancement in EG-treated samples: (1) quartz-$CaCO_3$-quartz bonding and (2) connectivity of the EG network.

EICP EG4 exhibits a consistent inlet–outlet decrease in λ, consistent with EICP-treated sand. However, EG incorporation markedly increases thermal conductivity, with values of 1.838 W/m·K (inlet) and 1.113 W/m·K (outlet), compared to 1.472 W/m·K and 0.949 W/m·K, respectively, for the EICP sand-only sample. Similarly, the PI-EG sample has an inlet λ of 1.654 W/m·K and an outlet of 1.032 W/m·K. Paraffin infusion was expected to enhance thermal conductivity further, and the observed reduction may relate to changes in the wettability of EG post-infusion, altering where $CaCO_3$ crystals form during treatment.

6.4.2 Dense solid distribution

The distribution of dense solids (quartz and $CaCO_3$) is a key factor in thermal conductivity enhancement following bio-cementation, as denser regions typically correspond to greater $CaCO_3$ precipitation and improved heat transfer pathways. Figure 6.5 illustrates inlet–outlet variations in quartz grain connectivity and $CaCO_3$ precipitation across treated samples.

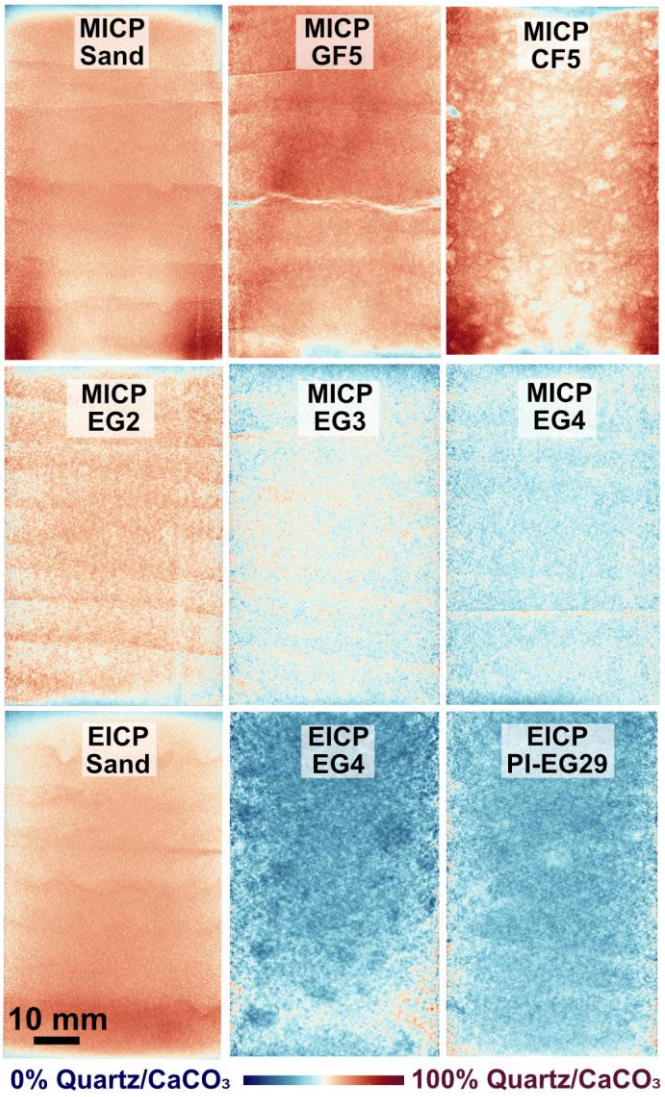

Figure 6.5 Heat maps of average dense solid distribution (quartz + $CaCO_3$) for MICP and EICP-treated samples MICP Sand, GF and CF show lower density near the injection point, likely due to bacterial detachment at higher flow velocities. EG samples display layering from compaction and reduced dense solid content at higher EG percentages. EICP treated sand exhibits a denser inlet region than MICP treated sand, consistent with higher inlet thermal conductivity. Paraffin-infused EG exhibits less density variation than EICP EG4, likely due to changes in EG wettability, which may shift preferential nucleation sites for $CaCO_3$ precipitation.

MICP Sand, GF5, and CF5 show reduced dense solid content near the inlet relative to the edges. This pattern is further evidence for bacterial detachment caused by high inlet flow velocity, which reduces $CaCO_3$ precipitation in this region.

MICP GF5 features a visible fracture in the XCT data, likely formed during demoulding, though this has no impact on thermal probing due to its shallow depth (<

10 mm). Blotchy patterns in CF indicate additive clumping of fibres, consistent with poor thermal performance.

MICP-EG samples display clear layering patterns caused during compaction, which appear to be more pronounced at low EG content, despite scarification between layers during packing. This effect is likely due to the higher quartz fraction at low EG contents, which resists compression and preserves packing interfaces, making stratification more distinct. At higher EG contents, the compressible graphite particles deform across larger layers, reducing visible stratification. These differences are important, as they may influence both fluid migration (see Section 4.3) and the uniformity of $CaCO_3$ precipitation.

Although higher EG loadings reduce the fraction of dense solids, λ continues to rise (unlike Section 5.4.2), indicating that heat transfer becomes increasingly governed by the connected EG network rather than quartz–$CaCO_3$ contact bridging.

Greyscale attenuation along the inlet–outlet axis of EG samples indicates a relatively uniform distribution of dense solids, suggesting uniform $CaCO_3$ precipitation on quartz throughout the sample While this appears to contradict our initial hypothesis that bacterial straining would lead to localized $CaCO_3$ accumulation at the inlet, straining may occur primarily within the EG network, where $CaCO_3$ precipitation is not fully captured by dense solid segmentation due to the overlapping attenuation of EG, air, and $CaCO_3$.

6.4.3 $CaCO_3$ precipitation on expanded graphite

Dense solid masking (quartz + $CaCO_3$ on quartz) enabled analysis of the remaining pore space, comprising EG, air, or $CaCO_3$ deposited on EG (combined attenuation lower than dense solids), as quantified in Figure 6.6.

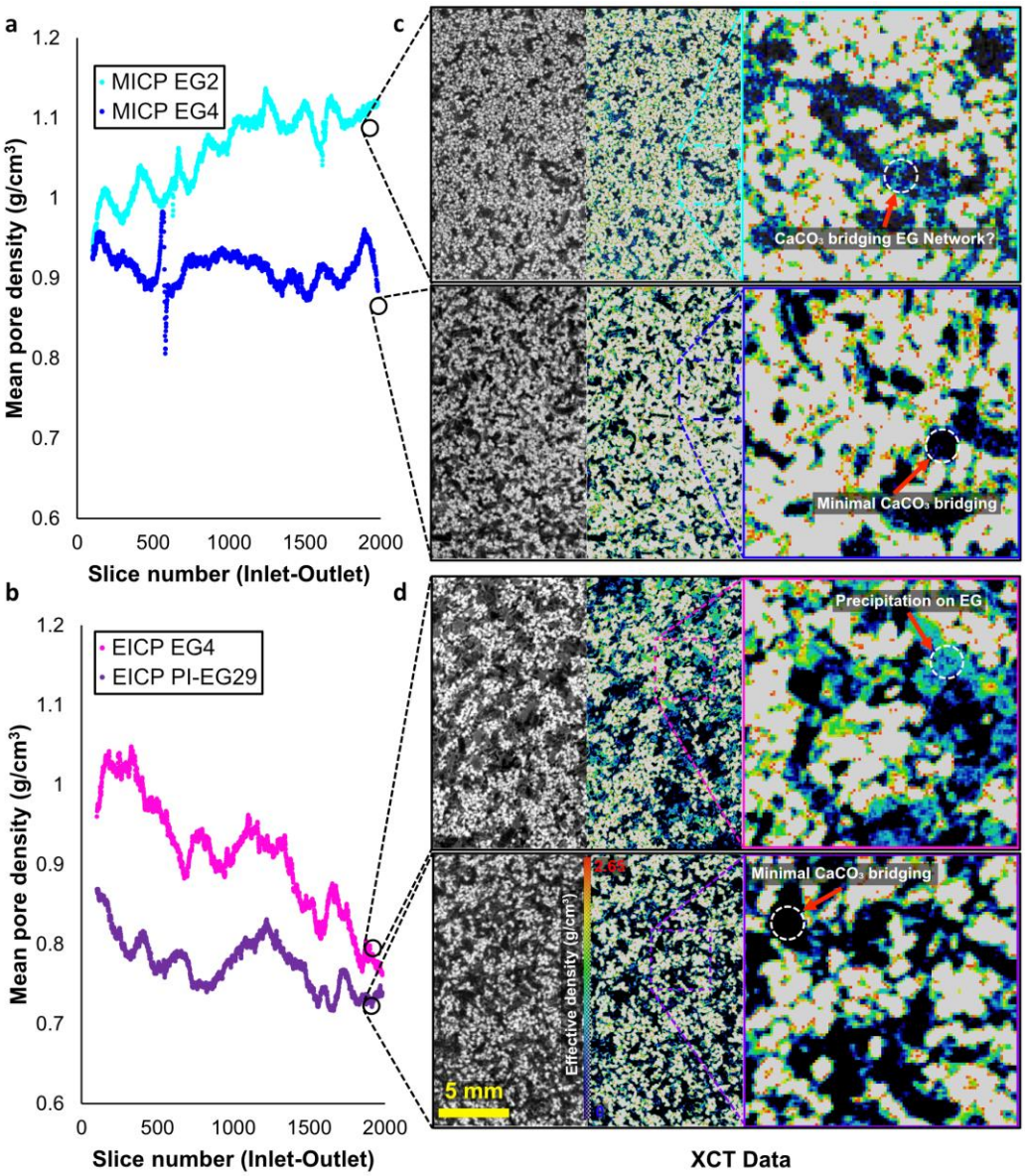

Figure 6.6 Relationship between thermal conductivity trends and the distribution of $CaCO_3$ within the EG network. Effective mean pore density (g/cm³) plotted as a function of slice number for (**a**) MICP and (**b**) EICP specimens with varying EG and paraffin content. Higher mean pore densities correspond to increased $CaCO_3$ precipitation and denser pore networks. MICP EG2 exhibits the highest pore density, which increases along the column. In contrast, MICP EG4 and EICP EG4 show a progressive decrease from inlet to outlet. The EICP PI-EG29 sample displays the lowest overall pore density, indicating reduced $CaCO_3$ precipitation on EG due to paraffin infusion. (**c** and **d**) Representative XCT slices from the highest (top) and lowest (bottom) density regions (circled in a/b). Left: Greyscale XCT images showing material structure. Middle: Corresponding pore space maps, where density is colour-coded from black (air) to red (quartz density). Right: Zoomed-in regions highlighting density variations within the EG network, illustrating differences in $CaCO_3$ bridging and precipitation with increasing EG and paraffin content.

There is a strong correlation between pore space density (Fig. 6.6a-b) and λ measurements (Fig. 6.4), indicating that $CaCO_3$ precipitation within the EG network contributes directly to heat transfer. Three clear trends emerge: (i) pore density is consistently higher in low-EG than high-EG systems; (ii) pore density increases from inlet to outlet at low EG but decreases at high EG; and (iii) untreated EG shows higher pore densities than paraffin-infused EG, though both exhibit similar inlet–outlet gradients.

In low-EG MICP systems (e.g., EG2), the quartz framework allows bacterial transport and more uniform $CaCO_3$ bridging, while local stress on EG particles makes them appear more compacted than in high-EG systems – a structure likely to promote anisotropic heat transfer. In high-EG MICP (e.g., EG4), bacterial straining at the inlet elevates pore density and λ, but distal nucleation is suppressed, limiting EG-$CaCO_3$ bridging.

EICP EG4 shows a steeper outlet decline in pore density, closely matching λ trends. Paraffin-infused systems (e.g., PI-EG29) record the lowest densities, consistent with paraffin reducing $CaCO_3$ precipitation on EG. XCT data (Fig. 6.6d) confirm precipitation is spatially restricted in PI-EG, while untreated EG shows more even $CaCO_3$ coverage. Thus, EG wettability strongly governs nucleation. Despite reduced pore density, PI-EG29 still achieves λ gains relative to MICP-treated sand, underscoring the intrinsic role of the EG network in heat transfer.

6.4.4 Microstructural evidence from XCT analysis and optical microscopy

While XCT analysis provided insights into the internal 3D architecture of the specimens, its spatial resolution (~42 μm) was insufficient to resolve crystal morphology or detect fine-scale variations in surface precipitation across different sample types.

To further assess $CaCO_3$ precipitation on both EG and quartz during MICP, as well as potential differences in crystal morphology between specimens, optical microscopy was employed. Figure 6.7 shows optical microscopy of $CaCO_3$ precipitation on quartz and EG in MICP systems with low and high EG content.

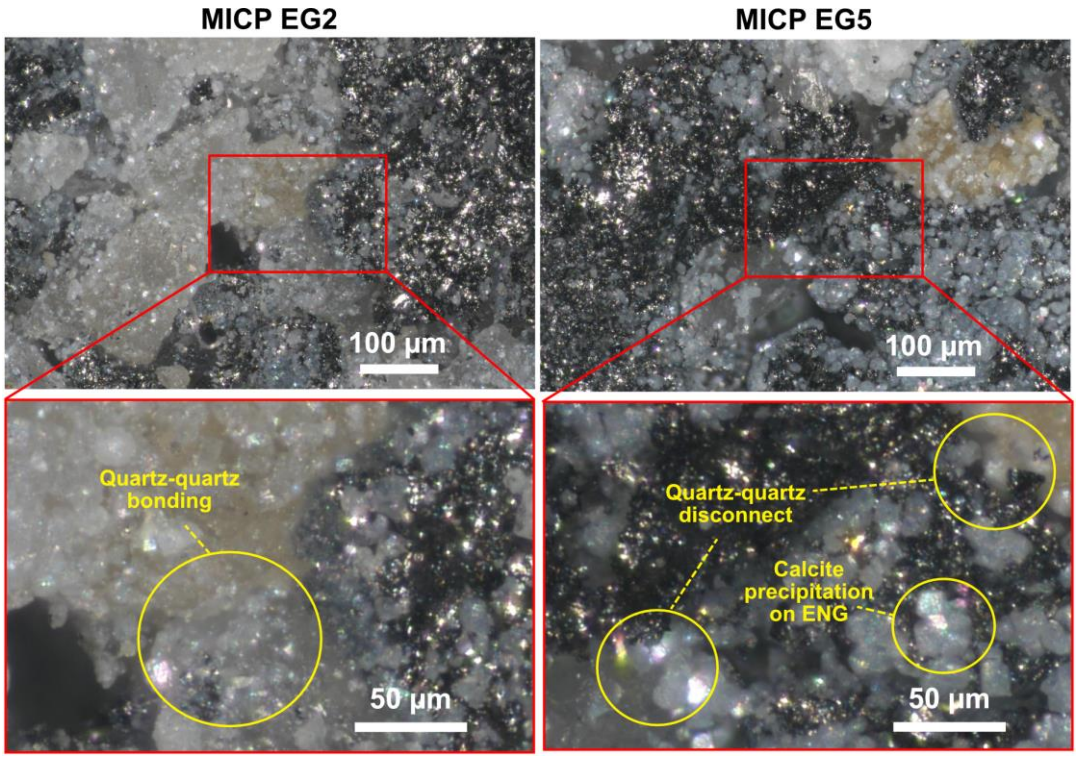

Figure 6.7 Optical microscope images of MICP-treated specimens at high and low EG content. Optical microscopy confirms that $CaCO_3$ precipitates on both EG and quartz surfaces, with notable differences in deposition patterns between low (MICP EG2) and high (MICP EG5) EG content samples. At low EG content (left), $CaCO_3$ preferentially bridges quartz grains, supporting quartz-$CaCO_3$-quartz thermal transport pathways. In contrast, at high EG content (right), quartz grains exhibit reduced direct contact, with $CaCO_3$ precipitation increasingly localized on EG surfaces, reinforcing thermal transport within the EG network. Insets highlight key microstructural differences, including enhanced quartz-quartz bonding at low EG content and increased $CaCO_3$ deposition on EG at high EG content. The precipitated $CaCO_3$ primarily forms large rhombohedral crystals, approximately 15–20 µm in diameter.

6.4.5 Anisotropic thermal behaviour of expanded graphite

Isotropic λ values alone do not capture the anisotropic effects of EG. EG-containing samples exhibit more complex anisotropic thermal behaviour (Fig. 6.8) driven by changes in graphite connectivity during packing and compression.

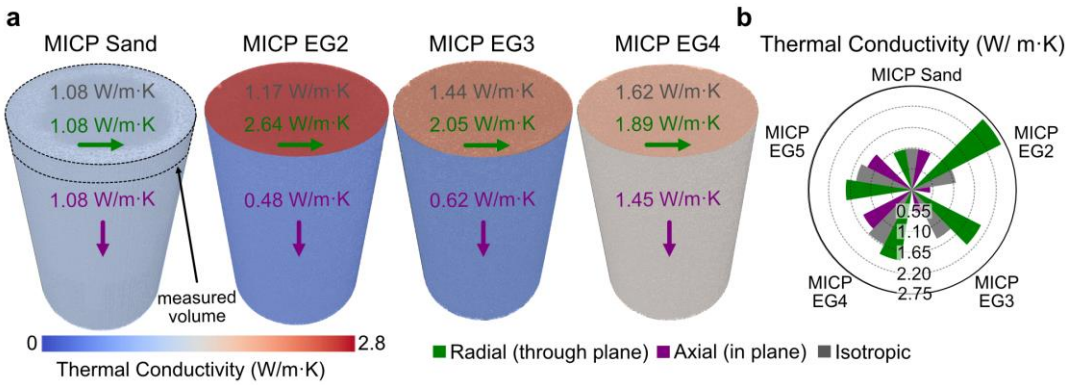

Figure 6.8 Anisotropic and isotropic thermal conductivity of MICP-treated samples (**a**) Thermal conductivity values for MICP-treated samples represented along axial (purple) and radial (green) directions, with isotropic values (grey) measured from the top (outlet) slice. MICP Sand demonstrates isotropic behaviour with consistent axial and radial values of 1.08 W/m·K. EG-containing samples show clear anisotropic trends. At just 2% EG content, radial thermal conductivity significantly increases to 2.64 W/m·K while axial conductivity decreases to 0.48. W/m·K. Increasing EG content (MICP EG3 and MICP EG4) results in reduced anisotropy with decreasing radial enhancement and increasing axial thermal conductivity (**b**) Radial bar plot of thermal conductivity measurements (isotropic, axial, radial) for all samples. Axial and radial bars are plotted relative to the isotropic values, showing the contrast in heat transfer performance.

MICP sand displays isotropic thermal properties due to uniform quartz-grain connectivity. In contrast, the MICP + 2% EG sample shows the strongest anisotropy, with radial (in-plane) λ reaching 2.64 W/m·K (a 956% increase compared to untreated sand), while axial (through-plane) λ remains lower at 0.48 W/m·K (a 92% increase). This anisotropy decreases at higher EG contents, where radial and axial λ values gradually converge.

At 2% EG, the enhanced radial λ is likely supported by sparse but well-aligned EG pathways, which reinforce connectivity while maintaining some quartz-$CaCO_3$-quartz contacts. At higher EG fractions, the reduced quartz proportion means that EG increasingly dominates axial thermal transport. This shift produces a more isotropic thermal response, as a denser, more interconnected EG network supports heat transfer in multiple directions. These conceptual mechanisms are illustrated schematically in Figure 6.9.

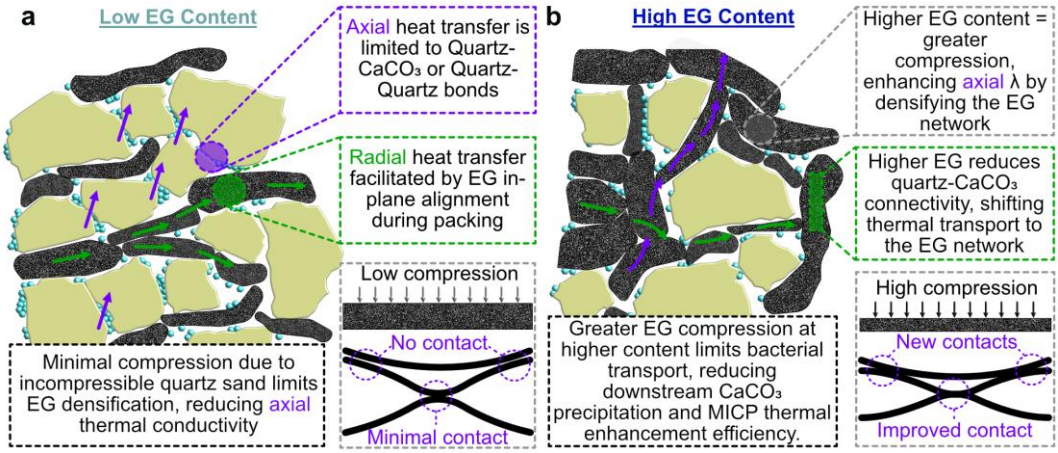

Figure 6.9 Schematic representation of thermal transport mechanisms in MICP-treated samples with low and high expanded graphite (EG) content (**a**) Low EG Content: Compression enhances the radial alignment of EG (black), facilitating in-plane heat transfer (green arrows) while maintaining sufficient quartz (yellow)-$CaCO_3$ (blue)-quartz connectivity for axial heat transfer (purple arrows). Limited EG content allows for more efficient radial pathways while preserving quartz-to-quartz grain contacts. (**b**) High EG Content: Leads to increased compression, enabling a more uniform EG network that supports both radial and axial heat transfer. However, higher EG content reduces quartz-$CaCO_3$-quartz connectivity, shifting the dominant thermal transport mechanism to the EG network. The denser EG network at high compression may limit bacterial transport, reducing $CaCO_3$ precipitation and the efficiency of MICP thermal enhancement. Insets illustrate the transition from minimal axial contact at low compression to improved contact at high compression due to densification of EG layers.

6.4.6 Thermal energy storage potential of paraffin-infused expanded graphite

Beyond its role in enhancing conductivity, EG also possesses a high specific surface area and an interconnected pore network, making it an effective support for PCMs. When impregnated with paraffin wax, EG forms a composite thermal energy storage (TES) medium with higher conductivity and stability than pure paraffin.

The TES potential was evaluated by comparing the thermal response of EICP EG4 and EICP PI-EG29 under controlled heating and cooling. Infrared thermography (Fig. 6.10) revealed clear differences in behaviour across the paraffin phase transition. Although both samples had similar thermal conductivity values (Fig. 6.4), their temperature evolution diverged markedly due to the latent heat effects of paraffin.

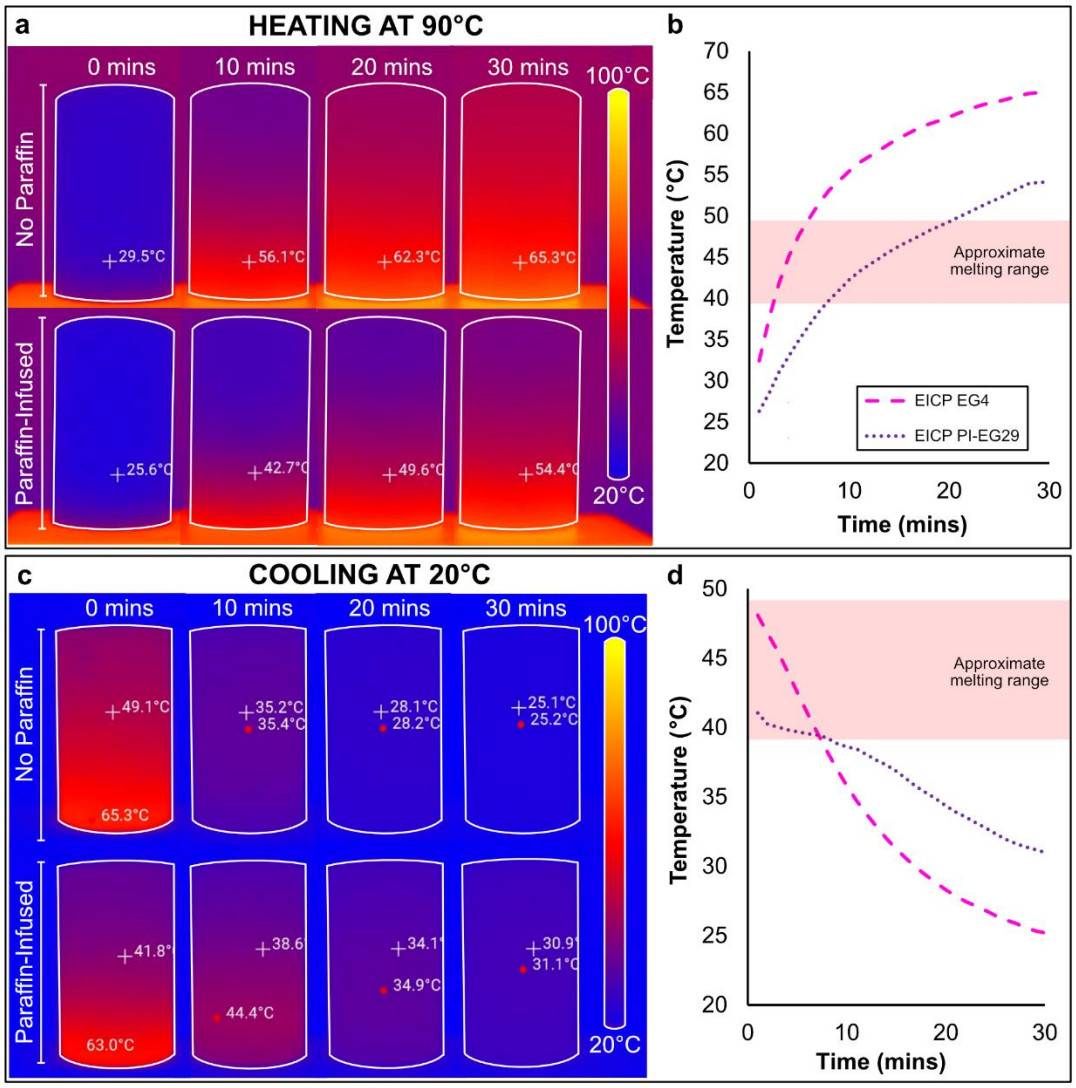

Figure 6.10 Thermal response of EICP-treated sand + expanded graphite specimens with and without paraffin wax during controlled heating and cooling (**a**) Infrared thermal images acquired at selected time intervals during heating on a 90 °C hot plate for EICP EG4 (no paraffin) and EICP PI-EG29 (paraffin-infused). The paraffin-infused specimen exhibits a slower rise in surface temperature relative to the non-infused control. (**b**) Corresponding surface temperature-time curves during heating, showing a reduced heating rate for the paraffin-infused sample. The shaded region indicates the approximate phase-change temperature range of the paraffin wax, inferred from the onset of rate reduction during heating. (**c**) Infrared images acquired during cooling at 20 °C, where the paraffin-infused sample shows delayed surface cooling relative to the control. (**d**) Cooling curves highlighting a reduced cooling rate for the paraffin-infused specimen over the same temperature interval, consistent with latent heat release during solidification. Surface temperatures are reported; the shaded regions denote an inferred phase-change window rather than a discrete melting point.

During the first 10 minutes of heating, EG4 warmed by 26.6 °C, compared with only 17.2 °C for PI-EG29, directly demonstrating paraffin's latent heat absorption. The paraffin-infused sample maintained consistently lower temperatures throughout heating.

On cooling, PI-EG29 exhibited a distinct thermal plateau (0–10 min) associated with latent heat release during paraffin crystallisation, delaying the temperature drop relative to the continuously cooling EG4. Even after 45 minutes of cooling (not shown), PI-EG29 retained heat, remaining at 28 °C, while EG4 had already cooled to that temperature within ~20 minutes. Notably, this effect persisted despite PI-EG29 reaching a lower maximum temperature (41.8 °C vs. 49.1 °C).

Paraffin remained absorbed within the EG framework throughout phase change, as indicated by the absence of weight loss after cycling. This stability overcomes a major limitation in many PCM systems, where leakage restricts practical use. The reduced permeability of the $CaCO_3$ matrix may further reinforce paraffin retention, potentially enhancing durability during thermal cycling. Together, these results confirm that biocemented systems can integrate both conductivity enhancement and latent heat storage – a dual functionality not achievable with sand-only matrices.

6.4.7 Trade-Offs in Thermal Enhancement Strategies

The incorporation of EG into biocemented systems clearly improves thermal conductivity, while also reducing mixture density, which could benefit handling and transport. However, these advantages are counterbalanced by several trade-offs. At low EG contents (~2 wt%), radial alignment reinforced strong in-plane conduction but limited through-plane transport, producing marked anisotropy. This anisotropy may be undesirable in applications requiring vertical heat transfer (e.g., energy piles), yet advantageous where lateral heat dissipation is needed, such as thermal barriers or heat-spreading layers.

At higher EG fractions, densification improved isotropy by supporting EG connectivity in multiple directions. Yet this also inhibited microbial transport, promoting preferential $CaCO_3$ precipitation near injection points (Fig. 5.2). Although mechanical strength was not directly tested, reduced quartz-$CaCO_3$-quartz contacts at high EG content likely compromise structural integrity, reflecting the balance between thermal and mechanical performance.

Paraffin infusion introduced another dimension of complexity. Latent heat storage significantly altered heating and cooling responses, but reduced $CaCO_3$ precipitation, most likely due to wettability effects. Nevertheless, paraffin remained stable within the EG framework without leakage, overcoming a major limitation of PCM composites.

Together, these findings underline that additive-based enhancement strategies involve compromises between conductivity, anisotropy, precipitation behaviour, and strength. The appropriate choice will depend on whether the application prioritises conductivity, thermal storage, structural performance, or ease of processing.

6.4.8 Limitations

Several limitations should be considered when interpreting these results. One concern is whether similar thermal improvements could be achieved by simply compacting a mixture of sand and EG without inducing carbonate precipitation. A matched-compaction control (sand + EG compacted to the same dry density without ICP) would be required to isolate the incremental contribution of carbonate bonding. This study demonstrated clear correlations between thermal conductivity and the attenuation of pore space occupied by EG, air, or $CaCO_3$ deposits on EG (all of which exhibited lower combined attenuation than dense solids), but the relative contribution of ICP bonding compared with simple packing effects remains uncertain. Another limitation is the reliance on a uniform quartz sand matrix; more heterogeneous or native soils may display different packing behaviour, precipitation dynamics, and additive dispersion. In addition, all samples were tested in a dry state. While this isolates the role of solid contacts, in situ applications often involve partially or fully saturated conditions where fluid phases contribute to heat transfer. Finally, the treatment protocol was fixed at nine cycles for all samples. Although this regime was effective in producing measurable enhancements, an optimal number of cycles that balances strength, conductivity, and economic efficiency likely exists but was not explored here.

6.5 Conclusions & Implications

This study investigated the integration of conductive and phase-change additives into bio-cemented materials to enhance thermal performance. EG acted as a dual-function additive, increasing conductivity while also changing where carbonate precipitation contributed to heat-transfer pathways. At low EG contents, thermal transport was primarily supported by quartz-$CaCO_3$-quartz bridging, whereas at higher EG contents a connected EG network increasingly governed heat transfer, producing large conductivity gains and a shift from strongly anisotropic to more isotropic behaviour.

XCT analysis indicates that EG influences both compaction architecture and precipitation patterns. At lower loadings, more distinct packing layers promoted radial alignment and exceptional in-plane conductivity. At higher loadings, densification likely limited bacterial transport and favoured precipitation closer to the inlet, yet thermal performance remained high due to EG connectivity. These trends imply a trade-off: increasing EG enhances heat transfer but may reduce the fraction of load-bearing quartz-$CaCO_3$ contacts.

Paraffin-infused EG introduced latent heat storage in addition to conductivity enhancement. Infrared thermography confirmed delayed heating and extended cooling plateaus consistent with phase-change behaviour, and no leakage was detected, indicating effective shape stabilisation within the EG scaffold.

Overall, the results demonstrate that bio-cementation can be used to stabilise functional carbon-based networks and enable composites with both enhanced heat conduction and tuneable heat storage. Future work should isolate compaction-only effects with matched controls, evaluate mechanical consequences of reduced quartz bonding, and test behaviour in more representative soils and saturation states.

In the context of the thesis objectives, this chapter addresses Critical Challenge 5 by demonstrating that the thermal performance of biocemented materials can be enhanced not only through increased carbonate precipitation, but through deliberate incorporation and stabilisation of functional additives. By combining expanded graphite and paraffin within a bio-cemented framework, the work shows that both heat conduction and thermal energy storage can be engineered independently and in combination. The findings also intersect with Critical Challenge 2, as changes in additive wettability and microstructure were shown to alter $CaCO_3$ precipitation

pathways, and with Critical Challenge 4, highlighting trade-offs between permeability, transport, and functional performance at higher additive loadings.

The thesis now turns to the implications of these material-level controls at system and application scales. Chapter 7 therefore builds on the mechanistic insights from Chapters 3–6 to examine how controlled precipitation, permeability modification, and thermal functionality translate into application-relevant performance, with particular emphasis on systems where hydraulic, mechanical, and thermal requirements must be satisfied simultaneously.

Chapter 7: Applying Induced Carbonate Precipitation: Insights, Trade-offs, and Future Directions

This thesis set out to address five critical challenges (outlined in Chapter 1). Each is revisited below, with findings from Chapters 3–6 synthesised to highlight contributions and remaining gaps. A central aim was to bridge pore-scale observations with bulk engineering outcomes (Objective 1), achieved by combining time-lapse XCT, fluid flow simulations, mechanical testing, and thermal property analysis. Together, these approaches provide new insights into how mixing dynamics, treatment strategies, and material modifications govern ICP performance across scales. Three overarching conclusions emerge from this work:

- Mixing mechanisms determine the spatial distribution of $CaCO_3$ and thus treatment efficiency, with density driven mixing shown to be a central factor for controlling where and when crystals form.
- ICP enables tuneable permeability control, ranging from targeted reductions for CO_2 sequestration and groundwater barriers, to controlled retention in geothermal and hydrogeological settings.
- ICP enhances both thermal and mechanical properties, demonstrating its potential for structural reinforcement, energy storage, and high-performance construction materials.

Assessed against the five critical challenges (Section 1.6), the results collectively show that precipitation uniformity governs ICP performance across flow control, strength, and thermal outcomes. Sections 7.1–7.4 address these challenges in turn, concluding with recommendations for scale-up, efficiency, and advances in biomineralisation.

7.1. EICP can create spatially targeted barriers

Objective 3 (sweep efficiency) and Objective 4 (permeability control) are addressed by showing for the first time that density driven mixing and tailored injection protocols can spatially target $CaCO_3$ away from the wellbore to form anisotropic barriers. Chapters 4–6 show that EICP enables permeability modification at scales and

distributions not typically achievable with MICP. Whereas both single (Section 4.3) and multiphase MICP produced highly localised precipitation near injection points (Section 5.4.1), often clogging inlet zones, EICP demonstrated more gradual and evenly distributed reduction in permeability. This contrast underpins EICP's potential to create spatially targeted flow barriers that can be tailored to the requirements of CO_2 sequestration and groundwater control.

7.1.1 Density driven mixing governs the spatiotemporal distribution of $CaCO_3$

Density driven mixing can be used to direct carbonate precipitation downstream of injection points (as shown in Section 3.4.3) and away from wellbores, enabling the design of barriers without premature clogging. Furthermore, pulsed injection (Section 4.4.2) can introduce transient inertial effects at pore-scale mixing interfaces, disrupting otherwise stable laminar flow paths and promoting more homogeneous carbonate distribution in proximal regions. These findings suggest that mixing strategies can be deliberately exploited to engineer anisotropic permeability barriers (Fig. 7.1c), reducing vertical flow while maintaining lateral pathways (Objective 3). Section 4.3 further supports this by showing greater permeability reduction in fine layers (e.g., naturally occurring strata) following SB-EICP, highlighting the importance of lithological contrasts. This is relevant for CCS, where improving sweep efficiency and limiting caprock leakage rely on such anisotropy control (Bump et al., 2023), particularly in unconfined sediment (Oko et al., 2020).

7.1.2 Comparing EICP and MICP for permeability control

Soybean-based EICP consistently produced precipitation near grain contacts and gradual permeability reduction (Section 5.4.1). The observed lag between fluid mixing and calcite nucleation (Sections 4.1–4.2) allowed crystallisation to occur further from injection points, extending treatment range beyond what can be achieved with MICP. In Chapter 4, single-phase MICP treatments showed that microbial cells struggled to penetrate finer layers, limiting transport across heterogeneous pore networks. By contrast, the same lithological contrasts were shown to enhance precipitation control under EICP, where delayed nucleation allowed carbonate formation to be preferentially concentrated within fine layers. To improve MICP penetration, a multi-phase strategy was adopted in Chapter 5, separating bacterial and cementing solutions; however, localised blocking still occurred near the inlet region (Fig. 5.2a).

Taken together, these observations indicate that while MICP can be effective for sealing discrete fractures or micro-annuli (Fig. 7.1b), EICP is better suited to distributed permeability modification in layered and heterogeneous media.

Chapter 5 highlighted an additional limitation: in some plant-based EICP formulations, permeability reduction was partly due to suspended organic content rather than carbonate alone. This finding emphasises the importance of refining crude enzyme extracts. Removal of organic curds (Section 5.3.1) improved the consistency of permeability modification and is expected to improve durability, as flow reduction is then governed primarily by mineral $CaCO_3$ precipitation rather than organic phases that may degrade or redistribute over time.

7.1.3 Engineering applications of spatially targeted flow barriers

Taken together, these results suggest a division of roles: MICP is best suited to highly localised sealing, while EICP can be engineered for distributed, large-scale permeability modification particularly in layered formations, where fine-grained horizons act as natural controls on precipitation localisation (Section 4.4.2). The effectiveness of EICP depends not only on mixing conditions (Chapter 3) but also on enzyme formulation and injection protocol (Chapters 4–5). A hybrid deployment strategy could therefore use MICP for near-well sealing and EICP for controlled flow modification over metre-to-tens-of-metres scales around the wellbore (Fig. 7.1c), addressing both local leakage risks and near-field CO_2 migration pathways. In doing so, this work advances Objective 3 (enhancing sweep efficiency in CCS) and Objective 4 (controlling permeability), demonstrating how EICP strategies can be tuned to form anisotropic barriers over metre-to-tens-of-metres scales around the wellbore. However, while these findings highlight strong potential for CCS, they are based on laboratory systems. Field-scale heterogeneity and multiphase flow will present additional challenges.

Figure 7.1 synthesises the chapter-level findings into a deployment concept that allocates MICP and EICP to their most effective roles around a CO_2 wellbore.

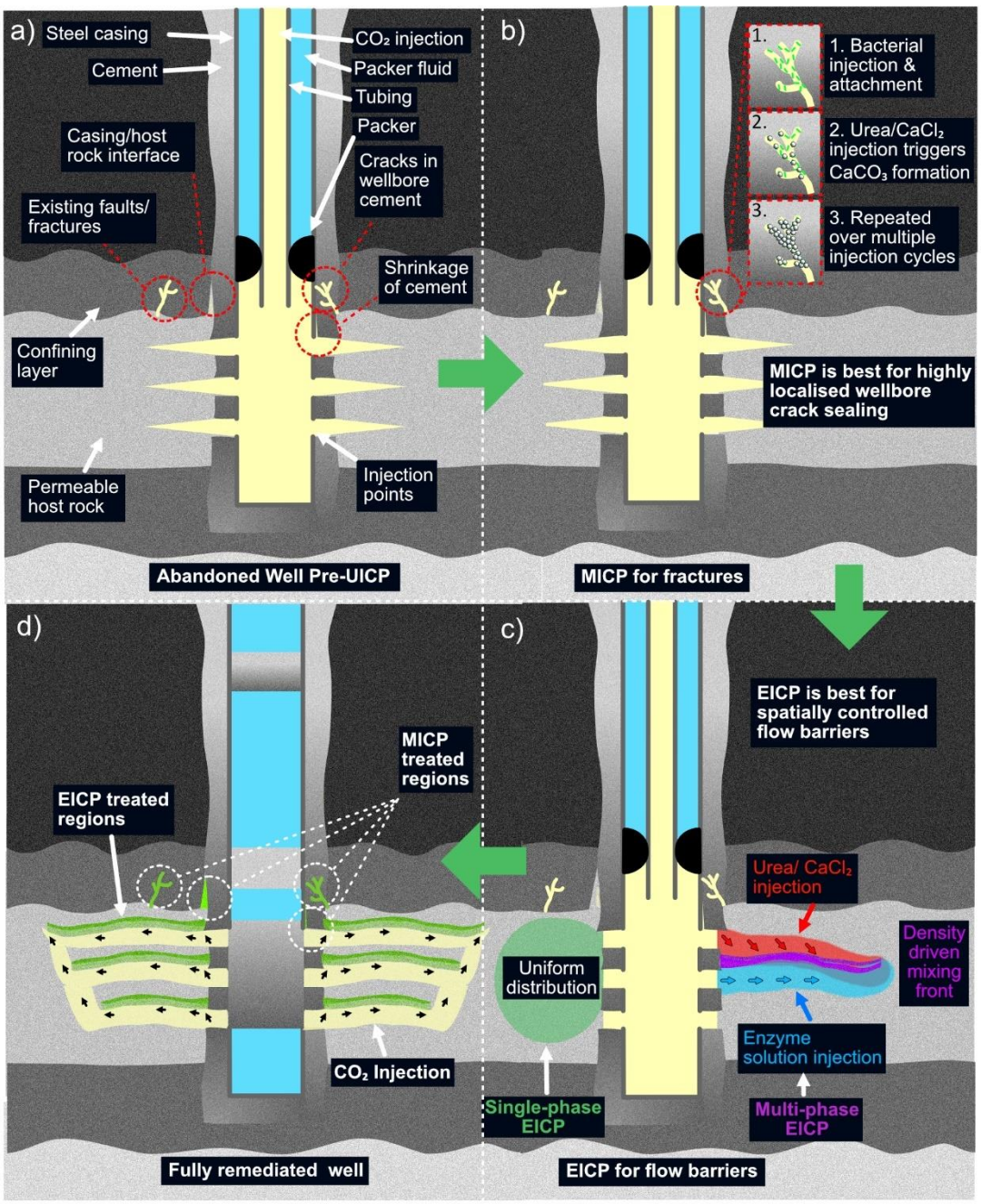

Figure 7.1 Application of ICP strategies for sealing CO_2 injection wells and creating targeted flow barriers (**a**) Legacy oil and gas wells present multiple leakage risks, including fractures, cement shrinkage, and casing/rock interface pathways. (**b**) MICP is best for fracture sealing in the near wellbore, where microbial attachment and successive urea/$CaCl_2$ injections induce localized $CaCO_3$ precipitation. (**c**) EICP strategies enable spatially controlled flow barriers. On the right, multi-phase EICP leverages density driven mixing mechanisms (Ch. 3) to promote targeted carbonate precipitation. On the left, single-phase soybean EICP (Ch. 5) provides uniform permeability reduction. (**d**) The fully remediated well integrates MICP for fractures and EICP for flow control to mitigate CO_2 leakage risk while maintaining controlled permeability.

7.2. ICP can enhance strength while retaining permeability

Objective 2 (treatment optimisation) and Objective 4 (permeability control) are addressed by showing that soybean EICP can deliver substantial UCS gains while retaining controlled permeability, with outcomes governed by enzyme formulation (e.g. curd removal to reduce turbidity) and injection strategy. Traditional cement-based grouts and chemical stabilisers often cause excessive clogging, disrupting natural drainage and increasing the risk of pore pressure build-up and ground heave (Z.-F. Wang et al., 2020). In contrast, soybean-based EICP achieved substantial strength enhancement, with UCS values up to 17.9 MPa (Fig. 5.5), while retaining controlled permeability, thereby meeting the requirements of Objective 4.

Chapters 4 and 5 demonstrated that $CaCO_3$ precipitation and uncoagulated organics are the key controls on this balance. Removing curds increased UCS by preserving fluid pathways and allowing further injection cycles, emphasising the importance of enzyme preparation. For example, a 9-cycle soybean EICP sample at 16.2% $CaCO_3$ (Section 5.4.3) retained a hydraulic conductivity of 3.40×10^{-4} m s^{-1}, an order of magnitude higher than the 1.59×10^{-5} m s^{-1} reported by Meng et al. (2021) at 20% $CaCO_3$. Their soybean EICP treatment achieved ~10 MPa UCS compared to ~7.5 MPa in our study; however, this difference is consistent with their ~4% higher carbonate content.

When expressed as percentage reduction, our method achieved a 80.3% decrease in hydraulic conductivity compared to 93.4% in Meng et al. (2021). This greater permeability retention likely reflects differences in treatment method: our bottom-up injections (Fig. 5.1) contrast with Meng's free-drained percolation, highlighting the influence of injection strategy on treatment outcome.

It is also important to note that the starting hydraulic conductivity of our sand (1.73×10^{-3} m s^{-1}) was substantially higher than Meng's (2.40×10^{-4} m s^{-1}). This initial condition likely explains the lower relative reduction in our tests despite comparable carbonate contents.

7.2.1 Engineering applications of strength enhancement with retained permeability

Soybean EICP can increase strength while maintaining hydraulic function (Chapters 4 and 5), opening opportunities in urban infrastructure, coastal protection, and renewable energy systems where complete sealing would be detrimental. In urban environments, conventional impermeable pavements exacerbate flooding by preventing infiltration (Imran et al., 2013). By contrast, the biocemented materials developed here exhibit a combination of retained permeability and load-bearing capacity (up to 17.9 MPa; Fig. 5.5) that is consistent with the functional requirements of permeable paving systems, supporting stormwater infiltration, urban greening, and long-term soil stability in line with sustainable drainage strategies (Mullaney et al., 2016).

In coastal and slope settings, where excessive sealing can cause water pooling and instability, EICP provides a reinforcement mechanism while preserving controlled drainage, thereby reducing the risk of mass movement and failure in hydraulic structures (Z.-F. Wang et al., 2020). Maintaining connected pore networks allows hydraulic pressures to dissipate while avoiding the formation of impermeable barriers that can promote uplift or shear localisation. This balance of strength and permeability is particularly valuable where soil-structure interaction must be carefully managed under fluctuating hydraulic and thermal loads.

For renewable energy systems such as ground source heat pumps, energy piles, and borehole heat exchangers, permeability plays a dual role: it supports mechanical integrity while enabling groundwater-mediated heat transport. EICP offers the ability to strengthen surrounding soils while retaining connected flow pathways that can enhance convective heat exchange and moderate thermal gradients around heat exchangers. By avoiding excessive clogging, EICP-treated materials may reduce thermal stress accumulation, settlement, and stress fracturing during repeated heating-cooling cycles (Yang et al., 2023).

These findings directly advance Objective 2 (optimising treatment strategies) by showing how crude enzyme formulations and organic content influence $CaCO_3$ distribution and bulk material properties, and Objective 4 (controlling permeability) by demonstrating how injection design determines whether permeability is sealed or deliberately retained.

However, it should be noted that all experiments in this thesis used a uniform quartz sand for consistency across chapters and compatibility with XCT. In real-world soils, variations in grain size, mineralogy, and organic content are likely to produce different permeability and strength responses, and further work is required to validate these findings under field conditions.

7.3. ICP can enhance thermal conductivity in bio-cemented materials

Objective 5 (thermal performance) is achieved by linking $CaCO_3$ contact bridging to bulk conductivity gains and by identifying where additional treatment cycles yield diminishing returns. Soybean EICP treatments (Chapter 5) increased thermal conductivity by forming $CaCO_3$ bridges at grain contacts, reducing contact resistance and improving solid-phase connectivity.

Thermal conductivity gains plateaued beyond approximately nine treatment cycles, indicating diminishing returns once intergranular contacts became sufficiently bridged by $CaCO_3$. While additional cycles may still be justified to enhance mechanical strength (Section 5.6.2), they contribute little further improvement to heat transfer. Moreover, strongly cemented zones can introduce sharp spatial contrasts in material properties, potentially limiting lateral heat transfer across treated-untreated interfaces. Results from Chapters 4–6 also show that permeability can be deliberately managed through treatment design, suggesting that under appropriate hydraulic conditions, groundwater flow may contribute to convective heat transport alongside conduction.

Taken together, these findings show that thermal enhancement depends not only on the total $CaCO_3$ content, but on treatment strategy, specifically the balance between cycle number, permeability control, and material cost. When considered alongside the additive-based enhancements demonstrated in Chapter 6, the results show that EICP formulations can be deliberately tuned to navigate trade-offs between mechanical performance, thermal function, and economic efficiency.

7.3.1 Conductive additives for enhanced thermal performance

Conductive additives (Chapter 6), particularly expanded graphite (EG), provide a complementary route to thermal enhancement. Modest EG additions (~2–5 wt%) achieved thermal conductivity increases comparable to, and in some cases greater than, those obtained through substantially increasing EICP cycle number (up to ~25 cycles). This directly addresses the diminishing-returns behaviour observed beyond ~9 treatment cycles (Section 5.4.2; Objective 5), indicating that additive-based strategies can partially substitute for reagent-intensive treatments. Such substitution has the potential to reduce both material consumption and environmental footprint.

A practical challenge is EG's very low density (~0.0063 g/cm³ compared to ~2.65 g/cm³ for quartz sand), which makes untreated mixtures prone to segregation. ICP stabilises these blends by locking EG within the carbonate-bonded pore network, allowing thermal gains to be preserved under load. Performance was also sensitive to dosage and distribution: ~2 wt% EG promoted strongly anisotropic conductivity (radial > axial), whereas ~5 wt% yielded a more isotropic response, desirable for borehole exchangers and energy piles that rely on uniform thermal gradients. These trends must be interpreted in light of known limitations, including compaction effects, matrix heterogeneity, dry testing conditions, and the fixed treatment protocol used here (discussed in Chapter 6).

7.3.2 Engineering implications of thermally enhanced ICP materials

The ability to enhance thermal conductivity while increasing strength and, in some cases, retaining controlled permeability broadens ICP's application scope. In geothermal systems, carbonate bridging provides durable solid-phase thermal pathways alongside structural reinforcement (Chapter 5), while expanded graphite offers a route to comparable or greater conductivity gains at lower chemical intensity (Chapter 6). In underground electrical corridors, ICP treatments could be applied *in situ* and, where additives are used, blended directly with excavated native soils, avoiding the extensive material removal and replacement associated with cement-based backfills. In nuclear waste storage contexts, $CaCO_3$–additive composites offer a potential route to engineered backfills that combine mechanical stability with controlled heat dissipation.

While the conductivity gains demonstrated in Chapters 5–6 are significant, they were established in a uniform, dry quartz matrix chosen for experimental control and XCT

compatibility. In field conditions, saturation state, soil heterogeneity, and groundwater flow will alter both conductive and convective heat-transfer pathways, and therefore the magnitude and spatial distribution of thermal enhancement.

7.4. ICP can create thermal energy storage materials

Objective 5 is extended from thermal conductivity enhancement to thermal energy storage through the incorporation of EG and EG-PCM composites. While ICP-treated materials without additives already combine structural stability, controlled permeability, and improved thermal conductivity, the introduction of EG-based composites enables an additional functionality: latent heat storage. By buffering temperature changes through phase change, these materials can store and release heat over narrow temperature ranges, extending the role of biocemented media beyond heat transfer alone.

This behaviour is directly relevant to subsurface thermal energy storage concepts such as borehole thermal energy storage (BTES) and sand-based thermal batteries, where both efficient heat transport and temporary heat retention are required (Drake Landing Solar Community, n.d.; Polar Night Energy, n.d.).

7.4.1 Sensible heat storage in ICP-treated materials

Sensible heat storage systems, such as BTES and sand-based thermal batteries, rely on granular or porous media to transfer heat by conduction and store energy as sensible heat. Their efficiency is dictated by thermal conductivity and heat capacity (Vyas & Kushwah, 2023), making material selection critical for long-term performance.

In BTES, system efficiency depends not only on material conductivity but on how thermal gradients and fluid pathways evolve during repeated charging and discharging. Unlike cementitious grouts that fully seal boreholes and suppress both conduction and convection, EICP-treated materials retain controlled permeability, enabling conductive heat transfer alongside selective convective contributions where advantageous. This combination allows thermal performance to be enhanced without sacrificing mechanical stability or hydraulic functionality.

Additionally, bio-cemented materials incorporating electrically conductive additives such as expanded graphite could, in principle, support resistive heating, allowing thermal energy to be generated *in situ* from surplus renewable electricity. This suggests a potential route for integrating biomineralisation with electrical-to-thermal energy storage concepts, including seasonal heat storage and grid-balancing systems. Figure 7.2 sketches a conceptual BTES configuration in which biomineralised backfills provide both structural stability and enhanced thermal functionality.

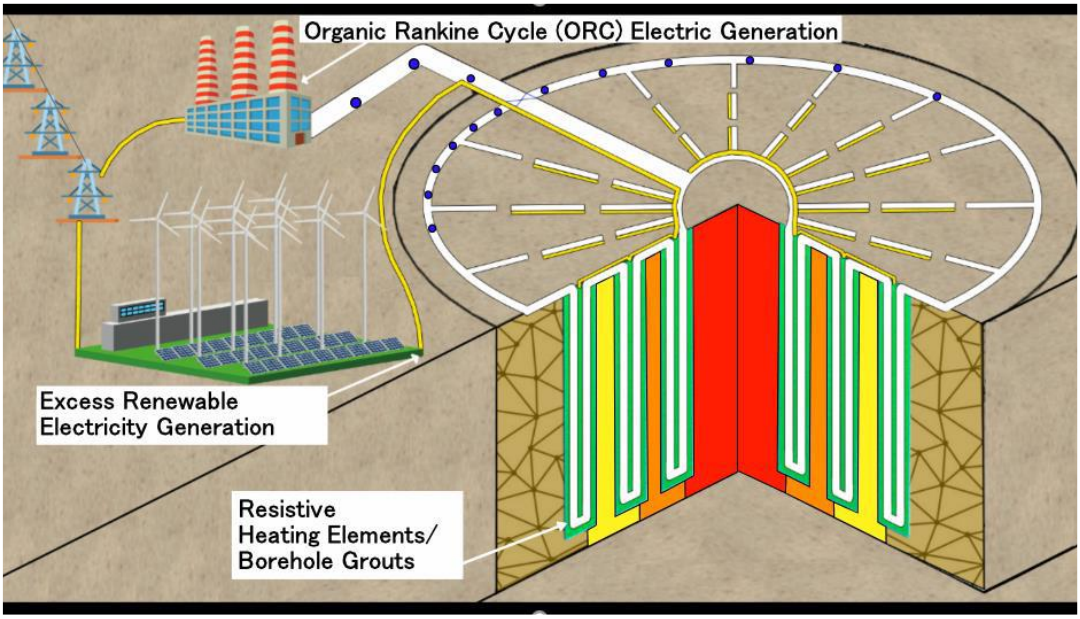

Figure 7.2 Concept for BTES with biomineralised, and additive-enhanced backfill. Excess renewable electricity is routed to resistive heating elements/borehole grouts to charge a circular BTES field (white loop). Biomineralised sand provides structural stability and enhanced conductivity; zones with expanded graphite (EG) and EG-PCM composites can increase thermal conductivity and introduce latent heat buffering. Stored heat is later recovered to drive an Organic Rankine Cycle (ORC) generator. Still frame from author-produced animation; see Appendix D3 for link and details.

7.4.2 Latent heat storage with conductive additives

Latent heat storage systems utilise PCMs to store and release thermal energy during solid-liquid transitions. Unlike sensible heat storage, which depends solely on temperature gradients, PCMs can absorb and release substantial quantities of heat over a narrow temperature interval, making them attractive for passive thermal regulation and buffering applications.

However, the deployment of PCMs in engineering materials is constrained by several practical limitations, including low intrinsic thermal conductivity, phase segregation, and leakage during repeated cycling (Sharshir et al., 2023).

The biocemented EG-PCM composites developed in Chapter 6 provide a novel route for integrating latent heat storage within mechanically stable and thermally conductive matrices. Infrared thermography demonstrated that paraffin-infused expanded graphite exhibited delayed heating and extended cooling plateaus, consistent with phase-change behaviour, with no observable leakage under the experimental cycling conditions tested. These observations highlight three key implications of ICP-stabilised PCM systems:

- **Structural confinement and stability** – Carbonate precipitation within the EG network provides physical confinement of the PCM, which may mitigate leakage and improve durability relative to unconstrained PCM composites.
- **Thermal buffering through phase change** – The observed heating and cooling plateaus indicate effective latent heat absorption and release, enabling passive moderation of temperature fluctuations (Darkwa et al., 2006; Kuznik et al., 2008).
- **Design flexibility for thermal storage media** – The combination of mechanical integrity, enhanced conductivity, and latent heat capacity suggests a route toward compact and structurally robust thermal energy storage elements, distinct from conventional bulk TES materials (Sunamp, n.d.).

Potential application domains span both subsurface and near-surface systems. In subsurface contexts, EG-PCM composites could enhance borehole heat exchangers, BTES installations, and sand-battery concepts by combining improved heat transfer with thermal buffering. In near-surface infrastructure, such materials may offer thermal regulation benefits for underground power cables or building elements where mechanical stability and controlled heat dissipation are required.

Together, these findings advance Objective 5 by extending bio-cementation from thermal conductivity enhancement toward latent heat storage, while also linking to Objectives 2 and 4 through the demonstrated influence of additive selection, microstructure, and permeability control. Although demonstrated at laboratory scale, the results position ICP-stabilised EG and EG-PCM composites as promising candidates for engineered thermal buffering. Scaling to field applications will depend on long-term cycling durability, coupled heat- and mass-transfer modelling at system scale, and manufacturability within heterogeneous native soils.

7.5. Recommendations for Future Research

Building on the findings of Chapters 3–6, several priority research directions emerge for advancing biocementation from laboratory validation toward field-scale deployment.

7.5.1 Scaling density driven mixing & permeability contrast for CO_2 storage

Chapter 3 showed that density driven mixing can spatially target carbonate precipitation, offering a route to engineered permeability control in CO_2 storage. Future work should extend these mechanisms to field-scale injection models. CFD and reactive transport simulations at well scale are needed to capture multiphase CO_2 flow, geochemical reactions, and precipitation dynamics. Comparative EICP/MICP studies under CO_2-rich conditions will clarify dissolution risks and long-term seal stability. Beyond seal formation, ICP could also engineer spatial contrasts that improve CO_2 sweep efficiency. Pulsation-based injection (Section 4.4) requires further optimisation, particularly testing a range of frequencies and amplitudes to maximise mixing and precipitation uniformity.

7.5.2 Optimizing enzyme sources & treatment efficiency for cost-effective implementation

While soybean-derived urease proved effective in achieving controlled precipitation and favourable strength-permeability trade-offs (Chapters 5–6), further work is required to improve robustness, cost efficiency, and long-term durability under field-relevant conditions. Key priorities include:

- **Durability testing** of EICP-treated materials under environmental exposure, including freeze–thaw cycling, wet–dry cycling, and seasonal temperature variation, to assess long-term mechanical and hydraulic stability.
- **Refinement of low-cost enzyme sources and preparation methods**, focusing on reproducibility, organic content control, and scalability. While alternative soybean-derived fractions (e.g. hulls) may offer cost advantages, their ureolytic performance and impact on precipitation behaviour require evaluation.
- **Effluent management and recycling strategies**, including recovery and reuse of ammonium-rich effluent, to reduce reagent demand and improve the overall environmental and economic viability of EICP.

Reducing reagent intensity while maintaining controlled carbonate precipitation and durability is essential for translating soybean-based EICP from laboratory demonstrations to practical ground engineering and subsurface applications.

7.5.3 Enhancing geothermal applications & thermal energy storage

Significant thermal gains were achieved through both carbonate contact bridging and the incorporation of conductive and phase-change additives (Chapters 5–6), demonstrating multiple pathways for tailoring heat transfer and storage behaviour in biocemented materials. To translate these findings toward geothermal and thermal energy storage applications, several research priorities emerge:

- **Long-term performance under repeated thermal cycling**, including mechanical stability, permeability evolution, and retention of thermal functionality in BTES, GSHPs, and energy pile systems.
- **Optimisation of additive dispersion and cementation at larger scales**, with particular focus on controlling anisotropic versus isotropic heat transfer as a function of packing, compaction, and treatment strategy.

- **Evaluation of paraffin-infused EG composites across a range of loadings and phase-change temperatures**, to quantify trade-offs between latent heat capacity, conductivity, and structural integrity.
- **Development of coupled thermal-hydraulic-mechanical models** to simulate system-level performance, enabling optimisation of treatment intensity, additive content, and spatial placement for specific geothermal and storage applications.

Scaling these strategies will be essential for integrating biocementation into renewable heat storage and dissipation systems, where material performance must be evaluated not only at specimen scale but within interacting thermal and hydraulic fields.

7.5.4 Transitioning ICP to field applications

The next stage in advancing induced carbonate precipitation is validation under representative field conditions, where geological heterogeneity, scale, and operational constraints dominate performance. Based on the findings of this thesis, several priorities emerge:

- Demonstrating efficacy across diverse soil types and engineering contexts, including CO_2 wells, geothermal boreholes, and permeable pavement systems, to assess how grain size distribution, mineralogy, and saturation state influence transport and precipitation behaviour.
- Integrating biomineralisation into established ground improvement and infrastructure workflows, ensuring compatibility with existing drilling, grouting, and monitoring practices rather than requiring bespoke deployment.
- Assessing long-term environmental behaviour, including treatment durability, reversibility, and the fate of ammonium- and chloride-rich effluents under realistic hydrogeochemical conditions.

Beyond externally supplied enzymes or microbes, future work could explore whether native ureolytic microbial communities in deep subsurface environments can be stimulated to induce carbonate precipitation at greater transport distances, potentially reducing material inputs and improving scalability.

Together, these priorities reinforce that ICP should not be viewed as a single, fixed technology, but as a family of related approaches whose effectiveness depends on how biochemical formulation, injection strategy, and substrate characteristics are

combined. Table 7.1 therefore synthesises the findings of this thesis by mapping ICP variants to the engineering contexts for which they are best suited, highlighting both opportunities and trade-offs.

Table 7.1 Recommended ICP methods for different engineering applications

Application	**Best ICP Route**	**Notes/ Trade-offs**
CCS well sealing, micro-annuli	MICP	Effective for highly localised fracture and annulus sealing; transport range limited by microbial attachment and filtration.
CCS sweep efficiency, reservoir barriers	EICP (density-driven mixing)	Enables more distributed and anisotropic permeability control over tens of metres; performance sensitive to heterogeneity and injection design.
Soil stabilisation, geotechnical reinforcement	Soybean EICP	Provides strength enhancement while retaining drainage; enzyme preparation and organic content are critical.
Urban permeable pavements	Soybean EICP	Maintains infiltration capacity while achieving load-bearing performance; durability under traffic loading requires validation.
Geothermal (energy piles, GSHPs, BTES)	Soybean EICP ± additives	Balances conductivity enhancement and permeability retention; treatment intensity and additive loading trade off against cost.
Thermal energy storage	Soybean EICP + EG/PCM	Enables combined sensible and latent heat storage; long-term cycling durability and scale-up remain open challenges.

7.5.5 Final Remarks

This thesis has advanced the understanding of microbial and enzyme induced carbonate precipitation from pore-scale mechanisms to material-scale performance, showing how mixing dynamics, enzyme formulation, and additive integration govern both treatment efficiency and functional outcomes. Collectively, the findings demonstrate that biocementation is not only a ground improvement technique but a platform for engineering multifunctional materials with coupled structural, hydraulic, and thermal properties.

By integrating time-lapse imaging, controlled laboratory treatments, and application-oriented analysis, this work establishes a foundation for translating ICP from laboratory validation toward real-world systems. The results highlight the central trade-offs inherent to treatment design – between strength and permeability, conductivity and durability, cost and sustainability – and provide a mechanistic framework to navigate these decisions in practice.

In doing so, the thesis reframes biomineralisation as more than a niche soil improvement method. It positions ICP as a versatile and tuneable technology with relevance to carbon sequestration, geothermal energy, and climate-resilient infrastructure, offering credible pathways toward more sustainable subsurface engineering in a rapidly changing world.

Appendices

Appendix A: Image Processing and Quantitative XCT Analysis

This appendix provides supplementary detail on the XCT image processing and quantitative analysis procedures used throughout Chapters 3–6. The purpose is to document the image pre-processing, segmentation, and resolution-handling steps that underpin pore-scale quantification, without duplicating the core methodological discussion presented in Chapter 2.

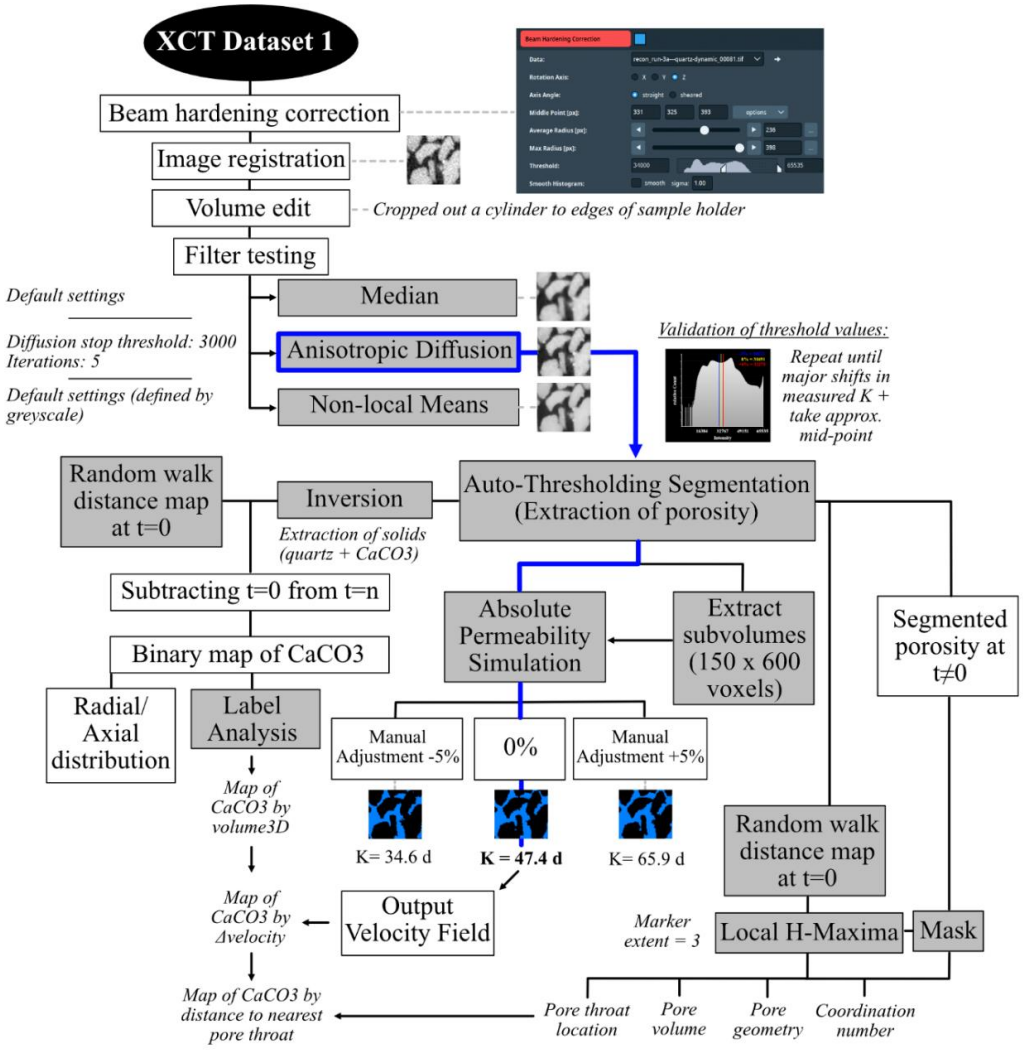

Figure A1 Image Processing and Analysis Workflow for Chapter 3

The image processing workflow applied to the datasets analysed in Chapter 3 is summarised in Fig. A1. This workflow was applied consistently across all time points to ensure comparability of pore-scale metrics during progressive $CaCO_3$ precipitation.

Although the absolute grayscale value associated with the global auto-threshold varied between samples, the threshold consistently intersected the same relative position at the material interface (Fig. A1, inset). The selected threshold (yellow line) therefore represents a stable boundary between pore space and solid phases (quartz sand and $CaCO_3$), despite variations in scan intensity and material composition.

A similar segmentation strategy was applied to the 6.6 mm diameter specimens analysed in Chapter 5, as illustrated in Fig. A2. While absolute threshold values differed between samples, the relative position of the pore–solid interface remained invariant, enabling consistent phase separation across datasets with differing $CaCO_3$ contents.

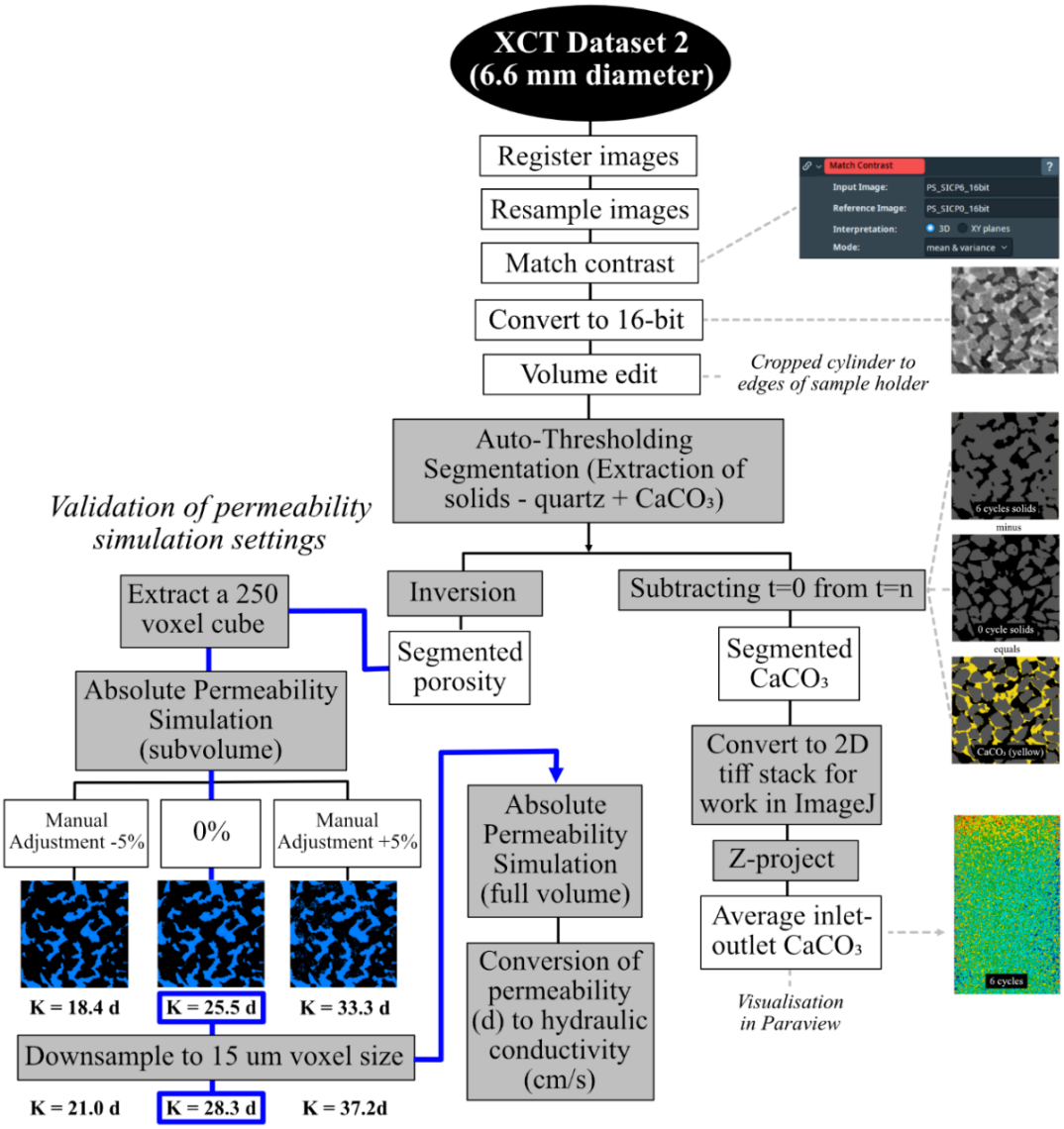

Figure A2 Image Processing and Analysis workflow for 6.6mm diameter micro-CT cell

For quantitative pore-scale analysis, pore sphericity was calculated using the following expression:

$$\psi = \frac{\pi^{1/3}(6V)^{2/3}}{A}$$

Where V is volume and A is the pore surface area. To ensure consistent segmentation across samples with varying degrees of $CaCO_3$ precipitation, greyscale normalisation was applied using the *Match Contrast* module in Avizo.

As the number of SB-EICP treatment cycles increased, overall sample density rose due to progressive $CaCO_3$ precipitation. Although all XCT scans were acquired under

identical energy settings (60 kV), this resulted in systematic shifts in absolute greyscale values between datasets. Histogram matching to a common reference scan enabled consistent thresholding of pore and solid phases across all time points.

The workflow for image processing and analysis for the 27mm diameter XCT samples (Section 5.4.5) is presented in Fig. A3.

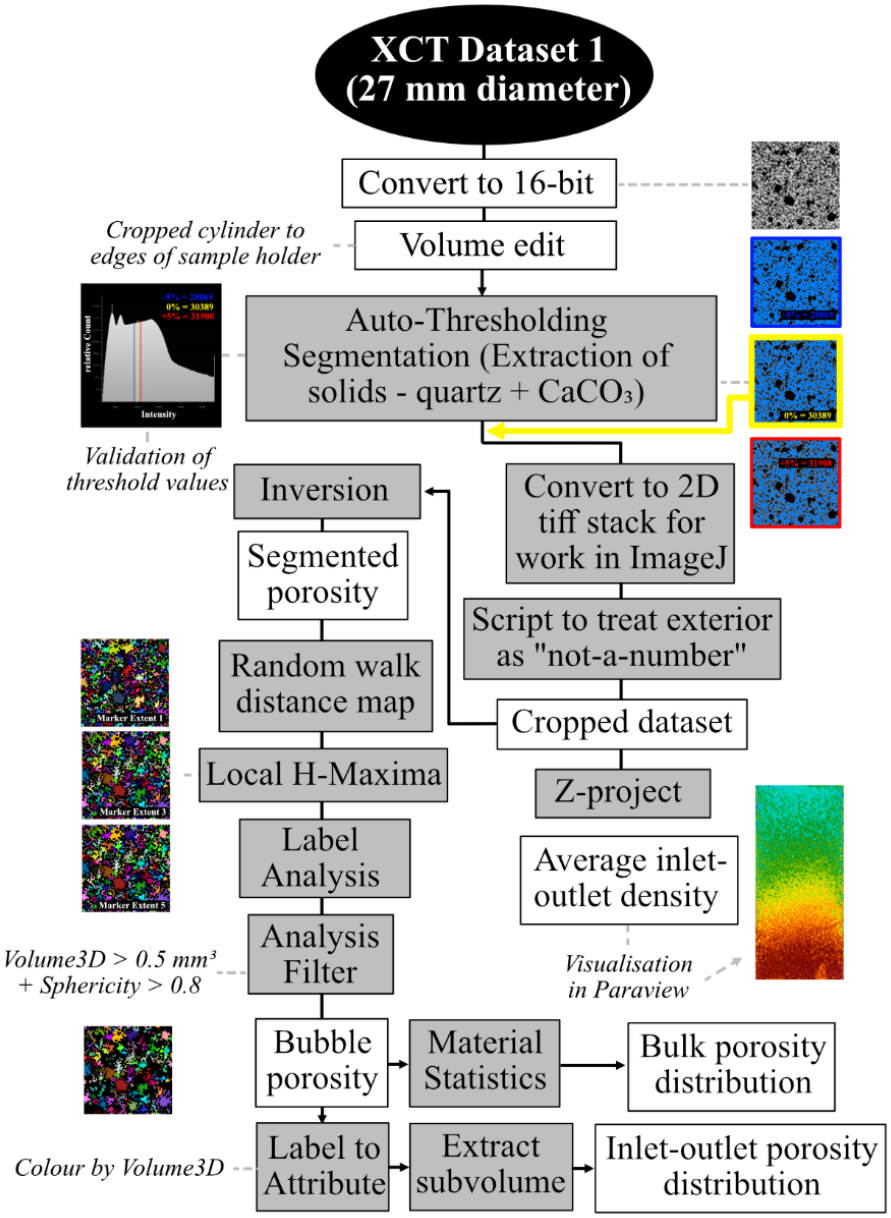

Figure A3 Image Processing and Analysis workflow for 27 mm diameter columns

The processing steps used to prepare XCT datasets for the analyses presented in Chapter 6 are summarised below. These steps were applied consistently to all samples to enable comparison of density and porosity distributions along the inlet–outlet axis:

- Cropping of raw images and manual alignment of top and bottom scans
- Conversion from 32-bit to 16-bit unsigned format, with rescaling to a common greyscale range (–40 to 120 for paraffin-containing samples)
- Removal of poorly reconstructed overlap regions (300 slices from the bottom of the upper scan and 300 slices from the top of the lower scan)
- Image registration using normalised mutual information
- Resampling and merging of aligned images using standard interpolation
- Cropping to the physical bounds of the specimen (Fig. A4)
- Removal of the sample holder using the *Volume Edit* module
- Greyscale normalisation using *Match Contrast*, with the MICP EG4 sample selected as the reference
- Automated thresholding to segment dense solids (quartz sand and $CaCO_3$)
- Export of the dense solid field as TIFF stacks for further analysis

The segmented TIFF stacks were imported into ImageJ, where pixels outside the cylindrical specimen boundary were masked as *not-a-number*. Images were re-sliced, rotated by 90°, and averaged along the depth axis using the *Z-project* function. Resulting density fields were visualised in ParaView to highlight spatial variations along the inlet–outlet direction.

To obtain porosity fields, the dense solid phase was inverted in Avizo. The minimum and maximum porosity values, determined using the Image Statistics module, were used to rescale all datasets to a common range (0–100), where 0 represents air-filled pore space and 100 represents segmented solid. Normalised inlet–outlet density profiles were then extracted and plotted using the Image Statistics outputs.

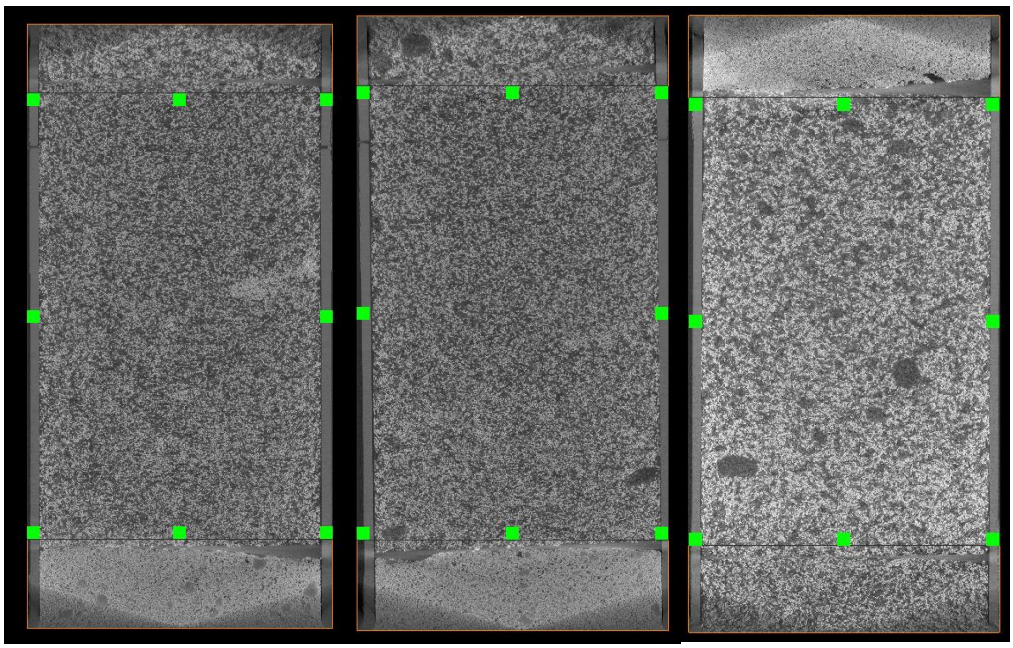

Figure A4 Examples of cropped regions from merged datasets.

Appendix B: Flow Modelling Framework and Assumptions

This appendix provides supplementary detail on the preparation and execution of the fluid mixing model described in Chapters 3 and 4. The overall modelling workflow implemented in OpenFOAM is summarised in Fig. B1, while the key model parameters and numerical settings used in the simulations are listed in Table B1.

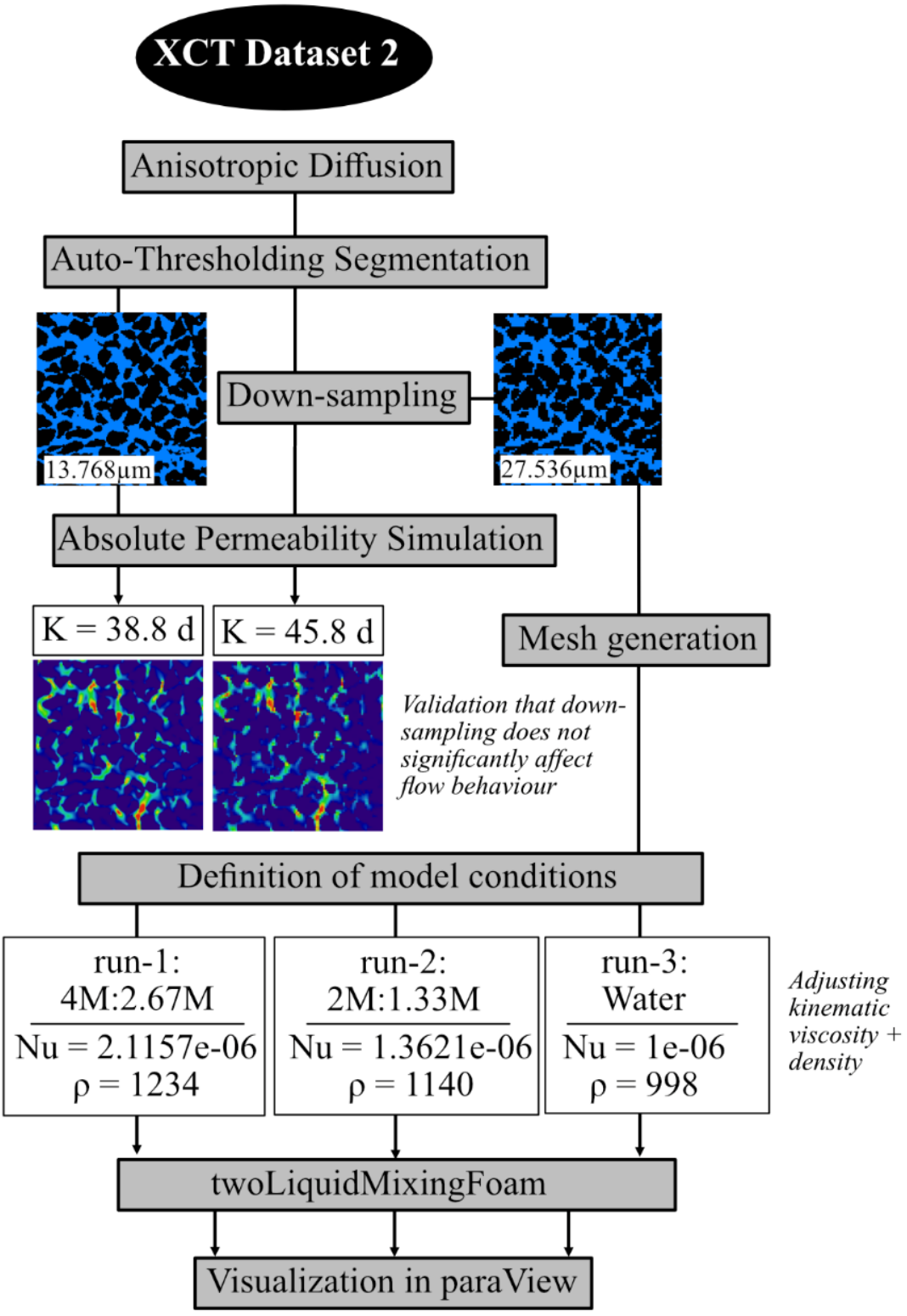

Figure B1 Image processing, mesh preparation, and model setup for the CFD mixing simulations described in Chapter 3.

Table B1 OpenFOAM mixing model parameters and settings

Parameter	Description	Value
Solver	Name of the solver used	twoLiquidMixingFoam
Time discretization	Temporal scheme for time-stepping	Euler
Gradient scheme	Scheme for gradient calculations	Gauss linear
Divergence scheme	- div(rhoPhi,U)	Gauss linear
	- div(phi,alpha)	Gauss vanLeer
	- div(phi,k)	Gauss limitedLinear 1
	- div(((rho*nuEff)*dev2(T(grad(U)))))	Gauss linear
Laplacian scheme	Scheme for laplacian calculations	Gauss linear corrected
Interpolation scheme	Scheme for interpolating values	Linear
Surface-normal gradient scheme	Surface-normal gradient calculation method	Corrected
Solver algorithm	Algorithm used for solving equations	PIMPLE
Convergence criterion	Residual tolerance for p_rgh (pressure)	Tolerance: 1e-7, relTol: 0.01
	Residual tolerance for U (velocity)	Tolerance: 1e-7, relTol: 0.1
Solver for pressure (p_rgh)	Solver type for pressure equations	GAMG
Solver for velocity (U)	Solver type for velocity equations	smoothSolver
Smoother	Type of smoother used	GaussSeidel
Number of correctors	Number of PIMPLE correctors	2
Number of outer correctors	Number of outer correctors for coupled solvers	1
Simulation start time	Starting time of the simulation	0
Simulation end time	Ending time of the simulation	5*
Time step (deltaT)	Time step size for the simulation	0.0001
Write interval	Frequency of data output	0.1
Maximum Courant number	Maximum allowed Courant number	1
Maximum Alpha Courant number	Maximum allowed Courant number for alpha phase	0.5
Viscosity of enzyme solution (Pa·s)	Dynamic viscosity of the fluid	1.00E-06
Density of enzyme solution (kg m^{-3})	Fluid density	998
Viscosity of cementing solution (Pa·s)	Run 1 - 4M urea, 2.67M $CaCl_2$	2.12E-06
	Run 2 - 2M urea, 1.33M $CaCl_2$	1.36E-06
	Run 3 - water	1.00E-06
Density of cementing solution (kg m^{-3})	Run 1 - 4M urea, 2.67M $CaCl_2$	1234
	Run 2 - 2M urea, 1.33M $CaCl_2$	1140
	Run 3 - water	998
Turbulence model	Turbulence model used	Laminar
Gravitational acceleration (m s^{-2})	Magnitude and direction of gravity	-9.81
* Due to limitations on maximum job size imposed by the supercomputer cluster, simulations were executed in consecutive 5 s intervals.		

For pulsed flow simulations, time-varying inlet velocity boundary conditions were implemented using tabulated *uniformFixedValue* profiles in OpenFOAM. The key parameters defining the pulse structure are summarised in Table B2, while the resulting velocity waveforms are illustrated in Fig. 4.9.

Table B2 Inlet velocity boundary condition parameters used in pulsed flow simulations.

Parameter	Value	Notes
Boundary condition type	uniformFixedValue (tabulated)	Applied at both inlets
Pulse frequency	100 Hz	All pulsed cases
Pulse duration	100 µs	See Fig. 4.9
Peak inlet velocity	1.05 m s^{-1}	Matches steady-flow case
Base inlet velocity	0 m s^{-1}	During pulse off-period
Ramp duration	1 µs	Linear ramp to avoid numerical discontinuities
Phase relationship	In-phase / out-of-phase	Depends on injection strategy
Non-pulsed inlet	Constant velocity	Hybrid case only

Appendix C: Conversion Factors for Non-Standard UCS Specimens

The UCS values of the 60 mm diameter samples presented in Chapter 5 were corrected for non-standard geometry using the Turk and Dearman (1986) factor of 1.024, which adjusts results to reflect a standard height-to-diameter ratio of 2:1. For samples SB3, SB6, and MICP9, error bars were set to ±10% of the corrected UCS to conservatively represent variability arising from application of this correction factor.

Sample SB9 required a different treatment. It underwent two UCS tests. In the first test, the sample reached the machine's maximum load of 25,000 N without failing. This corresponds to an uncorrected UCS of 8.844 N/mm², calculated using the cross-sectional area of the 60 mm diameter sample. After applying the Turk and Dearman correction, this yields a corrected UCS lower bound of 8.637 N/mm².

In the second test, the sample did fail under load, producing a corrected UCS of 7.569 N/mm².

An XCT scan taken between the two tests revealed no visible microcracking or structural damage, suggesting the first test did not compromise the integrity of the sample. Therefore, the first test result was taken as the best estimate of the true UCS, and 8.637 N/mm² was used as the plotted value for SB9 in Figure 7.

The error bars for SB9 were defined as:

- Lower bound: the difference between the two corrected UCS values
  $8.637 - 7.569 =$ **1.07** MPa
- Upper bound: a conservative 10% uncertainty margin
  $0.10 \times 8.637 =$ **0.864** MPa

This results in asymmetric error bars, reflecting both the tested performance and the inherent uncertainty in estimating the true failure point of a sample that did not initially break. While the actual UCS may exceed 8.637 N/mm², this approach provides a conservative estimate consistent with the rest of the dataset.

Appendix D: Supplementary Media

This appendix provides links to supplementary video material referenced in the thesis, included to support qualitative visualisation of experimental processes and material behaviour that cannot be fully conveyed through static figures.

D1: Time-lapse video of optical microscopy showing the full 4-hour SBEICP progression is available at https://vimeo.com/1058970225

D2: Water droplets on SB25 sample to demonstrate absorbance/permeability. Available at https://vimeo.com/1115640502

D3: Video of Concept for BTES with biomineralised, additive-enhanced backfill, From: https://vimeo.com/763753164

References:

Achal, V., & Mukherjee, A. (2015). A review of microbial precipitation for sustainable construction. *Construction and Building Materials*, *93*, 1224–1235. https://doi.org/10.1016/j.conbuildmat.2015.04.051

Adebayo, P., Beragama Jathunge, C., Darbandi, A., Fry, N., Shor, R., Mohamad, A., Wemhöner, C., & Mwesigye, A. (2024). Development, modeling, and optimization of ground source heat pump systems for cold climates: A comprehensive review. *Energy and Buildings*, *320*. https://doi.org/10.1016/j.enbuild.2024.114646

Ahenkorah, I., Rahman, M. M., Karim, M. R., Beecham, S., & Saint, C. (2021). A Review of Enzyme Induced Carbonate Precipitation (EICP): The Role of Enzyme Kinetics. *Sustainable Chemistry*, *2*(1), 92–114. https://doi.org/10.3390/suschem2010007

Ahmed, A. A., Assadi, M., Kalantar, A., Sliwa, T., & Sapińska-Śliwa, A. (2022). A Critical Review on the Use of Shallow Geothermal Energy Systems for Heating and Cooling Purposes. *Energies*, *15*(12). https://doi.org/10.3390/en15124281

Al-Thawadi, S., & Cord-Ruwisch, R. (2012). Calcium Carbonate Crystals Formation by Ureolytic Bacteria Isolated from Australian Soil and Sludge. *Journal of Advanced Science and Engineering Research*, *2*, 12–26.

Almajed, A., A. (2017). *Enzyme Induced Carbonate Precipitation (EICP) for Soil Improvement* Arizona State University]. https://www.proquest.com/dissertations-theses/enzyme-induced-carbonate-precipitation-eicp-soil/docview/1944515215/se-2

Almajed, A., Tirkolaei, H. K., Kavazanjian, E., Jr., & Hamdan, N. (2019). Enzyme Induced Biocementated Sand with High Strength at Low Carbonate Content. *Sci Rep*, *9*(1), 1135. https://doi.org/10.1038/s41598-018-38361-1

Alotaibi, E., Arab, M. G., Abdallah, M., Nassif, N., & Omar, M. (2022). Life cycle assessment of biocemented sands using enzyme induced carbonate precipitation (EICP) for soil stabilization applications. *Sci Rep*, *12*(1), 6032. https://doi.org/10.1038/s41598-022-09723-7

Arab, M. G., Refaei, M., Alotaibi, E., Omar, M., Almajed, A., & Haridy, S. (2024). Optimizing the Compressive Strength of Sodium Alginate-Modified EICP-Treated Sand Using Design of Experiments. *Journal of Materials in Civil Engineering*, *36*(4). https://doi.org/10.1061/jmcee7.Mteng-16400

Armstrong, R., & Ajo-Franklin, J. (2011). Investigating biomineralization using synchrotron based X-ray computed microtomography. *Geophysical Research Letters*, *38*(8), n/a–n/a. https://doi.org/10.1029/2011gl046916

B.V Venkatarama Reddy, K. S. J. (2003). Embodied energy of common and alternative building materials and technologies. *Energy and Buildings*, *35*(2), 129–137. https://doi.org/https://doi.org/10.1016/S0378-7788(01)00141-4

Bao, J., Xu, W., & Zhou, D. (2025). Operational thresholds of urease-mediated microbial cementation: Multivariate optimization and field validation in ambient groundwater environments. *PLoS One*, *20*(8), e0330481. https://doi.org/10.1371/journal.pone.0330481

Baum, D., Weaver, J. C., Zlotnikov, I., Knotel, D., Tomholt, L., & Dean, M. N. (2019). High-Throughput Segmentation of Tiled Biological Structures using Random-Walk Distance Transforms. *Integr Comp Biol*, *59*(6), 1700–1712. https://doi.org/10.1093/icb/icz117

References

Baveye, P. C., Laba, M., Otten, W., Bouckaert, L., Dello Sterpaio, P., Goswami, R. R., Grinev, D., Houston, A., Hu, Y., Liu, J., Mooney, S., Pajor, R., Sleutel, S., Tarquis, A., Wang, W., Wei, Q., & Sezgin, M. (2010). Observer-dependent variability of the thresholding step in the quantitative analysis of soil images and X-ray microtomography data. *Geoderma*, *157*(1-2), 51–63. https://doi.org/10.1016/j.geoderma.2010.03.015

Belatrache, D., Bentouba, S., & Bourouis, M. (2017). Numerical analysis of earth air heat exchangers at operating conditions in arid climates. *International Journal of Hydrogen Energy*, *42*(13), 8898–8904. https://doi.org/10.1016/j.ijhydene.2016.08.221

Bernard, D., Guillon, O., Combaret, N., & Plougonven, E. (2011). Constrained sintering of glass films: Microstructure evolution assessed through synchrotron computed microtomography. *Acta Materialia*, *59*(16), 6228–6238. https://doi.org/10.1016/j.actamat.2011.06.022

Bump, A. P., Bakhshian, S., Ni, H., Hovorka, S. D., Olariu, M. I., Dunlap, D., Hosseini, S. A., & Meckel, T. A. (2023). Composite confining systems: Rethinking geologic seals for permanent CO2 sequestration. *International journal of greenhouse gas control*, *126*. https://doi.org/10.1016/j.ijggc.2023.103908

Business Analytiq. (2024). *Urea Price Index*. https://businessanalytiq.com/procurementanalytics/index/urea-price-index/

Caniani, D., Calace, S., Mazzone, G., Caivano, M., Mancini, I. M., Greco, M., & Masi, S. (2018). Removal of Hydrocarbons from Contaminated Soils by Using a Thermally Expanded Graphite Sorbent. *Bull Environ Contam Toxicol*, *101*(6), 698–704. https://doi.org/10.1007/s00128-018-2395-4

Carmona, J. P. S. F., Oliveira, P. J. V., & Lemos, L. J. L. (2016). Biostabilization of a Sandy Soil Using Enzymatic Calcium Carbonate Precipitation. *Procedia Engineering*, *143*, 1301–1308. https://doi.org/10.1016/j.proeng.2016.06.144

Cermak, M., Perez, N., Collins, M., & Bahrami, M. (2020). Material properties and structure of natural graphite sheet. *Sci Rep*, *10*(1), 18672. https://doi.org/10.1038/s41598-020-75393-y

Chedburn, L., Underhill, J. R., Head, S., & Jamieson, R. (2022). The critical evaluation of carbon dioxide subsurface storage sites: Geological challenges in the depleted fields of Liverpool Bay. *AAPG Bulletin*, *106*(9), 1753–1789. https://doi.org/10.1306/07062221120

Chen, R., Li, G., Mi, Z., & Wei, K. (2024). Experimental and simulation study of calcium carbonate non-uniform distribution characteristics of bio-cemented sand. *Case Studies in Construction Materials*, *21*. https://doi.org/10.1016/j.cscm.2024.e03926

Cheng, L., Afur, N., & Shahin, M. A. (2021). Bio-Cementation for Improving Soil Thermal Conductivity. *Sustainability*, *13*(18). https://doi.org/10.3390/su131810238

Cheng, L., & Cord-Ruwisch, R. (2014). Upscaling Effects of Soil Improvement by Microbially Induced Calcite Precipitation by Surface Percolation. *Geomicrobiology Journal*, *31*(5), 396–406. https://doi.org/10.1080/01490451.2013.836579

Cheng, L., Cord-Ruwisch, R., & Shahin, M. A. (2013). Cementation of sand soil by microbially induced calcite precipitation at various degrees of saturation. *Canadian Geotechnical Journal*, *50*(1), 81–90. https://doi.org/10.1139/cgj-2012-0023

Cheng, L., Qian, C. X., & Wang, R. X. (2007). Study on the Mechanism of Calcium Carbonate Formation Induced by Carbonate-mineralization Microbe. *Acta Chimica Sinica*, *61*(19), 2133–2138.

References

Cheng, L., Shahin, M. A., & Chu, J. (2018). Soil bio-cementation using a new one-phase low-pH injection method. *Acta Geotechnica*, *14*(3), 615–626. https://doi.org/10.1007/s11440-018-0738-2

Chongxi, B., & Zhang, Z. (2024). Carbon emission quantification analysis of excavation engineering under road transport conditions. *PLoS One*, *19*(12), e0315765. https://doi.org/10.1371/journal.pone.0315765

Chu, J., Ivanov, V., Stabnikov, V., & Li, B. (2013). Microbial method for construction of an aquaculture pond in sand. *Géotechnique*, *63*(10), 871–875. https://doi.org/10.1680/geot.SIP13.P.007

Chunxiang, Q., Jianyun, W., Ruixing, W., & Liang, C. (2009). Corrosion protection of cement-based building materials by surface deposition of CaCO3 by Bacillus pasteurii. *Materials Science and Engineering: C*, *29*(4), 1273–1280. https://doi.org/10.1016/j.msec.2008.10.025

Ciurli, S., Marzadori, C., Benini, S., Deiana, S., & Gessa, C. (1996). Urease from the soil bacterium Bacillus pasteurii: immobilization on Ca-polygalacturonate. *Soil Biology and Biochemistry*, *28*(6), 811–817.

Civan, F. (2023). Reservoir stress-induced formation damage: formation compaction, subsidence, sanding tendency, sand migration, prediction and control, and gravel-pack damage. In *Reservoir Formation Damage* (pp. 457–488). https://doi.org/10.1016/b978-0-323-90228-1.00020-0

Claria, J. J., Goldsztein, G. H., & Santamarina, J. C. (2012). AC Diffusion: Transport in Porous Networks Subjected to Zero-Time-Average Advective Flow. *Transport in Porous Media*, *93*(1), 51–61. https://doi.org/10.1007/s11242-012-9943-x

Cnudde, V., & Boone, M. N. (2013). High-resolution X-ray computed tomography in geosciences: A review of the current technology and applications. *Earth-Science Reviews*, *123*, 1–17. https://doi.org/10.1016/j.earscirev.2013.04.003

Comadran-Casas, C., Schaschke, C. J., Akunna, J. C., & Jorat, M. E. (2022). Cow urine as a source of nutrients for Microbial-Induced Calcite Precipitation in sandy soil. *J Environ Manage*, *304*, 114307. https://doi.org/10.1016/j.jenvman.2021.114307

Cui, M.-J., Lai, H.-J., Hoang, T., & Chu, J. (2020). One-phase-low-pH enzyme induced carbonate precipitation (EICP) method for soil improvement. *Acta Geotechnica*, *16*(2), 481–489. https://doi.org/10.1007/s11440-020-01043-2

Czapp, S., & Ratkowski, F. (2021). Optimization of Thermal Backfill Configurations for Desired High-Voltage Power Cables Ampacity. *Energies*, *14*(5). https://doi.org/10.3390/en14051452

Dadda, A., Geindreau, C., Emeriault, F., du Roscoat, S. R., Garandet, A., Sapin, L., & Filet, A. E. (2017). Characterization of microstructural and physical properties changes in biocemented sand using 3D X-ray microtomography. *Acta Geotechnica*, *12*(5), 955–970. https://doi.org/10.1007/s11440-017-0578-5

Dadda, A., Geindreau, C., Emeriault, F., Rolland du Roscoat, S., Esnault Filet, A., & Garandet, A. (2018). Characterization of contact properties in biocemented sand using 3D X-ray micro-tomography. *Acta Geotechnica*, *14*(3), 597–613. https://doi.org/10.1007/s11440-018-0744-4

Darkwa, K., O'Callaghan, P. W., & Tetlow, D. (2006). Phase-change drywalls in a passive-solar building. *Applied Energy*, *83*(5), 425–435. https://doi.org/10.1016/j.apenergy.2005.05.001

Davit, Y., Iltis, G., Debenest, G., Veran-Tissoires, S., Wildenschild, D., Gerino, M., & Quintard, M. (2011). Imaging biofilm in porous media using X-ray computed microtomography. *J Microsc*, *242*(1), 15–25. https://doi.org/10.1111/j.1365-2818.2010.03432.x

References

De Muynck, W., Verbeken, K., De Belie, N., & Verstraete, W. (2013). Influence of temperature on the effectiveness of a biogenic carbonate surface treatment for limestone conservation. *Appl Microbiol Biotechnol*, *97*(3), 1335–1347. https://doi.org/10.1007/s00253-012-3997-0

DeJong, J. T., Fritzges, M. B., & Nüsslein, K. (2006). Microbially Induced Cementation to Control Sand Response to Undrained Shear. *Journal of Geotechnical and Geoenvironmental Engineering*, *132*(11), 1381–1392. https://doi.org/doi:10.1061/(asce)1090-0241(2006)132:11(1381)

DeJong, J. T., Martinez, B. C., Mortensen, B. M., Nelson, D. C., Waller, J. T., Weil, M. H., Ginn, T. R., Weathers, T., Barkouki, T., Fujita, Y., Redden, G., Hunt, C., Major, D., & Tanyu, B. (2009). Upscaling of bio-mediated soil improvement. In *Proceedings of the 17th International Conference on Soil Mechanics and Geotechnical Engineering*. https://doi.org/10.3233/978-1-60750-031-5-2300

DeJong, J. T., Mortensen, B. M., Martinez, B. C., & Nelson, D. C. (2010). Bio-mediated soil improvement. *Ecological Engineering*, *36*(2), 197–210. https://doi.org/10.1016/j.ecoleng.2008.12.029

Delaleux, F., Py, X., Olives, R., & Dominguez, A. (2012). Enhancement of geothermal borehole heat exchangers performances by improvement of bentonite grouts conductivity. *Applied Thermal Engineering*, *33-34*, 92–99. https://doi.org/10.1016/j.applthermaleng.2011.09.017

Dilrukshi, R. A. N., Watanabe, J., & Kawasaki, S. (2015). Sand Cementation Test using Plant-Derived Urease and Calcium Phosphate Compound. *Materials Transactions*, *56*(9), 1565–1572. https://doi.org/10.2320/matertrans.M-M2015818

Dobson, K. J., Coban, S. B., McDonald, S. A., Walsh, J. N., Atwood, R. C., & Withers, P. J. (2016). 4-D imaging of sub-second dynamics in pore-scale processes using real-time synchrotron X-ray tomography. *Solid Earth*, *7*(4), 1059–1073. https://doi.org/10.5194/se-7-1059-2016

Dong, Z., Zhang, X., Tong, C., Chen, X., Feng, H., & Zhang, S. (2022). Grouting-induced ground heave and building damage in tunnel construction: A case study of Shenzhen metro. *Underground Space*, *7*(6), 1175–1191. https://doi.org/10.1016/j.undsp.2022.04.002

Drake Landing Solar Community. (n.d.). *Drake Landing Solar Community*. Retrieved 11 December from

Eze, V. H. U., Eze, E. C., Alaneme, G. U., & Bubu, P. E. (2025). Recent progress and emerging technologies in geothermal energy utilization for sustainable building heating and cooling: a focus on smart system integration and enhanced efficiency solutions. *Frontiers in Built Environment*, *11*. https://doi.org/10.3389/fbuil.2025.1594355

Feder, M. J., Akyel, A., Morasko, V. J., Gerlach, R., & Phillips, A. J. (2020). Temperature-dependent inactivation and catalysis rates of plant-based ureases for engineered biomineralization. *Engineering Reports*, *3*(2). https://doi.org/10.1002/eng2.12299

Gao, Y., He, J., Tang, X., & Chu, J. (2019). Calcium carbonate precipitation catalyzed by soybean urease as an improvement method for fine-grained soil. *Soils and Foundations*, *59*(5), 1631–1637. https://doi.org/10.1016/j.sandf.2019.03.014

Gat, D., Tsesarsky, M., Shamir, D., & Ronen, Z. (2014). Accelerated microbial-induced CaCO3 precipitation in a defined coculture of ureolytic and non-ureolytic bacteria. *Biogeosciences*, *11*(10), 2561–2569. https://doi.org/10.5194/bg-11-2561-2014

Genedy, M., Matteo, E. N., Stenko, M., Stormont, J. C., & Taha, M. R. (2019). Nanomodified Methyl Methacrylate Polymer for Sealing of Microscale Defects

in Wellbore Systems. *Journal of Materials in Civil Engineering*, *31*(7). https://doi.org/10.1061/(ASCE)MT.1943-5533.0002754

Geosciences, T. (n.d.). *MuCalc*. https://www.ctlab.geo.utexas.edu/software/mucalctool/

Go, G.-H., Lee, S.-R., N.V, N., & Yoon, S. (2015). A new performance evaluation algorithm for horizontal GCHPs (ground coupled heat pump systems) that considers rainfall infiltration. *Energy*, *83*, 766–777. https://doi.org/10.1016/j.energy.2015.02.086

Godinho, Ma, Chai, Storm, & Burnett. (2019). Mineral Precipitation in Fractures and Nanopores within Shale Imaged Using Time-Lapse X-ray Tomography. *Minerals*, *9*(8). https://doi.org/10.3390/min9080480

Godinho, J. R. A., & Withers, P. J. (2018). Time-lapse 3D imaging of calcite precipitation in a microporous column. *Geochimica et Cosmochimica Acta*, *222*, 156–170. https://doi.org/10.1016/j.gca.2017.10.024

Gomez, M. G., Martinez, B. C., DeJong, J. T., Hunt, C. E., deVlaming, L. A., Major, D. W., & Dworatzek, S. M. (2015). Field-scale bio-cementation tests to improve sands. *Proceedings of the Institution of Civil Engineers - Ground Improvement*, *168*(3), 206–216. https://doi.org/10.1680/grim.13.00052

Gowthaman, S., Iki, T., Ichinohe, A., Nakashima, K., & Kawasaki, S. (2022). Feasibility of bacterial-enzyme induced carbonate precipitation technology for stabilizing fine-grained slope soils. *Frontiers in Built Environment*, *8*. https://doi.org/10.3389/fbuil.2022.1044598

Gowthaman, S., Koizumi, H., Nakashima, K., & Kawasaki, S. (2023). Field experimentation of bio-cementation using low-cost cementation media for preservation of slope surface. *Case Studies in Construction Materials*, *18*. https://doi.org/10.1016/j.cscm.2023.e02086

Guibert, R., Nazarova, M., Horgue, P., Hamon, G., Creux, P., & Debenest, G. (2015). Computational Permeability Determination from Pore-Scale Imaging: Sample Size, Mesh and Method Sensitivities. *Transport in Porous Media*, *107*(3), 641–656. https://doi.org/10.1007/s11242-015-0458-0

Gustafsson, S. E. (1991). Transient plane source techniques for thermal conductivity and thermal diffusivity measurements of solid materials. *Review of Scientific Instruments*, *62*(3), 797–804.

Gustavsson, M., Karawacki, E., & Gustafsson, S. E. (1994). Thermal conductivity, thermal diffusivity, and specific heat of thin samples from transient measurements with hot disk sensors. *Review of Scientific Instruments*, *65*(12), 3856–3859. https://doi.org/https://doi.org/10.1063/1.1145178

Hamdan, N., Zhao, Z., Mujica, M., Kavazanjian Jr, E., & Ximin, H. (2016). Hydrogel-Assisted Enzyme-Induced Carbonate Mineral Precipitation. *ASCE*. https://doi.org/10.1061/(ASCE)MT.1943-5533

Hammes, F., & Verstraete, W. (2002). Key roles of pH and calcium metabolism in microbial carbonate precipitation. *Reviews in Environmental Science and Biotechnology*, *1*, 3–7.

Handley-Sidhu, S., Sham, E., Cuthbert, M. O., Nougarol, S., Mantle, M., Johns, M. L., Macaskie, L. E., & Renshaw, J. C. (2013). Kinetics of urease mediated calcite precipitation and permeability reduction of porous media evidenced by magnetic resonance imaging. *International Journal of Environmental Science and Technology*, *10*(5), 881–890. https://doi.org/10.1007/s13762-013-0241-0

Hommel, J., Lauchnor, E., Gerlach, R., Cunningham, A. B., Ebigbo, A., Helmig, R., & Class, H. (2015). Investigating the Influence of the Initial Biomass Distribution and Injection Strategies on Biofilm-Mediated Calcite Precipitation in Porous Media. *Transport in Porous Media*, *114*(2), 557–579. https://doi.org/10.1007/s11242-015-0617-3

References

Hou, T. Y., & Lowengrub, J. S. S., M.J. (1994). Removing the stiffness from interfacial flows with surface tension. *Journal of Computational Physics*, *114*(2), 312–338. https://doi.org/https://doi.org/10.1006/jcph.1994.1170

IMARC Group. (2024). *Calcium Chloride Prices, Trend, Chart, Demand, Market Analysis, News, Historical and Forecast Data Report 2024 Edition*. https://www.imarcgroup.com/calcium-chloride-pricing-report

Imran, H. M., Akib, S., & Karim, M. R. (2013). Permeable pavement and stormwater management systems: a review. *Environ Technol*, *34*(17-20), 2649–2656. https://doi.org/10.1080/09593330.2013.782573

Imran, M. A., Nakashima, K., & Kawasaki, S. (2021). Bio-Mediated Soil Improvement Using Plant Derived Enzyme in Addition to Magnesium Ion. *Crystals*, *11*(5). https://doi.org/10.3390/cryst11050516

Javadi, H., Mousavi Ajarostaghi, S., Rosen, M., & Pourfallah, M. (2018). A Comprehensive Review of Backfill Materials and Their Effects on Ground Heat Exchanger Performance. *Sustainability*, *10*(12). https://doi.org/10.3390/su10124486

Javadi, N., T, K., Hamed & Hamdan., N., & Kavazanjian, E. (2018). *EICP Treatment of Soil by Using Urease Enzyme Extracted from Watermelon Seeds* IFCEE 2018,

Khanjani, M., Westenberg, D. J., Kumar, A., & Ma, H. (2021). Tuning Polymorphs and Morphology of Microbially Induced Calcium Carbonate: Controlling Factors and Underlying Mechanisms. *ACS Omega*, *6*(18), 11988–12003. https://doi.org/10.1021/acsomega.1c00559

Khosravi, M., Stenby, E. H., & Yan, W. (2024). Simulation analysis of salt precipitation in large-scale CO2 storage using periodic injection via a horizontal well. *International journal of greenhouse gas control*, *138*. https://doi.org/10.1016/j.ijggc.2024.104263

Kim, D. H., Mahabadi, N., Jang, J., & Paassen, L. A. (2020). Assessing the Kinetics and Pore-Scale Characteristics of Biological Calcium Carbonate Precipitation in Porous Media using a Microfluidic Chip Experiment. *Water Resources Research*, *56*(2). https://doi.org/10.1029/2019wr025420

Kirkland, C. M., Akyel, A., Hiebert, R., McCloskey, J., Kirksey, J., Cunningham, A. B., Gerlach, R., Spangler, L., & Phillips, A. J. (2021). Ureolysis-induced calcium carbonate precipitation (UICP) in the presence of CO2-affected brine: A field demonstration. *International journal of greenhouse gas control*, *109*. https://doi.org/10.1016/j.ijggc.2021.103391

Kirkland, C. M., Thane, A., Hiebert, R., Hyatt, R., Kirksey, J., Cunningham, A. B., Gerlach, R., Spangler, L., & Phillips, A. J. (2020). Addressing wellbore integrity and thief zone permeability using microbially-induced calcium carbonate precipitation (MICP): A field demonstration. *Journal of Petroleum Science and Engineering*, *190*. https://doi.org/10.1016/j.petrol.2020.107060

Kohlhaas, R., Hommel, J., Weinhardt, F., Class, H., Oladyshkin, S., & Flemisch, B. (2025). Numerical Investigation of Preferential Flow Paths in Enzymatically Induced Calcite Precipitation Supported by Bayesian Model Analysis. *Transport in Porous Media*, *152*(12). https://doi.org/10.1007/s11242-025-02240-x

Konstantinou, C., Wang, Y., & Biscontin, G. (2023). A Systematic Study on the Influence of Grain Characteristics on Hydraulic and Mechanical Performance of MICP-Treated Porous Media. *Transport in Porous Media*, *147*(2), 305–330. https://doi.org/10.1007/s11242-023-01909-5

Kozhevnikov, E. V., Turbakov, M. S., Riabokon, E. P., Gladkikh, E. A., & Poplygin, V. V. (2023). Cyclic confining pressure and rock permeability: Mechanical

compaction or fines migration. *Heliyon*, *9*(11), e21600. https://doi.org/10.1016/j.heliyon.2023.e21600

Krevor, S., de Coninck, H., Gasda, S. E., Ghaleigh, N. S., de Gooyert, V., Hajibeygi, H., Juanes, R., Neufeld, J., Roberts, J. J., & Swennenhuis, F. (2023). Subsurface carbon dioxide and hydrogen storage for a sustainable energy future. *Nature Reviews Earth & Environment*, *4*(2), 102–118. https://doi.org/10.1038/s43017-022-00376-8

Kumar, R., Sonnenthal, E., Phillips, A., Cunningham, A., Spangler, L., & Gerlach, R. (2023). Reactive-Transport Model for Thermally Induced Calcium Carbonate Precipitation (TICP) In EGS: Geochemical and Fracture Permeability Evolution in Batch and Fractured-Core Experiments. In Using the Earth to Save the Earth. Geothermal Rising Conference,

Kuznik, F., Virgone, J., & Roux, J.-J. (2008). Energetic efficiency of room wall containing PCM wallboard: A full-scale experimental investigation. *Energy and Buildings*, *40*(2), 148–156. https://doi.org/10.1016/j.enbuild.2007.01.022

Lai, H.-J., Cui, M.-J., Wu, S.-F., Yang, Y., & Chu, J. (2021). Retarding effect of concentration of cementation solution on biocementation of soil. *Acta Geotechnica*, *16*(5), 1457–1472. https://doi.org/10.1007/s11440-021-01149-1

Landa-Marbán, D., Tveit, S., Kumar, K., & Gasda, S. E. (2021). Practical approaches to study microbially induced calcite precipitation at the field scale. *International journal of greenhouse gas control*, *106*. https://doi.org/10.1016/j.ijggc.2021.103256

Lebedev, M., Zhang, Y., Sarmadivaleh, M., Barifcani, A., Al-Khdheeawi, E., & Iglauer, S. (2017). Carbon geosequestration in limestone: Pore-scale dissolution and geomechanical weakening. *International journal of greenhouse gas control*, *66*, 106–119. https://doi.org/10.1016/j.ijggc.2017.09.016

Li, S., Huang, M., Cui, M., Xu, K., & Jin, G. (2023). Thermal and mechanical properties of bio-cemented quartz sand mixed with steel slag. *Biogeotechnics*, *1*(3). https://doi.org/10.1016/j.bgtech.2023.100036

Li, X., Tao, J., & van Paassen, L. A. (2024). Reactive transport modeling of microbial-induced calcite precipitation treatment through shallow underwater injection. *Computers and Geotechnics*, *174*. https://doi.org/10.1016/j.compgeo.2024.106601

Li, Y., Guo, Z., Wang, L., Zhu, Y., & Rui, S. (2024). Field implementation to resist coastal erosion of sandy slope by eco-friendly methods. *Coastal Engineering*, *189*. https://doi.org/10.1016/j.coastaleng.2024.104489

Lin, Q., Neethling, S. J., Dobson, K. J., Courtois, L., & Lee, P. D. (2015). Quantifying and minimising systematic and random errors in X-ray micro-tomography based volume measurements. *Computers & Geosciences*, *77*, 1–7. https://doi.org/10.1016/j.cageo.2014.12.008

Lin, W., Gao, Y., Lin, W., Zhuo, Z., Wu, W., & Cheng, X. (2023). Seawater-based bio-cementation of natural sea sand via microbially induced carbonate precipitation. *Environmental Technology & Innovation*, *29*. https://doi.org/10.1016/j.eti.2023.103010

Liu, L., Gao, Y., Geng, W., Song, J., Zhou, Y., & Li, C. (2023). Comparison of jack bean and soybean crude ureases on surface stabilization of desert sand via enzyme-induced carbonate precipitation. *Geoderma*, *435*. https://doi.org/10.1016/j.geoderma.2023.116504

Ma, G., Xiao, Y., He, X., Wu, S., & Chu, J. (2025). Comparison of biomineralization kinetics induced by bacteria, bacterial enzyme, and soybean enzyme. *Acta Geotechnica*. https://doi.org/10.1007/s11440-024-02479-6

References

Ma, L., Pang, A. P., Luo, Y., Lu, X., & Lin, F. (2020). Beneficial factors for biomineralization by ureolytic bacterium Sporosarcina pasteurii. *Microb Cell Fact*, *19*(1), 12. https://doi.org/10.1186/s12934-020-1281-z

Madigan, M. T., Martinko, J. M., & Bender, K. S. (2018). *Brock Biology of Microorganisms* (15 ed.). New York City: Pearson.

Martinez, A., Huang, L., & Gomez, M. G. (2019). Thermal conductivity of MICP-treated sands at varying degrees of saturation. *Géotechnique Letters*, *9*(1), 15–21. https://doi.org/10.1680/jgele.18.00126

McCartney, J. S., Martinez, A., Huang, L., Gomez, M. G., & Tomac, I. (2020). Enhancement of the thermal conductivity of sands via microbially-induced calcite precipitation. *E3S Web of Conferences*, *205*. https://doi.org/10.1051/e3sconf/202020509011

Medic, J., Atkinson, C., & Hurburgh, C. R. (2014). Current Knowledge in Soybean Composition. *Journal of the American Oil Chemists' Society*, *91*(3), 363–384. https://doi.org/10.1007/s11746-013-2407-9

Meng, H., Shu, S., Gao, Y., Yan, B., & He, J. (2021). Multiple-phase enzyme-induced carbonate precipitation (EICP) method for soil improvement. *Engineering Geology*, *294*. https://doi.org/10.1016/j.enggeo.2021.106374

Menke, H. P., Reynolds, C. A., Andrew, M. G., Pereira Nunes, J. P., Bijeljic, B., & Blunt, M. J. (2018). 4D multi-scale imaging of reactive flow in carbonates: Assessing the impact of heterogeneity on dissolution regimes using streamlines at multiple length scales. *Chemical Geology*, *481*, 27–37. https://doi.org/10.1016/j.chemgeo.2018.01.016

Menke, J. M. a. H. (2021). GeoChemFoam: Direct modelling of multiphase reactive transport in real pore geometries with equilibrium reactions. *Preprint/Early Stage*.

Minto, J. M., Hingerl, F. F., Benson, S. M., & Lunn, R. J. (2017). X-ray CT and multiphase flow characterization of a 'bio-grouted' sandstone core: The effect of dissolution on seal longevity. *International journal of greenhouse gas control*, *64*, 152–162. https://doi.org/10.1016/j.ijggc.2017.07.007

Minto, J. M., Tan, Q., Lunn, R. J., El Mountassir, G., Guo, H., & Cheng, X. (2018). 'Microbial mortar'-restoration of degraded marble structures with microbially induced carbonate precipitation. *Construction and Building Materials*, *180*, 44–54. https://doi.org/10.1016/j.conbuildmat.2018.05.200

Mitchell, J. K., & Santamarina, J. C. (2005). Biological Considerations in Geotechnical Engineering. *Journal of Geotechnical and Geoenvironmental Engineering*. https://doi.org/10.1061/共ASCE禿1090-0241共2005禿131:10共1222禿

Miyake, M., Kim, D., & Hata, T. (2022). Casein-assisted enhancement of the compressive strength of biocemented sand. *Sci Rep*, *12*(1), 12754. https://doi.org/10.1038/s41598-022-16879-9

Mo, Y., Yue, S., Zhou, Q., & Liu, X. (2021). Improvement and Soil Consistency of Sand-Clay Mixtures Treated with Enzymatic-Induced Carbonate Precipitation. *Materials (Basel)*, *14*(18). https://doi.org/10.3390/ma14185140

Montoya, B. M., DeJong, J. T., Boulanger, R. W., Wilson, D. W., Gerhard, R., Ganchenko, A., & Chou, J. C. (2012). Liquefaction mitigation using microbial induced calcite precipitation. GeoCongress 2012: State of the Art and Practice in Geotechnical Engineering,

Mortensen, B. M., Haber, M. J., DeJong, J. T., Caslake, L. F., & Nelson, D. C. (2011). Effects of environmental factors on microbial induced calcium carbonate precipitation. *J Appl Microbiol*, *111*(2), 338–349. https://doi.org/10.1111/j.1365-2672.2011.05065.x

References

Mujah, D., Cheng, L., & Shahin, M. A. (2019). Microstructural and Geomechanical Study on Biocemented Sand for Optimization of MICP Process. *Journal of Materials in Civil Engineering*, *31*(4). https://doi.org/10.1061/(asce)mt.1943-5533.0002660

Mullaney, J., Lucke, T., Trueman, S. J., & Hosseini Bai, S. (2016). The growth and health of street trees planted in permeable pavements. *Acta Horticulturae*(1108), 77–82. https://doi.org/10.17660/ActaHortic.2016.1108.10

Mullin, J. W. (2001). *Crystallization* (4th ed.). Elsevier Science.

Murugan, P., Nagarajan, R. D., Shetty, B. H., Govindasamy, M., & Sundramoorthy, A. K. (2021). Recent trends in the applications of thermally expanded graphite for energy storage and sensors - a review. *Nanoscale Adv*, *3*(22), 6294–6309. https://doi.org/10.1039/d1na00109d

Nayanthara, P. G. N., Dassanayake, A. B. N., Nakashima, K., & Kawasaki, S. (2019). Microbial Induced Carbonate Precipitation Using a Native Inland Bacterium for Beach Sand Stabilization in Nearshore Areas. *Applied Sciences*, *9*(15). https://doi.org/10.3390/app9153201

Nemati, M. (2003). Modification of porous media permeability, using calcium carbonate produced enzymatically in situ. *Enzyme and Microbial Technology*, *33*(5), 635–642. https://doi.org/10.1016/s0141-0229(03)00191-1

Nemati, M., Greene, E. A., & Voordouw, G. (2005). Permeability profile modification using bacterially formed calcium carbonate: comparison with enzymic option. *Process Biochemistry*, *40*(2), 925–933. https://doi.org/10.1016/j.procbio.2004.02.019

Ng, S., & Chu, J. (2024). Frozen enzyme EICP method for more effective soil improvement. *Acta Geotechnica*, *19*(11), 7117–7124. https://doi.org/10.1007/s11440-024-02348-2

Ng, W.-S., Lee, M.-L., & Hii, S.-L. (2012). An Overview of the Factors Affecting Microbial-Induced Calcite Precipitation and its Potential Application in Soil Improvement. *World Acad. Sci. Eng. Technol*, *6*(2), 188–194.

Ni, H., & Meckel, T. A. (2021). Characterizing the Effect of Capillary Heterogeneity on Multiphase Flow Pulsation in an Intermediate-Scale Beadpack Experiment Using Time Series Clustering and Frequency Analysis. *Water Resources Research*, *57*(11). https://doi.org/10.1029/2021wr030876

Noiriel, C., Steefel, C. I., Yang, L., & Bernard, D. (2016). Effects of pore-scale precipitation on permeability and flow. *Advances in Water Resources*, *95*, 125–137. https://doi.org/10.1016/j.advwatres.2015.11.013

Ocłoń, P. (2021). The effect of soil thermal conductivity and cable ampacity on the thermal performance and material costs of underground transmission line. *Energy*, *231*. https://doi.org/10.1016/j.energy.2021.120803

Oko, C. O., Igbo, N. E., Igbo, M. E., & Kalu, J. (2020). Evaluation of Petro Physical Properties of the Reservoirs in XY Field Gulf of Mexico (GOM). *International Journal of Innovative Science and Research Technology*, *5*(11), 703–710.

Okwadha, G. D., & Li, J. (2010). Optimum conditions for microbial carbonate precipitation. *Chemosphere*, *81*(9), 1143–1148. https://doi.org/10.1016/j.chemosphere.2010.09.066

Omarov, K., Alarifi, S. A., Mahmoud, M., Kamal, M. S., Murtaza, M., Humam, A., & AlAhmari, M. M. (2023). Sand consolidation using enzyme-induced carbonate precipitation: new insights on temperature and particle size effects. *Sci Rep*, *13*(1), 15528. https://doi.org/10.1038/s41598-023-42792-w

Otsu. (1979). A Threshold Selection Method from Gray Level Histograms. *IEEE Transactions on Systems, Man, and Cybernetics*, *9*(1), 62–66.

References

Pak, T., Archilha, N. L., Berg, S., & Butler, I. B. (2023). Design considerations for dynamic fluid flow in porous media experiments using X-ray computed micro tomography – A review. *Tomography of Materials and Structures*, *3*. https://doi.org/10.1016/j.tmater.2023.100017

Park, J., & Choi, B.-Y. (2021). Feasibility study of enzyme-induced calcium carbonate precipitation (EICP) for CO2 leakage prevention. *Geosciences Journal*, *26*(2), 279–288. https://doi.org/10.1007/s12303-021-0033-3

Peng, J., & Liu, Z. (2019). Influence of temperature on microbially induced calcium carbonate precipitation for soil treatment. *PLoS One*, *14*(6), e0218396. https://doi.org/10.1371/journal.pone.0218396

Peng, S., Di, H., Fan, L., Fan, W., & Qin, L. (2020). Factors Affecting Permeability Reduction of MICP for Fractured Rock. *Frontiers in Earth Science*, *8*. https://doi.org/10.3389/feart.2020.00217

Polar Night Energy. (n.d.). *Heat and power without burning*. Retrieved 20 February from

Putra, H., Yasuhara, H., Kinoshita, N., Erizal, & Sudibyo, T. (2018). Improving Shear Strength Parameters of Sandy Soil using Enzyme-Mediated Calcite Precipitation Technique. *Civil Engineering Dimension*, *20*(2), 91‑95. https://doi.org/10.9744/ced.20.2.91-95

Putra, H., Yasuhara, H., Kinoshita, N., Neupane, D., & Lu, C. W. (2016). Effect of Magnesium as Substitute Material in Enzyme-Mediated Calcite Precipitation for Soil-Improvement Technique. *Front Bioeng Biotechnol*, *4*, 37. https://doi.org/10.3389/fbioe.2016.00037

Qin, C.-Z., Hassanizadeh, S. M., & Ebigbo, A. (2016). Pore-scale network modeling of microbially induced calcium carbonate precipitation: Insight into scale dependence of biogeochemical reaction rates. *Water Resources Research*, *52*(11), 8794–8810. https://doi.org/10.1002/2016wr019128

Rabbani, A., Ayatollahi, S., Kharrat, R., & Dashti, N. (2016). Estimation of 3-D pore network coordination number of rocks from watershed segmentation of a single 2-D image. *Advances in Water Resources*, *94*, 264–277. https://doi.org/10.1016/j.advwatres.2016.05.020

Rahman, M. M., Hora, R. N., Ahenkorah, I., Beecham, S., Karim, M. R., & Iqbal, A. (2020). State-of-the-Art Review of Microbial-Induced Calcite Precipitation and Its Sustainability in Engineering Applications. *Sustainability*, *12*(15). https://doi.org/10.3390/su12156281

Rajasekar, A., Moy, C. K. S., & Wilkinson, S. (2017). MICP and Advances towards Eco-Friendly and Economical Applications. *IOP Conf. Series: Earth and Environmental Science*, *78*. https://doi.org/doi:10.1088/1755-1315/78/1/012016

Rawson, S. D., Maksimcuka, J., Withers, P. J., & Cartmell, S. H. (2020). X-ray computed tomography in life sciences. *BMC Biol*, *18*(1), 21. https://doi.org/10.1186/s12915-020-0753-2

Ringrose, P. S., & Meckel, T. A. (2019). Maturing global CO(2) storage resources on offshore continental margins to achieve 2DS emissions reductions. *Sci Rep*, *9*(1), 17944. https://doi.org/10.1038/s41598-019-54363-z

Rodriguez-Blanco, J. D., Shaw, S., & Benning, L. G. (2011). The kinetics and mechanisms of amorphous calcium carbonate (ACC) crystallization to calcite, viavaterite. *Nanoscale*, *3*(1), 265–271. https://doi.org/10.1039/c0nr00589d

Salhein, K., Kobus, C. J., Zohdy, M., Annekaa, A. M., Alhawsawi, E. Y., & Salheen, S. A. (2024). Heat Transfer Performance Factors in a Vertical Ground Heat Exchanger for a Geothermal Heat Pump System. *Energies*, *17*(19). https://doi.org/10.3390/en17195003

Salter, P. J., Minto, J., & Dobson, K. J. (2025). Bio-Cementation for Structural and Thermal Soil Enhancement with Retained Hydraulic Conductivity. *Biogeotechnics*. https://doi.org/10.1016/j.bgtech.2025.100216

Salter, P. J., Minto, J. M., Warnett, J., & Dobson, K. J. (2025). The Influence of Density Driven Mixing Mechanisms on Ureolysis Induced Carbonate Precipitation. *InterPore Journal*, *2*(1), IPJ260225–260224. https://doi.org/10.69631/ipj.v2i1nr59

Sang, G., Lunn, R. J., El Mountassir, G., & Minto, J. M. (2023). Meter-scale MICP improvement of medium graded very gravelly sands: Lab measurement, transport modelling, mechanical and microstructural analysis. *Engineering Geology*, *324*. https://doi.org/10.1016/j.enggeo.2023.107275

Sang, G., Lunn, R. J., El Mountassir, G., Minto, J. M., McLachlan, E., Bradley, D., & Henderson, K. (2024). Improving non-uniform gravelly sand using microbially induced carbonate precipitation: An outdoor cubic-meter scale trial by engineering contractors. *Engineering Geology*, *343*. https://doi.org/10.1016/j.enggeo.2024.107791

Sani, A. K., & Singh, R. M. (2020). Response of unsaturated soils to heating of geothermal energy pile. *Renewable Energy*, *147*, 2618–2632. https://doi.org/10.1016/j.renene.2018.11.032

Sarbu, I., & Sebarchievici, C. (2014). General review of ground-source heat pump systems for heating and cooling of buildings. *Energy and Buildings*, *70*, 441–454. https://doi.org/10.1016/j.enbuild.2013.11.068

Sari, P. T. K., Mochtar, I. B., & Chaiyaput, S. (2023). Effectiveness of Horizontal Sub-drain for Slope Stability on Crack Soil Using Numerical Model. *Geotechnical and Geological Engineering*, *41*(8), 4821–4844. https://doi.org/10.1007/s10706-023-02550-1

Schindelin, J., Arganda-Carreras, I., Frise, E., Kaynig, V., Longair, M., Pietzsch, T., Preibisch, S., Rueden, C., Saalfeld, S., Schmid, B., Tinevez, J.-Y., White, D. J., Hartenstein, V., Eliceiri, K., Tomancak, P., & Cardona, A. (2012). Fiji: an open-source platform for biological-image analysis. *Nature Methods*, *9*(7), 676–682. https://doi.org/10.1038/nmeth.2019

Sharshir, S. W., Joseph, A., Elsharkawy, M., Hamada, M. A., Kandeal, A. W., Elkadeem, M. R., Kumar Thakur, A., Ma, Y., Eid Moustapha, M., Rashad, M., & Arıcı, M. (2023). Thermal energy storage using phase change materials in building applications: A review of the recent development. *Energy and Buildings*, *285*. https://doi.org/10.1016/j.enbuild.2023.112908

Sheng Han, Y., Hadiko, G., Fuji, M., & Takahashi, M. (2006). Crystallization and transformation of vaterite at controlled pH. *Journal of Crystal Growth*, *289*(1), 269–274. https://doi.org/10.1016/j.jcrysgro.2005.11.011

Shu, S., Yan, B., Ge, B., Li, S., & Meng, H. (2022). Factors Affecting Soybean Crude Urease Extraction and Biocementation via Enzyme-Induced Carbonate Precipitation (EICP) for Soil Improvement. *Energies*, *15*(15). https://doi.org/10.3390/en15155566

Shu, S., Yan, B., Meng, H., & Bian, X. (2022). Comparative study of EICP treatment methods on the mechanical properties of sandy soil. *Soils and Foundations*, *62*(6). https://doi.org/10.1016/j.sandf.2022.101246

Singh, A., Paramkusam, B. R., & Maiti, P. R. (2021). Cyclic degradation and pore pressure dynamics of EICP treated hydrocarbon contaminated sands. *Soil Dynamics and Earthquake Engineering*, *140*. https://doi.org/10.1016/j.soildyn.2020.106369

Smirnova, M., Nething, C., Stolz, A., Gröning, J. A. D., Funaro, D. P., Eppinger, E., Reichert, M., Frick, J., & Blandini, L. (2023). High strength bio-concrete for the

production of building components. *npj Materials Sustainability*, *1*(1). https://doi.org/10.1038/s44296-023-00004-6

Statista. (2024a). *Average price of crude gypsum on a free-on board (FOB) mine basis in the U.S. from 2010 to 2024*. https://www.statista.com/statistics/219363/wallboard-products-crude-price-in-the-us/

Statista. (2024b). *Average prices for soybeans worldwide from 2014 to 2026*. https://www.statista.com/statistics/675817/average-prices-soybeans-worldwide/#:~:text=This%20statistic%20depicts%20the%20average,U.S.%20dollars%20per%20metric%20ton

Studholme, C., Hill, D. L. G., & Hawkes, D. J. (1999). An overlap invariant entropy measure of 3D medical image alignment. *Pattern Recognition*, *32*(1), 71–86. https://doi.org/https://doi.org/10.1016/S0031-3203(98)00091-0

Sunamp. (n.d.). *World leading thermal energy storage technologies*. https://sunamp.com/en-gb/

Tarantino, A., Minto, J. M., El Mountassir, G., Lunn, R. J., & Ibraim, E. (2019). Micro-continuum modelling of injection strategies for microbially induced carbonate precipitation. *E3S Web of Conferences*, *92*. https://doi.org/10.1051/e3sconf/20199211019

Terzis, D., & Laloui, L. (2018). 3-D micro-architecture and mechanical response of soil cemented via microbial-induced calcite precipitation. *Sci Rep*, *8*(1), 1416. https://doi.org/10.1038/s41598-018-19895-w

Terzis, D., & Laloui, L. (2019). Cell-free soil bio-cementation with strength, dilatancy and fabric characterization. *Acta Geotechnica*, *14*(3), 639–656. https://doi.org/10.1007/s11440-019-00764-3

Theo Renaud, P. V., , G. F., & , L. P. (2021). Heat Transfer Modelling of an Unconventional, Closed-Loop Geothermal Well. *Proceedings World Geothermal Congress*.

Tobler, D. J., Cuthbert, M. O., & Phoenix, V. R. (2014). Transport of Sporosarcina pasteurii in sandstone and its significance for subsurface engineering technologies. *Applied Geochemistry*, *42*, 38–44. https://doi.org/10.1016/j.apgeochem.2014.01.004

Tobler, D. J., Maclachlan, E., & Phoenix, V. R. (2012). Microbially mediated plugging of porous media and the impact of differing injection strategies. *Ecological Engineering*, *42*, 270–278. https://doi.org/10.1016/j.ecoleng.2012.02.027

Tobler, D. J., Minto, J. M., El Mountassir, G., Lunn, R. J., & Phoenix, V. R. (2018). Microscale Analysis of Fractured Rock Sealed With Microbially Induced CaCO

3

Precipitation: Influence on Hydraulic and Mechanical Performance. *Water Resources Research*, *54*(10), 8295–8308. https://doi.org/10.1029/2018wr023032

Todorovic, J., Raphaug, M., Lindeberg, E., Vrålstad, T., & Buddensiek, M.-L. (2016). Remediation of Leakage through Annular Cement Using a Polymer Resin: A Laboratory Study. *Energy Procedia*, *86*, 442–449. https://doi.org/10.1016/j.egypro.2016.01.045

Tourney, J., & Ngwenya, B. T. (2009). Bacterial extracellular polymeric substances (EPS) mediate CaCO3 morphology and polymorphism. *Chemical Geology*, *262*(3-4), 138–146. https://doi.org/10.1016/j.chemgeo.2009.01.006

Turbett, G. R., Hoj, P. B., Horne, R., & Mee, B. J. (1992). Purification and Characterization of the Urease Enzymes of Helicobacter Species from Humans and Animals. *Infection and Immunity*, *60*(12), 5259–5266.

Turk, N., & Dearman, W. R. (1986). A correction equation on the influence of length-to diameter ratio on the uniaxial compressive strength of rocks. *Engineering*

Geology, *22*(3), 293–300. https://doi.org/https://doi.org/10.1016/0013-7952(86)90030-X

Van Paassen, L. A. (2009). *Biogrout, ground improvement by microbial induced carbonate precipitation* TU Delft].

Venda Oliveira, P. J., & Neves, J. P. G. (2019). Effect of Organic Matter Content on Enzymatic Biocementation Process Applied to Coarse-Grained Soils. *Journal of Materials in Civil Engineering*, *31*(7). https://doi.org/10.1061/(asce)mt.1943-5533.0002774

Venuleo, S., Laloui, L., Terzis, D., Hueckel, T., & Hassan, M. (2016). Microbially induced calcite precipitation effect on soil thermal conductivity. *Géotechnique Letters*, *6*(1), 39–44. https://doi.org/10.1680/jgele.15.00125

Vyas, A. M., & Kushwah, G. S. (2023). *Sand Battery: An Innovative Solution for Renewable Energy Storage (A Review)* 2023 IEEE Renewable Energy and Sustainable E-Mobility Conference (RESEM),

Wang, G., Gou, Q., Hao, Y., Zhao, H., & Zhang, X. (2020). Dynamics of Soil Water Content Across Different Landscapes in a Typical Desert-Oasis Ecotone. *Frontiers in Environmental Science*, *8*. https://doi.org/10.3389/fenvs.2020.577406

Wang, H., Miao, L., Sun, X., Wu, L., & Fan, G. (2022). Experimental Study of Enzyme-Induced Carbonate Precipitation for High Temperature Applications by Controlling Enzyme Activity. *Geomicrobiology Journal*, *39*(6), 502–514. https://doi.org/10.1080/01490451.2022.2045649

Wang, H., Sun, X., Miao, L., Cao, Z., Fan, G., & Wu, L. (2022). Induced CaCO3 mineral formation based on enzymatical calcification for bioremediation under different pressure conditions. *Journal of Petroleum Science and Engineering*, *216*. https://doi.org/10.1016/j.petrol.2022.110787

Wang, J., Xu, N., Wang, H., Zhou, R., Shi, Y., Pan, W., Huang, X., & Long, Y. (2025). Laboratory experiment and micro-mechanism analysis on the influence of particle size and distribution on MICP enhanced soil. *Construction and Building Materials*, *471*. https://doi.org/10.1016/j.conbuildmat.2025.140679

Wang, K., Wu, S., & Chu, J. (2023). Mitigation of soil liquefaction using microbial technology: An overview. *Biogeotechnics*, *1*(1). https://doi.org/10.1016/j.bgtech.2023.100005

Wang, Y., Liu, H., Zhang, Z., Xiao, P., He, X., & Xiao, Y. (2019). Study on Low-Strength Biocemented Sands Using a Temperature-Controlled MICP (Microbially Induced Calcite Precipitation) Method. In *New Prospects in Geotechnical Engineering Aspects of Civil Infrastructures* (pp. 15–26). https://doi.org/10.1007/978-3-319-95771-5_2

Wang, Y., Soga, K., DeJong, J. T., & Kabla, A. J. (2019). A microfluidic chip and its use in characterising the particle-scale behaviour of microbial-induced calcium carbonate precipitation (MICP). *Géotechnique*, *69*(12), 1086–1094. https://doi.org/10.1680/jgeot.18.P.031

Wang, Y., Sun, X., Miao, L., Wang, H., Wu, L., Shi, W., & Kawasaki, S. (2024). State-of-the-art review of soil erosion control by MICP and EICP techniques: Problems, applications, and prospects. *Sci Total Environ*, *912*, 169016. https://doi.org/10.1016/j.scitotenv.2023.169016

Wang, Z.-F., Shen, S.-L., Modoni, G., & Zhou, A. (2020). Excess pore water pressure caused by the installation of jet grouting columns in clay. *Computers and Geotechnics*, *125*. https://doi.org/10.1016/j.compgeo.2020.103667

Wang, Z., Zhang, J., Li, Q., Zhang, N., & Feng, W. (2022). A theoretical thermal conductivity model for soils treated with microbially induced calcite precipitation (MICP). *International Journal of Heat and Mass Transfer*, *183*. https://doi.org/10.1016/j.ijheatmasstransfer.2021.122091

Wang, Z., Zhang, N., Cai, G., Jin, Y., Ding, N., & Shen, D. (2017). Review of ground improvement using microbial induced carbonate precipitation (MICP). *Marine Georesources & Geotechnology*, *35*(8), 1135–1146. https://doi.org/10.1080/1064119x.2017.1297877

Wang, Z., Zhang, N., Ding, J., Li, Q., & Xu, J. (2020). Thermal conductivity of sands treated with microbially induced calcite precipitation (MICP) and model prediction. *International Journal of Heat and Mass Transfer*, *147*. https://doi.org/10.1016/j.ijheatmasstransfer.2019.118899

Wang, Z., Zhang, N., Lin, F., Ding, J., & Yang, H. (2019). Thermal Conductivity of Dry Sands Treated with Microbial-Induced Calcium Carbonate Precipitation. *Advances in Materials Science and Engineering*, *2019*, 1–8. https://doi.org/10.1155/2019/4562958

Waqas, H., Muzaffar, A., Amir, F., Ali, A., Hafiz, Q. A., & Yasir, I. (2017). Correlation of maximum laboratory dry density and optimum moisture content of soil with soil parameters. *NFC IEFR Journal of Engineering and Scientific Research*, *5*. https://doi.org/10.24081/nijesr.2017.1.0003

Weinhardt, F., Class, H., Dastjerdi, S. V., Karadimitriou, N., Lee, D., & Steeb, H. (2021). Experimental Methods and Imaging for Enzymatically Induced Calcite Precipitation in a Microfluidic Cell. https://doi.org/10.1029/2020WR029361

Whiffin, V. S., van Paassen, L. A., & Harkes, M. P. (2007). Microbial Carbonate Precipitation as a Soil Improvement Technique. *Geomicrobiology Journal*, *24*(5), 417–423. https://doi.org/10.1080/01490450701436505

Willems, C., Cheng, C., Watson, S., Minto, J., Williams, A., Walls, D., Milsch, H., Burnside, N., & Westaway, R. (2021). Permeability and Mineralogy of the Újfalu Formation, Hungary, from Production Tests and Experimental Rock Characterization: Implications for Geothermal Heat Projects. *Energies*, *14*(14). https://doi.org/10.3390/en14144332

WMO. (2023). *State of Global Climate 2023*. https://library.wmo.int/idurl/4/68835

Wu, C., Chu, J., Cheng, L., & Wu, S. (2019). Biogrouting of Aggregates Using Premixed Injection Method with or without pH Adjustment. *Journal of Materials in Civil Engineering*, *31*(9). https://doi.org/10.1061/(asce)mt.1943-5533.0002874

Wu, R., Chen, P., Liu, X., Xu, H., Zhang, G., & Chen, A. (2024). Investigation of the Long-Term Performance of Waste Backfill Materials of High Thermal Conductivity in Vertical Ground Heat Exchangers. *Buildings*, *14*(6). https://doi.org/10.3390/buildings14061699

Xiao, Y., Tang, Y., Ma, G., McCartney, J. S., & Chu, J. (2021). Thermal Conductivity of Biocemented Graded Sands. *Journal of Geotechnical and Geoenvironmental Engineering*, *147*(10). https://doi.org/10.1061/(asce)gt.1943-5606.0002621

Xiao, Y., Zhao, C., Cui, H., Chen, Y., Wu, B., & Liu, H. (2025). Microscale insights into enzyme-induced carbonate precipitation in rock-based microfluidic chips. *Géotechnique*, *75*(7), 846–857. https://doi.org/10.1680/jgeot.24.01104

Xie, P., Huang, H., He, Y., Zhang, Y., & Wei, J. (2021). Heat Storage of Paraffin-Based Composite Phase Change Materials and Their Temperature Regulation of Underground Power Cable Systems. *Materials (Basel)*, *14*(4). https://doi.org/10.3390/ma14040740

Xu, K., Huang, M., Cui, M., & Li, S. (2023). Retarding effect of cementation solution concentration on cementation ability of calcium carbonate crystal induced using crude soybean enzyme. *Acta Geotechnica*, *18*(11), 6235–6251. https://doi.org/10.1007/s11440-023-01987-1

Xu, K., Huang, M., Liu, Z., Cui, M., & Li, S. (2023). Mechanical properties and disintegration behavior of EICP-reinforced sea sand subjected to drying-

wetting cycles. *Biogeotechnics*, *1*(2). https://doi.org/10.1016/j.bgtech.2023.100019

Xu, K., Huang, M., Zhen, J., Xu, C., & Cui, M. (2023). Field implementation of enzyme-induced carbonate precipitation technology for reinforcing a bedding layer beneath an underground cable duct. *Journal of Rock Mechanics and Geotechnical Engineering*, *15*(4), 1011–1022. https://doi.org/10.1016/j.jrmge.2022.06.012

Yang, W., Sun, T., Zhang, C., & Wang, F. (2023). Experimental and numerical investigations of thermo-mechanical behaviour of energy pile under cyclic temperature loads. *Energy*, *267*. https://doi.org/10.1016/j.energy.2022.126516

Yang, Y., Chu, J., Liu, H., & Cheng, L. (2022). Improvement of uniformity of biocemented sand column using CH3COOH-buffered one-phase-low-pH injection method. *Acta Geotechnica*. https://doi.org/10.1007/s11440-022-01576-8

Yasuhara, H., Neupane, D., Hayashi, K., & Okamura, M. (2012). Experiments and predictions of physical properties of sand cemented by enzymatically-induced carbonate precipitation. *Soils and Foundations*, *52*(3), 539–549. https://doi.org/10.1016/j.sandf.2012.05.011

Zambare, N. M., Naser, N. Y., Gerlach, R., & Chang, C. B. (2020). Mineralogy of microbially induced calcium carbonate precipitates formed using single cell drop-based microfluidics. *Sci Rep*, *10*(1), 17535. https://doi.org/10.1038/s41598-020-73870-y

Zehner, J., Royne, A., & Sikorski, P. (2021). Calcite seed-assisted microbial induced carbonate precipitation (MICP). *PLoS One*, *16*(2), e0240763. https://doi.org/10.1371/journal.pone.0240763

Zehner, J., Røyne, A., Wentzel, A., & Sikorski, P. (2020). Microbial-induced calcium carbonate precipitation: an experimental toolbox for in situ and real time investigation of micro-scale pH evolution. *RSC Advances*, *10*(35), 20485–20493. https://doi.org/10.1039/d0ra03897k

Zeng, C., Veenis, Y., Hall, C. A., Young, E. S., van der Star, W. R. L., Zheng, J.-j., & van Paassen, L. A. (2021). Experimental and Numerical Analysis of a Field Trial Application of Microbially Induced Calcite Precipitation for Ground Stabilization. *Journal of Geotechnical and Geoenvironmental Engineering*, *147*(7). https://doi.org/10.1061/(asce)gt.1943-5606.0002545

Zhang, G., Li, C., & Xiao, S. (2022). Investigation of in situ thermomechanical behaviors of soil around an energy pile with flat dilatometer tests. *Acta Geotechnica*, *17*, 1985–1999. https://doi.org/https://doi.org/10.1007/s11440-021-01349-9

Zhang, J., Yin, Y., Shi, W., Bian, H., Shi, L., Wu, L., Han, Z., Zheng, J., & He, X. (2023). Strength and uniformity of EICP-treated sand under multi-factor coupling effects. *Biogeotechnics*, *1*(1). https://doi.org/10.1016/j.bgtech.2023.100007

Zhang, J., Zhao, C., Zhou, A., Yang, C., Zhao, L., & Li, Z. (2019). Aragonite formation induced by open cultures of microbial consortia to heal cracks in concrete: Insights into healing mechanisms and crystal polymorphs. *Construction and Building Materials*, *224*, 815–822. https://doi.org/10.1016/j.conbuildmat.2019.07.129

Zhang, Q., Ye, W., Liu, Z., Wang, Q., & Chen, Y. (2023). Influence of injection methods on calcareous sand cementation by EICP technique. *Construction and Building Materials*, *363*. https://doi.org/10.1016/j.conbuildmat.2022.129724

References

Zhang, Y., Guo, H. X., & Cheng, X. H. (2014). Influences of calcium sources on microbially induced carbonate precipitation in porous media. *Materials Research Innovations*, *18*(sup2), S2–79–S72–84. https://doi.org/10.1179/1432891714z.000000000384

Zhao, J., Shan, Y., Tong, H., Yuan, J., & Liu, J. (2022). Study on calcareous sand treated by MICP in different NaCl concentrations. *European Journal of Environmental and Civil Engineering*, *27*(10), 3137–3156. https://doi.org/10.1080/19648189.2022.2130439

Zhu, D., Peng, S., Zhao, S., Wei, M., & Bai, B. (2021). Comprehensive Review of Sealant Materials for Leakage Remediation Technology in Geological CO2 Capture and Storage Process. *Energy & Fuels*, *35*(6), 4711–4742. https://doi.org/10.1021/acs.energyfuels.0c04416